A Finite Element and Experimental Analysis of Energy Absorbing Systems under Static and Dynamic Loading Conditions.

by

Edmund Morris B.Eng (Hons)

This thesis is submitted to Dublin City University as the fulfilment of the requirement for award to Ph.D.

Supervisor:

Dr. Abdul Ghani Olabi.

Professor Saleem Hashmi.

School of Mechanical and Manufacturing Engineering

Dublin City University.

2006

Declaration.

I hereby certify that this material, which I now submit for assessment on the programme of study leading to the award of PhD is entirely my own work and has not been taken from the work of others save and to the extent that such work has been cited and acknowledged within the text of my work.

Signed: Edmund Morris ID Number: 53150333

Edmund Morris

Date: 26/9/06

Acknowledgements.

Firstly, I would like to thank Dr. Abdul Olabi for his continuing guidance, patience and excellent assistance for helping me get where I am today. I would like to thank Professor Saleem Hashmi for his expert advice pertaining to my work. Also, I would like to thank the DCU technicians Chris, Jim, Keith and Liam for their support on technical issues regarding the computational and experimental aspects of my work. My gratitude also goes to Professor Michael Gilchrist whom allowed me to use the Zwick Roell Impact Tester based in UCD in which I gained excellent results. I would also like to thank him for his advice in relation to the publication of certain papers, it was much appreciated. I would also like to show my appreciation to Khaled Benyounis for offering me very useful advice and guidance throughout my three years in DCU.

As regards my family, I want to thank each and every one of you for supporting me through extremely difficult times both emotionally and financially, particularly through my 8 years in college. I would especially like to thank my dad whom had an immense influence on me. He is a great father figure and he always supported and encouraged me in difficult situations throughout my life. Last but not least, I want to pay a very special thanks to someone very dear to me, my mother, who brought me into this world and who made me believe in myself.

This thesis is dedicated in loving memory of her –

"A life that touches the heart of others lives on forever."

A Finite Element and Experimental Analysis of Energy Absorbing Systems under Static and Dynamic Loading Conditions.

Edmund Morris B.Eng (Hons).

Abstract.

Knowledge of the behaviour of kinetic energy absorbers or impact attenuating devices is of paramount importance to design and research engineers involved in the automobile, aircraft, spacecraft, and nuclear industries. The main function of these devices is to minimise injury to personnel, to protect cargo that contain hazardous materials or to protect delicate structures from possible impact damage. Such industries require these devices to dissipate kinetic energy into an irreversible form and more importantly, in a controlled and desired manner. The performance of kinetic energy absorbers is significantly affected by various physical parameters such as material properties, mode of deformation and the nature of loading, with strain rate and inertial effects playing an important role due to high velocity impact.

This work details the experimental and computational analysis of circular and oblong shaped kinetic energy absorbers subjected to quasi-static and dynamic lateral loading. The objective of this research was twofold; firstly, to design optimised kinetic energy absorbers which exhibit a desirable force-deflection response and secondly, to increase the specific energy absorbing capacity of such systems. The energy absorbers were in the form of a nested system consisting of a number of mild steel tubes of varying diameters assembled internally. The longitudinal axis of each tube was in parallel and an eccentric tube configuration was used. These systems were compressed laterally using three different devices: a flat platen, a cylindrical rod and a longitudinal line load indenter.

It was found that the optimised designs for both the circular and oblong shaped devices exhibited very desirable features in terms of its force-deflection response. This was achieved by using a simple design modification which was incorporated into the optimised designs. Also, it was concluded that the specific energy absorption capacity of these nested systems can be increased notably by introducing external constraints which subject them to extra volumetric deformation. Both objectives were achieved using the finite element method, the results of which were validated using experimental techniques. It can be concluded that a new family of kinetic energy absorbers in the form of nested metallic systems have been designed which meet the objectives outlined and can thereby contribute to the literature in the field of kinetic energy absorbers.

Nomenclature

Acronym	Definition
CIPSS	Circular In Plane Standard System
SCIPSS	Slotted Circular In Plane Standard System
COPSS	Circular Out of Plane Standard System
SCOPSS	Slotted Circular Out of Plane Standard System
SCIPDS	Slotted Circular In Plane Damped System
CIPDS	Circular In Plane Damped System
OIPSS	Oblong In Plane Standard System
OIPDS	Oblong In Plane Damped System

Roman Symbol	Definition	Units
A	Area under the curve	m^2
B	Strain Displacement Matrix	-
c	Damping Matrix	-
D	Differential Operator Matrix	-
D	Material Constant	s^{-1}
E_{kin}	Kinetic Energy	Nm
E_{int}	Internal Energy	Nm
E_{si}	Sliding Energy (friction energy)	Nm
E_{rw}	Rigid Wall Energy	Nm
E_{damp}	Damping Energy	Nm
E_{hg}	Hourglass Energy	Nm
E_{kin}^{0}	Initial Kinetic Energy	Nm
E_{int}^{0}	Initial Internal Energy	Nm
E_{ext}	External Work Done	Nm

Roman Symbol	Definition	Units
E	Elasticity Matrix	-
e_E	Energy Efficiency	-
e_g	Crush Efficiency	-
F^e	Body Forces	N
K	Stiffness Matrix	-
K^e	Element Stiffness Matrix	-
k	Stiffness Matrix	-
L_o	Original Length of Tube	m
N	Interpolation Shape Function Matrix	-
P_δ	Peak Load	N
Q^{oe}	Equivalent Element Load Vector	-
Q	Yield function	-
q	Material Constant	-
q	Nodal Displacement Vector	-
R	Load vector	-
R^o	External Load Vector	-
r	Displacement Vector	-
S_s^c	Specific Energy Absorbing Capacity	Nm/Kg
t	Time	s
T^e	Work Done by External Forces	Nm
u	Nodal Displacement Vector	-
u	Displacement	m
$\dot{u}$	Velocity	m/s
$\ddot{u}$	Acceleration	m/s^2
V^e	Element Volume	m^3
W_{eff}	Weight Effectiveness	Nm/Kg
δ	Virtual Displacement	m
ε^o	Element Initial Strains Vector	-
$d\varepsilon^{pl}$	Plastic Strain	-

Greek Symbol	Definition	Units
ε	Uniaxial Plastic Strain Rate	1/s
λ	Plastic Multiplier	-
σ^o	Element Initial Stress Vector	-
$\{\sigma\}$	Stress Vector	N/m^2
$\{\sigma_e\}$	Equivalent Stress Vector	N/m^2
σ_y	Yield Stress	N/m^2
$\sigma_1, \sigma_2, \sigma_3$	Principle Stresses	N/m^2
σ_d	Dynamic Flow Stress	N/m^2
σ_s	Static Flow Stress	N/m^2

Table of Contents.

1 Overview.

1.1 Introduction.

Owing to the advances in transport technology and increased spending money pertaining to this, there has been a noticeable increase in the number of transportation vehicles in society. This has resulted in a greater number of fatalities, casualties due to impact collisions of one form or another, not to mention the increase in the financial burden placed on society. Due to these associated increases, society has become more aware and concerned for the safety aspects of transportation. This has fuelled people, particularly in the last few decades, to research and develop energy absorbers to increase the safety aspects by reducing the effect of impact on people and structures. Energy absorbers are not only applicable to the transportation sector but also to other fields of engineering such as the safety of nuclear reactors, safety of oil-rigs and oil-tankers, crash barriers for roadsides, air-drop cargo etc.

1.2 Review of the Literature Available for the Study Energy Absorbers.

To acquire a sound understanding of impact phenomena in relation to transport vehicles and structures, one is required to have sound combined knowledge of related topics such as mechanics of materials, structural mechanics, impact dynamics and plasticity. Various sources of related literature can be found in the following areas which allow interested readers to gain a detailed insight in the area of energy absorbers: The International Journal of Mechanical Science which commenced publication in 1960 has many research papers related in the field of structural mechanics (buckling and deformation of metallic and composite structures under impact). The International Journal of Impact Engineering founded in 1983 is also a strong reference point to study the response of structures and bodies subjected to dynamic loads arising from exposure to blast, collision or other impact events. A more recent journal, namely the International Journal of Crashworthiness was launched in 1996 which is devoted to the crash behaviour of vehicles, structures, materials and impact biomechanics. Relevant literature can also be found in the International Journal of Solids and Structures, International Journal of Pressure Vessels and Piping and the Journal of Thin-Walled Structures. Hardback manuscripts such as Crashworthiness of Vehicles edited by Johnson and Mamalis [1], Structural Impact and Crashworthiness edited by Morton [2], Structural crashworthiness and failure edited by Wierzbicki [3] provide worthwhile reading. Finally, Lu an Yu [4] published a manuscript which combined

fundamental topics pertaining to energy absorbers in order to gain a sound understanding of these devices subjected to impact loading.

Over the last decade due to availability of increased computing power, the finite element method as a form of numerical analysis is being used as a powerful tool to understand the underlying deformation mechanisms and responses of energy absorbers under impact loading. The finite element method can also be used to optimise products in order to achieve a desired output. This can help to eradicate the need to for expensive physical prototyping of such devices. Zukas [5] provided two useful tables to describe the characteristics of the finite element computer code used to simulate high and low velocity impact of structures which are inherent in vehicle crashworthiness, transportation safety etc.

Table 1: Description of Finite Element Code for High Velocity Impact.

The Characteristics of the Computer Code - High Velocity.	
• Mesh Description	Eulerian and Lagrangian.
• Spatial Discretization	Finite Difference / Finite Element.
• Temporal Integration	Explicit.
• Artificial Viscosity	Explicit Formulation.
• Material Model	Incremental elastic-plastic.
• Failure Criteria	Principle stress, strain, plastic work, damage mechanics
• Methods of Material Characterisation	
•	Wave propagation methods.
•	Split Hopkinson Bar.
•	Plate Impact.
•	Bar-Bar impact.
•	Exploding cylinder.
• Boundary Conditions	Reflective and transmittable.
• Initial Conditions	Velocity.

Phenomena associated with High Velocity Impact.	
• Extent of Deformation	Local.
• Modal response	High frequency.
• Loading/response time	Sub milliseconds.
• Strains	>60%.
• Strain rates	$>10^5$/s.
• Failure	Physical separation of material.

Table 2: Description of Finite Element Code for Low Velocity Impact.

The Characteristics of the Computer Code - Low Velocity.	
• Mesh Description	Predominantly Lagrangian.
• Spatial Discretization	Predominantly Finite Element; high order elements
• Temporal Integration	Predominantly implicit.
• Artificial Viscosity	None, or implicit through discretization scheme.
• Material Model	No definitive model.
• Failure Criteria	Plastic flow.
• Methods of Material Characterisation	Conventional hydraulic testing machine.
• Boundary Conditions	Wide selection of internal and boundary constraints.
• Initial Conditions	Force, displacement, velocity.
Phenomena associated with Low Velocity Impact.	
• Extent of Deformation	Global.
• Modal response	Low frequency.
• Loading/response time	Milliseconds-seconds.
• Strains	0.5 – 10%.
• Strain rates	$10^{-2} – 10^{1}$ / s.
• Failure	Large plastic flow.

Ezra [6] detailed a useful overview on the assessment of energy absorbing devices for prospective use in the Aircraft industry. It was outlined that energy absorption can fall into three categories: 1) material deformation, 2) friction and 3) extrusion, hence, the energy absorbers analysed in this work is based on material deformation. The performance of energy absorbers depends on their specific application and suitability in terms of specific energy, crush efficiency, reliability and cost.

1.3 The Multi Collisional Situation for Multi-Transport Bodies.

A transporting body which can be exposed to vehicular impact may be classified into five main classes of vehicle such as motor cars, aircraft/spacecraft, ships, locomotives and escalators/elevators. Such transporting bodies may be considered as a bounding envelope of a well defined outer shape and the contents which are to be transported. To minimise

damage to this bounding envelope and/or to the contents, ideally the relative velocity should be kept to a minimum. In a collision, it is this envelope which experiences the first collision, undergoing inadvertent plastic deformation along with some component fracture. The contents continue to move, due to Newton's first law of motion, while the bounding envelope is arrested and a short time after the impact collision, the contents will collide with the inner surface of the bounding envelope. This is termed a secondary collision. However the driver may be considered as an 'envelope and contents' in respect to protection of the human brain. Damage to the skull may be regarded as damage to the envelope and due to the semi-liquid nature of the brain and its ability to transmit stress waves, the brain contents may also undergo damage, this would be a third collision. This set of phenomena may be referred to as a three-collision situation. In conclusion, the outer surface of any moving body undergoes the primary collision and consecutively the contents within sustain the secondary collision and subsequent collisions [1].

1.4 Impact Crushing of Vehicles: Retardation Rate and Vehicle Length.

Assuming a long moving uniform tubular structure colliding end-on with a flat rigid body experiences a resisting force F = σ A , where σ is the mean crushing stress of the structure and A is the cross sectional area . The mass of the structure is ρAL where ρ is the density and L is the length. Thus according to Newton's second law, the uniform retardation a is $\frac{\sigma}{\rho L}$. Therefore with this idealized approach and if structures differ only in length, the retardation would be inversely proportional to its length. This implies that if injury is to arise from a deceleration that is too great, it can be said stated that ships are relatively safe, locomotives and aircraft are some what less safe and finally, cars are dangerous [1].

1.5 The Momentum Equation.

Usually in an impact event, a collision of rapidly moving vehicles happens in a very short space of time. By examining the momentum equation $F = \frac{mv}{t}$ we can see that the force F is inversely proportional to time t and hence the shorter time t, the greater will be the impacting force F. Also from this equation, we can see that the mass m of the body in question is directly proportional to the impacting force F and therefore any relatively large masses involved in an accident will generate large impact forces upon collision. As a consequence, this large impact force will cause a significant acceleration (or deceleration) and hence serious damage to the occupants of the vehicle or the structure in question. It is

usual to analyse energy absorption of structures and materials in terms of kinetic energy dissipation. Ideally, to dissipate the kinetic energy upon impact in a controlled fashion, the longer time t in which the impacting force prevails, the gentler will be the reactive force required to absorb this kinetic energy upon impact [4].

1.6 Principles in the Design of Energy Absorbing Systems.

Metallic tubes are one of the most commonly used structural elements due to their common occurrence and availability. Circular tubes for example can dissipate elastic energy and plastic work through different modes of deformation resulting in different energy absorption responses. Such methods of deformation comprise of lateral compression, lateral indentation, axial crushing and tube splitting. In the design of such energy absorbing devices involving any of the above deformation modes, the designer must be aware of the following six principles in order to achieve the best possible design [4]. Such a design will ultimately serve to play a role in mitigating the effect of kinetic energy arising from the moving mass impinging on the structure or personnel in question.

A) Irreversible Energy Conversion:

Upon impact structures/materials should be able to convert kinetic energy into non-recoverable energy (inelastic) such as plastic deformation, viscous energy dissipation, and friction or fracture energy.

B) Restricted and Constant Reactive Force:

Upon deformation of a structure from impact, the resisting force (and hence the corresponding decelerating force) should remain constant during the stroke length of deformation. In doing so, injury to personnel or damage to structures subjected to these decelerating forces can be minimised.

C) Low Cost and Easy Installation:

Energy absorbing devices are usually one-shot items, i.e. once they are deformed due to plastic displacement, they are discarded and replaced, and hence the ability to manufacture, install and maintain these devices economically is of paramount importance since the design of energy absorbers is always constrained by the available budget.

D) Long Stroke Characteristic:

From the simple expression $W = F * D$ where W is the energy absorbed, F is the applied force and D is the line of action in which the force acts, we can see that in order to

maximise the energy absorbing capacity along the acting line of the force, the displacement stroke of the deforming structure should be as long as possible.

In the study of rings/tubes as a form of energy absorbing devices, it is useful to describe the behaviour using performance characteristics. For example, the crush efficiency can be defined as the stroke length divided by its characteristic length. Therefore in this work, the mean diameter of a ring/tube can be taken as the characteristic length.

E) Stable and Repeatable Deformation Mode.

To ensure the reliability of the device in its service, the deformation mode and specific energy absorbing capacity should be stable and repeatable. It should be noted that energy absorbers usually absorb dynamic loads but these loads introduce uncertainties such as load magnitude, pulse shape, direction and distribution, hence these energy absorbers should be designed such that they are insensitive to these characteristics mentioned.

F) Light Weight and High Specific Energy Absorption Capacity:

In the area of vehicle design, which may consist of energy absorbers, high specific energy absorption is of vital importance since any increase in weight reduces the specific energy absorption capacity while also increasing fuel consumption and air pollution, which is not desirable due to environmental reasons.

1.7 The Consequences of Vehicular Accidents/Crashworthiness.

In the study of energy absorbers as a means of absorbing kinetic energy, the term crashworthiness needs to be explained. This term refers to the quality of response the structures undergoes when involved in an impact collision situation. The less damage the structure and/or its occupants experience after the collision, the higher the crashworthiness value of that structure.

The consequence of an impact collision can be categorised in the following way:

1) Injury to people or damage to other living organisms: This relates to the physical and/or psychological injury imposed on the vehicles occupants and/or people external to the vehicle.

2) Damage to vehicle structure: This relates to the dissipation of kinetic energy in the form of plastic deformation which is irreversible. Fire can also cause a large degree of destruction to the vehicle in question.

3) Damage to cargo: This can relate to oil spills due to a tanker grounding or damage of cargo due to inadequate tie-down strength during transportation.

4) Damage to other objects that exist in the environment: Examples such as buildings, trees, guardrails etc [7].

1.8 Injury to the Human Body: Human Head.

The human head is one of the more serious injuries personnel can acquire as a result of vehicular crashes. The types of head injury that occur are usually in the form of scalp damage, skull fracture, extra cerebral bleeding and most severely, brain damage. It is exceedingly difficult to protect the head, one of the most complicated portions of the human body. Other life threatening injuries such as neck, chest spine damage may also occur. Therefore it is desirable to minimise these injuries by designing appropriate energy absorbers, whether it be in the automobile, aircraft or nuclear industries. [1].

1.9 Vehicle Accidents Statistics.

One of the worlds major health problems are motor vehicle related and this is a huge economic loss to society. For example in the US vehicular crashes cause more death between the ages of 1 and 34 than any other type of injury of disease. Motorway related accidents account for 95% of all transportation death in comparison to 2% for rail and 2% for air-accidents. In 2003, there were an estimated 6,328,000 police reported traffic crashes in which 42,643 people were killed and 2,889,000 were injured. This works out at 117 people dying each day or one every twelve minutes in vehicular road crashes. [8]

According to the ATSB (Australian Transport Safety Bureau) the annual cost of road crashes by type of crash are as follows: 7.15 Billion AUD for serious injury crashes, 2.92 Billion AUD for fatal crashes, 2.44 Billon AUD for property damage and 2.47 Billion AUD for minor injury crashes. Altogether, the annual cost of road crashes in Australia was approximately 15 Billion AUD. [9]

In the UK, the Metropolitan police services have reported 3,431 road fatalities, 35,975 serious injuries and 263,198 slight injuries in the year of 2002. The most common vehicular crash been the rear-end collision resulting in a high number of whiplash injuries which can cause debilitating back, neck and nerve injuries. [10]

Figure 1-1 illustrates the number of people killed on Irish roads due to impact collisions obtained from the Garda National Traffic Bureau. As expected drivers are the largest category to suffer fatalities followed by passengers, pedestrians motor cyclists and pedal cyclists respectively [11].

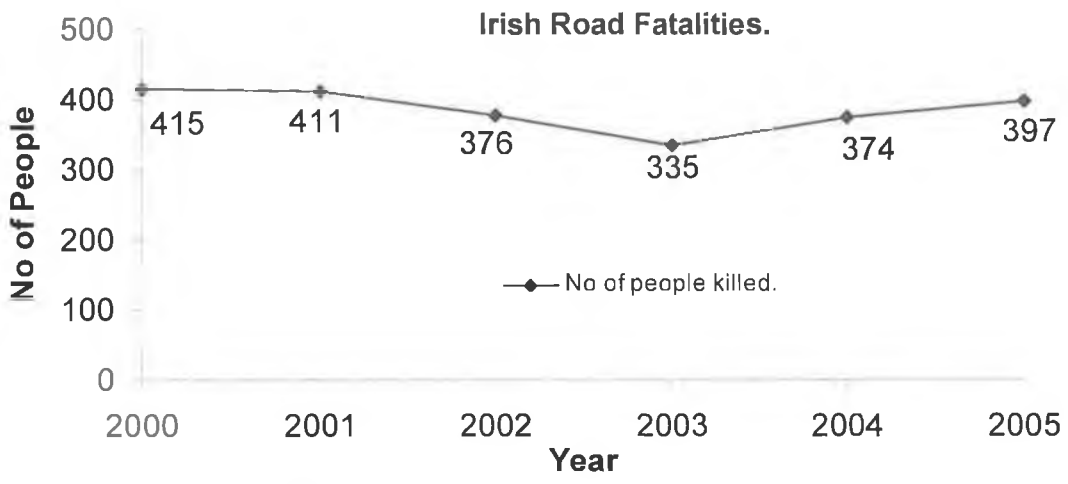

Figure 1-1: A graph illustrating the number of people killed on Irish roads per year.

1.10 Objective of the Present Research.

The objective of this research was to focus on two of the six design principles outlined in section 1.6:

- The first and most important objective is based on the design of nested metallic energy absorbers which exhibits a constant reactive force. This may be in the form of a *monotonically increasing* response or a *monotonic / rectangular* shaped response, the latter of which is the more desirable feature that the design engineer should strive to achieve.
- To accomplish this, various designs of nested systems were modelled and simulated using finite element techniques and analysed to determine the shape of the force-deflection response. These standard designs were verified using experimental techniques in order to ensure the validity of the numerical models. Consequently, numerous modified designs based on the standard models were simulated and analysed until the desired rectangular force-deflection response was achieved.
- The new optimised designs were then verified using both quasi-static and dynamic experimental techniques. In addition to this, an attempt was made to increase the crushing displacement of an energy absorber as outlined in section 0, by modifying the standard designs such that the displacement stroke is increased. This was attained by elongating the circular tubes plastically to form oblong tubes. In doing so, the energy absorption response can be maximised.
- The second and final objective was to maximize the specific energy absorbing capacity of nested metallic systems by means of exposing more volume within the energy absorbers to plastic deformation. In doing so; the resulting energy

absorption can be increased. These numerical models were also verified using experimental techniques in order to endure their validity.

- It should be noted that increasing the stroke length can also maximise the energy response as outlined in the preceding paragraph, however this is treated as a separate entity.
- Finally, Table 3 in Appendix Two. illustrates an overview of the various energy absorbers conducted experimentally under both quasi – static and dynamic loading conditions. Various schematics of the different systems are also provided in Figure 10-1 in Appendix One.

1.11 Summary of Chapter One.

- A number of areas which are important and relevant in the study of energy absorbers have been identified and various important sources of literature were outlined.
- The mechanics of the momentum equation have been explored in relation to impacting bodies and suitable approaches to minimise injury to personnel or to fragile structures were outlined.
- Six principles in the design of energy absorbers were briefly outlined which provide simple but crucial guidelines that should be adhered to.
- The consequences of vehicular accidents were outlined and a description was given on the various forms of head injury that may occur due to impact collisions.
- For the automobile industry, it is useful to have some knowledge of vehicular accident statistics in various countries, how these accidents contribute to worldwide health problems and its knock-on effect in terms of economic loss.
- The objectives of the study in relation to the six principles have been detailed.

2 Literature Review.

2.1 Introduction.

The objective of this chapter is to examine and highlight previous research, similar or related to this work conducted by various researchers and also, to develop a basic understanding of metallic tube type energy absorbers subjected to various modes of deformation. The chapter is divided into six sections with the first section providing a brief overview of energy absorbers which can be categorised into Type one and Type two structures. The remaining five sections detail the various modes of deformation that can be applied in order to create functional energy absorbers. The various researchers analysed these devices using theoretical, experimental and computational techniques.

2.2 Type I and Type II Structures.

Calladine and English [12] studied the strain rate and inertial effects on the collapse of two types of structures. Typically the lateral or axial compression of rings/tubes can represent a Type I structure while axial loading of two steel plates clamped at either end represent a Type II structure. The authors revealed the latter are sensitive to both strain rate and inertial effects; hence in the scale modelling of these structures, special care of these parameters must be taken into account. It was confirmed that inertial effects are sensitive only to the initial 'straightness' of the specimen i.e. the two plates clamped together, hence from an inertial point of view, the lateral compression of ring/tubes were not considered.

Zhang and Yu [13] provided a detailed discussion on the velocity sensitivity of a Type II structure using theoretical techniques. An attempt was made by the authors to provide a quantitative account of the effects of both strain-rate and inertia on such a structure and to provide a comparison with the results obtained by Calladine [12].

Tam and Callidine [14] presented a thorough analysis on the response of Type II structures with respect to inertia and strain-rate effects. The work details the study by means of analytical and experimental methods. The aim of the authors was to remove the various limitations imposed on the work by Calladine [12] since their work was not entirely definitive. As a means of improving the phenomena behind the response of Type II structures, the authors endeavoured to introduce more variables such as changing the material and size of the specimens and consequently a more comprehensive theoretical analysis is provided using the concept of dimensional analysis.

Su et al [15] analysed theoretically the effects of inertia and elasticity on a Type II structure when subjected to impact loading. An elastic-perfectly plastic constitutive relation for the

material was employed to predict the peak load which is important in the design of energy absorbers. The mathematical model consists of four compressible elastic-plastic rods connected by four elastic-plastic hinges as shown in Figure 2-1. Also, Figure 2-2 depicts Type I and Type II structures. It was identified that the dynamic behaviour of a type II structure is significantly different from its quasi-static counterpart even when the effect of strain-rate is neglected; thereby suggesting that inertia played an important role in this problem. In a companion paper [16], the effect of strain-rate was analysed with the aid of the Cowper-Symonds relation. It was found that strain-rate effects play an equally important role as inertial effects on the dynamic behaviour of Type II structures. The combined effects of inertia and strain-rate cause the peak load to be much higher than its quasi-static counterpart and the resulting displacement is much smaller. The authors observed the strain energy stored in the structure (strain-rate dependant) due to increase in the yield stress which expands the range of elastic deformation, is notably larger than that of a structure which is made of a rate-independent material. Therefore when strain-rate effects are involved, elasticity plays a very important part in the structures response to impact loading.

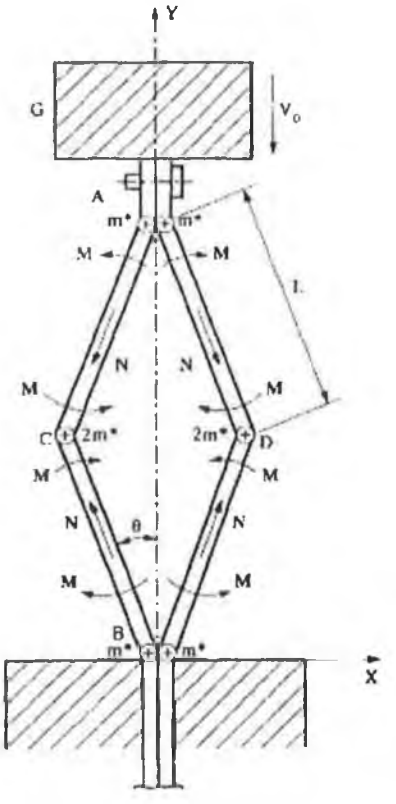

Figure 2-1: A structural model for analysing a typical type II structure [16].

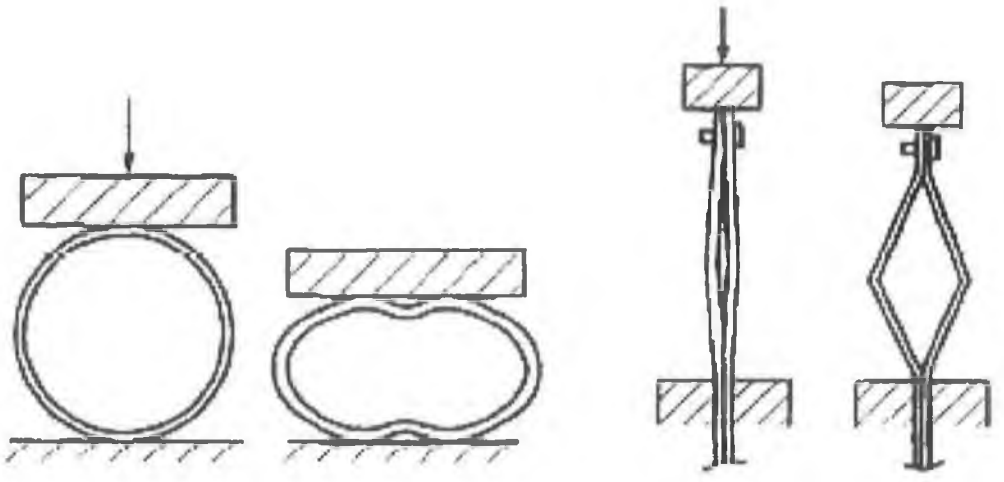

Figure 2-2: Type I and Type II structures: Initial and final stages respectively [16].

2.3 Axial Loading / Buckling.

Reid [17] provided an insight into the various modes of deformation that can be achieved from the axial compression of ductile material such as mild steel. Discussion was made on the axial splitting, inversion and buckling modes of deformation in which attention was given to the gross plastic deformation of the various specimens. Also, some reference was made to thin-walled tubes filled with polyurethane foam which can increase the specific energy absorption capacity of such a devise without compromising it weight.

Reid and Reddy [18] researched the quasi - static and dynamic crushing of tapered sheet metal tubes of rectangular cross-section using mainly experimental techniques with the assistance of theoretical methods to obtain the mean crushing loads of such devices. It appears that tapered tubes offer the distinct advantage of absorbing off-axis/oblique loads which are commonly encountered in vehicular collisions. Good estimates of the mean crushing forces were estimated in both the quasi - static and dynamic cases. The authors concluded that tapered tubes as opposed to straight tubes are the preferred energy absorber since they are more efficient in absorbing energy from oblique impacts and are less likely to fail by global buckling.

A detailed experimental analysis was carried out on the quasi-static axial compression of thin-walled circular aluminium tubes by Guillow et al [19]. A classification chart was developed to characterise the various modes of deformation for D/t= 10 – 450. Empirical formulae were developed using the average force which was non-dimensionalised. The effect of filling aluminium tubes with polyurethane foam was also briefly examined.

Wang and Lu [20] subjected a cylindrical shell to axial impact velocities in the region of 300 m/s and discovered a particular deformation mechanism termed the 'Mushrooming'

effect which caused the walls of the shell to thicken. It appears that the high end impact deformation mechanism generates a complex problem and the only feasible means of analysing such problems is by means of experiment and finite element analysis. Figure 2-3 shows a typical cylindrical specimen subjected to high impact velocity. In general, three modes of deformation can occur; dynamic progressive folding for thin tubes under low impact, end mushrooming with folds formed away from the striking end at medium velocity and finally mushrooming and wrinkling for thick tubes at high velocity. The authors stated that direct correlation between actual and numerical results were difficult because no well-verified material model existed with the ability to capture the dynamic failure of these structures at high impact velocities. However the current simulations which predicted the deformation mechanism at lower impact velocities offer valuable information to the designer since this information can be difficult to achieve through experimental testing alone.

Figure 2-3: **Mild steel samples: Deformation states at velocities of 385 m/s, 277 m/s, 227 m/s, 173 m/s and 0 /ms respectively [20].**

Hsu and Jones [21] investigated the response of thin-walled circular stainless steel, mild steel and aluminium alloy tubes subjected to quasi-static and dynamic axial loading. Stainless steel was chosen to examine the effects of strain rate properties and strain hardening. Aluminium alloy 6063 T6 was chosen in order to assess the influence of inertia while the materials strain-rate sensitivity are negligible and the choice of mild steel in order to assess the outcome of strain-rate effects with negligible strain hardening. Comparisons were made on the performance of these three material types in terms energy absorbing efficiency and capacity. It was found that stainless steel tubes absorb the most energy per unit volume however; its dimensionless energy absorbing efficiency was the lowest of the

three materials. The aluminium alloy was found to be the most efficient but absorbing the least energy per unit volume.

An experimental study on axially preloaded steel tubes subjected to lateral impacts was examined by Zeinoddini et al [22]. A common occurrence which employs steel tubes is the collision of supply ships with bracing members of offshore oil rigs. It was commented by the author that tubular structural members will be carrying their usual service loads before impact accidents occur. Therefore, it is very important to understand the effect of preload on a tubular member if the effect of impact damage is to be accurately measured. The work describes an experimental program in which axially preloaded tubes were subjected to lateral impact at their mid-span using a drop weight test rig as shown in Figure 2-4. It was concluded that pre-loading has a substantial effect on the level of damage when combined with lateral impacts. It should be noted that only one influential parameter, the magnitude of axial preload, was adjusted during the testing. However, other parameters such as indenter shape, impact location, orientation of indenter and the residual stress level inherent within the tube can also have a marked effect on the response of such devices when subjected to lateral impact. Therefore more work would be needed in this area in order to obtain a greater understanding of how the various parameters interact with each other and their effect on the output response.

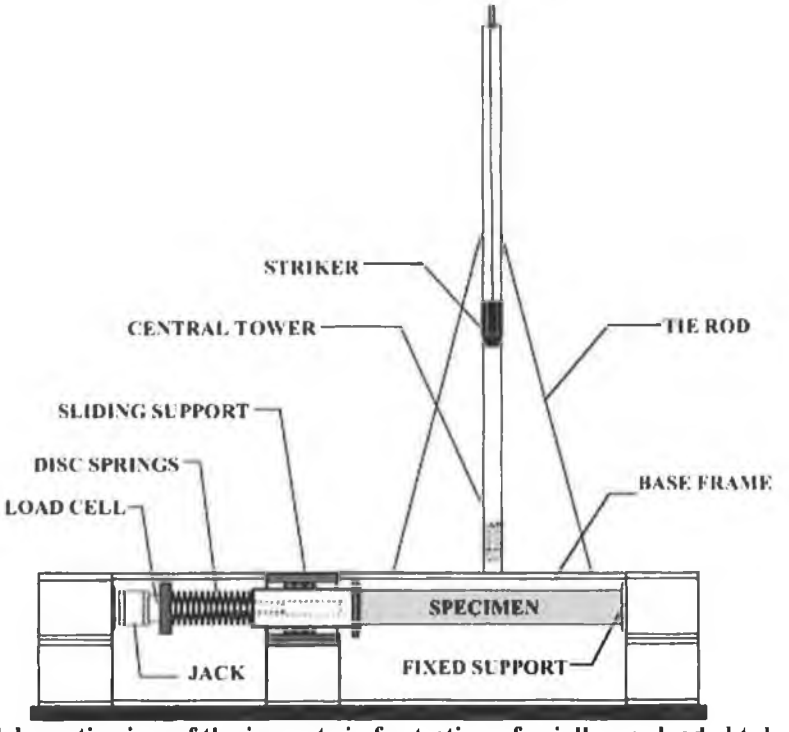

Figure 2-4: **Schematic view of the impact rig for testing of axially pre-loaded tubes subject to lateral impact [22].**

Langseth et al [23] presented finite element simulations validated by experimental findings of quasi - statically and dynamically axially loaded square aluminium extrusions. Excellent correlations were achieved based on using isotropic elasticity, the Von Mises yield criterion, the associated flow rule and non-linear isotropic strain hardening. The uniaxial tensile test was used to obtain the yield stress and strain hardening characteristic of the aluminium tubing. In order to generate a symmetric folding mechanism, the authors incorporated a 'trigger' mechanism into the numerical model as shown in Figure 2-5. Once the simulations were validated, a parametric study was used to study the effect of the impact velocity of the projectile on the response parameter, the mean load. It was shown that the response parameter was an increasing function with respect to an increase in impact velocity and the mass ratio of the specimen to the projectile had no effect on this parameter.

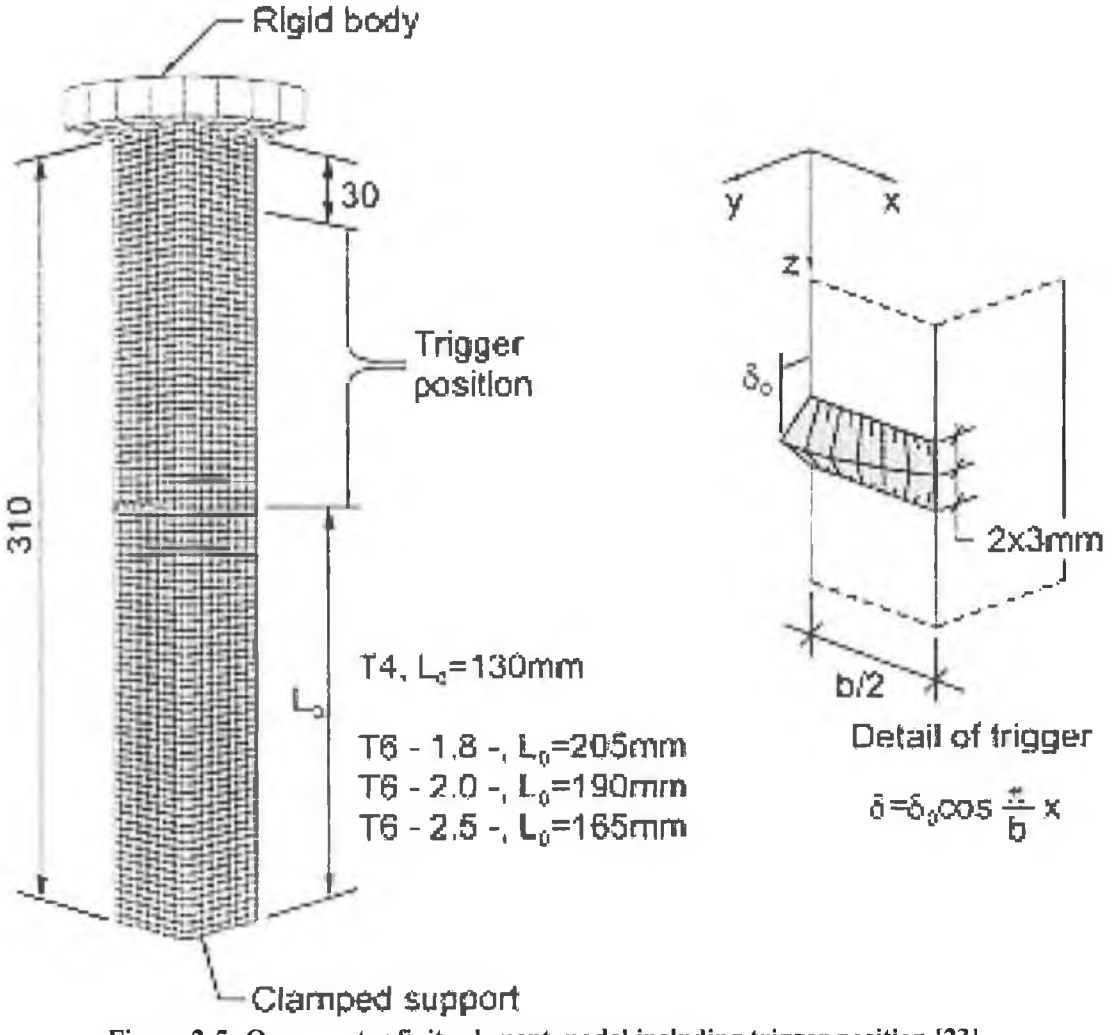

Figure 2-5: One quarter finite element model including trigger position [23].

The axial collapse of aluminium alloy extruded polygon sections was analysed by Rossi et al [24] in order to develop an understanding of the post buckling behaviour of such systems subjected to impact loads. Their goal was to achieve this using the finite element software package LS-DYNA. The work was divided into two sections; firstly to validate the numerical results related to thin walled aluminium square tubes with existing published experimental data and secondly, to analyse the post-buckling deformation features such as symmetric and asymmetric behaviour. It was found that the numerical study can accurately predict both these modes of deformation, as with the prediction of the mean dynamic crushing force and permanent displacement which were within +/- 5% of actual values. Figure 2-6 illustrates the final post buckling deformation state of a hexagonal sectioned model.

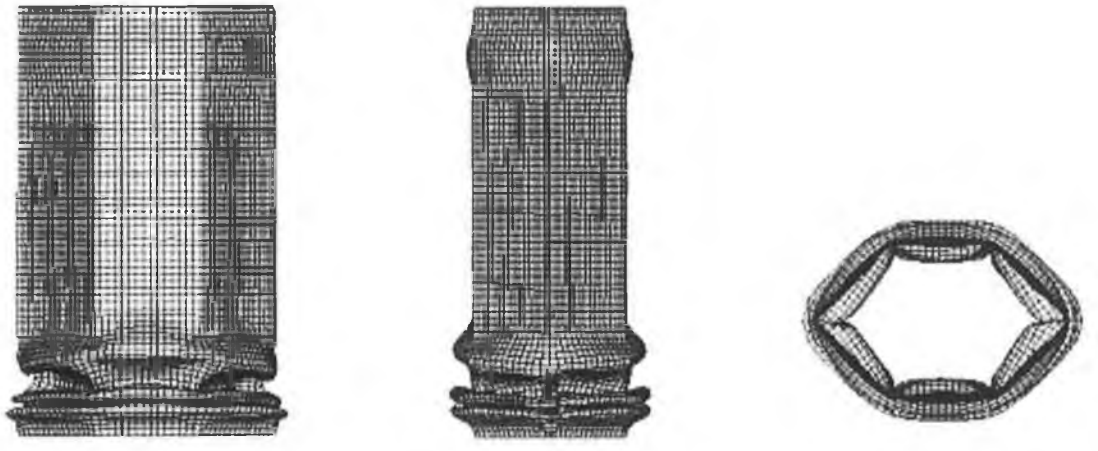

Figure 2-6: Final post-buckling deformation of an LS-DYNA hexagonal section model [24].

A numerical study was reported by Nagel and Thambiratnam [25] on the impact response and energy absorption of tapered thin-walled tubes. An advantage of such devices is that they are proficient at absorbing oblique as well as axial loads which is desirable in the design of energy absorbing devices. The main aim of the paper was to compare the energy absorption response of both the tapered and straight specimens subjected to quasi-static and dynamic loading conditions. Also, a detailed account was reported on the effect of inertia of both specimens. It was found that tapered tubes are less influenced by lateral effects than straight tubes. A factorial study was used to determine the influence of the input parameters such as thickness, angle of taper, impact velocity on the output response. It was concluded that the most important parameters that control the energy absorbing response are the taper angle and wall thickness. Figure 2-7 and Figure 2-8 illustrates a finite element model of a straight and taper energy absorber in its initial and final deformed conditions respectively.

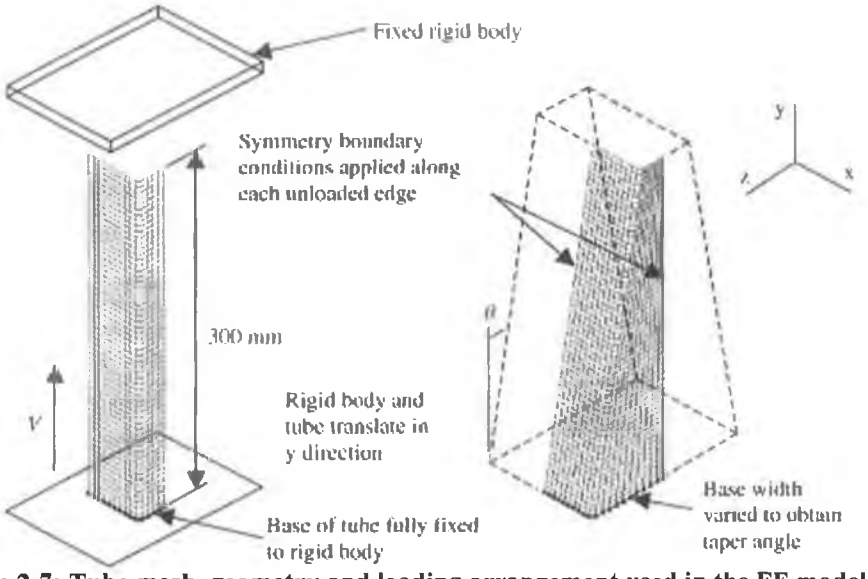

Figure 2-7: Tube mesh, geometry and loading arrangement used in the FE model [25].

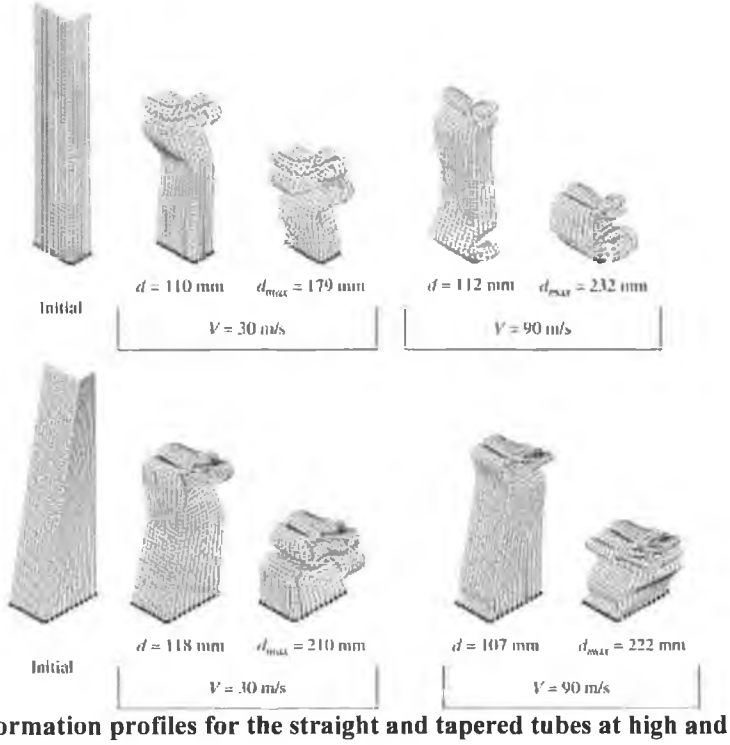

Figure 2-8: Deformation profiles for the straight and tapered tubes at high and low impact velocities [25].

In a companion paper by the same authors [26], attention was given to the behaviour of tapered tubes consisting of either a straight, double taper, triple taper and finally frusta (four tapered sides). The aim of the work was to study the dynamic energy absorption response of these devices under impact loading conditions. The simulations showed that triple tapered tubes have the highest energy absorption capacity followed by straight tubes and frusta's. However, it was realised that increasing the number of tapers decreases the specific energy absorption per unit mass. Therefore it appears that straight tubes are the

most efficient for absorbing energy when mass or weight is an important consideration. In general, this work was seen as outlining the advantages of using tapered tube devices that may be used in the transportation industry. Additional study was conducted by the same authors [27] on the energy absorption response of tapered thin-walled tubes. The primary outcome of the work was to gather important research information that will facilitate the design engineer in creating efficient tapered tube type energy absorbers.

In another work Nagel and Thambiratnam [28] applied the concept of the tapered wall tube to enhance the energy absorption of an existing VFPS (Vehicle Frontal Protection Systems). Such a device acts to minimise the damage that may be caused due to animal strike. Since there is a gap between the chassis rail of the vehicle and the VFPS, it was decided that this space could be utilised to improve the energy absorption feature of the VFPS by introducing one of three possible energy absorption mechanisms. These three mechanisms consisted of the axial crushing of honeycomb, recoverable semi-rigid foams and tapered tubes. The outcome of using each mechanism and their suitability in the enhancement of the VFPS is to be published in a future paper.

The axial collapse of mild steel and aluminium tubes with cut-outs and in both their 'as-received' and 'annealed' conditions was analysed by Gupta and Gupta [29]. Tubes of various L/D and D/t ratios were compressed quasi - statically in an Instron machine. The cut-outs were in the form of holes. It was found that without the presence of holes, the mode of deformation is dependant on the initial state of work hardening and the ensuing annealing process. With the presence of holes, it was discovered that the peak load of such devices is reduced. It was concluded that employing such devices offers the advantage of much longer crush displacements before the onset of Euler buckling that may occur which is usually associated with the crushing of tubes with large L/D ratios.

2.4 Axial Inversion.

Colokoglu and Reddy [30] analysed the strain-rate and inertial effects in the free inversion of mild steel circular tubes using experimental and theoretical techniques. As expected, the strain-rate sensitivity of mild steel was found to increase the resistance to inversion. Inertial effects were found to play a part in both resisting and assisting the force required for the inversion process. Just prior to impact between the striker mass and the tube mass, it was realised that the acceleration of both masses acted in the same direction as the compression force thereby assisting the inversion process. After impact to initiate plastic deformation, a net acceleration between both masses occurred giving rise to a resisting force and hence the

final force required to invert the tube was greater. The Cowper-Symonds relation was used to predict the dynamic flow stress of the material. It was found that the predicted values over-estimated the actual values, reason being that the values of the empirical constants D and q appeared to be too low for the strains that occur in the inversion process.

Webb et al [31] reported the simulation of quasi - static and dynamic axial inversion of tubes consisting of square or circular cross sections. A comparison of results between experimental and numerical was made. It was emphasised how the finite element method plays important role in the design of such energy absorbers and to assist in the planning of experimental programmes and therefore optimising the outcome of such procedures.

Kinkead [32] endeavoured to provide an improved correlation between the theory and experimental results for the external inversion of metallic circular tubes. An attempt was made to incorporate 'engineering strain' as opposed to 'natural strain' previously practiced in the current theory (Limit Analysis) of predicting the collapse load of inverted tubes. In doing so, a simpler technique was developed which was seen as acceptable since it introduces no large errors when correlated with experimental results. It was suggested by the author that the modified theory would help to engineers to design energy absorbing devices based on the inversion process with more precision and assurance.

The plastic deformation mechanism of circular metallic tubes during quasi-static internal inversion was analysed by Reid and Harrigan [33]. Attention was given by the authors to a particular mode of deformation called tube nosing which appears not to have received much attention in the area of energy absorbers. Tube nosing is analogous to force internal inversion with the exception that a larger die radius is employed to encourage increasing hoop compression in the leading edge of the tube. Figure 2-9 shows the deformed shapes produced by ABAQUS and that of experiment. Excellent agreement was found between the numerical code and experiment for the quasi-static internal inversion of mild steel tubes. Figure 2-10 shows the force-deflection response of such a tube.

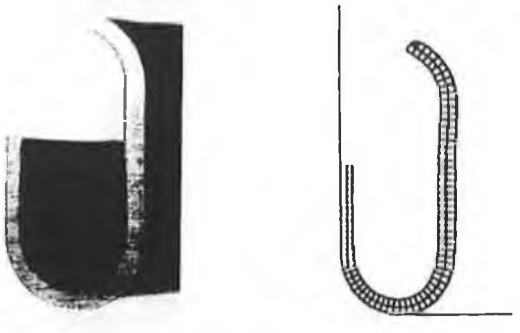

Figure 2-9: Comparison between ABAQUS and experimental deformed shape [33].

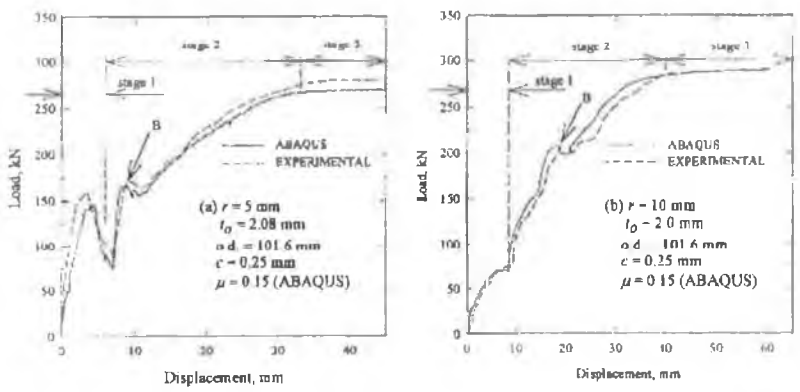

Figure 2-10: **Experimental results and ABAQUS solutions for quasi-static internal inversion of mild-steel tubes [33].**

In similar work by Harrigan et al [34], the inertial effects due to dynamic loading was analysed in the internal inversion of tapered circular metal tubes and also on aluminium honeycomb material. It was found that for both cases, lateral inertial effects cause early load peaks to occur due to impact loading, the magnitude of which is governed by the material of the tube and the honeycomb wall. The aim of analysing two different structures was to shed light on the role of inertia on the magnitude of force generated in these particular energy absorbing devices.

An experimental and theoretical analysis of an external inversion process was investigated by Miscow and Al-Qureshi [35]. The aim of the paper was to define a method to predict the dynamic inversion load based on quasi-static experimental data. Experiments were carried out on copper and brass tubes. Figure 2-11 shows a typical schematic of a tube subjected to an external inversion process.

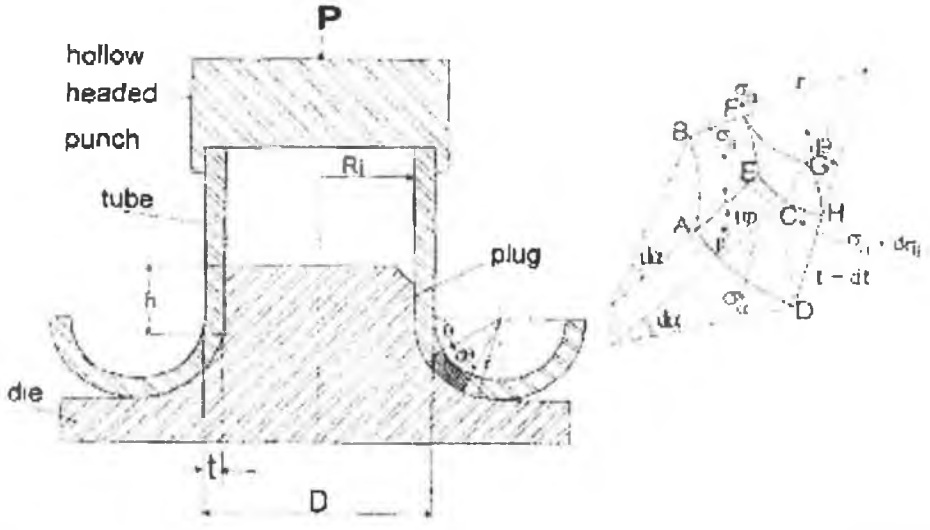

Figure 2-11: **Schematic cross-section of test arrangement for tube inversion process and stress on an infinitesimal element [35].**

It was noted by the authors that the predicted theoretical results such as collapse and dynamic mean load, impact velocity should not be taken as absolute values since other variables stemming from the dynamic testing have an influence on the estimated values. However despite this, it was found that a reasonable agreement existed between the theory and experiments.

2.5 Axial Splitting / Tearing.

The axial splitting of circular metallic tubes was conducted by Reddy and Reid [36] experimentally to examine the mode of deformation and it corresponding force-deflection response. The splitting of tubes can be seen as the intermediate between axial compression and axial inversion. The mean crushing force is somewhat lower, however high crush efficiencies in the order of 95% can be achieved. This type of device was analysed both quasi - statically and dynamically using experimental techniques. The splitting of tubes is a function of die radius and frictional effects, therefore these parameters can be modified in order to achieve a desired rectangular shaped force-deflection which is ideal in the design of energy absorbers. It was noted by the authors that a combination of a rectangular force-deflection response plus the successful operation over a wide range of tube properties and geometries cannot be coexistent with inversion or buckling modes associated with axial inversion and axial compression respectively.

Lu et al [37] sought to obtain experimentally the tearing energy required in a typical square tube splitting process. This provided a challenge for the authors since the tube splitting process involves a number energy dissipating mechanism such as frictional, bending and tearing. It was discovered that, by 'pre-cutting' some corners to different lengths, the tearing energy could be determined. This was possible because the tearing energy per unit torn area can be related to the ultimate tensile stress of the material and the strain to fracture.

Jiang et al [38] scrutinised the size effects in the axial tearing of circular tubes during quasi-static and impact loading conditions. This was achieved by using the Buckingham Pi theorem and consequently 11 input and 8 output parameters were identified. The effect of strain hardening on the mild steel tube specimens under dynamic loading conditions was analysed. It was found that the material strain hardening effects do not comply with the geometrically scaling laws. Divergences of approximately 11% to 57% were observed between the measured and predicted values as a result of this incompliance. The author therefore endeavoured to develop a new scaling law which included the effects of strain

hardening by means of a correction factor relating the dynamic yield stress of the prototype and the model. As a result of this solution, the corresponding deviations were reduced to a significant level. Consequently, this new scaling law can be seen as valuable for the design and safety assessment of larger scale energy absorbing devices.

Stronge et al [39] subjected a square tube to an axial force using a die causing the corners to split and curl outwards as deformation proceeds. For this mode of deformation, the energy absorbing mechanisms are fracture energy due to splitting, plastic deformation as large deformations ensue and frictional energy as the tube is passed over the mandrel. The advantage of using a square tube over any other cross section such as circular tubes stems from the fact that the specific energy dissipation processes can be separated analytically. This helps to accurately analyse the contribution and influence of each mechanism when a square is subjected to an axial splitting process.

Huang et al [40] detailed the study of energy absorption in splitting square metal tubes both theoretically and experimentally. The scope of the work was to analyse the role played by the different energy absorbing mechanisms in the splitting of these devices. Such mechanisms are bending, tearing and frictional energy and equations were presented for each mechanism. Good agreement was found between the actual observed values and those of theory. It was concluded that tubes which exhibit both splitting and curling behaviour may be used as efficient energy absorbing devices. Figure 2-12 depicts a typical theoretical model of subjecting a square tube against a pyramidal die.

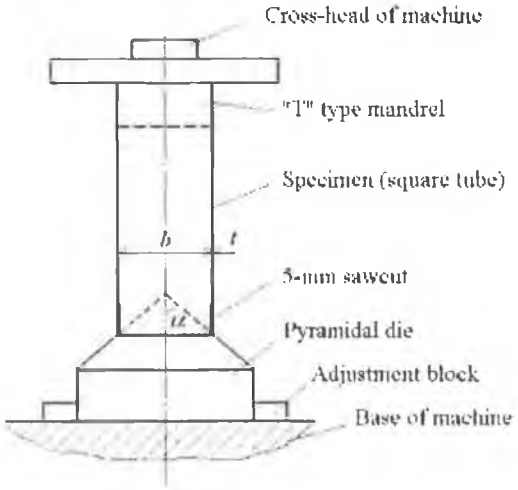

Figure 2-12: Sketch of the experimental set-up [40].

In a companion paper by Huang et al [41], a detailed discussion using both experimental and theoretical techniques in the axial splitting and curling of circular metal tubes was presented. Mild steel and aluminium tubes were pressed axially on a series of dies, each

with different semi-angles. An approximate analysis based on simplifying assumptions was successfully used to predict the number of propagated cracks, the curling radius and the applied force. Figure 2-13 illustrates photographs of typical mild steel specimens after testing. As in the previous work, the three energy dissipating mechanisms such as bending, tearing and frictional were involved in the splitting process. Each mechanism was separated in order to clarify the role of each in such a splitting process which may be of benefit to the designer.

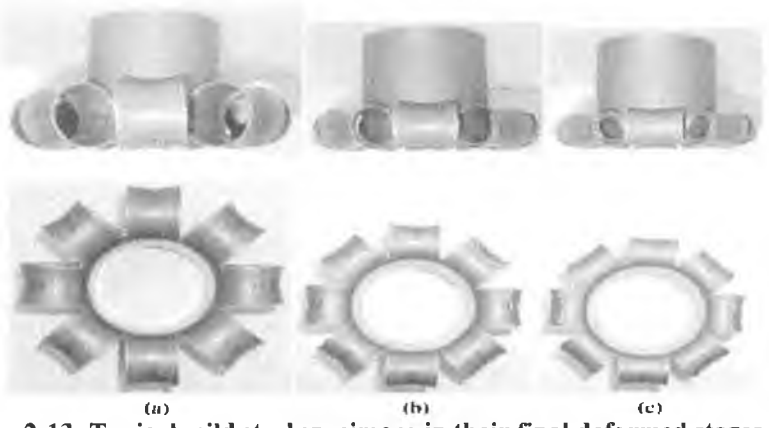

Figure 2-13: Typical mild steel specimens in their final deformed stages [41].

2.6 Lateral Indentation.

Sowerby et al [42] was one of the early authors to analyse the diametric compression of circular rings by point loads. An etching technique was used to reveal the specific shapes of the plastic hinges on the loaded ring. The collapse load was estimated using the slip-line field theory. This theory assumes rigid-perfectly plastic material, quasi-static loading and plain strain deformation. This theory can provide analytical solutions to problem involving large deformations and velocities discontinuities; however, it is limited only to simple structures. The author discovered that the collapse load predicted on the basis of this theory correlated well with experimentally measured values.

The response of 'square' cross-sectioned tubes under both quasi-static and dynamic lateral loading was conducted by Jing and Barton [43]. Experimental tests consist of tubes of two different thicknesses loaded in either a fully clamped or simply supported condition. The authors conducted research into the collapse mechanism of the tubes and the relationship between energy absorption and tube deflection. In the dynamic cases, velocities of up to 6m/s were loaded upon the specimens. DYNA3D, the finite element code, was used to simulate the dynamic events. It was found that the mode of deformation for the thin-walled tube is more complex since a 'wrinkle' occurs which indicates local buckling. This occurs in both the quasi-static and dynamic cases. There was a tendency for the numerical code to

under-predict the deformations of the fully clamped tube because complete constraint of the tube ends did not actually occur; instead, slippage occurred at the constrained ends. However, correlation between the numerical code and actual test proved to be satisfactory, considering that the impact loading conditions and interaction between the impinging mass and specimen tend to be complex. Most importantly, the author briefed that little difference was found between the mode of deformation of tubes tested statically and dynamically and hence the energy absorption capacities could be predicted using quasi-static methods. However, the issue of strain rate sensitivity of the material in question to accurately capture the force-deflection response must be considered.

Thomas et al [44] identified three modes of deformation for a tube subjected to quasi-static lateral load at its mid-span. The first mode was a pure crumpling phase in which the load increased sharply until a point was reached in which deflection of the base of the tube occurred. This load was defined as the maximum pure crumpling load. A bending and crumpling phase was identified as the second mode in which further crumpling of the tube combined with bending between the supports was observed. During this period of deformation, the force decreased slightly before increasing to its maximum. The final mode of deformation was structural collapse in which the maximum load was reached causing the tube to collapse followed by a drop in load. The drop in load was characterized by a large rotation of the tube ends about their supports.

In a companion paper [45], the authors experimentally observed the crushing of circular tubes by centrally opposed wedge shaped indenters. According to the authors, the purpose of this investigation was to facilitate the assessment of the energy absorbing capacity of tubes in an impact situation where the speed of deformation is not large enough to generate significant inertial forces. Upon experimentation, the author identified three modes of deformation. 1) Ring mode for short lengths ($L < 1.5D$), it was found that deformation was similar to that of a compressed ring and consist of hoop bending about the generators. 2) Transitional mode for medium lengths. In this case, the deformation starts as a quasi-static ring mode then proceeds into a mode involving 'increasing ovality' as the deformation continues. 3) Reversing Ovality for moderate to long length of tubes. In this mode, membrane stretching in the axial direction was observed and this behaviour predominates close to the indenters accompanied by axial bending of the generators.

Finally, in a concluding paper, [46] obtained further experimental results concerning the transverse loading of simply supported tubes. In this work, the authors examined the surface stresses generated by means of the brittle lacquer technique using strain gauges. By

using this technique, the authors revealed that the use of simple plastic beam theory to predict bending failure cannot be justified. They discovered that unlike normal beam problems, the section of the tube over hanging the supports play an active part in the force-deflection response.

Zhao et al [47] examined the quasi-static compression of metallic thin walled rings with arc shaped supports. The author conducted an approximate analysis based on the 'Equivalent Structure Technique' (EST) which provides an upper bound solution and is used to determine the collapse load of tubes under point loading. From experiments, they discovered that the structure deforms elastically followed by a soften stage. It was found from the theoretical analysis that the collapse load of the structure was accurately predicted, in addition to locating the positions of the plastic hinges.

Zhao and Fang [48] subjected metallic thin walled rings with arc shaped supports to a symmetrically concentrated impact load. Two supports of arc angle sixty and ninety degrees were used in which it was discovered that the deformation was a five-hinge model. The arc angle played an important role in the final deformation of the ring, such that the smaller the arc angle at the support, the bottom of the rings would become slightly straightened. Upon analysis of the high-speed photos from the Cranz-Schardin camera system, the authors found that the final deformation always occurred during the first impact of the drop hammer and that any rebounds of the hammer did not affect the final shape of the rings. An approximate linear relationship was found between the drop height and the residual displacement between the impact face and the base of the rings. Finally they noted that similar deformation mechanisms were found between the quasi-static and dynamic cases concluding that the impact velocity was low and hence strain rate could be neglected.

Reid and Bell [49] identified that the role of strain hardening is significant in the post collapse response of rings loaded by opposing point loads. The use of the 'Plastica' theory by the authors to analyse the plastic regions gives an insight into the effects of strain hardening and that the particular solution observed indicates certain limitations on the earlier rigid perfectly theory [56] derived for the compression of rings between flat plates.

Lu [50] conducted a study of the crushing of mild steel tubes by two indenters, the tubes having four different diameters and lengths. The aim of this paper was to conduct experiments using various combinations of diameter D and length L of the tubes, to obtain the corresponding force-deflection curves and thereby develop some empirical relations. It should be noted however that the empirical relations derived are only valid within the range of tube parameters and loading conditions specified in the work.

Liu et al [51] analysed both experimentally and numerically the dynamic behaviour of ring systems subjected to pulse loading. The objective of the work was to understand the mechanism of elastic stress wave propagation and how the elastic energy is distributed throughout the ring system owing to the physical nature of the ring systems. The explicit version of the numerical code via LS-DYNA was used to simulate the pulse loaded ring systems. The experimental procedure was carried using a modified split Hopkinson pressure bar test system (SHPB). Figure 2-14 illustrates such an apparatus with a finite element model of the system depicted in Figure 2-15. It was found that the numerical results were in good agreement with those of experiment. The main conclusion of the work showed that energy redistribution is primarily affected by the thickness of the rings and not by the loading duration or the number of rings in the system.

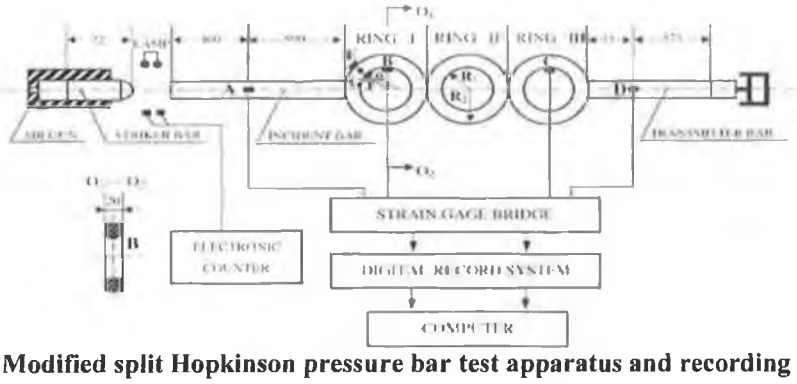

Figure 2-14: Modified split Hopkinson pressure bar test apparatus and recording system [51].

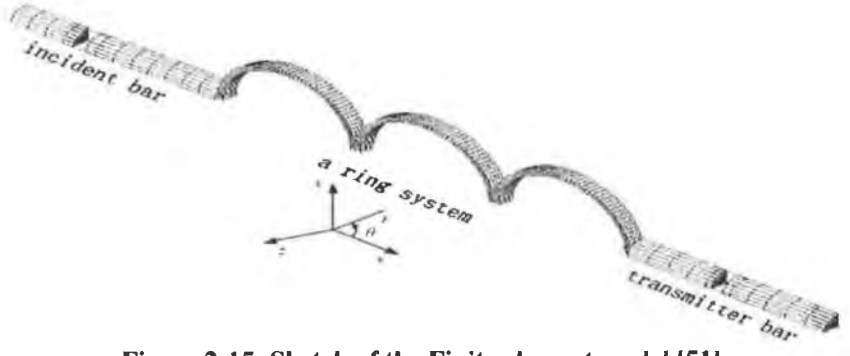

Figure 2-15: Sketch of the Finite element model [51].

Shim and Stronge [52] examined the post-collapse response of ductile, thin walled tubes compressed between cylindrical indenters. It was discovered that, depending on the radius of curvature of the indenters along with the degree of side constraints, the post collapse behaviour of laterally compressed tubes can either be stable (*monotonically*- increasing) or unstable (*monotonically*- decreasing). Post collapse stability increases as the curvature of the indenter becomes larger. It was found that side constrained tubes compressed between

cylindrical indenters are sensitive to load imperfections. Small shear forces are generated which in addition to the normal applied forces, initiate an asymmetric mode of deformation, therefore exhibiting a post collapse response that is initially unstable.

Kardaras and Lu [53] used the finite element method for the investigation of large deformations of thin cylindrical tubes subjected to point loads about its mid-span. The objective of the paper was to produce a detailed report on the effect of large deflections, stationary and travelling plastic hinges, rigid body rotations of the generators, change in curvature and finally the dominant strains that occur such as membrane and bending. It was concluded that the finite element method can be a powerful tool in providing detailed results on the aforementioned parameters that would have been more difficult using experimental or analytical techniques.

A theoretical insight into the indentation of tubes under combined loading was provided by Wierzbicki and Suh [54]. The combined loading was in the form of lateral indentation, bending moments and axially applied forces. The most significant conclusion was that the resistance of the tube to local indentation depends strongly on the type of boundary conditions such as axially and rotationally restrained and unrestrained tubes. The theoretical solutions provided an accuracy of 10%-20% in comparison with experimentally measured values.

Ghosh et al [55] analysed both theoretically and experimentally the deformation response of mild steel rings and short tubes of various thickness and lengths loaded centrally by opposed conically-headed cylindrical punchers. The mild steel specimens were tested in their 'as-received' and 'annealed' conditions. The aim of the work was to predict the collapse load of these short tubes as a function of yield stress, ultimate tensile strength and strain to failure. It was found that short rings of L/D ratio of up to 1.5 exhibited 'knee-shaped' response in the plastic stages of deformation. It is clear that the initial structural collapse load occurs somewhere along this 'knee-shaped' region. Interrupted annealed testing provided a very useful way of removing the strain-hardening of the short tubes and hence the initial collapse can be calculated for moderately deformed tubes. Finally they concluded that the prediction of the increase in the horizontal diameter as loading proceeds becomes more accurate for tubes with decreasing L/D ratios. This was achieved by using the rigid-perfectly plastic assumption and concept of plastic hinges.

2.7 Lateral Compression / Flattening.

Several researchers have analysed analytically the compression of a tube between rigid platens and proposed a deformation mechanism to describe the lateral compression process. DeRuntz and Hodge [56] analysed the compression of a mild steel tube subjected to quasi-static lateral loading. A rigid perfectly plastic material model was used to predict the load deformation response. The geometrical component of stiffening was accounted for in the theoretical model. However the rate of increase was under-estimated, this was due to omission of the material strain hardening phenomena. The deformed contour of the tube consists of four circular arcs which maintain their original radius and plastic deformation occurring at the hinges only.

Redwood [57] endeavoured to include the effects of material strain hardening which was excluded by DeRuntz. A rigid linear strain hardening material model as opposed to a rigid perfectly plastic model was used to predict the force and energy absorption response.

The effect of strain hardening was further examined by Reid and Reddy [58]. The theoretical model produced by the authors is based on a rigid linearly strain hardening material model and is the most accurate one to date. The authors improved the strain hardening prediction by replacing the localised hinges with an arc in which its length changes with deflection. Hence this theoretical model accounted for both the geometric and material strain hardening effect. An important dimensionless parameter which was developed governs the shape of the force-deflection curve. This parameter is defined as 'mR' and is a function of the yield stress in tension, the mean radius R of the tube, the strain hardening modulus E_p and the thickness t. According to Reid and Reddy it may be possible to maximise the energy absorbing capacity by choosing appropriate tube dimensions such that the 'mR' value is minimised since this is a function of tube geometry.

Reddy [59] studied the phenomenon associated with the crushing of metal tubes between rigid plates. Aluminium and mild steel tubes were compressed laterally in an Instron machine. It was found that intermittently annealed tubes corresponded closely to the perfectly plastic theory. This was due to the fact that strain-hardening effects were gradually removed due to this annealing process. For the 'as-received' tubes and the 'once' annealed tube, a large discrepancy was found between those of experiment and the perfectly plastic theory. This was due to existence of strain hardening in both materials which is not accounted for in the theory.

Gupta et al [60] conducted a comprehensive experimental and computational investigation of circular metallic tubes subjected to quasi-static lateral loading. Specimens analysed

consisted of both mild steel and aluminium tubes with different diameter to thickness ratios. Their corresponding force-deflection responses were obtained and examined in detail. An in depth description was provided on the deformation mechanism of a tube compressed between flat rigid platens. A quarter cross section of a typical tube was divided into zones to help describe the deformation mechanism as shown in Figure 2-16.

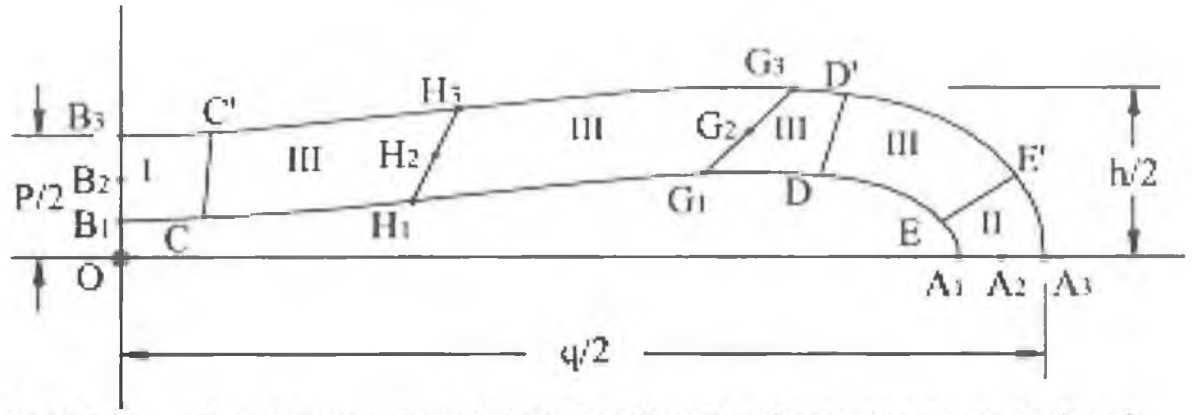

Figure 2-16: Quarter cross-section of a typically deformed profile showing zones and points of interest [60].

Avallel [61] examined the strain field generated during the lateral compression of aluminium tubes and proceeded to verify the various theoretical models such as [56, 57 and 58], it was found that the latter accounted for all the main features observed experimentally, hence this model seems the most realistic in describing the actual behaviour of the tube both qualitatively and quantitatively.

Reddy and Reid [62] examined both theoretically and experimentally the quasi-static lateral compression of a tube constrained so that its horizontal diameter is prevented from increasing. This is a way of increasing the specific energy absorption capacity of the tube by introducing more plastic hinges into the structure. Also the relationship between a single tube and a system of tubes with different configurations was investigated. It was found that the energy absorbed by a closed system (side constraints) is three times more than that of an open system (no constraints); however the maximum deflection of the former is less that that of an open system. Overall it can be concluded that the introduction of side constraints and creating a closed system is a feasible method of increasing its energy absorbing efficiency.

The compression of copper tubes with R/t ratios from 1.5 to 7.5 between flat plates were studied experimentally by Reid and Reddy [63]. It was found that the 'Plastica' theory developed by the authors could be used to predict the ring compression behaviour for a ring having an *R/t* value greater than 3.5. It was found that rings with *R/t* ratio less than 3.5 did

not correlate very well with the experiments, this was due to the fact that shear effects as opposed to bending effects was the dominant mode of deformation, and this is not accounted for in the aforementioned theory.

Reddy and Reid [64] proposed a method to calculate a more realistic force-deflection curve using a rigid linearly work hardening material model. These tubes were also compressed laterally between rigid platens. It was suggested that an average value of strain hardening modulus could be used to calculate the parameter *mR* [58], therefore these two parameters would considered constant throughout the deflection range. However, it has been further proposed that if the variation of strain hardening modulus with strain is known, this could be used to update *mR* at each load step or load increment and thus obtaining a more realistic load-deflection characteristic. It was suggested that the method described above could be used as a basis for obtaining some of the material properties from a ring compression test.

A nested system analysed by Shrive et al [65] consisted of two concentric rings with a layer of smaller tubes between them, the axis of all tubes been parallel. Tack welding was used to attach the rings to the concentric tubes. It was found that increases in system stiffness, maximum load and energy absorption was apparent as the level of tack welding increased. From the impact loading experiment, it was found that full deformation did not occur but maximum opposing forces similar to the quasi-static case were achieved.

A nested system in the form of orthogonal layers of aluminium and mild steel tubes under static lateral compression was investigated by Johnson et al [66]. Such an orthogonal layer consists of a row of tubes stacked upon each other with every second row rotated 90 degrees. The authors concluded that nested ductile tube systems play an important part in producing a *monotonic* load-deflection response and that the systems which exhibit cracks after loading only induce oscillations into the response and do not produce catastrophic failure in the system as a whole.

Reid et al [67] investigated the role of system inertia of nested energy absorbers in the form of a line of rings upon impact. Dynamic test were carried out on a simple one-dimensional apparatus. This apparatus consisted of a horizontal base plate with two guide rails in which the sledge is attached and impinges the line of rings. The sledge is propelled by means of a cartridge gun which can achieve velocities in the range 30-120 m/s. Various systems of rings were experimentally tested, with changing parameters such as different materials, diameter to thickness ratios and the number of rings. They concluded that system inertia has the effect of controlling the time over which particular elements of the system deforms.

Also, they concluded that the insertion of discrete masses in the form of small plates between the rings further increases the time in which the system deforms. This is seen as a more efficient use of the basic energy absorbing element.

The effect of strain rate on the dynamic lateral compression of tubes was examined by Reid and Reddy [68].They endeavoured to find a relationship between the dynamic and quasi-static load-deformation characteristic of thin walled tubes compressed laterally between rigid platens. This was achieved by using an existing quasi-static large deflection theory developed by Reid and Reddy [58]. The theory was modified to include the effects of strain rate due to the loading rates applied. They found that the modified theory can give a good estimate of the dynamic load-deflection response and subsequently the energy absorbing capacity of mild steel and aluminium tubes.

Nested systems in the form of a line of rings subjected to end impact loading were examined by Reid and Reddy [69]. The authors were principally concerned with identifying the main mechanism which controls the deformation of such systems. Upon experimentation, the main parameters were identified and varied, thereby leading to a suggestion for the construction of a mathematical model of the system. It was found that in low speed impact testing on tube systems, the effect of inertia was secondary; therefore the design of energy absorbing systems could be achieved provided that the material strain rate was taken into account. Reddy et al [70] described experiments in which a variety of one dimensional systems with free distal ends, as opposed to fixed ends, were subjected to lateral impact by a rigid projectile. An elastic–plastic structural shock wave theory, which employs a bilinear material model to describe the collapse behaviour of the rings, was used to analyse the deformation of typical ring chain systems.

Reid et al [71] experimentally analysed the energy absorbing capacity and collapse mechanism of braced metal tubes compressed under rigid platens. Their aim was to design an energy absorber to cope with both the 'redirectional' and 'trapping' of vehicles involved in side impacts. 'Redirectional' is a term used to describe where the vehicle moved back onto its original line of travel after the collision has occurred. 'Trapping' involves catching the vehicle so as to prevent the probability of secondary conflicts occurring with oncoming traffic. They conducted initial investigations on small scale components to explore the possibility of achieving the desired response by introducing tension members across the diameters of the mild steel tubes in question. Both single and double braced tubes of various angles were analysed. They stated that the response of a braced tube, whether singly or doubly, is sensitive to the direction of loading, however; significant enhancement

in the energy absorbing capacity of such systems can be achieved. Full scale testing was also carried out on the double braced tubes used as a cluster in a modular crash cushion.

The finite element simulation of the lateral compression of aluminium tubes was conducted and analysed by Leu [72]. An elastic-plastic model based on the updated Lagrangian algorithm was employed to predict the buckling, punch load and deformed geometries of aluminium tubes. The static explicit approach was used as opposed to the implicit method so as to avoid convergence problems. A power law relationship was used to represent the stress-strain curve of the aluminium tubes. The effect of the strain hardening exponent, friction coefficient values, elastic modulus, thickness of tube are examined in relation to deformation process and how these parameters affect the occurrence of buckling and punch load. It was concluded that such analysis of these parameters may help to understand the buckling mechanism of aluminium and clad tubes.

Gupta and Ray [73] studied the collapse of thin walled empty and filled square tubes under lateral loading compressed between rigid plates. Various sizes of tubes were analysed both in their 'as-received' and annealed conditions. The filler material was in the form of polyurethane foam and Kail wood. A theoretical analysis was presented to compute the peak load and load-deflection responses. Excellent agreement was found between the predicted and actual measured values. As expected, the inclusion of a filler material increases the specific energy absorbing capacity. Moreover, the major advantage of using foam like filler material is that the post collapse load-deflection response increases without increasing the collapse load. The other advantage as reported by the author was that the stroke length increases which was due to the filler material delaying the onset of locking until a later displacement was reached.

In view of how the effect of strain hardening becomes more important in impact situations due to high strain rates and large deformations, Sherbourne [74] analysed theoretically the compression of tubes under rigid platens using the 'Moving Hinge Method'. Although this theory is mainly applied to a rigid-perfectly plastic material, the author attempted to include the effects of strain hardening into the model. It was found that the load-deflection results were in good agreement with experimental data. Also in comparison to other theories such as 'Limit Analysis' by DeRuntz [56] and the 'Plastica Theory' by Reid [58] in predicting the collapse load, it was found that the 'Moving Hinge Method' permit for more manoeuvrability without compromising the accuracy of solution. Finally it was noted that the moving hinge method can also be applied to other deformation modes such as axial

compression of tubes. This appears to be an advantage of the theory since the other methods used are only applicable to tubes compressed laterally.

Wu and Carney [75] analytically analysed the initial collapse of braced elliptical tubes under later compression. Elliptical tubes provide a distinct advantage over their original circular tube counterparts in that their crush efficiency is greater. This automatically implies that the specific energy absorbing capacity of such devices increases, which is desirable in the design of impact attenuation devices. Another method of increasing the specific energy absorbing capacity of these cylindrical or elliptical devices is through the inclusion of metallic braces or wire. These can be attached to the devices either horizontally or at an angle. This generates a larger collapse load and hence the specific energy absorbing capacity is increased. Three possible collapse mechanisms for braced circular tubes as established by Reid [71] have also been found to exist for braced elliptical tubes. These three cases are tubes with small bracing angles, tubes with horizontal bracing and tubes with large bracing angles. It was found that the initial collapse load of braced elliptical tubes was dependant on both the ratio of the ellipse axes b/a, and the bracing angle. ABAQUS, a finite element software was used to capture the deformation mechanisms and initial collapse load of the devices. Figure 2-17 show the symmetric and asymmetric deformations for a 0^0 braced tube.

In a companion paper Wu and Carney [76], the same authors presented the experimental results of braced elliptical tubes compressed under rigid platens. This was to authenticate the numerical and theoretical results presented in their initial paper. It was found that for a ratio of b/a = 1 (Circular tubes), the initial collapse loads predicted from the EST method (Equivalent Structure Technique), ABAQUS and experiments were comparable particularly for small-angle braced tubes. However, for large brace angles, the experimental results are below theoretical predictions and according to the author are due to the tubes being highly sensitive to geometrical imperfections. Finally, it was noted that the ABAQUS results were much lower than the results predicted by the EST method and this appears to be due to the omission of membrane stresses in the latter case. Figure 2-18 shows the finite element model at two stages of displacement.

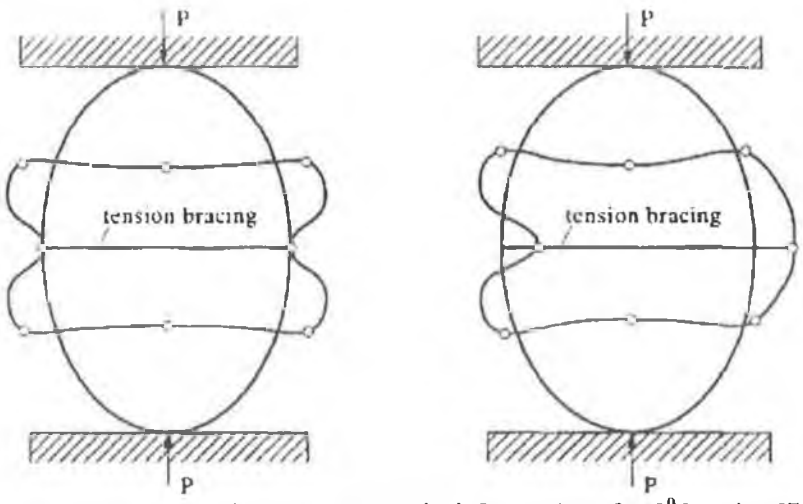

Figure 2-17: Symmetric and asymmetric deformations for 0^0 bracing [76].

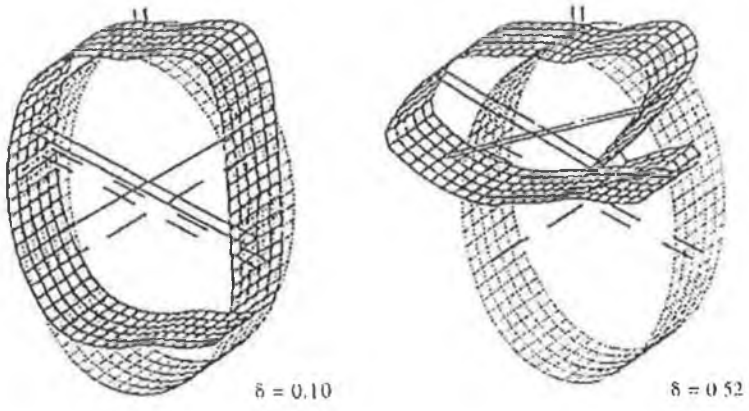

Figure 2-18: Finite element mesh and two deformation stages for a 20^0 braced elliptical tube [76].

2.8 Summary of Chapter Two.

- A brief description was given on how energy absorbers can be categorised into two forms based on the shape of its force-deflection response. Therefore, the analysis of the absorbers in this work are categorised as a Type I structure.
- Chapter two highlighted the work by several researchers involving the analysis of metallic energy absorbers using theoretical, experimental and computational techniques. Five specific modes of deformation pertinent to energy absorbers were identified.
- Various materials such as mild steel, aluminium, stainless steel, and copper were used as energy absorbers due to the fact that they are commonly available on the material supply market.
- Various cross sectional tubes were analysed both quasi - statically and dynamically, such as circular and square tubes, single, double and treble tapered tubes and finally frusta's which is equivalent to a four sided tapered tube.

- Experimental techniques usually involve mechanical apparatus with the ability to load the various energy absorbers at a low velocity so that dynamic effects are not present. For the analysis of impact phenomena, a drop test rig is usually employed in which the drop hammer mass can be varied in order to change both the velocity and inertial effects.
- The implicit version of the finite element code is usually employed to simulate and analyse the quasi-static loading of energy absorbers. Although kinetic energy absorbers are usually exposed to impact, it is normal to analyse their quasi-static response first since the same geometrical effects will occur in the impact cases. This helps the Design or Research Engineer to understand what should be expected to occur geometrically in the dynamic loading case. The explicit method is used to model the dynamic effect of energy absorbers subjected to impact loading. It is possible to simulate devices subjected to quasi-static loading using the explicit method however dynamic effects within the numerical model must be minimised to ensure the validity of the result.
- Limit analysis is the main theoretical method used in the field of plasticity to determine the critical load in which these energy absorbing device collapses, alternatively known as the collapse load. The method offers both the upper and lower bound version of the solution. Normally, the material model is assumed to elastic or rigid and perfectly plastic.
- According to the literature, there appears to be no research conducted on the lateral compression of nested systems in which a series of tubes are assembled internally. The advantage of such a system lies in the fact that an internally arranged system can be suited in situations where space or volume restrictions are important without compromising its energy absorbing requirements.
- Finally it should be noted that in the lateral compression of metallic tubes, the mode of deformation is bending dominated and hence the resulting force-deflection response is smooth, whereby the axial crushing or axial inversion of tubes generates a large fluctuation of force about a mean load which is less than the peak load. This is due to the buckling and fracture modes that are inherent with the axial compression and axial inversion of tube systems respectively.

3 Theoretical Background.

3.1 Introduction.

The objective of this chapter is to outline the theory used to assist in the analysis and solution of the various objectives as outlined in chapter one. The chapter is divided into two sections with the first section detailing a brief description of the Finite Element Method. This section is not intended to be exhaustive, but rather a brief description of important topics involving the theory behind this work. The interested reader can refer to the various quoted references throughout the chapter for a further in depth understanding of the underlying theory. Section two provides a description of miscellaneous topics used to assist in the analysis of the various energy absorbers examined.

3.2 The Finite Element Method.

Finite element analysis is a computer simulation technique used in engineering design and analysis across all branches of engineering and is based on the Finite Element Method. This method and its cousins such as the Finite Difference Method and the Boundary Element Method are numerical techniques for the solution of partial differential equations.

The Finite Element Method is accredited to a number of engineers and mathematicians who proposed the concept of discretization methods. It is generally accepted that the work of Turner et al [77], Argyris and Kelsey [78] are regarded as important contributions. Clough [79] is reported to have been the first to use finite elements.

The physical object or system to be analysed is mapped onto a discrete domain which consists discrete regions called finite elements. For each finite element within the discrete domain, the unknown variables such as displacement or velocity or some other quantity are approximated using known functions which may be linear or non-linear depending on the complexity of the problem. Hence, the governing partial differential equation representing each element is integrated over that element and the solution equation to be solved is summed over the entire discretized domain. In doing so, a set of approximate linear or non-linear equations are created and converted into matrix form. The solution of these matrices is then achieved using numerical techniques. While being an approximate method, the accuracy of the FEA method can be improved by refining the mesh in the model by using more elements and nodes. The following literature [80,81,82,83] provides for a deeper understanding of the underlying theory behind the Finite Element Method.

3.2.1 The Principle of Virtual Work.

The development of the finite element method is based on the principle of virtual work or more specifically, the principle of virtual displacement which states that the internal work in the body is equal to the external work imposed on the body due to external loads.[84]

The principle of virtual displacement for a given body states the mathematical identity of external and internal virtual work as:

$$\text{External Virtual Work} = \int_V \delta\varepsilon^T \sigma dV \tag{1}$$

The Virtual internal work may be obtained by summing the virtual work of all the individual elements representing the body. As shown in subsequent sections, equation 1 leads to the following governing equilibrium equation for the body:

$$R = Kr + R^o \tag{2}$$

where R = the vector of nodal forces representing the external forces applied to the systems nodes.

r = vector of the system's nodal displacement which yields the displacement at any point within the finite element mesh using interpolation functions.

R^o = the vector of equivalent nodal forces representing all external loads such as surface loads, body forces such as inertia , initial stress and strains.

K = the systems stiffness matrix which is established by assembling the individual stiffness matrices K^e.

Once the systems displacement constraints are accounted for, the solution of the nodal displacements r can be obtained through the inversion of the global stiffness matrix and is given by:

$$r = K^{-1}(R - R^o) \tag{3}$$

Subsequently, the strains and stresses arising from the nodal force R in the individual elements may be established as follows:

$$\varepsilon = Bq \tag{4}$$

$$\sigma = E(\varepsilon - \varepsilon^o) + \sigma^o \tag{5}$$

therefore,

$$\sigma = E(Bq - \varepsilon^o) + \sigma^o \tag{6}$$

where q = vector of the individual element's nodal displacement represented as a subset of the global system's displacement vector.

B = the strain displacement matrix that transforms the nodal displacements q to strains at any point in the element.

E = the elasticity matrix that converts the effective strains to stresses at any point in the element.

ε^o = vector of initial strains in the element.

σ^o = vector of initial stresses in the element.

3.2.1.1 Interpolation or Shape Functions.

Let q be the vector of nodal displacements of a typical element. The displacements at any point of the element may be found by interpolation functions and is given by:

$$u = Nq \tag{7}$$

where u = the vector of nodal displacements at any point of individual element.

N = Matrix of shape function used as interpolation functions to determine the displacement at any point in the element.

Equation (7) gives rise to other important quantities such as the virtual displacements which are consistent with the virtual nodal displacements:

$$\delta u = \delta N q \tag{8}$$

The strains in the element:

$$\varepsilon = Du = DNq \tag{9}$$

where D is the matrix of differential operators that convert the displacements into strains.

From equation (4), it can be seen that:

$$B = DN \tag{10}$$

The virtual strains which is consistent with the element's virtual nodal displacements:

$$\delta\varepsilon = B\delta q \tag{11}$$

3.2.1.2 Internal Virtual Work in a Typical Element.

For a typical element of volume V^e, the internal virtual work due to virtual displacements is obtained by substitution of (6) and (11) into (1):

$$\text{Internal virtual work} = \int_{V^e} \delta\varepsilon^T \sigma dV^e = \delta q^T \int_{V^e} B^T \left\{E\left(Bq - \varepsilon^o\right) + \sigma^o\right\} dV^e \tag{12}$$

The following matrices pertaining to a typical element may now be defined:

$$K^e = \int_{V^e} B^T EB dV^e \tag{13}$$

Equivalent element load vector

$$Q^{oe} = \int_{V^e} -B^T \left(E\varepsilon^o - \sigma^o\right) dV^e \tag{14}$$

Substitution of equation (13) and (14) into equation (12) and evaluating using numerical integration yields:

$$\text{Internal virtual work} = \delta q^T \left(K^e q + Q^{oe}\right) \tag{15}$$

The element virtual work in terms of system nodal displacement can be found by replacing q with r by expanding the size of the element matrices with new columns and rows of zeros since the nodal displacement vector q is a subset of the system nodal displacements r, therefore:

$$\text{Internal virtual work} = \delta r^T \left(K^e r + Q^{oe}\right) \tag{16}$$

where, for simplicity, we use the same symbols for the element matrices, which now have expanded size as well as suitably rearranged rows and columns.

3.2.1.3 Global System Virtual Work.

Hence, summing equation (16) for all elements gives the right-hand-side of equation (1):

$$\text{System internal virtual work} = \sum_e \delta r^T \left(K^e r + Q^{oe} \right) = \delta r^T \sum_e K^e r + \delta r^T \sum_e Q^{oe} \tag{17}$$

Considering now the left-hand-side of equation (1), the system external virtual work consists of:

The work done by the nodal forces:

$$R = \delta r^T R \tag{18}$$

The work done by external forces T^e on the part S^e of the element's edges or surfaces:

$$\sum_e \int_{S^e} \delta u^T T^e dS^e \tag{19}$$

The work done by the body forces F^e:

$$\sum_e \int_{V^e} \delta u^T f^e dV^e \tag{20}$$

Substitution of (8) gives:

$$\text{System external virtual work} = \delta q^T \sum_e \int_{S^e} N^T T^e dS^e + \delta q^T \sum_e \int_{V^e} N^T f^e dV^e \tag{21}$$

or alternatively

$$\text{System external virtual work} = -\delta q^T \sum_e \left(Q^{te} + Q^{fe} \right) \tag{22}$$

where we have introduced additional element's matrices as defined below:

$$Q^{te} = -\int_{S^e} N^T T^e dS^e \tag{23}$$

$$Q^{fe} = -\int_{V^e} N^T f^e dV^e \tag{24}$$

Similarly, the replacement of q in (22) with r gives, after rearranging and expanding the vectors Q^{te} and Q^{fe}:

$$\text{System external virtual work} = -\delta r^T \sum_e \left(Q^{te} + Q^{fe} \right) \tag{25}$$

3.2.1.4 Assembly of System Matrices.

Adding (18), (25) and equating the sum to (17) gives:

$$\text{System external virtual work} = \delta r^T R - \delta r^T \sum_e \left(Q^{ie} + Q^{fe}\right) = \delta r^T \left(\sum_e K^e\right) r + \delta r^T \sum_e Q^{oe} \quad (26)$$

Since the virtual displacements δr are arbitrary, the former equality reduces to:

$$R = \left(\sum_e K^e\right) r + \sum_e \left(Q^{oe} + Q^{ie} + Q^{fe}\right) \quad (27)$$

It can be shown from equation (2) that

- The system stiffness matrix is obtained by summing the elements' stiffness matrices:

$$K = \sum_e K^e \quad (28)$$

- The vector of equivalent nodal forces is obtained by summing the elements' load vectors:

$$R^o = \sum_e \left(Q^{ie} + Q^{fe} + Q^{oe}\right) \quad (29)$$

3.2.2 ANSYS: The Newton-Raphson Procedure.

The Newton-Raphson method is an algorithm within the field of numerical analysis which is used by ANSYS for the iterative solution of a set of non-linear simultaneous equations given by [85]:

$$[K]\{u\} = \{F^a\} \quad (30)$$

where $[K]$=coefficient matrix.

$\{u\}$ = vector of unknown DOF values.

$\{F^a\}$= Vector of applied loads.

If the coefficient matrix $[K]$ is itself a function of the unknown DOF values then equation (30) becomes a nonlinear equation.

$$[K_i^T]\{\Delta u_i\} = \{F^a\} - \{F_i^{nr}\} \quad (31)$$

$$\{u_{i+1}\} = \{u_i\} + \{\Delta u_i\} \tag{32}$$

where $\lfloor K_i^T \rfloor$=Jacobian matrix (Tangent matrix)

i = subscript representing the current equilibrium iteration.

$\{F_i^{nr}\}$= vector of restoring loads corresponding to the element loads. Both $\{F_i^{nr}\}$and $\lfloor K_i^T \rfloor$ are evaluated based on the values given by $\{u_i\}$. The right-hand side of equation 31 is the residual out-of balance vector or alternatively, how much the system is out of balance. Figure 3-1 illustrates a single solution iteration for a one DOF model.

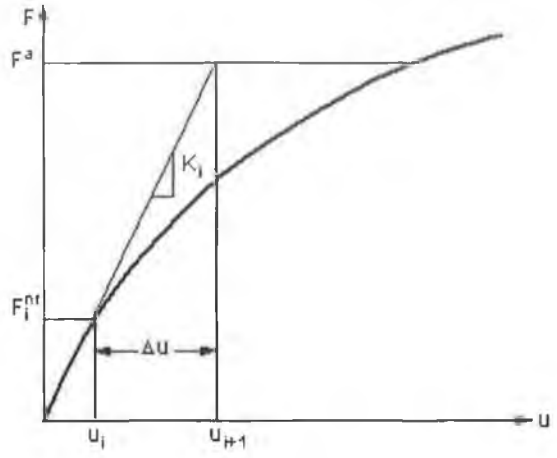

Figure 3-1: The Newton-Raphson Solution- First Iteration. [85]

It can be seen from the following figure that more than one Newton-Raphson iteration is needed to obtain a converged solution. The algorithm procedure is conducted as follows:

(1) On the first time step, $\{u_0\} = \{0\}$.

(2) The updated tangent matrix and restoring load is computed from configuration $\{u_i\}$.

(3) $\{\Delta u_i\}$ is calculated from equation 31.

(4) $\{\Delta u_i\}$is added to $\{u_i\}$in order to obtain the next approximation u_{i+1}.

(5) Steps two to four are repeated until convergence is obtained.

The solution obtained at the end of the iteration process would correspond to load a level $\{F^a\}$. The restoring load vector $\{F_i^{nr}\}$would be equal to the applied load vector $\{F^a\}$, and hence, the final converged solution would be in equilibrium.

However, if equation (31) included path dependant nonlinearities such as plasticity, then the iterative process requires that some intermediate steps are in equilibrium in order to follow the path correctly. This is achieved by applying the load in increments and performing the Newton-Raphson iteration at each step so that the final load vector $\{F^a\}$ is reached. Therefore equation (31) becomes:

$$\left[K_{n,i}^{T}\right]\{\Delta u_i\} = \{F_n^a\} - \{F_{n,i}^{nr}\} \tag{33}$$

where $[K_{n,i}]$=tangent matrix for time step n, iteration i.

$\{F_n^a\}$= total applied force vector at time step n.

$\{F_{n,i}^{nr}\}$= the resorting force vector for time step n, iteration i.

Figure 3-2 shows the incremental Newton-Raphson procedure. It should be noted that, even without a path dependant nonlinearity, this incremental approach is sometimes required in order to obtain a solution corresponding to the final load level.

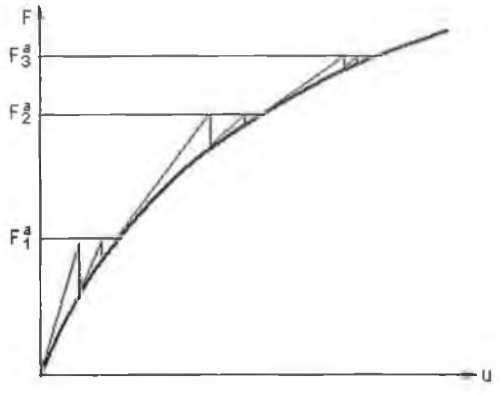

Figure 3-2: The Newton-Raphson Solution: Next iteration. [85]

3.2.3 LS-DYNA. Explicit Time Integration.

For physical problems involving an extreme amount of deformation or where stress wave propagation effects are significant, the explicit method is used to calculate the equation of motion [86]. Figure 3-3 illustrates a schematic of a single degree of freedom system subjected to damping, elastic and inertial forces which is equivalent to a time varying force P (t).

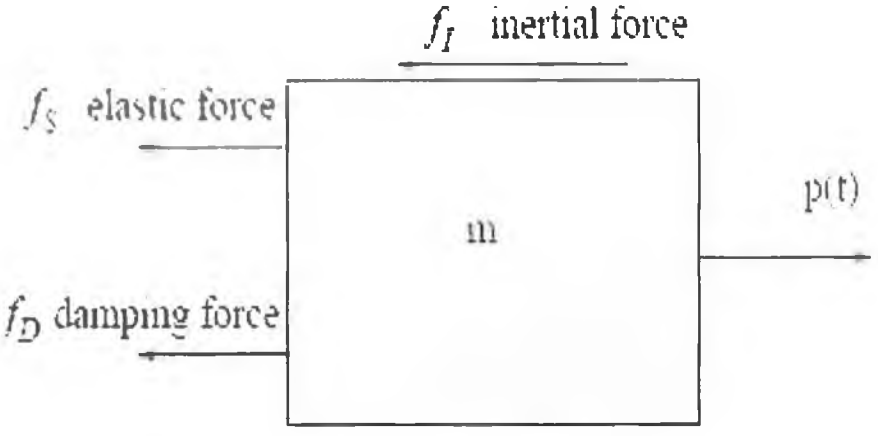

Figure 3-3: Schematic of the equation of motion. [86]

Equating these forces acting on mass m to the time varying force P (t) yields the following equation of motion:

$$m\ddot{u}+c\dot{u}+ku=p(t) \tag{34}$$

where $\ddot{u}=\frac{d^2u}{dt^2}$, $\dot{u}=\frac{du}{dt}$ $u=$ displacement, m is the mass of the body, c is the damping and K is the stiffness of the system.

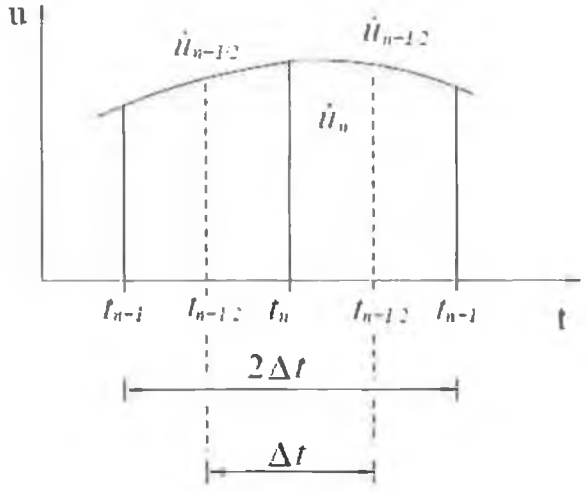

Figure 3-4: The Central difference method. [86]

As shown in Figure 3-4, the central difference scheme is utilised such that the velocity and acceleration are given respectively as:

$$\dot{u}=\frac{1}{2\Delta t}\left(u_{n+1}-u_{n-1}\right) \tag{35}$$

$$\ddot{u}_n=\frac{1}{\Delta t}\left(\dot{u}_{n+\frac{1}{2}}-\dot{u}_{n-\frac{1}{2}}\right) \tag{36}$$

$$=\frac{1}{\Delta t}\left(\frac{u_{n+1}-u_n}{\Delta t}-\frac{u_n-u_{n-1}}{\Delta t}\right) \tag{37}$$

$$\ddot{u}_n=\frac{1}{(\Delta t)^2}\left(u_{n+1}-2u_n+u_{n-1}\right) \tag{38}$$

Equilibrium at time t_n $\qquad M\ddot{u}+C\dot{u}_n+Ku_n=P_n$ (39)

Substitution of equation (35) and (38) into (39) yields

$$\left(M+\frac{1}{2}\Delta tC\right)u_{n+1}=(\Delta t)^2P_n-\left((\Delta t)^2K-2M\right)u_n-\left(M-\frac{\Delta t}{2}C\right)u_{n-1} \tag{40}$$

3.2.4 Elastic-Plastic Material Behaviour.

Plasticity theory provides a mathematical relationship to characterise the elastic-plastic response of materials subjected to loading and is based on three important concepts such as the yield criterion, the flow rule and the hardening rule [85].

The yield criterion establishes the stress level at which yielding commences. For multi-component stresses, this is represented as a function of the individual components, $f(\{\sigma\})$ which can be interpreted as an equivalent stress σ_e:

$$\sigma_e = (\{\sigma\}) \tag{41}$$

where $(\{\sigma\})$ is the stress vector.

Figure 3-5 presents the stress strain-behaviour of the material model used to describe the behaviour of Mild steel used in the various energy absorbers. This stress-strain is classified as a Bilinear material model.

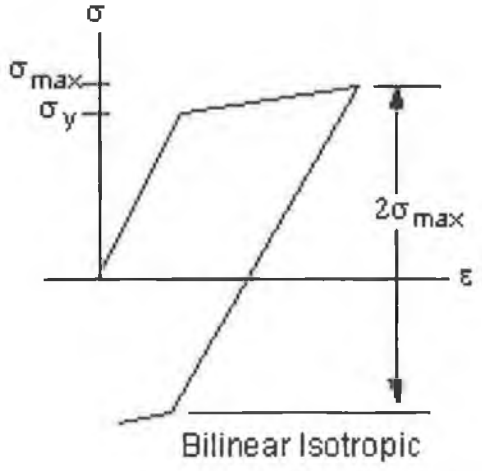

Figure 3-5: The bilinear stress-strain behaviour of the material model. [85]

The yield stress criterion is based on the Octahedral Shear Stress Yield criterion or the Von Mises criterion which states that yielding occurs when

$$\sigma_y = \frac{1}{\sqrt{2}}\sqrt{(\sigma_1 - \sigma_2)^2 + (\sigma_2 - \sigma_3)^2 + (\sigma_3 - \sigma_1)^2} \tag{42}$$

where σ_y is the yield stress

σ_1, σ_2 and σ_3 are the stresses defined in a three-dimensional principle stress space as shown in Figure 3-6.

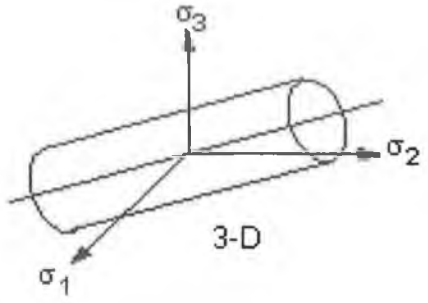

Figure 3-6: Yield surface in principle stress space. [85]

The hardening rule determines the changing of the yield surface with progressive yielding, so that the conditions (i.e. stress states) for successive yielding can be identified. Two hardening rules are available: isotropic hardening and kinematic hardening. In work hardening, the yield surface remains centred about its initial centreline and dilates (isotropic expansion) in size as the plastic strains develop. For materials with isotropic plastic behaviour this is termed isotropic hardening and is shown in Figure 3-7

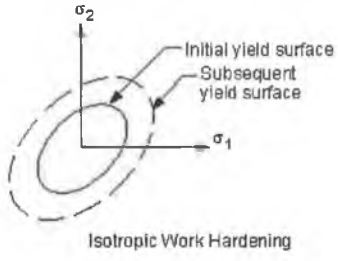

Figure 3-7: The Isotropic Hardening Rule. [85]

The flow rule determines the direction of plastic straining and is given as:

$$d\varepsilon^{pl} = \lambda\left\{\frac{\partial Q}{\partial \sigma}\right\} \tag{43}$$

Where $d\varepsilon^{pl}$ is the change in plastic strain.

λ is the plastic multiplier which determines the amount of straining.

Q is the yield function.

3.2.5 Contact Algorithms.

ANSYS offers a number of contact algorithms to simulate the non-linear contact phenomena, three of the more important methods are outlined below [87]. In contact problems, two important concepts must be taken into account and are as follows: (a) The contacting force which is transferred between the relevant bodies and (b) the

impenetrability condition which states one body cannot penetrate another. These two concepts are preserved by incorporating either one of three different contact algorithms: the penalty method, Lagrange multiplier method or the augmented Lagrange method.

For the solution of non-linear problems, the governing set of simultaneous equation is given by:

$$[K]\{x\} = \{F\} \tag{44}$$

For the penalty method we assume that the contact force is written in the form:

$$K_{contact}\Delta x_{penetration} = \Delta F_{contact}. \tag{45}$$

where $K_{contact}$ is the 'Contact Stiffness', $\Delta x_{penetration}$ is the distance between two existing nodes with each node connected to a separate contacting body. Due to the fact that $\Delta x_{penetration}$ describes that distance between existing nodes, $K_{contact}$ can then be added to the existing stiffness matrix as defined in equation (44).

For the Lagrange multiplier method $\Delta F_{contact}$ is treated as a separate DOF, therefore equation (45) is modified and is given in the from:

$$[K]\{x\} = \{F\} + \{F_{contact}\} \tag{46}$$

This equation has the benefit of satisfying the impenetrability condition without being concerned with the 'contact stiffness' or 'penetration'. This method offers an advantage over the pure penalty method due to the fact that the contact force is treated as a separate DOF and therefore the issue of achieving zero penetration (Infinite Contact Stiffness) as with the penalty method can be bypassed.

The augmented Lagrange method is an iterative series of the penalty method. The contact force is augmented during equilibrium iterations so that the final penetration is smaller than some specified tolerance within the algorithm. Lower stiffness values can lead to excessive penetration and hence produce an inaccurate solution. Ideally, a high enough contact stiffness is required such that the penetration is acceptably small, but a low enough stiffness so that the problem will converge without much difficulty. This method offers an advantage over the previous two algorithms in that less ill-conditioning of the global stiffness matrix is achieve due to the fact that the contact stiffness is updated at each

iteration of the solution process. The contact algorithm used by ANSYS/LS-DYNA to capture the contact phenomena is based on the penalty method. A detailed explanation of the theory of the penalty method based on the explicit method can be found from reference [88]

3.2.6 Contact Capabilities within ANSYS and ANSYS/LS-DYNA.

ANSYS offers a number of contact models such as node to node, node to surface and surface to surface models. The latter option was used to capture the deformation process of the various energy absorbers in this work. Figure 3-8 illustrates a surface to surface contact pair used to capture the interaction between the two solid bodies. As shown from the figure, the contact surface usually consists of the deformable body whilst the target surface may consist of either a deformable or rigid surface. Contact detection points are located at the integration points of the contact elements which are interior to the element surface. The contact element is constrained against penetration into the target surface at its integration points. However, the target surface can, in principle, penetrate through into the contact surface.

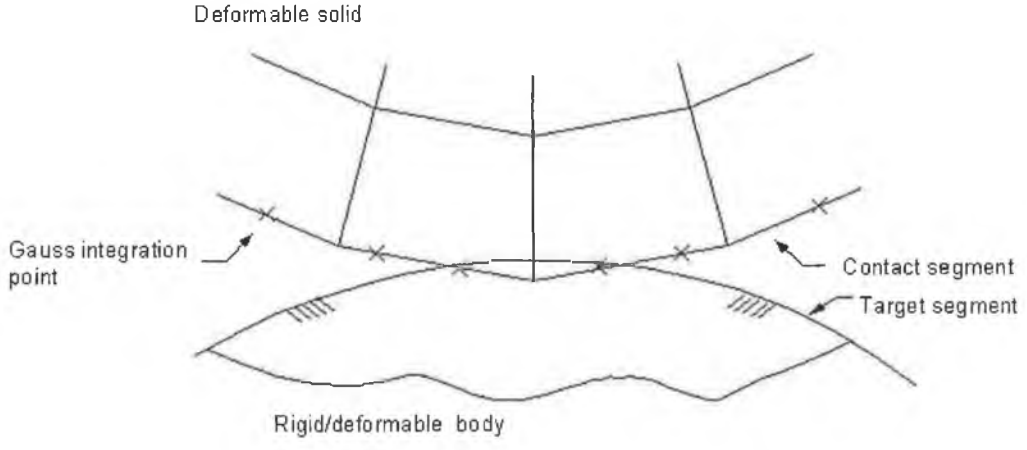

Figure 3-8: Illustration of a contact pair. [85]

In LS-DYNA, contact is defined by identifying (via parts, part sets, segment sets, and/or node sets) what locations are to be checked for potential penetration of a *slave* node through a *master* segment. LS-DYNA also uses the penalty method approach in which when a penetration is found, a force proportional to the penetration depth is applied to resist, and ultimately eliminate the penetration. An AUTOMATIC SURFACE to SURFACE contact format which is a two way contact, is used to simulate the contact interaction of the various energy absorbers subjected to dynamic impact as shown in Figure 3-9. This contact is typically used in impact analysis due to the fact that predetermination

of where contact will occur is almost impossible. In a two-way contact, nodes on the slave side are first checked for penetration thru the master surface and then master nodes are checked for penetration thru the slave surface.

Figure 3-9: Illustration of the surface to surface contact algorithm in ANSYS/LS-DYNA. [86]

3.3 Miscellaneous Theoretical Topics.

3.3.1 Energy Absorption Characteristics.

It is usual to describe the behaviour of energy absorbing systems in terms of performance indicators. Thornton [89] suggested various indicators such as the crush efficiency, energy efficiency, specific energy absorption capacity and weight effectiveness that may be useful in describing the performance of such systems. The crush efficiency is defined as the stroke length divided by a characteristic length of the structure such as the outer diameter of the tube. The specific energy absorption capacity is defined as the energy absorbed per unit kilogram. The energy efficiency as illustrated by Thornton is given as

$$e_E = \frac{A}{P_\delta * L_o} \qquad [47]$$

where A is the area under the force deflection curve, P_δ is the peak load observed and L_o is the original length. Upon examination of this equation, it can be seen that to achieve 100% energy efficiency requires a rectangular force-deflection curve such as a structural rigid perfectly plastic response. From a practical point of view, to achieve maximum energy efficiency, the force-deflection response needs to be adjusted so the peak force will occur in the early stages of deflection and preferably remaining at this magnitude for the remainder of the stroke. This is an ideal requirement in the design of energy absorbing systems. In achieving this, the occupant ride down deceleration as a result of this constant force, may be adjusted to be within acceptable limits so as to avoid injuries.

A final performance indicator that may be used to describe the behaviour of such systems is the weight effectiveness, which is given as

$$W_{eff} = e_g * S_s^c \quad [48]$$

where e_g is the crush efficiency and S_s^c is the specific energy absorption capacity. It is a useful indicator since the relative energy absorption capacity of the system is used in conjunction with an important variable in the response of energy absorbers, the stroke length, to describe the behaviour of the system.

3.3.2 Optimisation of Tube Geometry for a COPSS.

Due to the nature of the tubes being rotate ninety degrees, there exists a gap between the respective tubes for the COPSS subjected to lateral crushing under the three different indenters. The following approach can be taken to eliminate these gaps, and in doing so, the best possible *monotonic* force-deflection response can be achieved.

1) The elimination of the gaps between each tube can be accomplished by choosing a set of tubes such that, once assembled and loaded using any form of indenter, all tubes will deform synchronously. This will give rise to the smoothest response possible for any given set of tubes. To achieve this, the simple use of Pythagoras's theorem can be applied to obtain the radius of the tube in question such that it is just touching its neighbouring component. Figure 3-10 shows a cross sectional view of a typical COPSS. The design topography can consist of two methods; one in which the smallest or inner-most tube is selected and the resulting external tube dimensions are evaluated. The second method is selection of the largest or outer-most tube and the resulting internal tube dimensions are evaluated. In this example the latter method is used. Therefore to find the outer radius of central tube, the following equation is utilised:

$$R_3 = \sqrt{(R_2)^2 - \left(\frac{L}{2}\right)^2} \quad [49]$$

where R_3 is the outer radius of the central tube, R_2 is the inner radius of the outer tube and L is the axial length of the central tube. This obtains us the value of R_3 such that the outer and central tubes are just touching.

2) The thickness of each tube should be equal; this will instigate the collapse load for each to be approximately the same, resulting in minimal fluctuation in force throughout the deflection stroke.

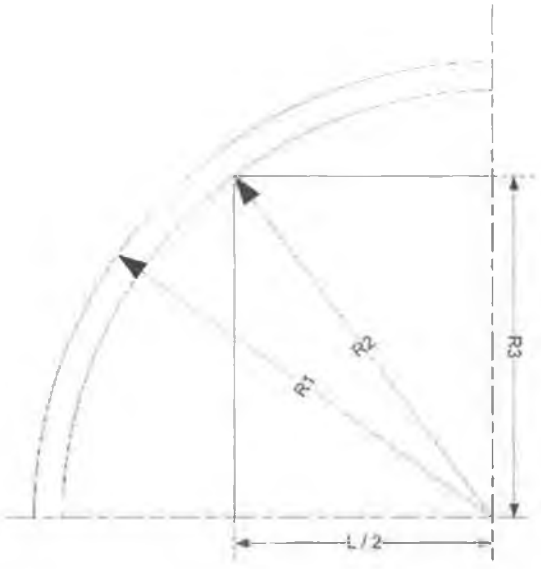

Figure 3-10: A one quarter cross sectional view of a COPSS.

3.3.3 Material Characterisation.

For material characterisation of the tubes subjected to dynamic loading, a bilinear stress–strain curve was incorporated into the finite element model using the 'PLASTIC KINEMATIC HARDENING' material model option. Values of 0.3 and 200 GPa were given for Poisson's ratio and Young's modulus respectively. The material is assumed to possess only isotropic strain hardening and strain rate effects due to dynamic loading are defined using the Cowper-Symonds constitutive equation given by

$$\sigma_d = \sigma_s \left(1 + \left(\frac{\dot{\varepsilon}}{D} \right)^{\frac{1}{q}} \right) \tag{50}$$

where σ_d is the dynamic flow stress at a uniaxial plastic strain rate $\dot{\varepsilon}$, σ_s is the associated static flow stress, the material constants given for D and q were given as 6844 s^{-1} and 3.91 respectively. These values were used in previous studies for the axial crushing of mild steel tubes and dynamic loading [25, 30].The values for the yield stress and plastic modulus as outlined in section 4.5 were incorporated into this material model.

3.3.4 Energy Balance.

To ensure that there were no numerical errors within the developed models to simulate the various energy absorbers, the energy equation was checked to ensure that it was in a balanced state. The following energy equation must hold true at all times during an analysis and is given by [90] -

$$E_{kin} + E_{\text{int}} + E_{st} + E_{rw} + E_{damp} + E_{hg} = E^0_{kin} + E^0_{\text{int}} + E_{ext} \tag{51}$$

where on the left hand side E_{kin} is the kinetic energy, E_{int} the internal energy, E_{st} the sliding energy (friction energy), E_{rw} rigid wall energy, E_{damp} is energy due to damping and E_{hg} hourglass energy, on the right hand side $E^0_{km}, E^0_{\text{int}}, E_{ext}$ are energies due to initial kinetic, initial internal and external work done respectively. Since the models in question only contain kinetic, internal and sliding energy and external work done on the system, the energy balance reduces to

$$E_{kin} + E_{\text{int}} + E_{st} = E_{ext} \tag{52}$$

The terms on the left hand side is equivalent to the total energy. Hence, graphical plots depicting the energy balance of each model analysed dynamically are illustrated throughout section 7.8.

3.3.5 Strain-Rate Effects.

When analysing the response of structures under dynamic impact, it is usual to study the response in terms of strain rate which can be characterised as a function of the impact velocity and the change in length of the structure. Strain rate is one of the very important parameters alongside inertial effects that must be considered when dealing with structures under dynamic loading. The strain rate of a uniform homogenous bar of metal as shown in can be derived as follow by defining the engineering tensile strain as [91]

$$e = (L - Lo)/Lo \tag{53}$$

and the increment of engineer tensile strain is

$$de = dL/Lo \tag{54}$$

in place of Lo in equation (53), we can write L

$$d\varepsilon = dL/L \tag{55}$$

where $d\varepsilon$ is defined as the incremental in the natural or logarithmic strain.

Tensile engineering strain rate $\dot{e}$ is the rate of increase in tensile strain, so that from equation (54),

$$\dot{e} = \frac{de}{dt} = \frac{dL/dt}{Lo} = \frac{v}{Lo} \tag{56}$$

where t denotes the time and v is the speed of separation of the points A and B as shown in Figure 3-11. The tensile natural or logarithmic strain from equation (55) is given as

$$\varepsilon = \frac{d\varepsilon}{dt} = \frac{dL/dt}{L} = \frac{v}{L} \tag{57}$$

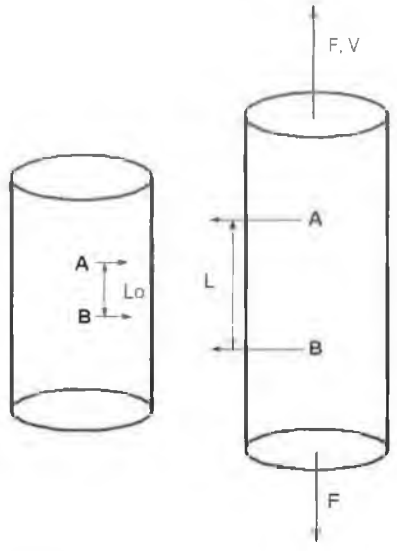

Figure 3-11: Schematic of a uniform homogenous bar of metal of length Lo and subjected to a tensile force F with velocity V.

Reid and Reddy [68] studied the effects of strain rate on the dynamic lateral compression of tubes. They discovered that the strain rate of a single tube of dimension 50mm diameter was $22.5s^{-1}$ when compressed dynamically at 5m/s. Hence, it can be seen that the CIPSS and the CIPDS subjected to dynamic loading of 5m/s in this work experience a strain rate of a similar magnitude. In the discussion of strain rates, it is usually the order of magnitude which is of significance. The systems analysed dynamically in this work are at the lower end of the 'Low Dynamic' spectrum as illustrated by [4]. The upper and lower range of strain rates pertaining to this spectrum is in the range of $10s^{-1}$and 10^3s^{-1}.

3.4 Summary of Chapter Three.

Chapter three gave a brief introduction into the various theoretical topics used to analyse the response of various energy absorbers:

- Section one provided an account of some of the important topics within the finite element method such as the principle of virtual work, solution methods, material models and contact methods used in both ANSYS and LS-DYNA.
- Section two outlined the energy absorption characteristics used to describe the behaviour of the various energy absorbers.

- A description was given on a method that may be used to optimise the geometry of a COPSS so as to achieve the most efficient response when such a device is compressed laterally.
- A description was given on the energy balance equation used to determine whether any artificial energy was introduced into each the numerical models simulated with LS-DYNA as result of any possible numerical instability.
- An account was given on the Cowper-Symons relation used to predict the dynamic yield stress of a given material under impact loading conditions.
- Finally, an explanation was given on the effect of strain rate and its relevance to the systems analysed dynamically in this work.

4 Experimental Techniques and Material Characterisation.

4.1 Introduction.

The chapter is divided into three sections in which the first two sections give an account of the quasi-static and dynamic experimental procedures taken to analyse the various specimens. The third section details the material characterisation of the energy absorbers used in the work.

4.2 Quasi - Static Analysis: Experimental Set-Up.

4.2.1 Mechanical Features of the Instron 4204 Series.

The quasi-static testing of the respective samples were carried out on the Instron Model 4204 testing instrument which is used for measuring the mechanical properties of materials and structures. The maximum capacity of the loading frame attached to the table mounted unit is 50KN. This loading frame consist of two vertical lead screws, a moving crosshead and an upper and lower bearing plate which bears the load of the lead screws.

4.2.2 Load Cell Features.

A highly sensitive load cell is mounted in the moving crosshead of the loading frame and measures the compressive or tensile loading force of the specimen. The load cell consists of multiple strain gauges bonded by means of an etched foil to an elastic element which deforms slightly under an applied load. In doing so, the resistance of the foil changes in direct proportion to the deformation of the element. The gauges are connected as a Wheatstone bridge and with the use of appropriate amplification; the small unbalances within this bridge are detected as a voltage. This voltage is then used to accurately determine the amount of load applied to the specimen.

4.2.3 Data Acquisition System.

The control unit is based on a CPU which provides control of crosshead, data acquisition and data readout from the loading frame. The results are displayed by the associated Instron 4204 series software. Various parameters such as loading, displacement, strain and energy can be calculated. Typically, all specimens were placed between the mounting table and a custom built platen and loaded in compression. Figure 4-1 shows the Instron model 4204 and a sample specimen in the machine.

4.2.4 Experimental Procedure.

To stimulate quasi-static conditions and to ensure no dynamic effect were present; a velocity between 3-10mm/min was applied to the moving crosshead of the Instron machine

[4]. Velocities between 0.5mm/min and 15mm/min have been applied by various researchers [59, 60, 61, 66] in the quasi-static lateral compression of tubes between various indenters.

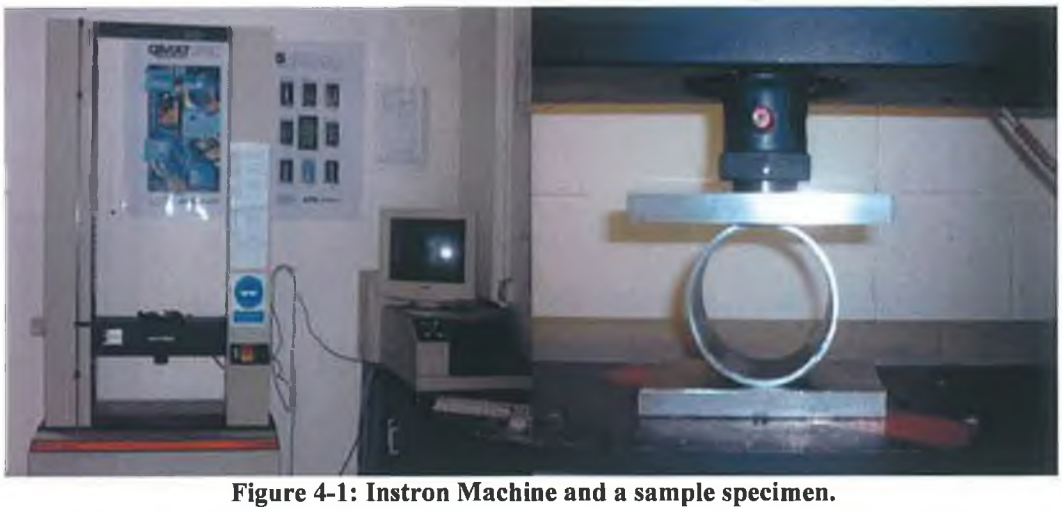

Figure 4-1: Instron Machine and a sample specimen.

4.3 Dynamic Analysis: Experimental Set-up.

4.3.1 Mechanical Features of the Zwick Roell 5HV Series.

A Kistler 9091 series piezoelectric force transducer was used to capture the load-time response of the impact events. This transducer has a large dynamic range and good frequency responses of 160,000 samples/sec. Maximum load magnitudes of up to 250KN are possible. The transducer is placed in the moving carriage and connected to the striker via a lock-unlock mechanism. The complete moving mass consisting of both the carriage mass and striker mass is allowed to drop vertically within two vertical sliding guide rails from a maximum height of 1.2 metres. A photo gate arrangement consisting of a photo diode which passes through a flagged gate was used to capture the initial velocity. The test sample is positioned in very close proximity to the gate so that the photo diode captures the velocity of the striker just prior to impact. Figure 4-2 illustrates the Zwick Roell 5HV series used to conduct the impact testing of the various samples.

Figure 4-2: Photographs displaying the Zwick Roell 5HV series used to conduct the impact experiments.

4.3.2 High Speed Camera.

A high speed video recording system namely the MOTIONSCOPE PCI 8000 S series was used to capture the impact event. The camera head is a 2 ½ * 2 ½ * 4 inch enclosure which contains the CCD (Circuit Charged Device) sensor. Up to 8000 fps (frame per seconds) of the impact event can be recorded. Video playbacks of 8000 fps in forward and reverse directions are also possible with frame by frame or freeze frame options available. The exposure of each frame is reduced at the higher frame rates, so more light exposure is required as the frame rate increases. Therefore a specialised lighting system was employed to increase illumination upon the specimen. The video files are in Microsoft avi (audio video interleaved) format by default however they can be converted to jpeg with resolutions of up to 480*420 pixels.

4.3.3 Data Acquisition System.

The data acquisition system Rosand IFW (Intelligent Free Wheel) V 1.10 was used to capture the signals from the force transducer. The maximum sampling rate is 670,000 samples/s and a total data point capture of 4000. The software gathers the force measurements with respect to time, the frequency of which is dependent on sweep time and number of data points selected. If the signal filter is selected, then the data is shown with a filter applied but this can be applied or removed retrospectively as raw data is always stored. The type of filter used is based on the second order Butterworth filter, implemented in the software as an IIR (infinite impulse response), i.e. a recursive filter. Figure 4-3 and Figure 4-4 illustrate a typical display of results and the interface used within the Rosand IFW software.

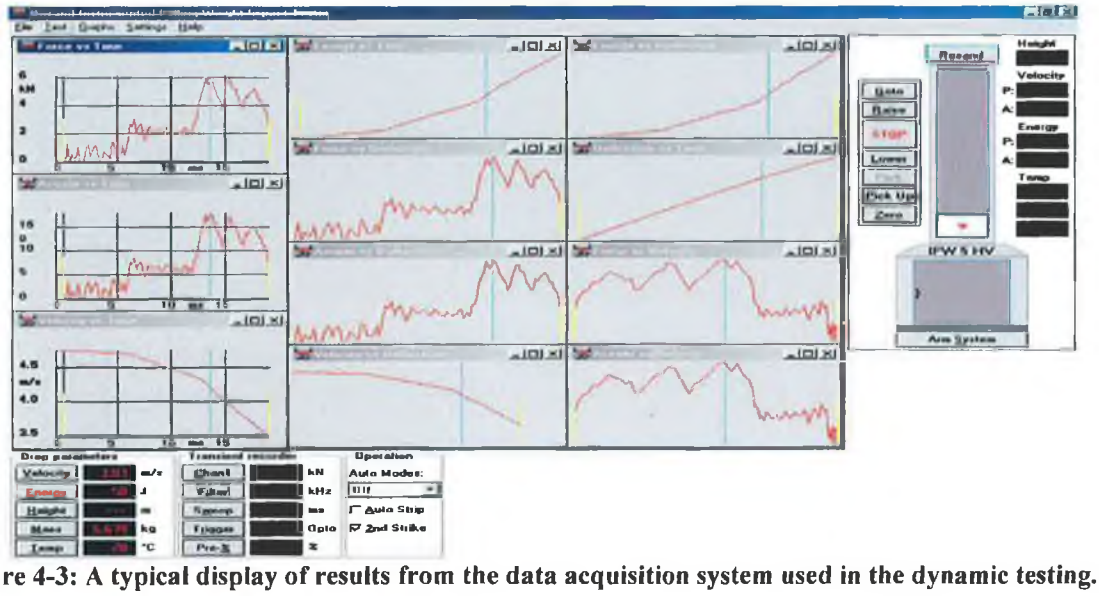

Figure 4-3: A typical display of results from the data acquisition system used in the dynamic testing.

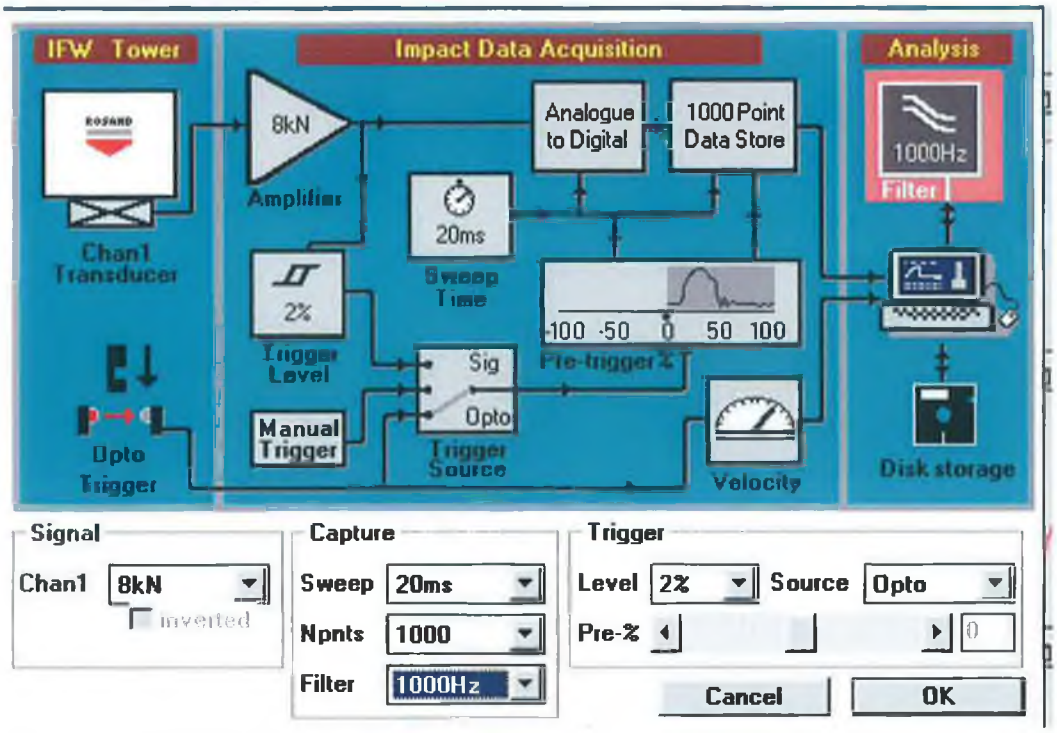

Figure 4-4: The interface within the data acquisition system used to input the various parameters.

4.3.4 Experimental Procedure.

For the dynamic analysis of the samples, a custom made fixture was designed and manufactured to hold the samples relative to the impinging striker as shown in Figure 4-5. It should be noted that such a fixture will automatically prevent the full displacement stroke to be achieved; i.e., approximately 5mm of a displacement stroke is lost. Table 4 and Table 5 in Appendix Two. illustrates displays their corresponding initial velocity, final velocity, impact duration, displacement and energy absorbed for each sample. For the testing of each sample, the impinging mass was kept at a constant value of 34.7kg. This total mass consisted of both the striker and the carriage. The machine allows the user to select one of three parameters to set the striker in motion. These parameters consist of velocity, drop height and energy absorption. The latter option was used and hence the corresponding velocity and drop height were calculated by the machine software. The velocity time response of each sample was summed and averaged and is shown in Figure 4-6. The length of the energy absorbers varied from 10mm to 15mm, the latter value being the upper limit due to the energy capacity restrictions of the machine. Prior to each test conducted on each sample, the drop height parameter was set to zero before specifying an energy absorption value. This was done by adjusting the striker such that it was just touching the tip of each sample. Once the energy absorption value was specified, the machine automatically adjusted the striker to its appropriate height. For each sample tested,

the data from the transducer was collected at a frequency of 1000Hz and a total of 100 data points were collected. The video recorder was mounted on a tripod and adjusted until a good viewing range was detected. In order to improve the quality of the video image, a black neutral material was placed behind the samples. In doing so, a clearer contrast of the sample image was achieved.

Figure 4-5: The fixture used to hold the samples in place upon impact.

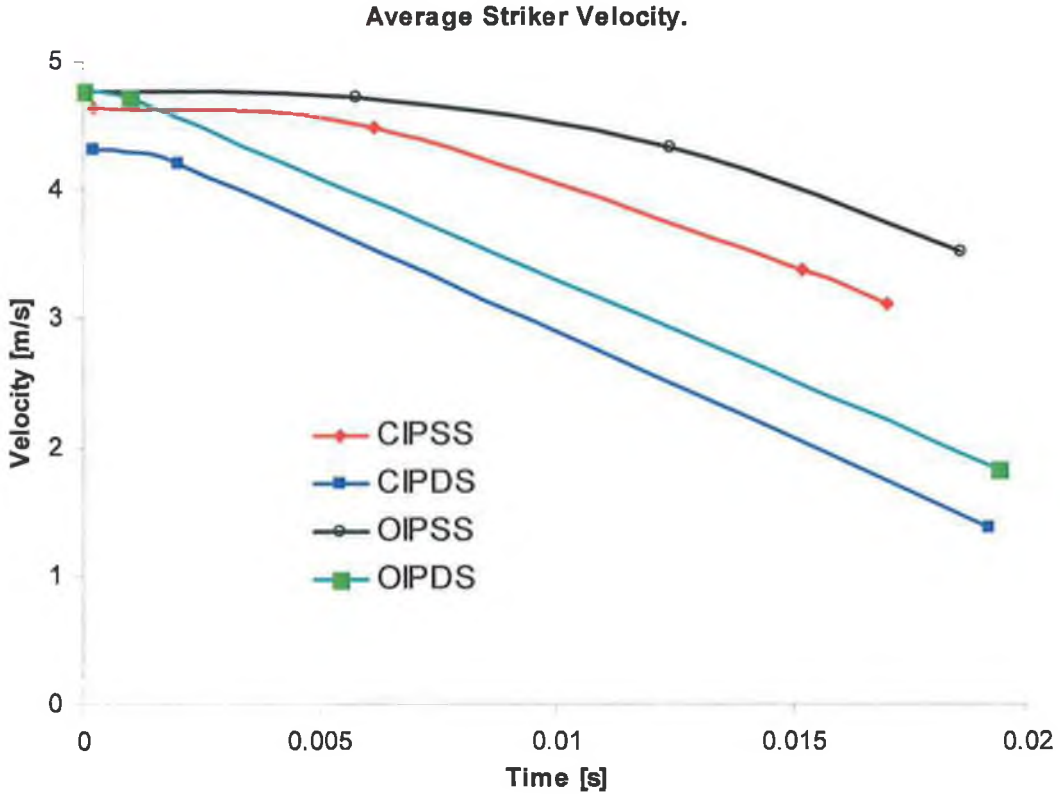

Figure 4-6: The average striker velocity for each of the four various energy absorbers.

4.4 Oblong Tube Specimen Preparation (OIPSS and OIPDS).

Initially two different methods were used to generate the oblong specimens. These consisted of the compression method using two rigid flat platens and the tension method which incorporated a custom built fixture. It was decided to employ both methods to determine which one would provide the greatest plastically elongated oblong shape possible. In doing so, when the tubes were assembled together and put under actual loading, the greatest displacement stroke could be obtained and hence, its energy absorbing capacity would be maximised.

For the compression method, a displacement of 40mm was applied to the larger 127mm O.D. tube. This was deemed the maximum displacement that could be applied, since any further displacement may cause the non-circular tube to buckle inwards due to the formation of four hinges at the quarter points of each tube as shown in Figure 4-7 The possibility of these tubes buckling inwards when used as an energy absorber is an undesirable feature, therefore an alternative method such as the application of the tensile method was considered.

Figure 4-7: The final stages of displacement for each tube using the compression method.

For the tension method, a simple fixture as shown in Figure 4-8 was designed to apply a tensile force to the selected tube specimens. A tension displacement of 50mm was applied to the larger 127mm O.D. tube and thereby giving a ratio of 2.54, since the ratio is the O.D of tube divided by the tensile displacement length. This ratio was used to calculate the displacement that should be applied for the remaining 101.6mm O.D. and 76.2mm O.D. tubes. Using this tensile method, it was found that a greater displacement could be applied to the tubes without the formation of severe hinges at the two horizontal points of the tube Therefore this method offered a distinct advantage over the compression method in that the possibility of the tubes buckling inwards could be greatly reduced or eliminated. Figure 4-9 shows the force deflection response for each of the different sized tubes using the tensile method.

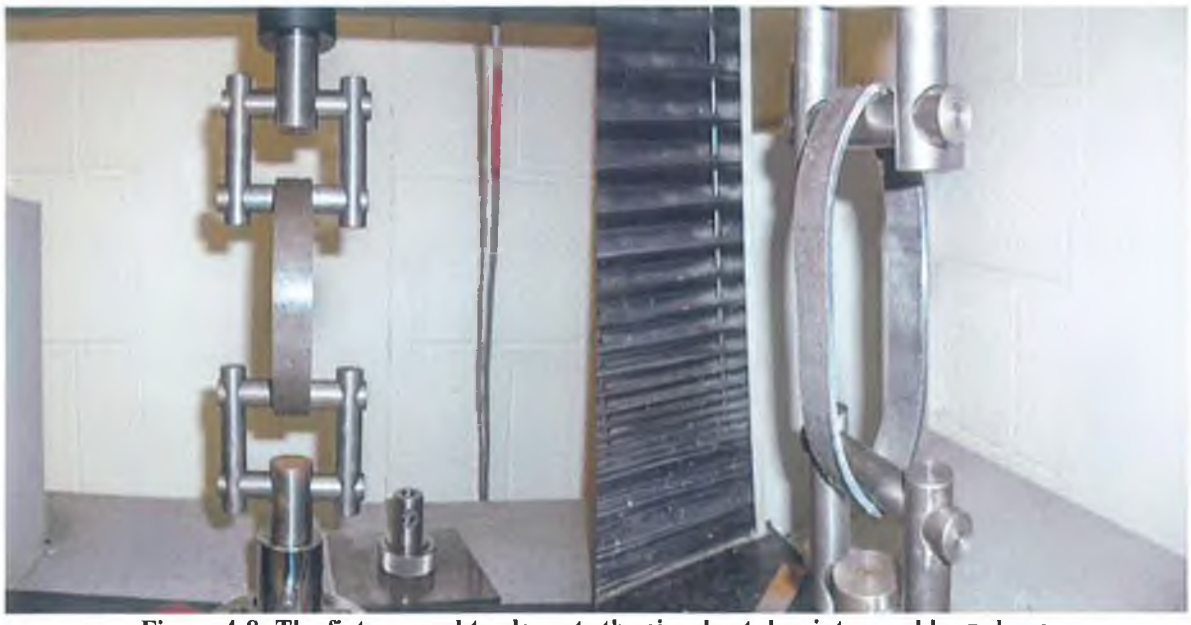

Figure 4-8: The fixture used to elongate the circular tubes into an oblong shape.

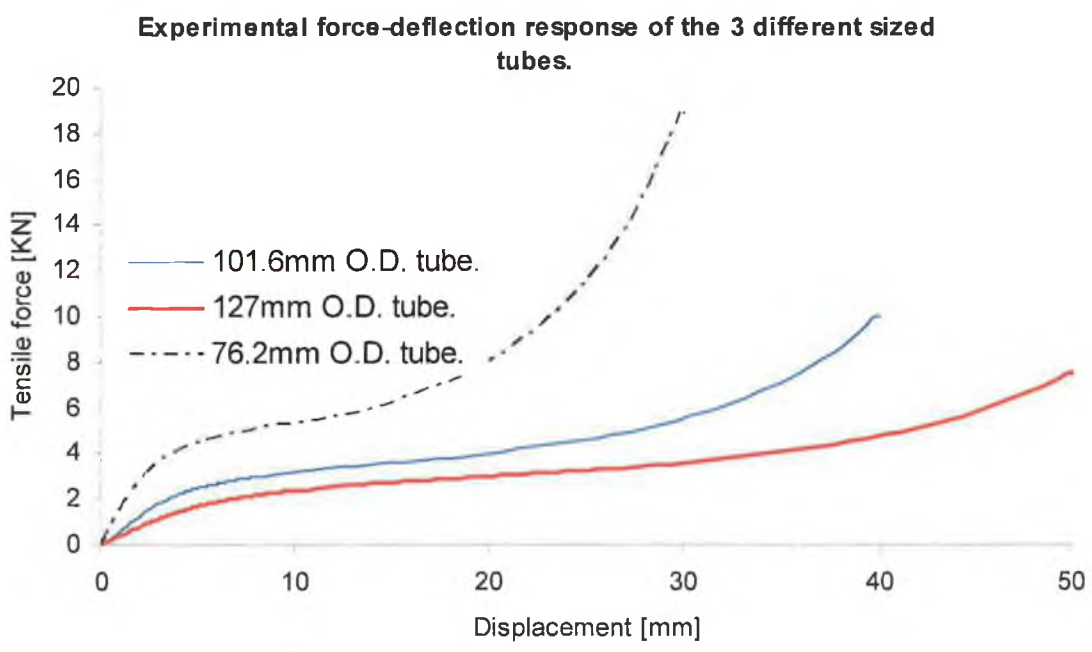

Figure 4-9: Tensile force-deflection response of the three individual tubes.

4.5 Material Properties Characterisation.

The tubes used in this work were made of mild steel which was cold finished, drawn over mandrel by the tube manufacturer according to DIN standards (DIN 2393 ST 37.2). The chemical composition of the material is illustrated in Table 6 in Appendix Two. Three dog bone samples for each of the three different sized tubes were analysed in order to ensure repeatable results as shown in Figure 4-10. The dog bone samples were machined from cut-out specimens obtained from the acquired tube stock. A sample specimen before and after testing is shown in Figure 4-11. The three tubes used in each energy absorber were of 127mm O.D., 101.6mm O.D. and 76.2mm O.D. respectively with the thickness of each

being 3.25mm. The true static stress-strain curve was obtained using a tensile test adhering to ASTM standards and is displayed in Figure 4-12. Each of the samples exhibited a high value of elastic modulus of 325GPa; therefore, it was decided to obtain the yield stress based on an elastic modulus of 200GPa which is more representative of mild steel. In doing so, the yield stress of 470MPa was carefully obtained from the experimental stress-strain curve as shown in Figure 4-13.Since the tubes were cold worked by the tube manufacturer, the true stress - strain curves obtained from the samples exhibited a deformation characteristic in which necking occurred immediately after yielding followed by a geometrical softening stage. This is to be expected since the cold rolling process, in addition to increasing the yield strength, decreases the ductility due to the concentrated dislocations in the material. Such behaviour is termed tension instability and hence Considère's criterion can be employed to determine the initial plastic stiffness of the material. This criterion states that $\sigma = d\sigma / d\varepsilon$, implying that the initial plastic modulus must be less than or equal to the yield stress. Therefore, it was decided to approximate the material property of the three tubes using a bilinear stress-strain curve. In doing so, the yield stress of 470MPa was carefully obtained from the experimental true stress-strain curve and according to Considère's criterion; the initial plastic modulus was assigned the same value of 470MPa. The yield stress is validated according to DIN standards which state the yield stress of this material to be within the range of 450 MPa to 525MPa.

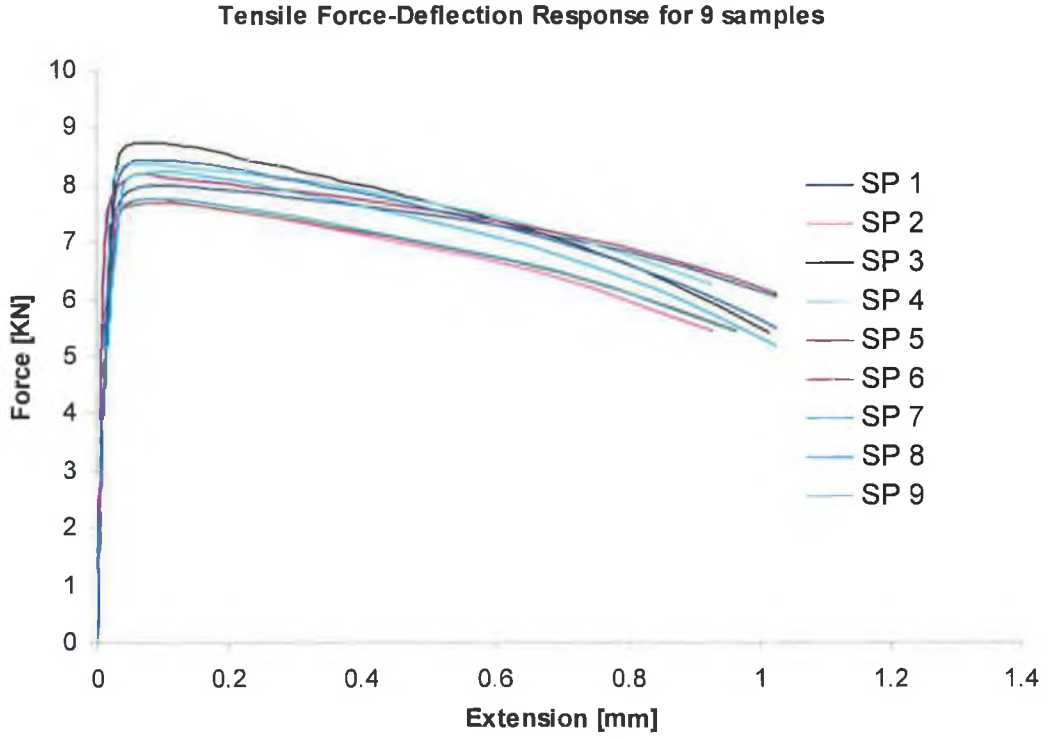

Figure 4-10: The tensile stress-strain curve for nine dog bone specimens.

Figure 4-11: A sample tensile specimen before and after tensile loading.

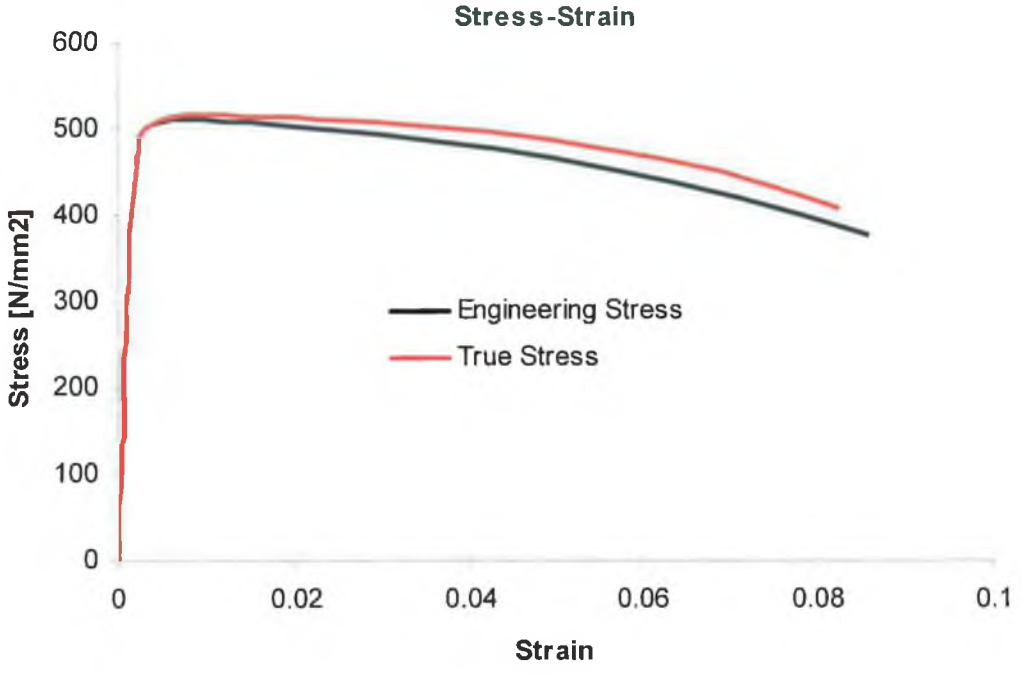

Figure 4-12: An engineering and true Stress-strain curve for sample one.

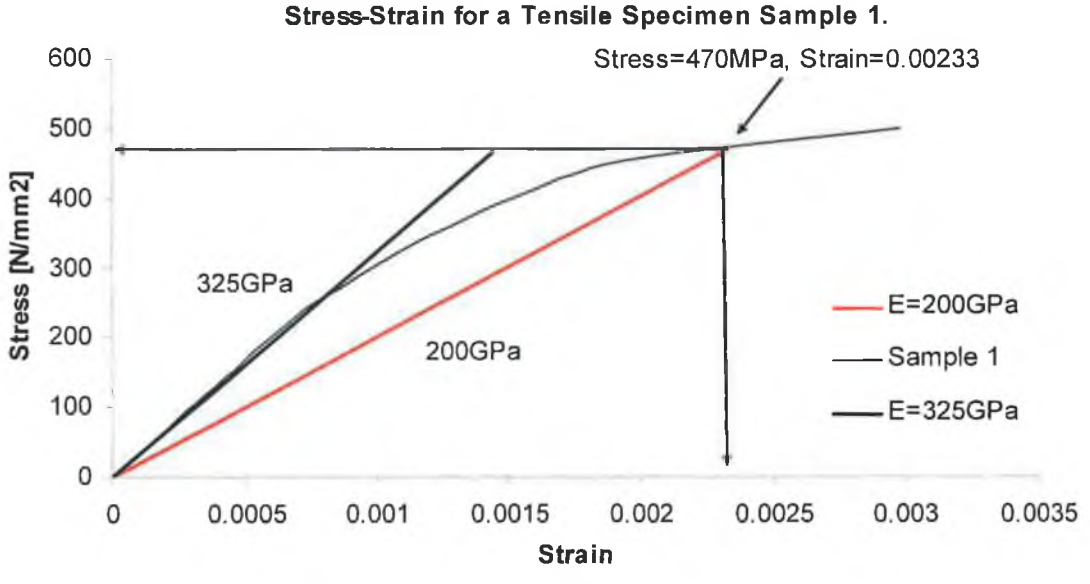

Figure 4-13: A detailed stress-strain plot of sample one

4.6 Summary of Chapter Four.

- A detailed account was given on the experimental procedure undertaken to compress the selected samples under quasi-static conditions. Also, a description of the load cell and the data acquisition used to capture the force magnitude and displacement was outlined.
- A description was given on the procedure used to conduct the physical testing of the selected samples under impact loading. An account was also given on the features of the high speed camera used to capture the displacement evolution of the various energy absorbers.
- A detailed account was given on the shaping process employed to convert the circular shaped tubes into oblong shapes.
- Finally, the experimental procedure used to obtain true tensile stress-strain curve from the mild steel dog bone specimens in order to characterise the material behaviour was detailed.

5 Response Optimisation of Nested Systems.

5.1 Introduction.

This chapter details the experimental analysis of various nested systems subjected to lateral quasi-static and dynamic loading. It is divided into three sections with section 5.2 and 5.3 analysing the quasi-static response of In Plane systems (IPS) and Out of Plane systems (OPS). Section 5.4 details the quasi-static response of In Plane Standard Systems (IPSS) and In Plane Damped Systems (IPDS). The aim of these sections is to analyse the response of each energy absorber and to interpret which design demonstrated the most desirable response, i.e., a rectangular shaped force-deflection curve. Finally section 5.5 analyses the dynamic response of the energy absorbers detailed in section 5.2.

5.2 Analysis of the Circular In-Plane Standard System (CIPSS).

Figure 5-2 shows the response of a basic nested energy absorber, i.e., CIPSS (Circular In-Plane Standard System) compressed under quasi-static conditions. Three specimens were tested to represent this type of absorber. As can be seen, results for each sample were identical indicating that three samples to capture the response of this system were sufficient. For this system there was an initial gap of approximately 17mm and 19mm between the tubes before crushing was initiated. These two gaps allowed all three components to deform sequentially as loading proceeded, hence the reason for the *non-monotonic* rise in force throughout the deformation stroke as illustrated by point A in Figure 5-2. Also illustrated in this figure are the stages at which each tube began to collapse in series (point B) and how the whole system strain hardened after approximately 41mm deflection. It can be seen that the energy response, which is the area under the force-deflection curve, became linear from this stage of deflection for the remainder of the displacement stroke. The initial and final stages of deformation for this CIPSS are illustrated in Figure 5-1.

Figure 5-1: Initial and final stages of compression for a CIPSS.

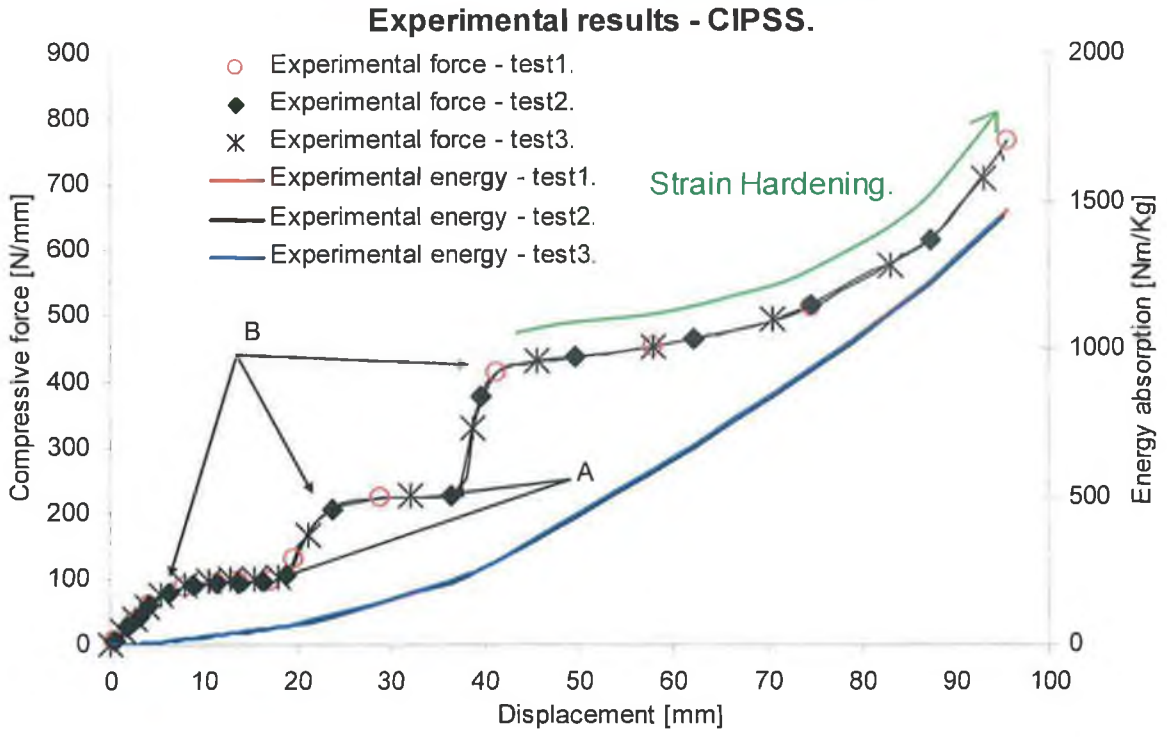

Figure 5-2: A typical force- and energy-deflection response for a CIPSS.

5.3 Geometric Variations of the CIPSS.

5.3.1 A COPSS Crushed under a Plate Indenter.

Figure 5-3 show the force- and energy- deflection response of a COPSS (Circular Out of Plane Standard System) with the initial and final stages of compression depicted in Figure 5-4. Note how the central tube was rotated 90 degrees relative to both the outer and inner tube. One important point to note is the difference in the mode of deformation between a CIPSS and a COPSS. This can be described as follows: For the CIPSS as explained previously in section 5.2, there was an initial gap of approximately 17mm and 19mm between the tubes before crushing was initiated. This resulted in a *non-monotonic* force-deflection response due to the rise in force as contact was established between each successive tube.

For the COPSS however, since there is a 90-degree orientation between the three tubes, the initial gaps have been reduced to approx 3mm and 5mm respectively. Therefore as a consequence the three tubes will begin to deform synchronously once initial contact has

been established giving rise to a much smoother response, i.e., a *monotonically* increasing response, as illustrated in Figure 5-3. There was a sharp increase in force at approximately 110mm deflection; this was due to the energy absorber been overloaded since vertical hinge points of the inner tube began to obstruct each other. This can be avoided by applying a smaller displacement stroke.

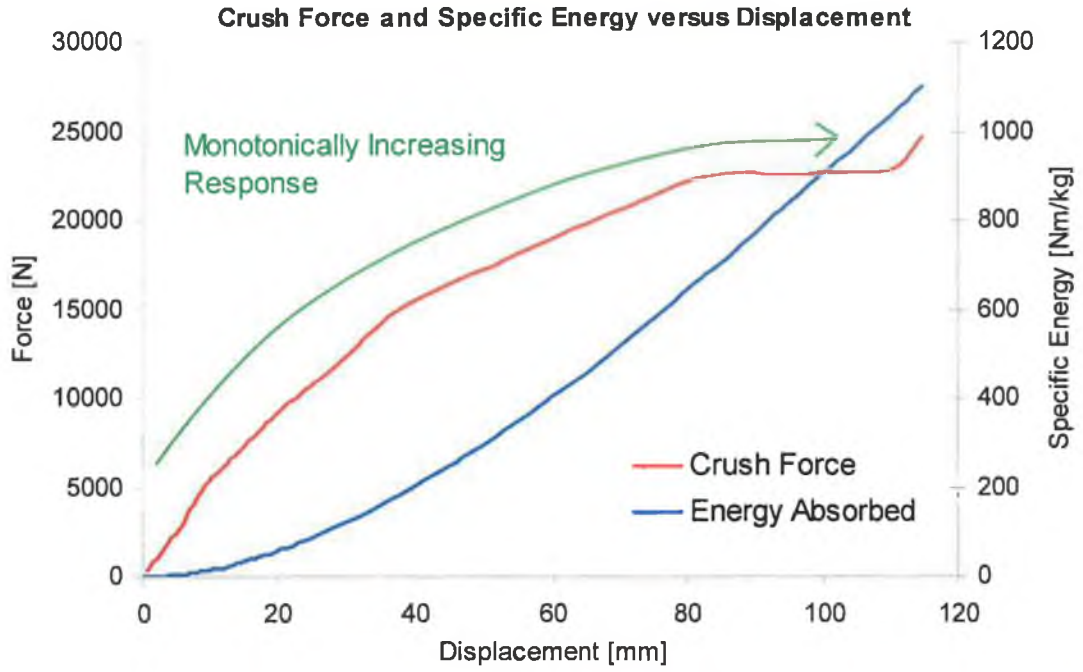

Figure 5-3: Force and specific energy response of a COPSS crushed under a flat platen.

Figure 5-4: Initial and final stages of deflection for a COPSS crushed under a rigid flat platen.

5.3.2 A COPSS Crushed under a Point Load Indenter.

The result for the compression of a COPSS crushed with a longitudinal line load indenter is shown in Figure 5-5. For convenience purposes, the longitudinal line load indenter will be referred to as a point load indenter throughout the work. This shows the corresponding force and energy absorption response for this system. It can be seen how compared to Figure 5-3, in the final stages of deflection, at approximately 100mm, a slight softening

stage occurred. This type of softening behaviour was discovered and analysed by Reid and Bell [49] on a single tube with concentrated point loads. The slight softening was due to the moment arm about the hinge point from the point load of application increasing, therefore resulting in less force required to maintain the deformation. The initial and final stages of compression are depicted in Figure 5-6 for this energy absorber.

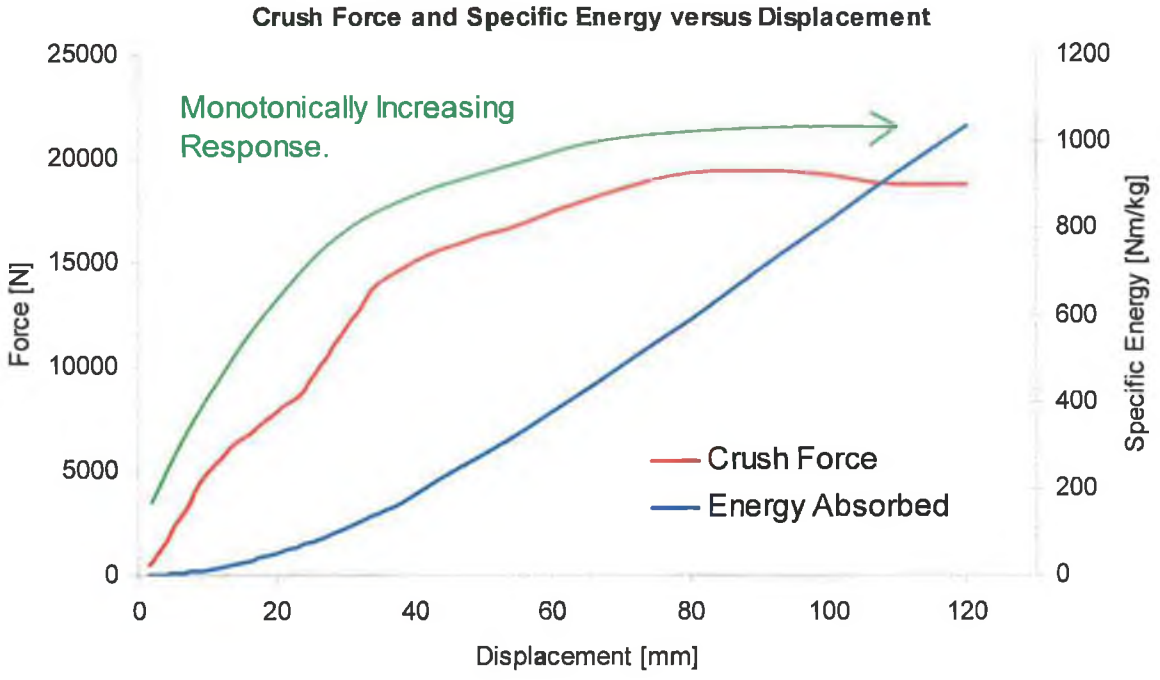

Figure 5-5: Force and specific energy response of a COPSS crushed under a point load indenter.

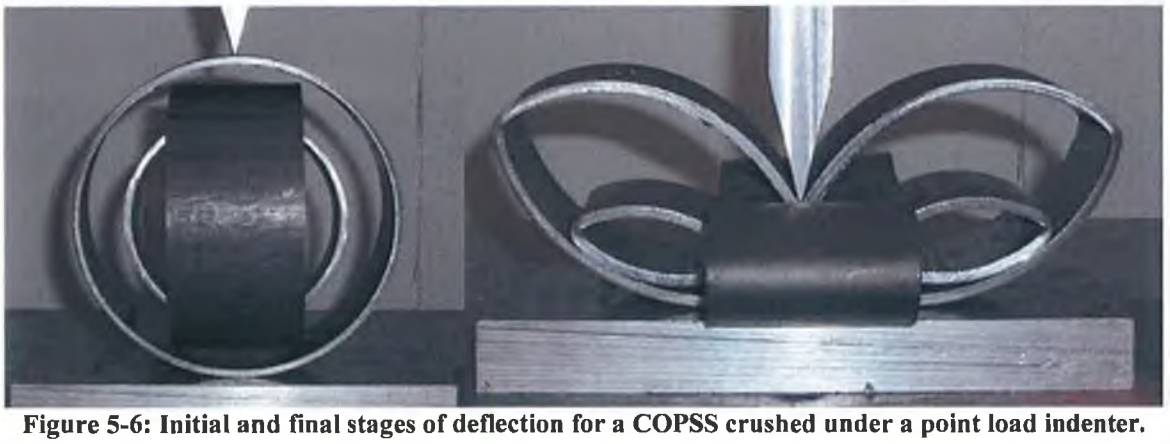

Figure 5-6: Initial and final stages of deflection for a COPSS crushed under a point load indenter.

5.3.3 A COPSS Crushed under a Cylindrical Indenter.

Figure 5-7 show the experimental results for the compression of COPSS crushed with a cylindrical indenter. This type of load application can be seen as an intermediate between the limiting cases of a flat plate and point load-indenter already illustrated by Shim et al [52]. As can be seen from this figure, the mode of deformation is quite similar to the system compressed with a point load indenter with the exception that the magnitude of

force is greater. The initial and final stages of compression for this absorber are shown in Figure 5-9. A 4% increase in the specific energy absorbed was observed in contrast to the previous system (Figure 5-5). An experimental force-deflection graph of all three systems is shown in Figure 5-8. Notice how the magnitude of force increased when progressing from a point- load indenter to rigid flat platens.

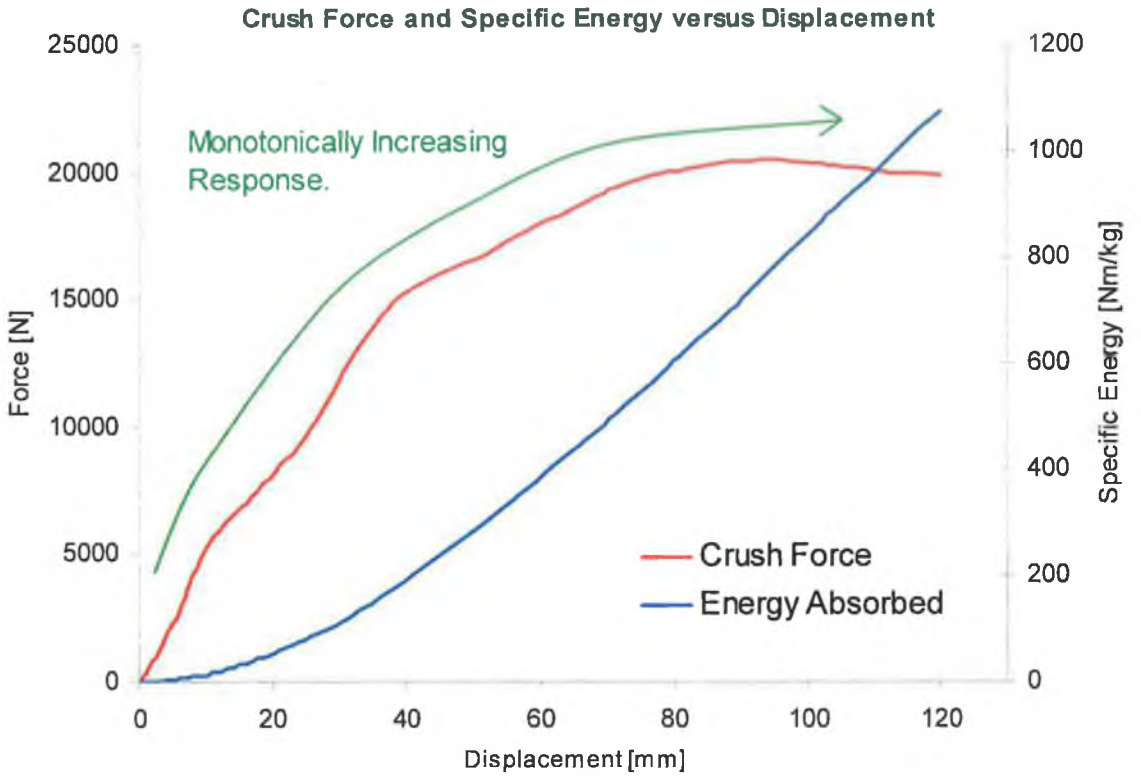

Figure 5-7: Force and specific energy response of a COPSS crushed under a cylindrical indenter.

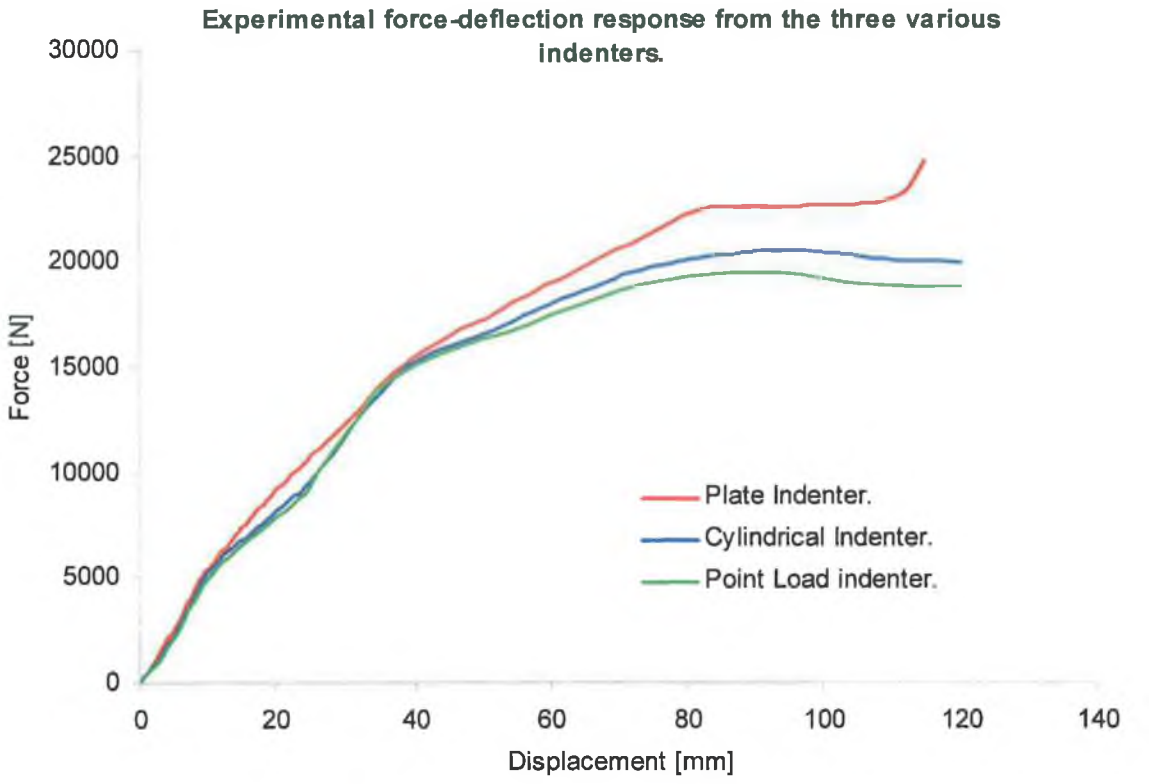

Figure 5-8: Global comparison of the three COPSS crushed under the various indenters.

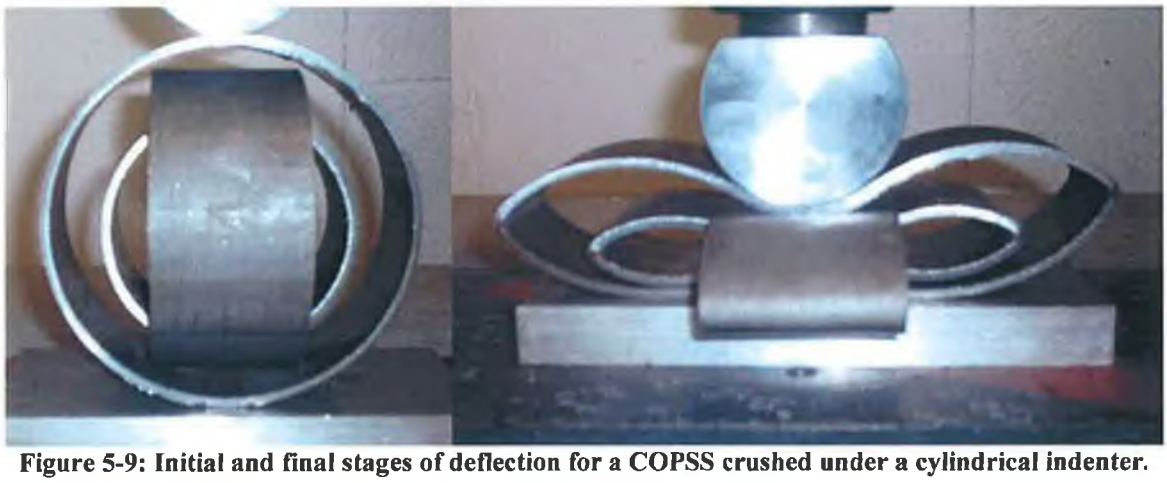

Figure 5-9: Initial and final stages of deflection for a COPSS crushed under a cylindrical indenter.

5.3.4 A SCIPSS Crushed under a Plate Indenter.

Figure 5-10 represents the experimental response of a SCIPSS (Slotted Circular In-Plane Standard System) subjected to a lateral crushing force. The initial and final displacement plots obtained from both methods are depicted in Figure 5-11. Normally, in the lateral compression of a single tube, as the load increases beyond the collapse load, the zone over which plastic deformation occurs expands rapidly. This causes the moment arm to reduce, resulting in rapid increase in force and is termed geometric strain hardening as illustrated by Reid and Reddy [58]. It is ideal in the design of energy dissipating devices to remove

this strain hardening phenomenon which occurs as shown in Figure 5-2. Therefore the aim of these slots in this particular energy absorber was to remove this hardening behaviour. The slots were 8mm deep of length 20mm with a total of eight slots per tube. Each slot was machined and positioned at an angle of 45degrees as shown in Figure 5-11. By examining sample one and two obtained from experiments in Figure 5-10, it can be seen that the machined slots had the effect of reducing this rate of strain hardening to a certain degree. This was due to the fact that the plastic hinges (collapse points) which normally take place at the quadrant points of each tube, occurred in the vicinity of each slot present in each tube in the early stages of deformation. As a consequence, due to less material available in between the slots, only a smaller magnitude of force was required to maintain the deformation. However, as deformation proceeded beyond this point, there was an increase in force at approximately 82mm; this was due to the plastic hinge moving away from the slotted regions and relocating at the horizontal points of each tube as shown in Figure 5-11. Sample one exhibited a total energy absorption of 1713Nm and sample two a value of 1700Nm.

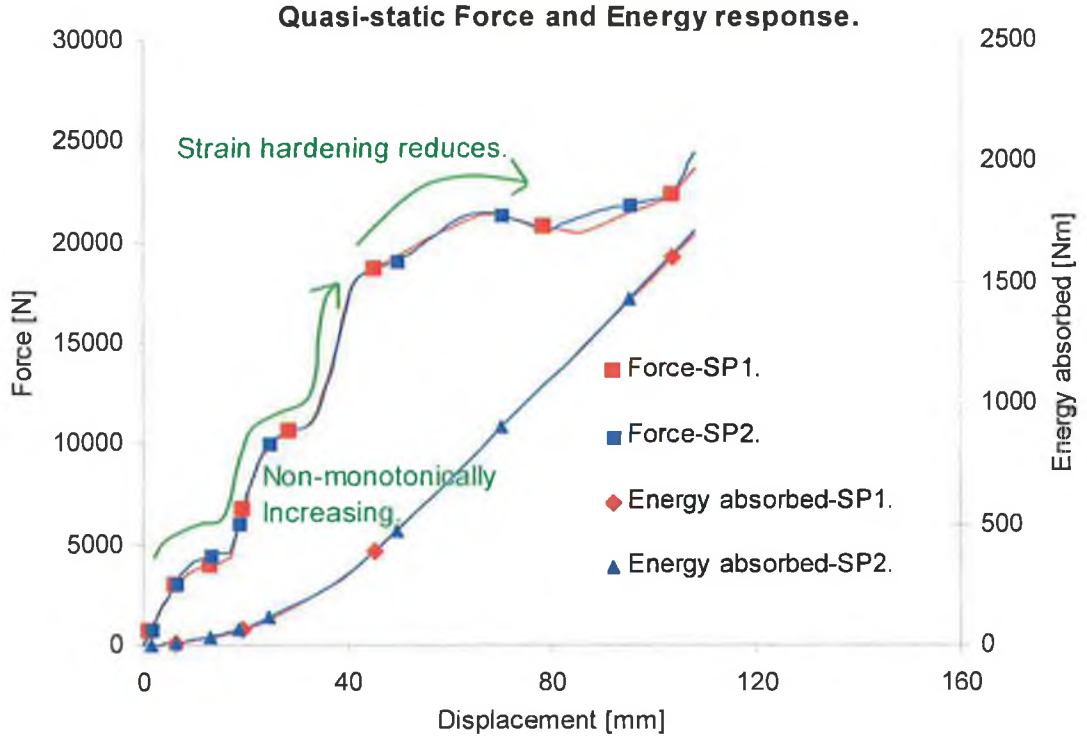

Figure 5-10: A force- and energy- deflection response for a SCIPSS

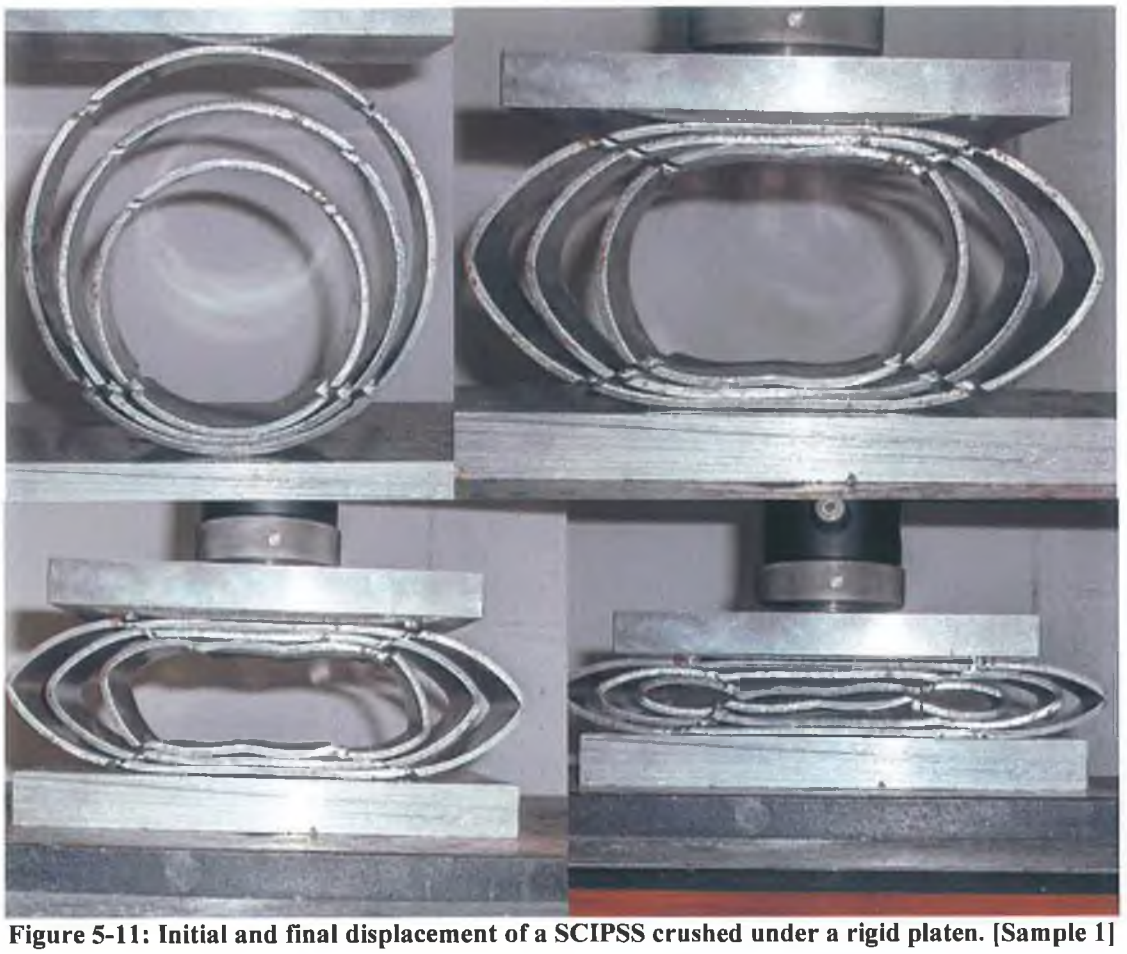

Figure 5-11: Initial and final displacement of a SCIPSS crushed under a rigid platen. [Sample 1]

5.3.5 A SCOPSS Crushed under a Plate Indenter.

Figure 5-12 depicts the experimental response of a Slotted Circular Out of-Plane Standard System (SCOPSS) with the initial and final stages of displacement as illustrated in Figure 5-13. This system is similar to the COPSS analysed in section 5.3.3 but with the addition of eight slots machine into each tube. For up to approximately 60mm deflection, the force response is very similar to the COPSS as shown in Figure 5-5. However, it appears that once the collapse load was reached, i.e., at 57mm deflection for sample 1 and 65mm deflection for samples two and three, the response showed an erratic behaviour, exhibiting an unstable response in that the samples displayed a drop in force for a period of time before increasing again for the remaining displacement stroke. The presence of the slots did not produce any positive effect in reducing the strain hardening effect; instead, each tube collapsed synchronously resulting in a rapid drop in force from approximately 57mm to 65mm deflection. Also, from close examination of Figure 5-13, it can be seen that the inner tube did not remain symmetric during the displacement stroke, indicating the sensitivity of this system to lateral crushing. This behaviour can be a contributing factor for the observed behaviour in this particular system.

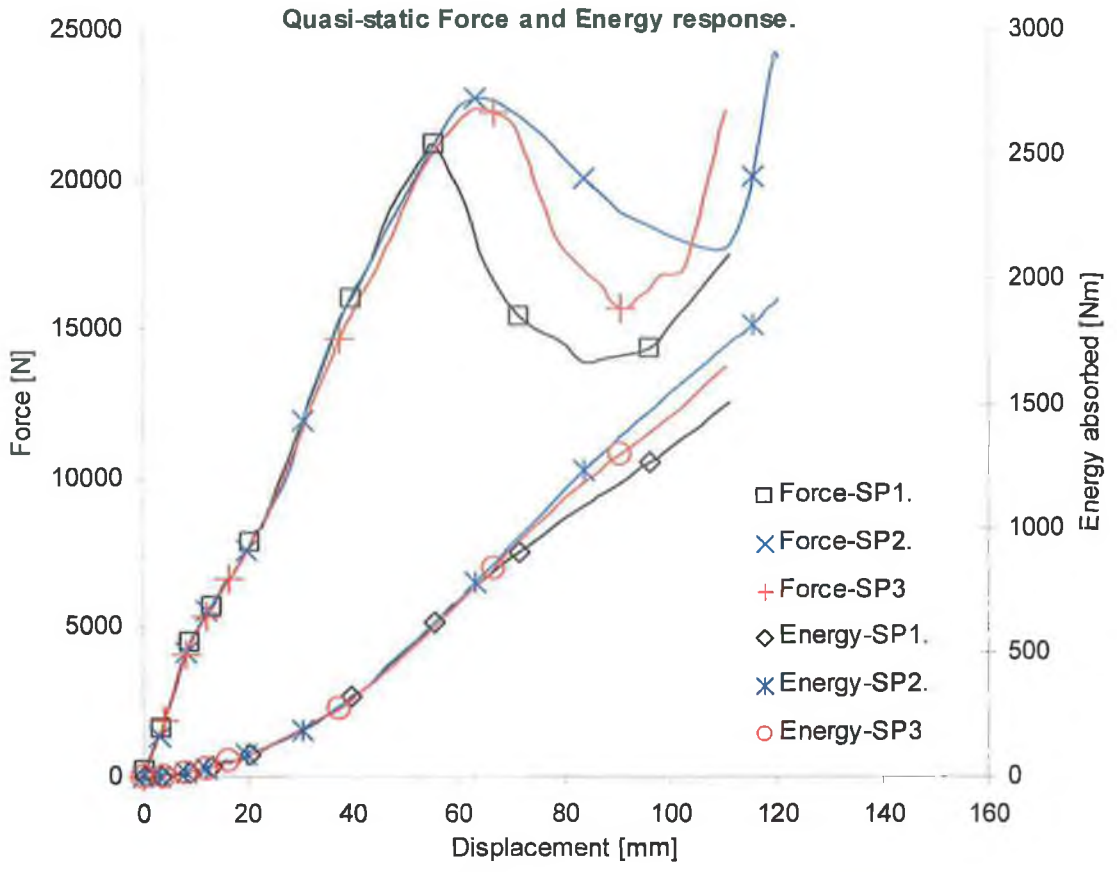

Figure 5-12: A force-and energy-deflection response of a SCOPSS.

Figure 5-13: Initial and final stages of deflection for a SCOPSS. [Sample 1]

5.3.6 A SCIPDS rushed under a Plate Indenter.

The experimental response of a Slotted Circular In Plane Damped System (SCIPDS) represented by two samples is depicted in Figure 5-14. The photographic evolution displacements of both samples are shown in Figure 5-15 and Figure 5-16 respectively. In

an attempt to obtain a rectangular force-deflection response, two cylindrical spacers were inserted in between the successive tube as illustrated by two figures. From this, it can be clearly seen that once the flat rigid platen impinges on this absorber, the three tube components will begin to deform synchronously and collapse at the same time as shown by pointer A in Figure 5-14. In addition to this, the presence of the eight slots in each tube caused the plastic hinges to occur in the vicinity of the slots in the early stages of deformation. An approximate rectangular force-deflection or a *monotonically* increasing response was achieved for a deflection of up to approximately 45mm for both samples. However, from therein, sample one appeared to behave inconsistently in that the force increased, which was due to the fact that the plastic hinges travelled from the vicinity of the slots to the quadrant points of each tube as shown in the last photograph in Figure 5-15. Sample two experienced a drop in force; this was due to the asymmetric deformation behaviour as illustrated in Figure 5-16, which resulted in an unstable response. It can be seen that this particular energy absorber was sensitive to lateral deformation due to the presence of the slots in each tube. Sample one exhibits an energy absorption value of 1530Nm and sample two a value of 1334Nm.

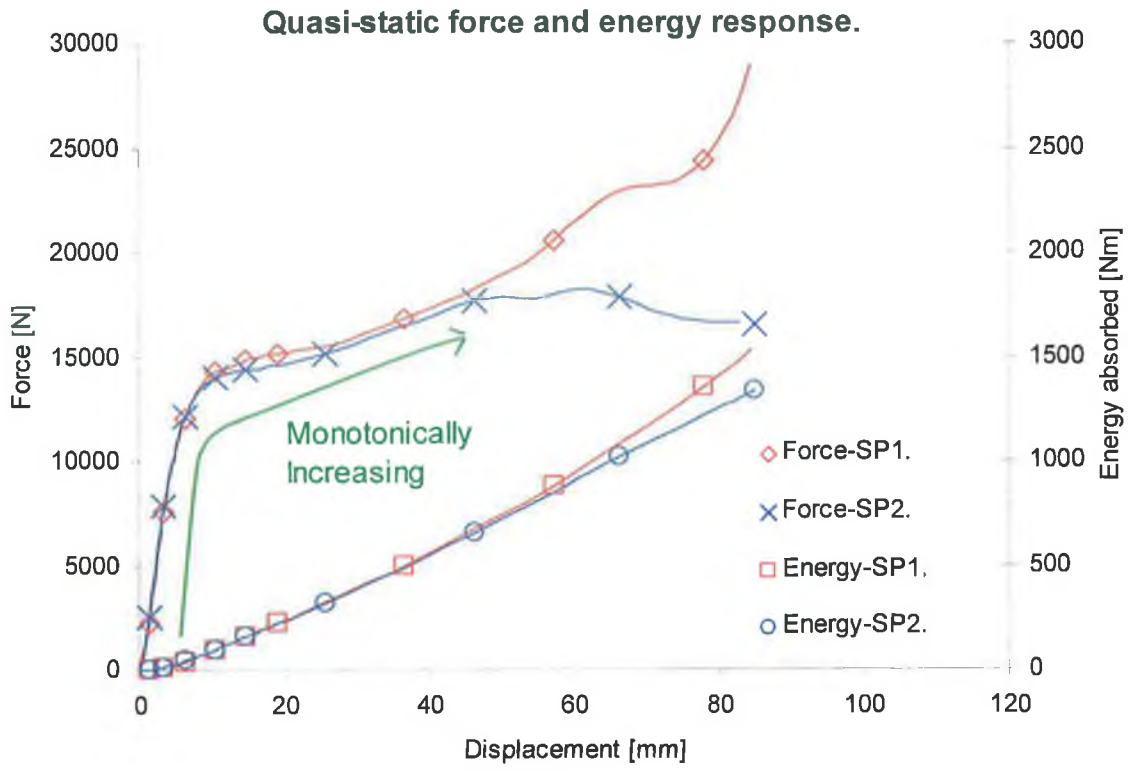

Figure 5-14: A force- energy- deflection response for a SCIPDS.

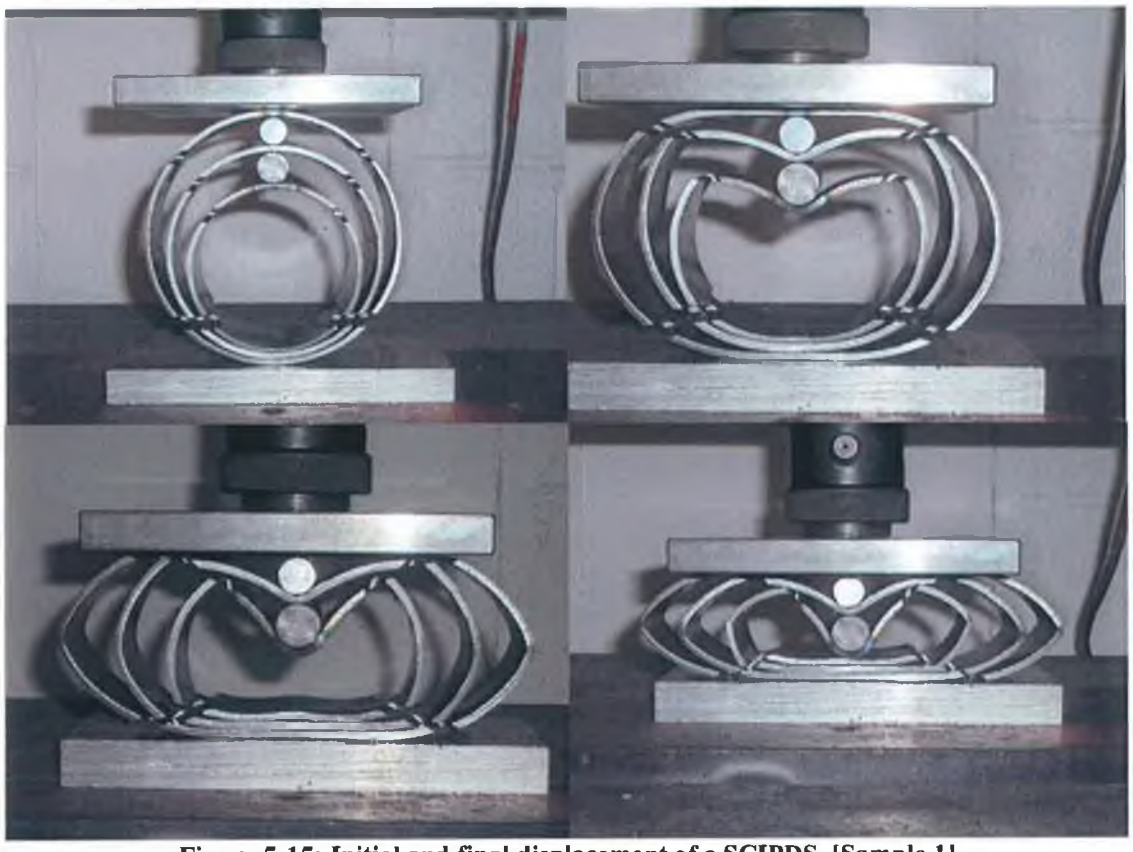

Figure 5-15: Initial and final displacement of a SCIPDS. [Sample 1]

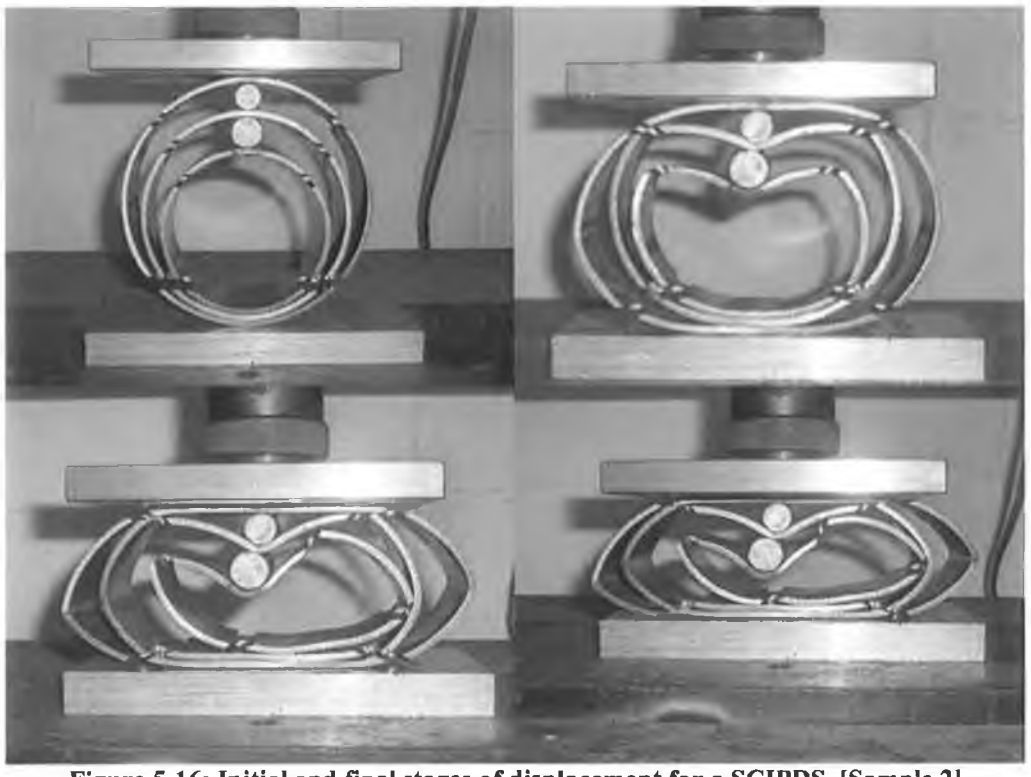

Figure 5-16: Initial and final stages of displacement for a SCIPDS. [Sample 2]

5.4 Quasi-Static Analysis of the CIPDS, OIPSS and the OIPDS.

5.4.1 Evaluation of the CIPDS.

The force- and energy-deflection response for a CIPDS (Circular In-Plane Damped System) is shown in Figure 5-17 with the initial and final stages of displacement for the three samples in Figure 5-18, Figure 5-19 and Figure 5-20 respectively. Upon examination of these displacement evolution photographs, two cylindrical spacers were inserted between the gaps of the three tubes. These spacers served two purposes; firstly, to eliminate the *non-monotonic* increase in force as contact was establish between tubes as deformation proceeded and secondly, to reduce the rate of strain hardening due to the radius of curvature of the spacers. Shim et al [52] analysed the lateral crushing of thin walled tubes using cylindrical indenters and side constraints. A complete range of indenter radii have been used varying from infinite radius of curvature (flat rigid platens) to zero radius of curvature (point load indenters) to crush these thin walled tubes and to examine their responses. It was discovered that, depending on the radius of curvature of the indenters, the post collapse behaviour of laterally compressed tubes can be either stable (deformation- hardening/monotonically increasing) or unstable (deformation-softening/monotonically decreasing). Therefore in this work, the radius of curvature of the spacers inserted between the three tubes can be seen as an intermediate between the limiting cases of a flat plate and point load-indenter resulting in a force-deflection response

that is approximately rectangular in shape as shown in Figure 5-17. Upon observation of this figure, there was a slight rise in force at approximately 60mm displacement for the three samples; this was due to the 'bottoming out' of each sample. This can be avoided by simple applying a slightly shorter displacement stroke. As a result of obtaining this rectangular shaped response, the corresponding energy absorption was quite linear for the entire deflection stroke. Note that for sample 1 (See Figure 5-18), how the deformation process was non-symmetric. This was due to the sensitivity of geometric imperfections within the structure. Such imperfections may be a function of how accurate the tubes and spacers were placed centrally with respect to one another. As deformation proceeds, the spacers shifted in the direction of least resistance which resulted in an asymmetric mode of deformation.

In an attempt to counteract this problem, a mild steel dowel was placed into the structure connecting the upper halves of the tubes and the two spacers. A spot weld was used to fuse both ends of the dowel to the structure in order to determine whether this would assist in maintaining symmetry; it can be seen that this was achieved as depicted in Figure 5-19 and Figure 5-20. Despite the asymmetric behaviour of sample one during lateral deformation, it appears that its corresponding force-deflection result still exhibited the desired rectangular shaped response.

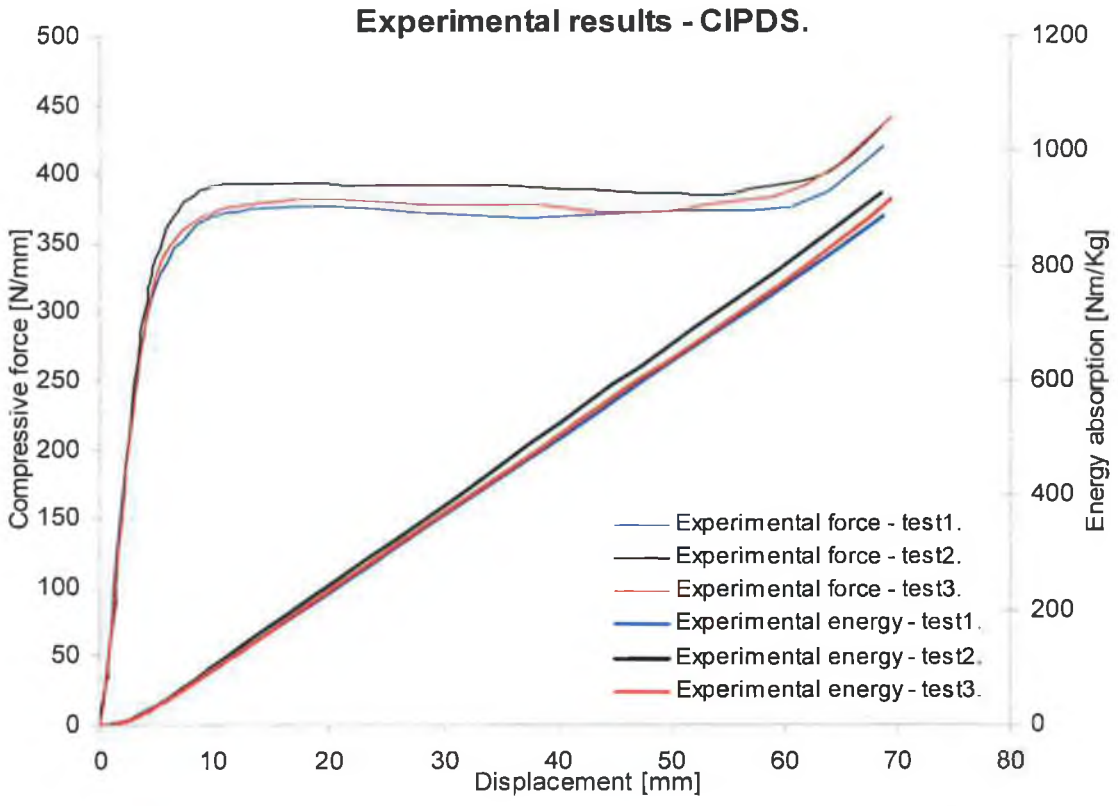

Figure 5-17: A typical force-and energy-deflection response for a CIPDS.

Figure 5-18: Initial and final stages of compression for a CIPDS. [Sample 1]

Figure 5-19: Initial and final stages of compression for a CIPDS. [Sample 2]

Figure 5-20: Initial and final stages of compression for a CIPDS. [Sample 3]

5.4.2 Evaluation of the OIPSS [Tension method].

The response of an OIPSS (Oblong In-Plane Standard System) represented by three samples using the tension method is depicted in Figure 5-21 followed by the various stages of deformation of a typical sample as shown in Figure 5-22. For this system, the initial gaps between the three tubes have increased from 17mm and 19mm to 28mm and 56mm respectively due to the tension method used to create the oblong tubes as outlined in section 4.4. An increase in the displacement stroke was possible since the tubes have been elongated in the vertical direction. Therefore, it can be seen that the specific energy absorption for this category of system will increase due the available increase in displacement stroke. Point A in Figure 5-21 shows that there was a slight softening stage which occurred in each tube, this was due to the geometrical changes which have occurred as a result of using the tension method. Since the tubes have been plastically elongated in the vertical direction, the radius of curvature has increased on both the top and bottom vertical hinge points of each tube. Therefore the contact between the rigid platen and the outer tube can be approximated as a 'point' load application as demonstrated by Shim and Stronge [92]. This creates a greater moment arm from the point of load application to the

horizontal hinge points of each tube and as a result less force is required to maintain the deformation and hence a geometrical - softening stage occurs. However, this softening is counteracted by two other strain - hardening phenomena. Firstly, upon initial contact, only one line of contact was established between the inner tube and the central tube, however as deformation proceeded, this contact line had split in two and moving away from the centreline, causing the moment arm about the horizontal hinge points to reduce. Therefore, as a consequence, a greater force was required to maintain the deformation. This is termed geometrical - hardening as illustrated by Reddy and Reid [58]. This description can be seen in the final stage of deformation as depicted by point B in Figure 5-21. Secondly and more importantly, the existence of the material strain hardening characteristic occurring in all three tubes will add significantly to the final strain hardening response of the structure.

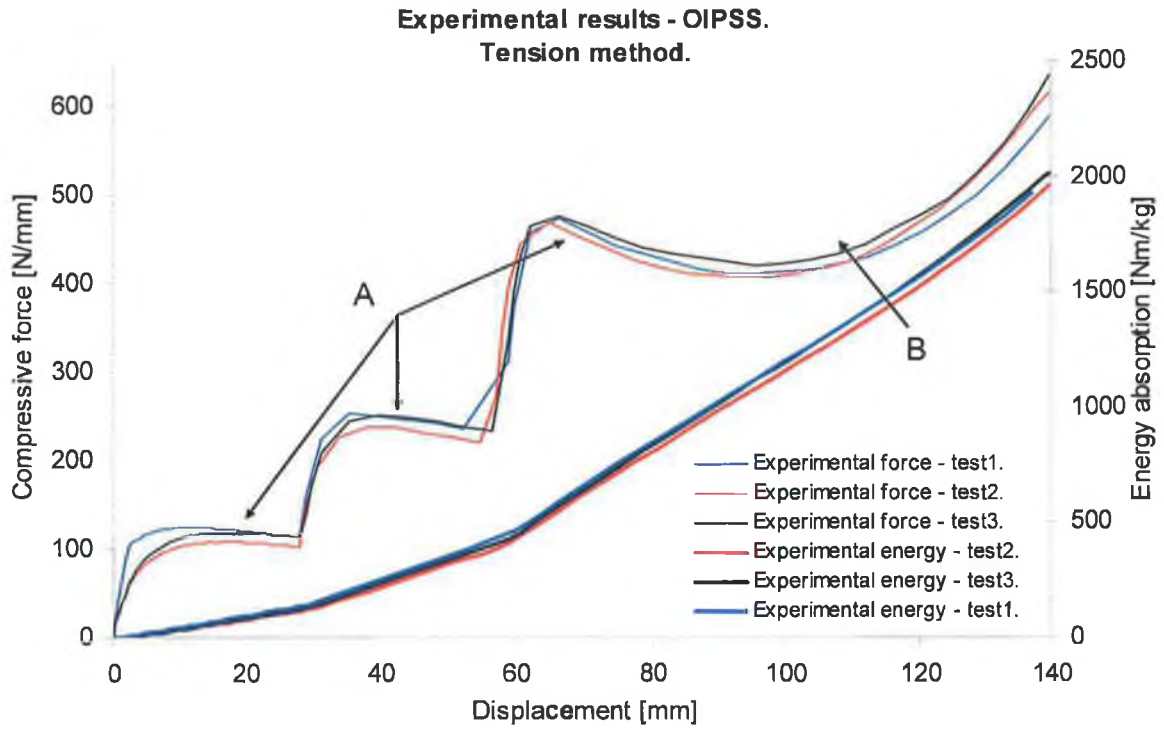

Figure 5-21: A typical force, energy-deflection response for an OIPSS. [Tension method]

Figure 5-22: Initial and final stages of compression for an OIPSS. [Tension method.]

5.4.3 Evaluation of the OIPSS [Compression method].

The force- and energy-deflection response of a similar OIPSS represented by three samples using the compression method is depicted in Figure 5-23. As shown by point A, the rate of strain softening was less than that using the tension method since only a total compression displacement of 120mm was possible as opposed to 140mm using the tension method. This resulted in the radius of curvature been less than that using the tension method and hence the corresponding moment arm was smaller from the point load of application to the horizontal hinge points. Therefore a greater magnitude of force was required to maintain the deformation. Point B in the same figure illustrates the material strain hardening that occurred in the three tubes which lead to a greater overall force required to compress the system. Figure 5-24 demonstrates the various stages of compression of a typical sample for this OIPSS.

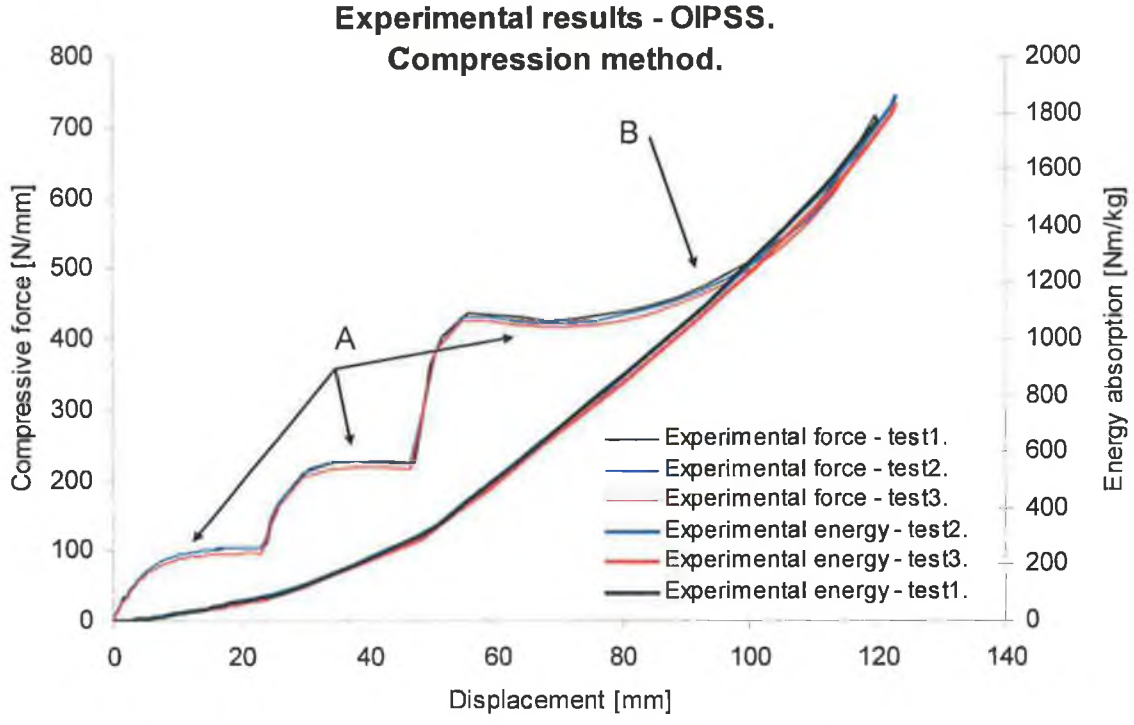

Figure 5-23: A typical force- and energy-deflection response for an OIPSS. [Compression method]

Figure 5-24: Initial and final stages of compression for an OIPSS. [Compression method]

5.4.4 Evaluation of the OIPDS [Tension Method].

Since the tension method allowed a greater displacement stroke possible without the possibility of each tube buckling inward during compression, it was decided to employ this method as a means of forming the oblong shaped tubes. Accordingly, the force and energy response of an OIPDS (Oblong In-Plane Damped System) using this tension method is shown in Figure 5-26 along with the various stages of deformation in Figure 5-27. As previously mentioned, a steel dowel was placed into this system connecting the upper halves of the tubes and the two cylindrical spacers. Since this dowel successfully maintained reasonable symmetry during the entire deformation stroke for the CIPDS, it was anticipated that a similar outcome would be achieved for this OIPDS. However, upon observation of Figure 5-27, it can be seen that symmetry was not achieved. Instead, the spacers had a tendency to shift in the direction which offered the least resistance. It appears that the response is more sensitive to geometrical imperfections compared to its CIPDS counterpart. A possible reason for this increased sensitivity may be due to the fact that there was a greater likelihood of each tube deforming in an asymmetric manner due to the increased displacement stroke that must be undergone by the system. Also, due to the oblong shape of the tubes and the assemblage of the spacers with a steel dowel, it was difficult to achieve perfect symmetry during manufacture before any loading was applied. This can be regarded as a contributing factor in the observed behaviour of the system. In an attempt to rectify the situation, the third sample was spot welded at various locations as shown in Figure 5-25 to determine whether this may counteract the asymmetric deformation. This approach was unsuccessful and resulted in an undesirable increased stiffness during compression as depicted by sample 3 in Figure 5-26. Note that a softening stage has also occurred for this system as described previously for the OIPSS. Finally, this geometrical - softening behaviour was counteracted by the materials strain-hardening response as large deflections ensue as illustrated by pointer B. Despite the asymmetric behaviour of the three samples, the desired rectangular response as depicted by tests one and two is still maintained.

Figure 5-25: The initial and final stages of compression for an OIPDS with spot welds. [test 3]

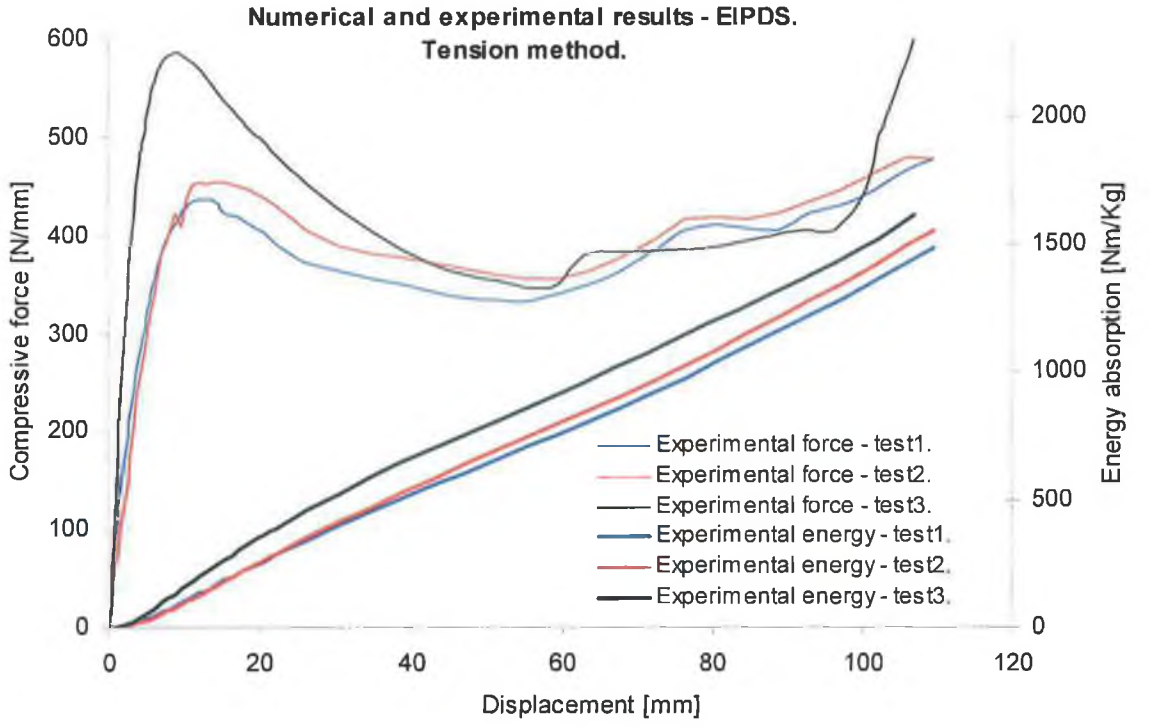

Figure 5-26: A typical force- and energy- deflection response for an OIPDS. [Tension method]

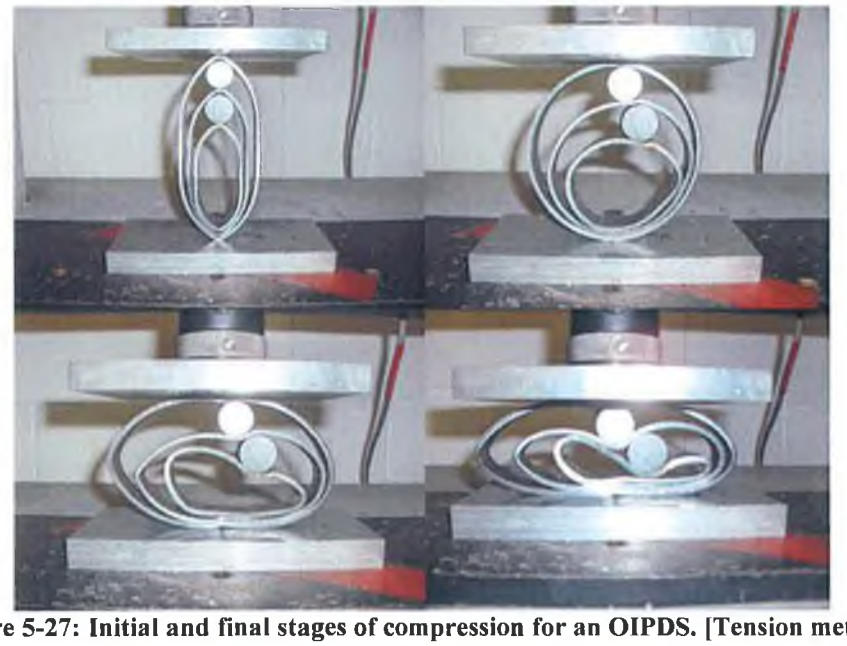

Figure 5-27: Initial and final stages of compression for an OIPDS. [Tension method]

5.4.5 Global Comparison of the In-Plane Standard Systems.

Figure 5-28 illustrates the comparison of the force-deflection response between the circular (CIPSS) in conjunction with the oblong tube absorbers (OIPSS) created using both the compression and tension methods. It can be seen how the various methods affect the hardening response of the absorbers. For example, when a greater plastic preload was applied to each tube in the preparation stages, the rate of strain hardening is reduced for each absorber compressed under between the rigid flat platens.

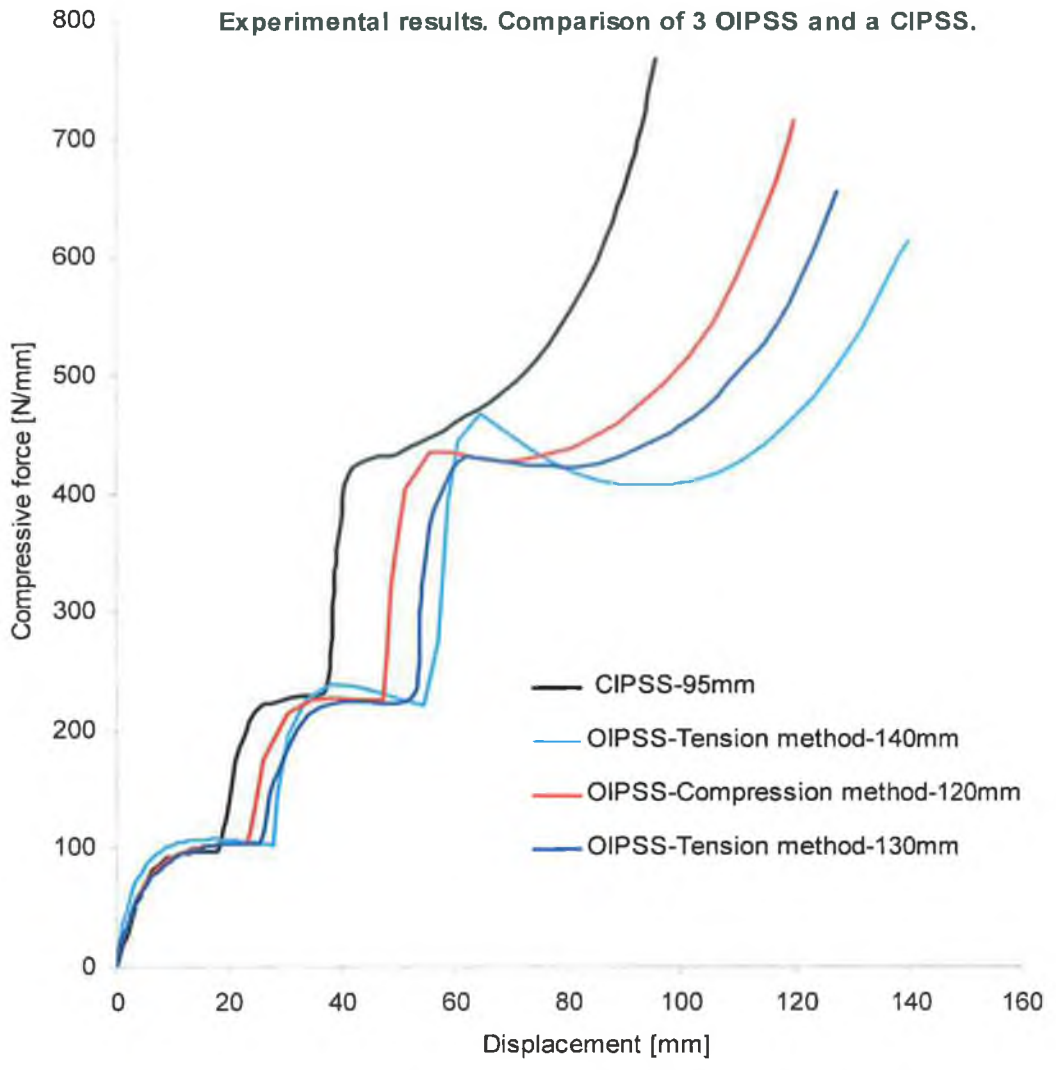

Figure 5-28: Experimental comparison of the CIPSS and the three OIPSS.

5.4.6 Energy Absorption Characteristics.

Upon examination of the response characteristics in Figure 5-29, it can be seen that both the CIPSS and the OIPSS exhibited the highest crush efficiencies followed by the CIPDS and the OIPDS. The latter two systems exhibit lower crush efficiency for the reason that the spacers inserted between the tubes reduced and compromised the overall displacement stroke. This is due to the fact that such components were solid cylindrical bodies and therefore will serve to act as rigid entities. In terms of energy efficiency, both the CIPDS and the OIPDS demonstrated the highest values of 46% and 47% respectively, where as the CIPSS and OIPSS showed values of 36% and 43% respectively (See section 3.3.1 for a description of the various characteristics). Figure 5-29 also illustrates the weight effectiveness of the four energy absorbers, where the OIPSS shows the greatest effectiveness followed by the CIPSS, OIPDS and the CIPDS respectively.

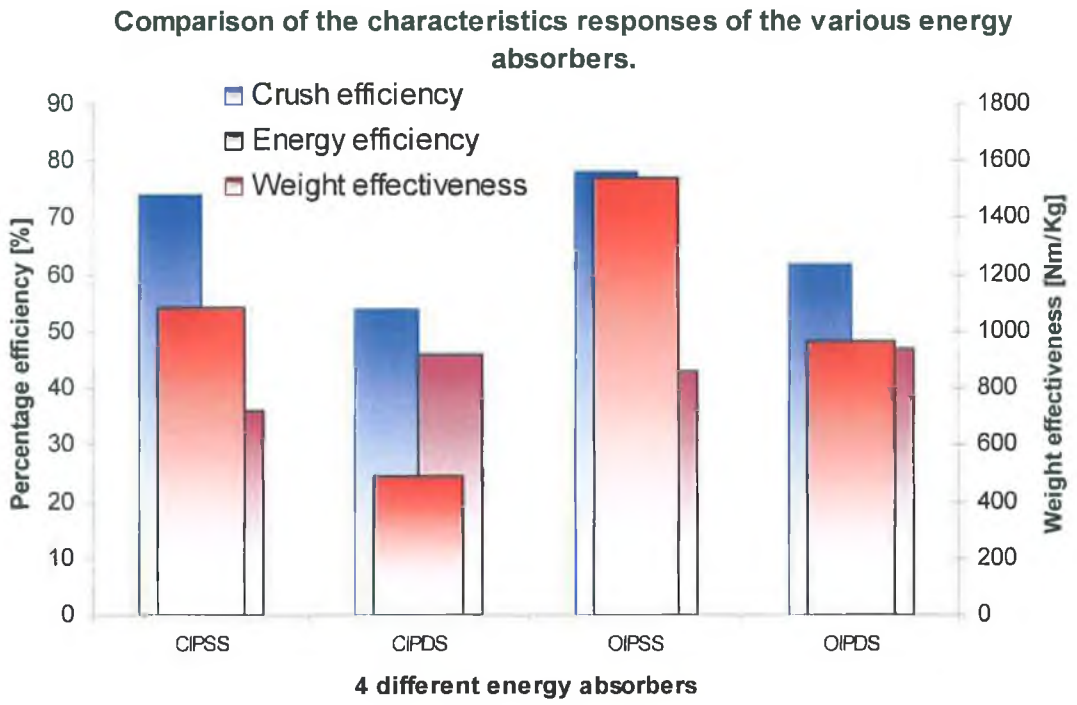

Figure 5-29: Column chart displaying the various performance characteristics of each absorber.

5.5 Dynamic Analysis of the IPSS and IPDS Energy Absorbers.

5.5.1 Evaluation of the CIPSS.

Figure 5-30 shows the response of a CIPSS (Circular In-Plane Standard System) compressed under dynamic loading conditions. Five specimens were tested to represent this category of absorber. As illustrated in this figure, the response from each sample was reasonably consistent. For this system there was an initial gap of approximately 17mm between the outer and central tube and 19mm between the central and inner tubes. These two gaps allowed all three components to deform sequentially as loading proceeds, hence the reason for the *non-monotonic* increase in force throughout the deformation stroke. Figure 5-31 depicts sample five in its filtered and unfiltered state, the former which was used for comparison purposes against numerical results at a later stage in this work. Since the force-time response was consistent, it can be seen that the input velocity applied to each sample (Figure 5-32) was also consistent indicating that the striker was raised to its correct height for each test. Upon examination of Figure 5-33, there was an increase in the rate of energy absorption as each tube was compressed in succession, reaching a final value of approximately 225J. The digital photographs (Figure 5-34) display the evolution of this energy absorber as recorded by the high speed video recorder with each image displaying the time of contact in milliseconds.

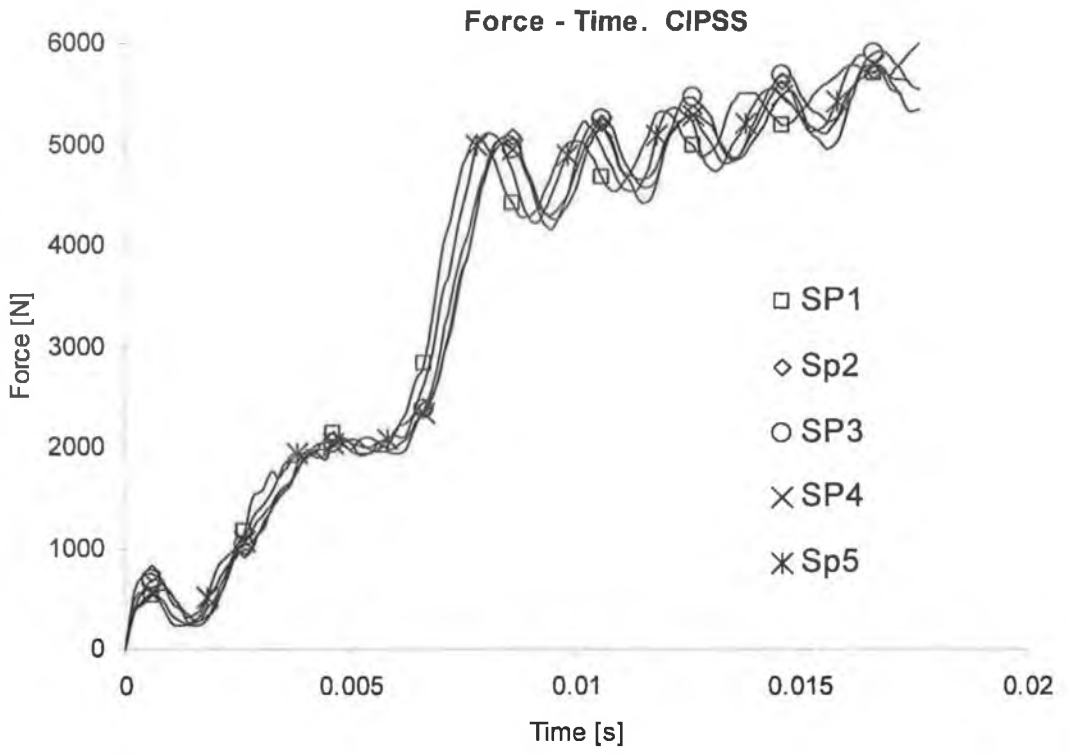

Figure 5-30: Dynamic force-time response of a CIPSS represented by five samples.

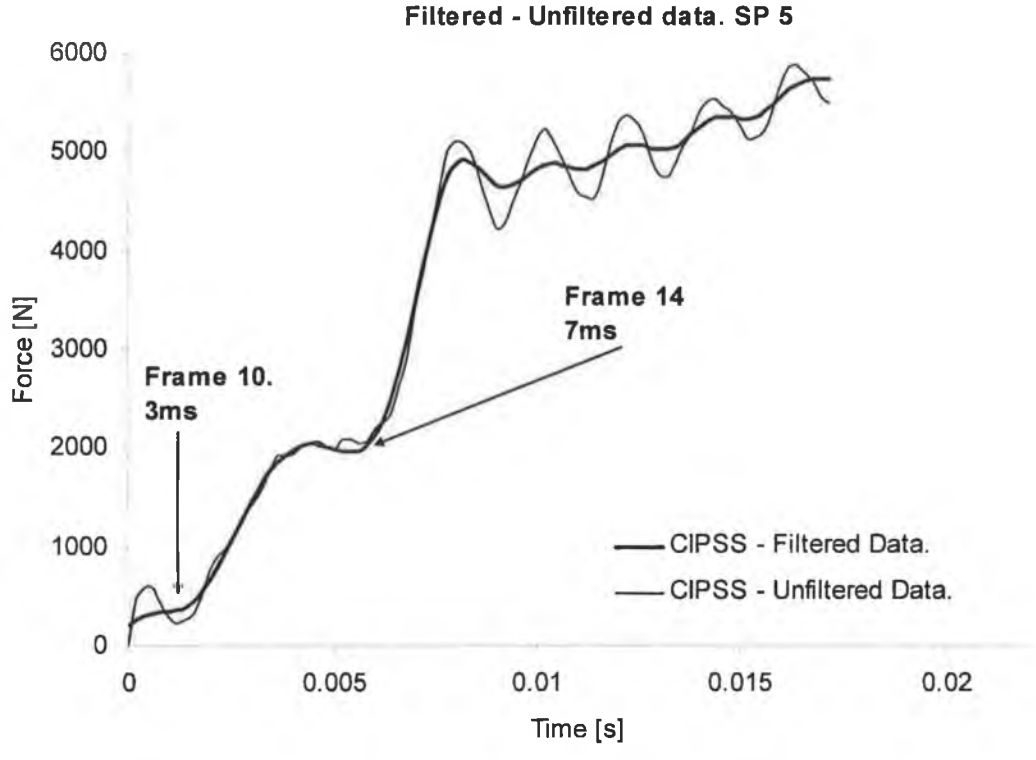

Figure 5-31: Sample five of a CIPSS in its filtered and unfiltered state.

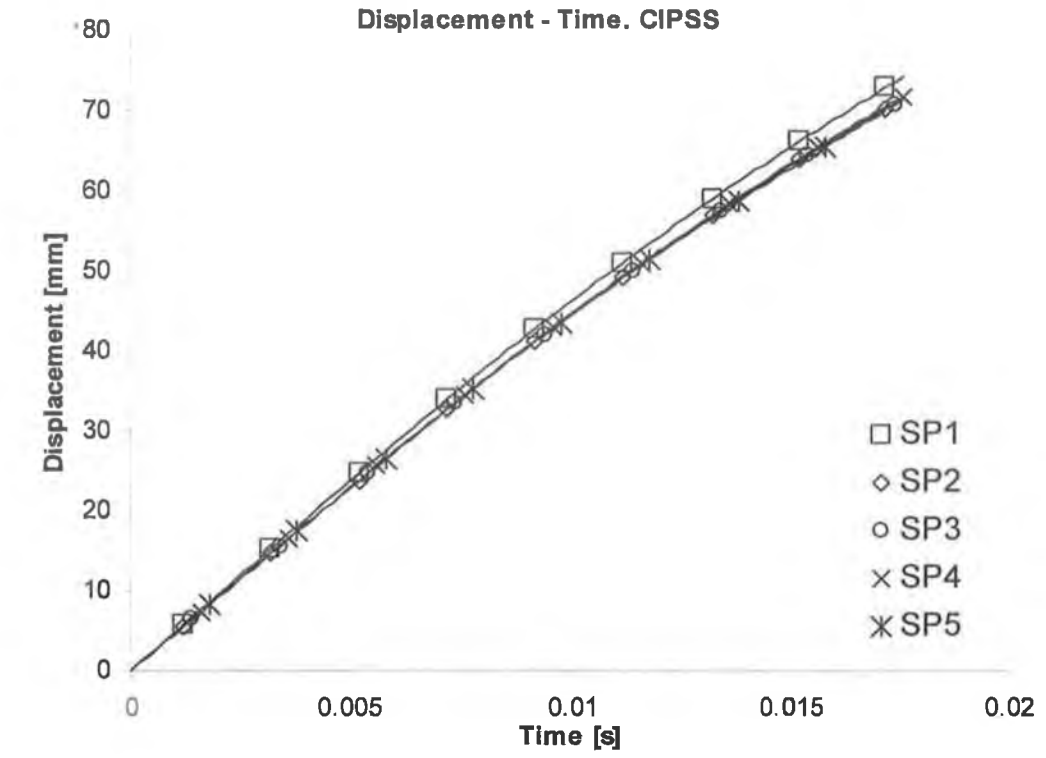

Figure 5-32: Displacement-time response of a CIPSS.

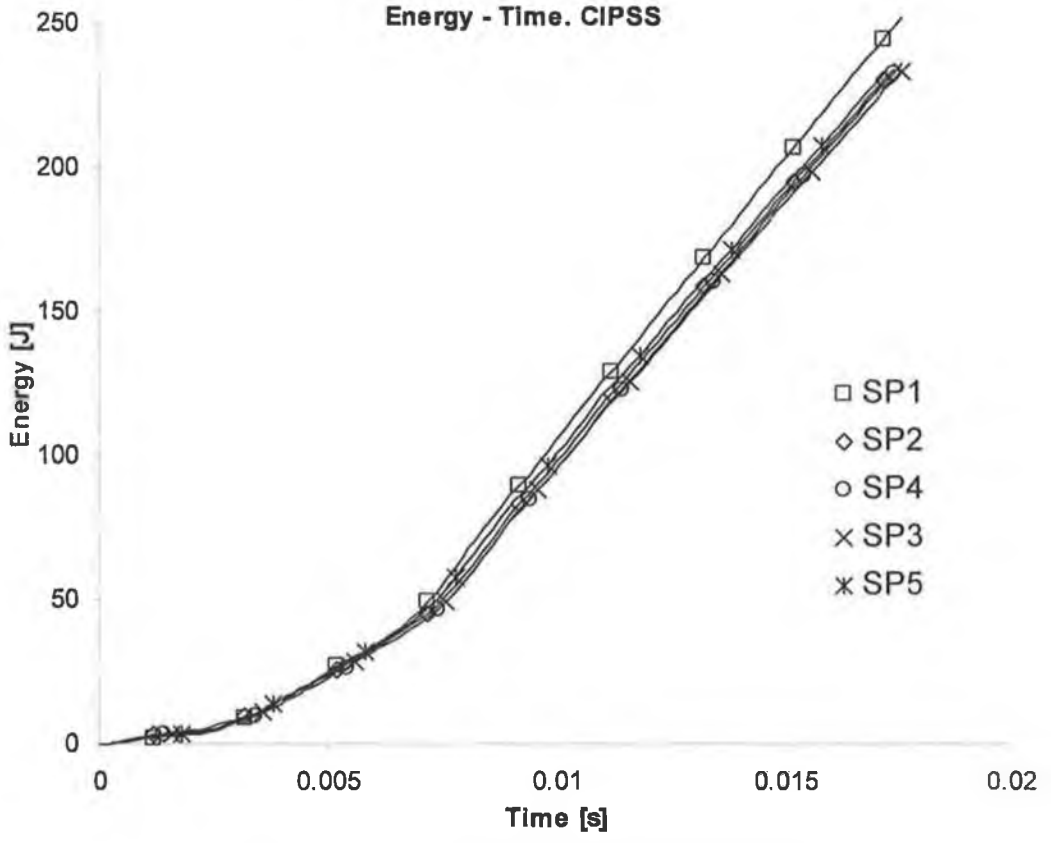

Figure 5-33: Energy-time response of a CIPSS.

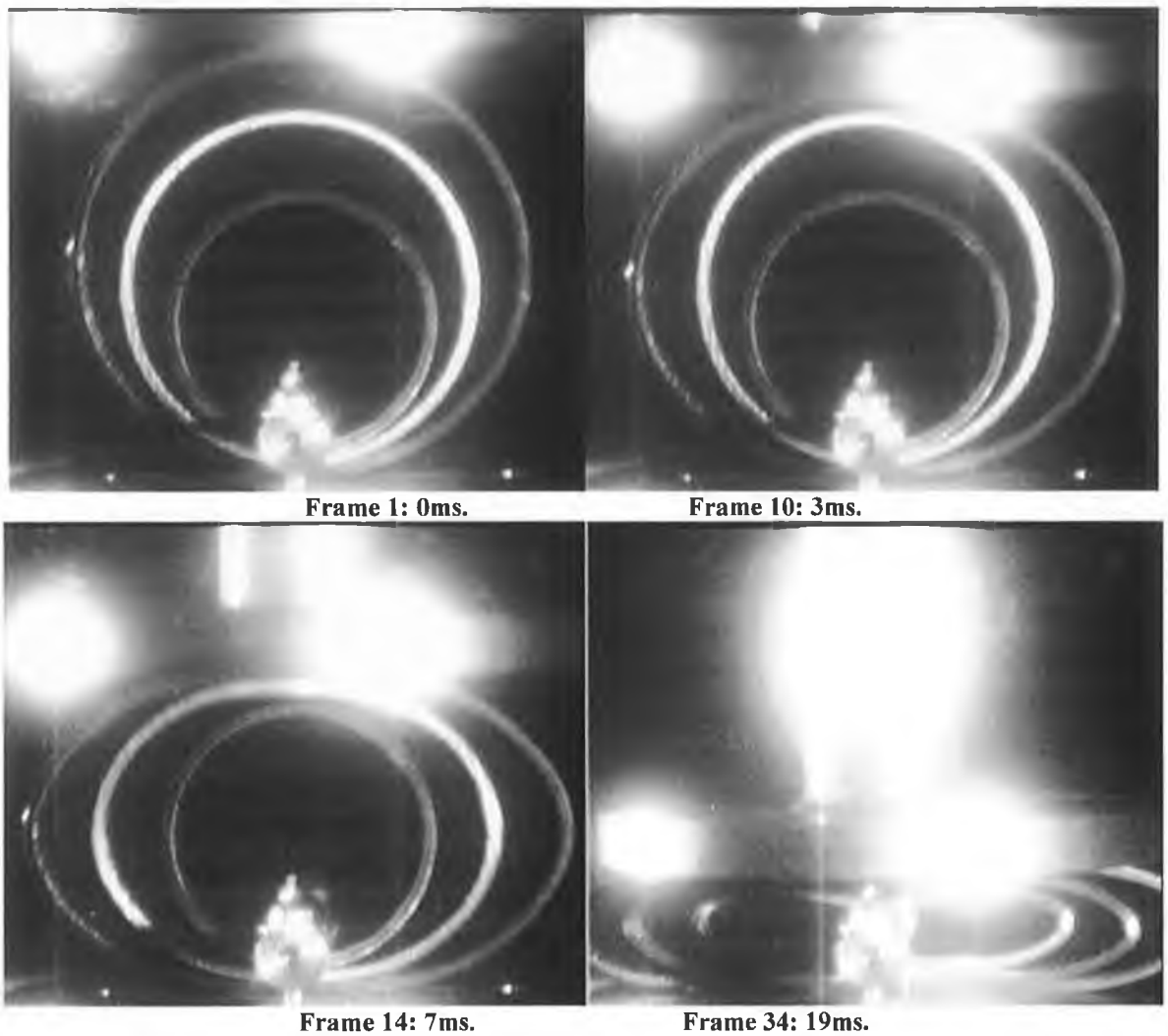

Frame 1: 0ms. Frame 10: 3ms.

Frame 14: 7ms. Frame 34: 19ms.

Figure 5-34: Dynamic displacement evolution of a CIPSS.

5.5.2 Evaluation of the CIPDS.

The experimental force-time output response of a CIPDS (Circular In Plane Damped System) is shown in Figure 5-35. In an attempt to achieve a smoother force-deflection response than that exhibited by a CIPSS (Figure 5-30), two cylindrical spacers were inserted in between the tubes as illustrated in Figure 5-39. From this, it can be clearly seen that once the moving mass impinges on this absorber, the three tube components will proceed to deform synchronously. It should be noted that in order for the spacers to remain in position during the displacement stroke and to maintain symmetry, a mild steel dowel was placed through the upper portions of the tubes and the two spacers. This approach was also employed for the quasi-static testing of a CIPDS. The placement of the cylindrical spacers inserted between the gaps of the tubes serves the same two purposes as outlined in section 5.4.1. It can be seen that the radius of curvature of the spacers inserted between the three tubes played a primary role in obtaining a force-deflection response that was approximately rectangular in shape as shown in Figure 5-35 or Figure 5-36. Examining the

displacement-time response of this system (see Figure 5-37), samples six and sample seven show final displacements of approximately 45mm each, whilst the remaining samples exhibited higher values. This was due to the unfamiliarity with the amount of energy that could be absorbed for the initial samples number six and seven. Consequently, the energy input was increased for the remaining samples in order to achieve full displacement stroke before 'bottoming out' occurred. The energy time curve (see Figure 5-38) exhibits a more linear response than that of a CIPSS but with a slight decrease in energy absorption in the later stages of the impact event. Figure 5-39 shows the evolution of sample eight with the inclusion of the cylindrical spacers.

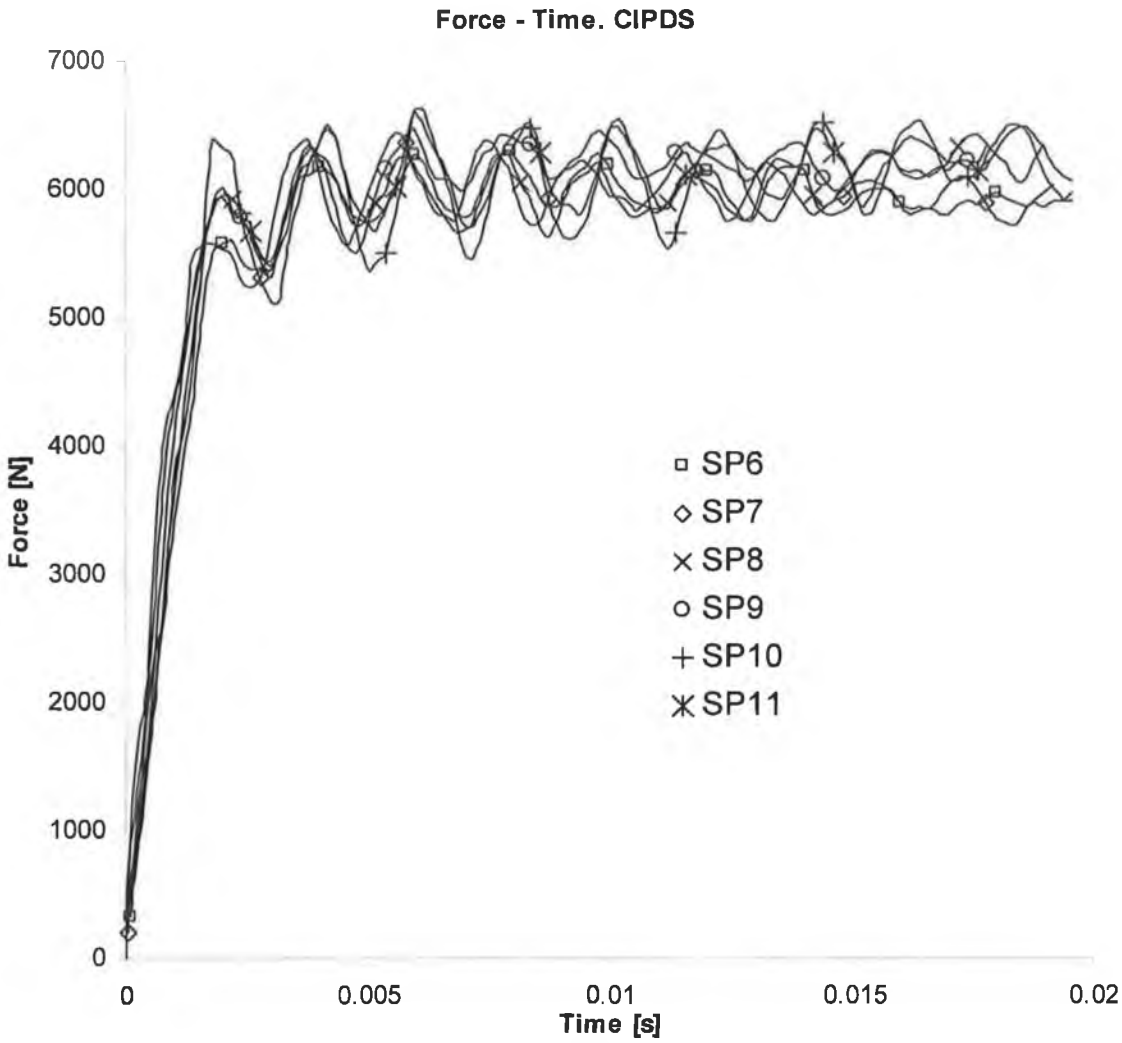

Figure 5-35: Dynamic force-time response of a CIPDS represented by six samples.

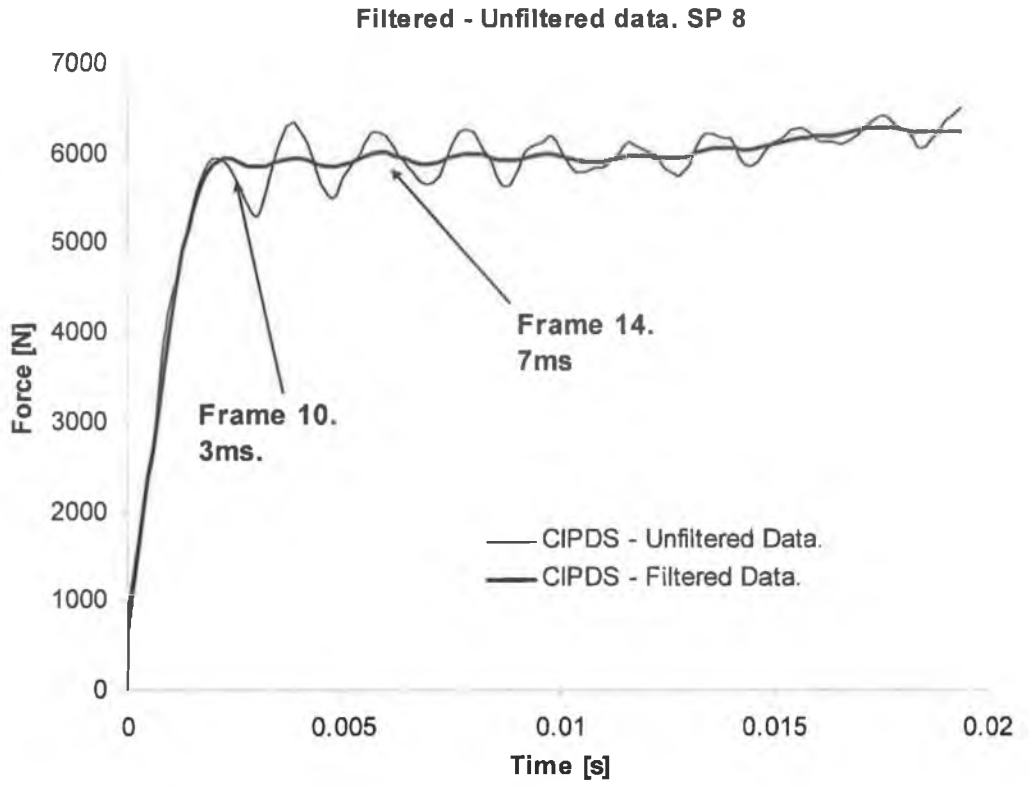

Figure 5-36: Sample eight of a CIPDS in its filtered and unfiltered state.

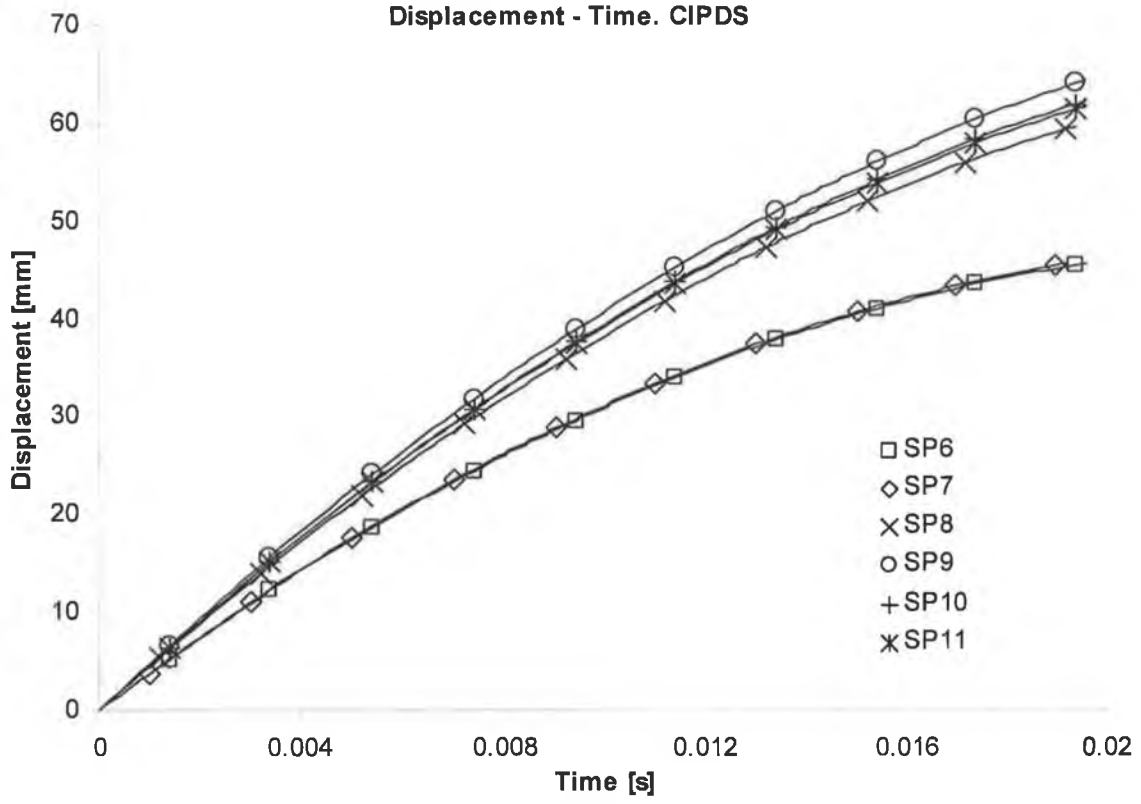

Figure 5-37: Displacement-time response of a CIPDS.

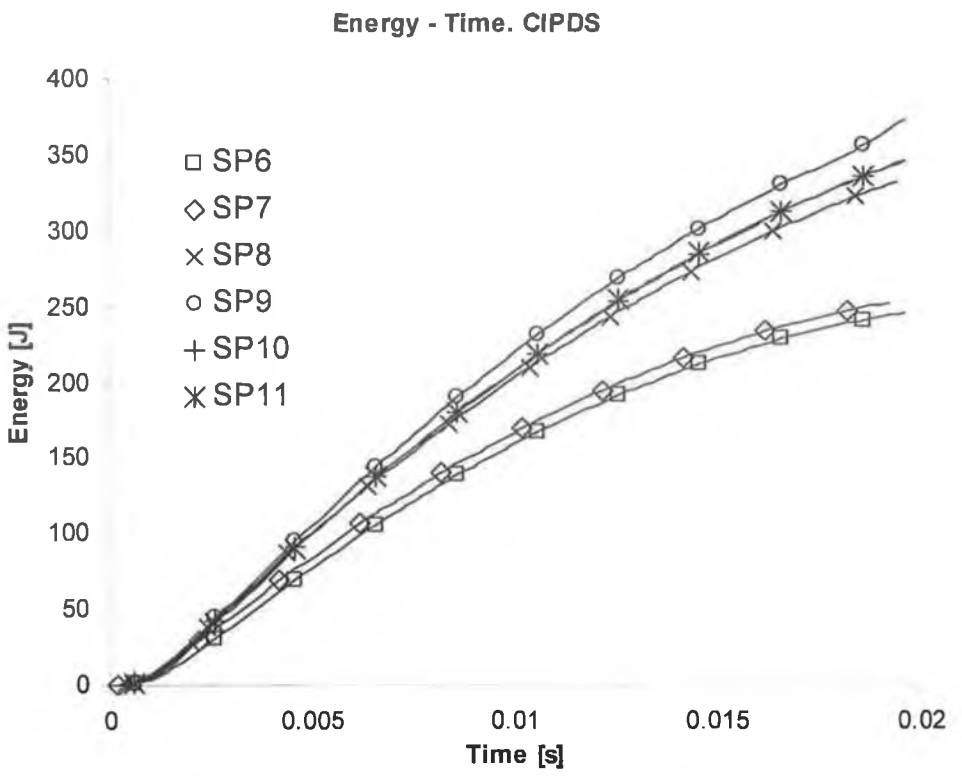

Figure 5-38: Energy-time response of a CIPDS.

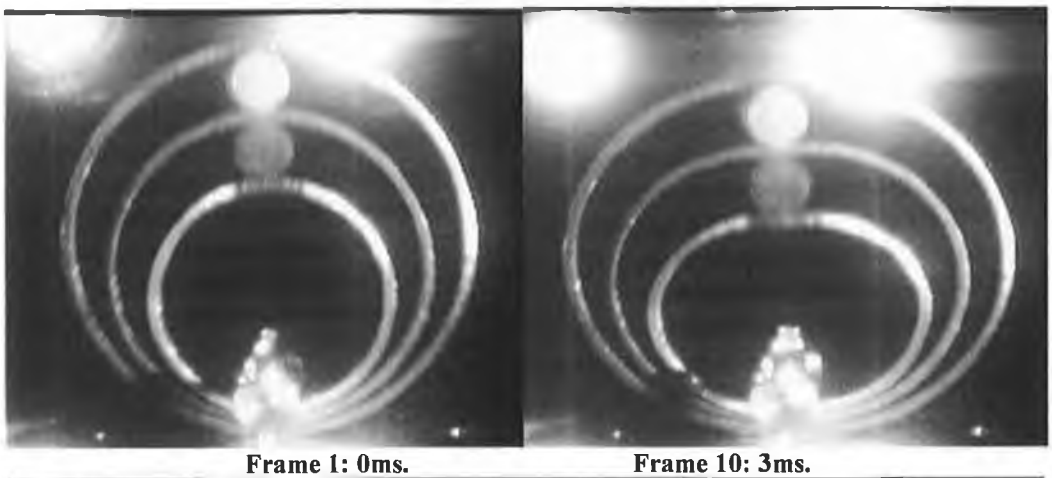

Frame 1: 0ms. **Frame 10: 3ms.**

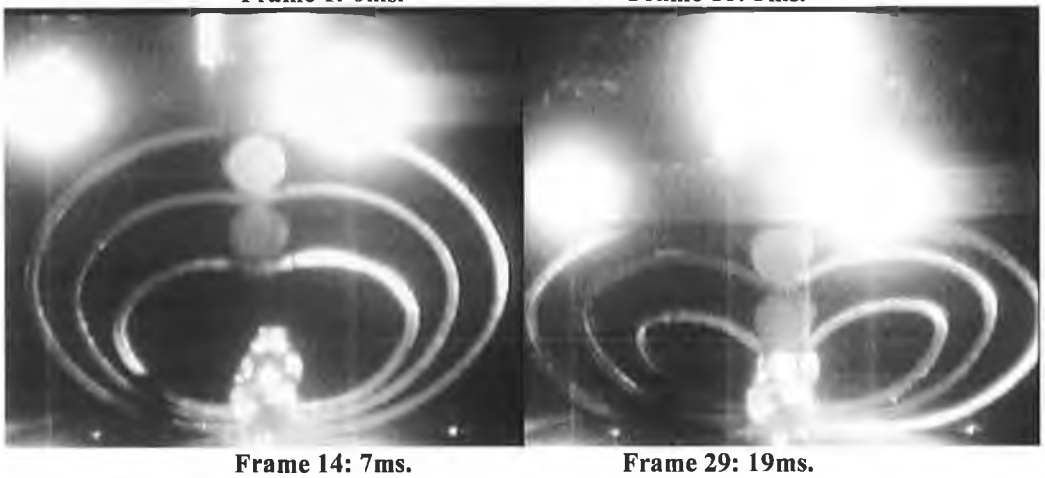

Frame 14: 7ms. **Frame 29: 19ms.**

Figure 5-39: Dynamic displacement evolution of an CIPDS.

5.5.3 Evaluation of the OIPSS.

The experimental force-time response of an OIPSS (Oblong In-Plane Standard System) represented by three samples is shown in Figure 5-40. For this system, the initial gaps between the three tubes have increased from 17mm and 19mm to 28mm and 56mm respectively due to the tension method used to create the oblong tubes. An increase in the displacement stroke was possible since the tubes have been elongated in the vertical direction. Therefore, it can be seen that the specific energy absorption of this kind of system will increase due the available increase in displacement stroke as observed from the quasi-static counterparts. Examining sample one from Figure 5-41 it can be seen how the force increased abruptly as each successive tube established contact. Once this rise in force reached its peak (the collapse load of each tube has been reached), there existed a reduction in force or a softening stage. This behaviour was also observed in the quasi-static cases of this particular system and an explanation was given in section 5.4.2. Figure 5-42 illustrates the energy - time response for such a system. It is clear how the curve can be approximated by three separate stages, each one representing the energy absorption of the outer, central and inner tubes respectively. Note how only partial displacement was achieved (see Figure 5-44) with this particular system. This was due to the maximum energy capacity that can be exerted by the impact tester. Therefore, it can be assumed that an extra displacement of 40mm would be achieved using a larger capacity machine.

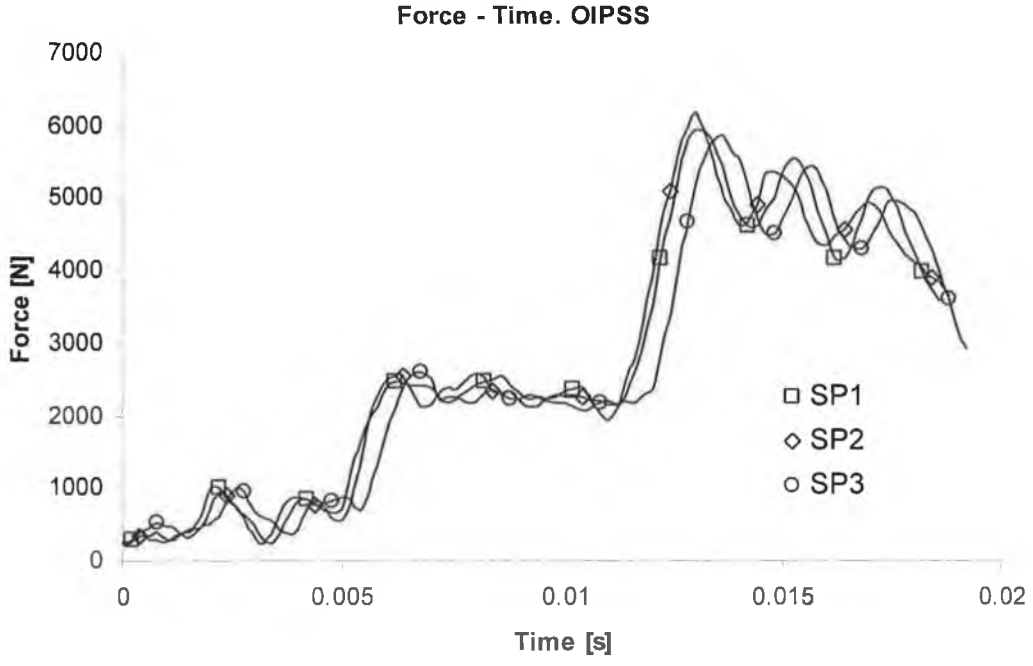

Figure 5-40: Dynamic force-time response of an OIPSS represented by three samples.

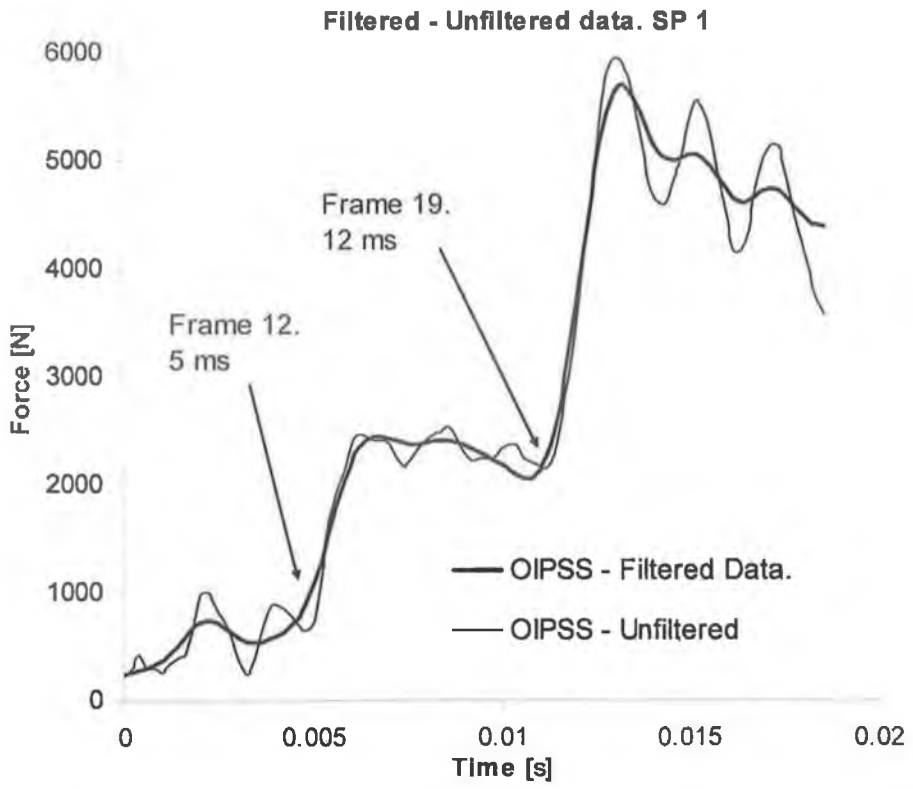

Figure 5-41: Sample one of an OIPSS in its filtered and unfiltered state.

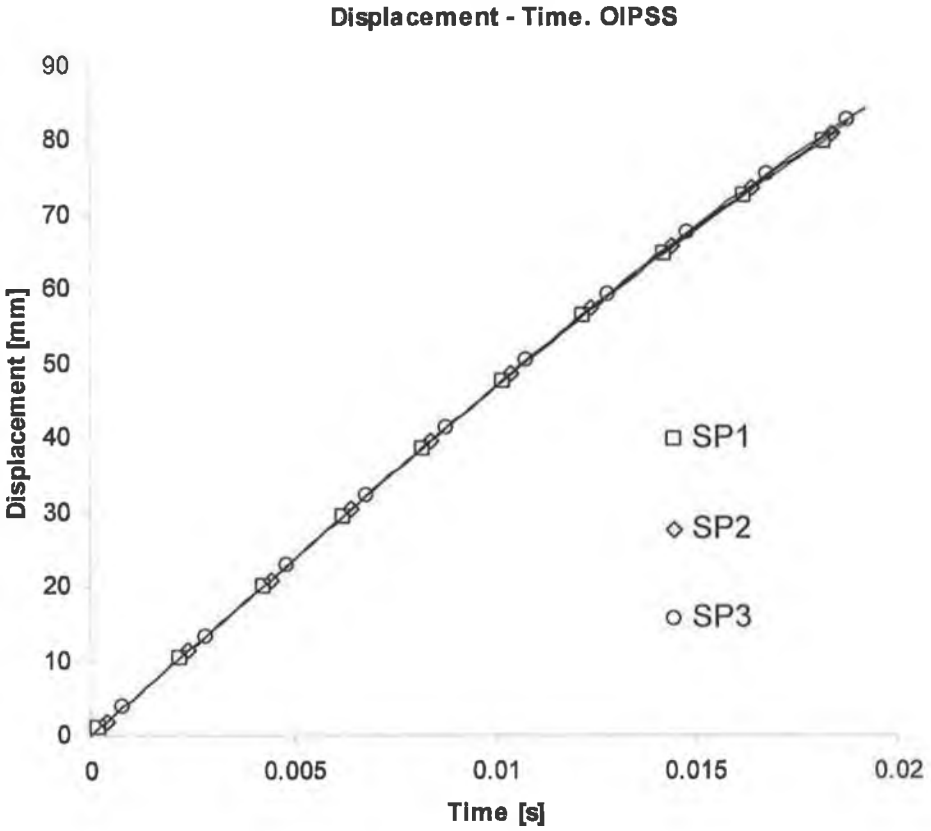

Figure 5-42: Energy-time response of an OIPSS.

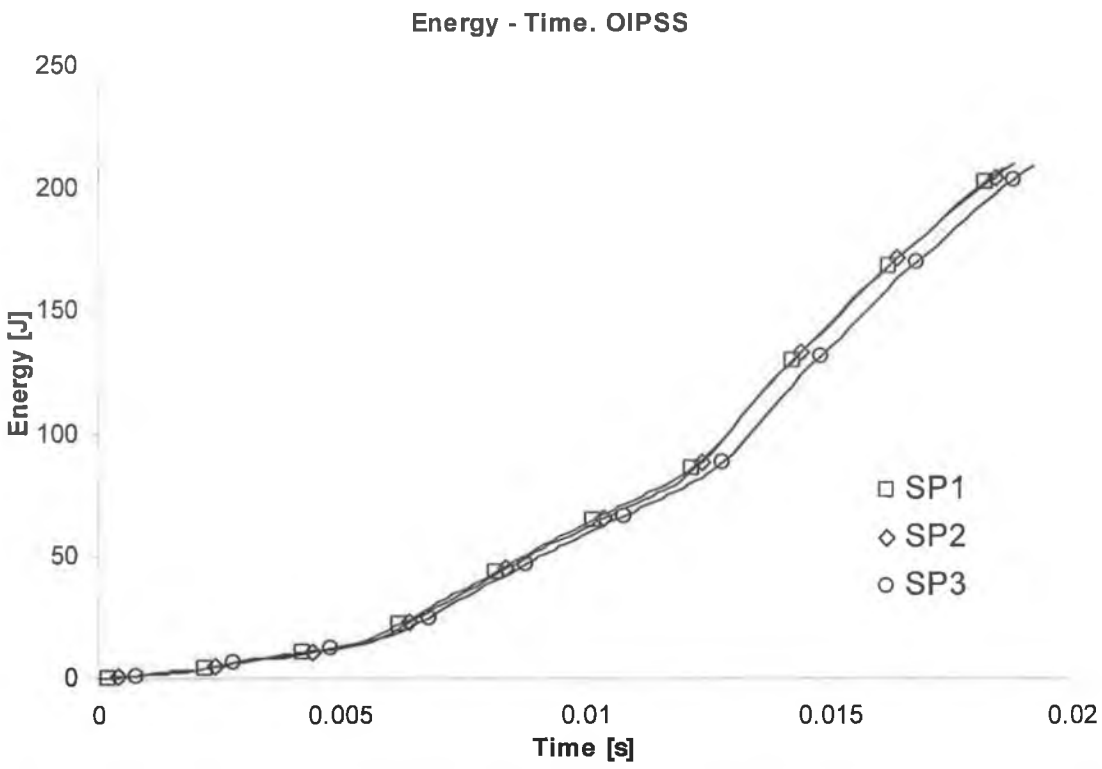

Figure 5-43: Displacement-time response of an OIPSS.

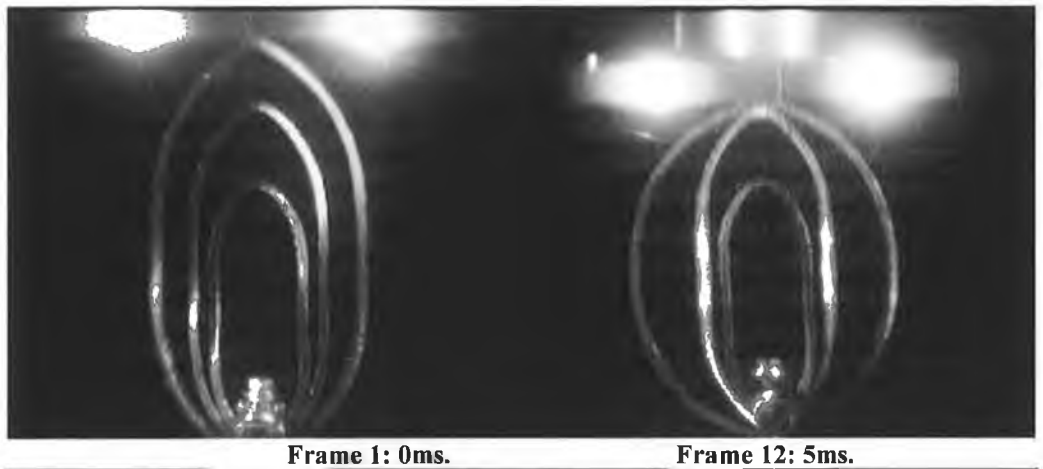

Frame 1: 0ms. **Frame 12: 5ms.**

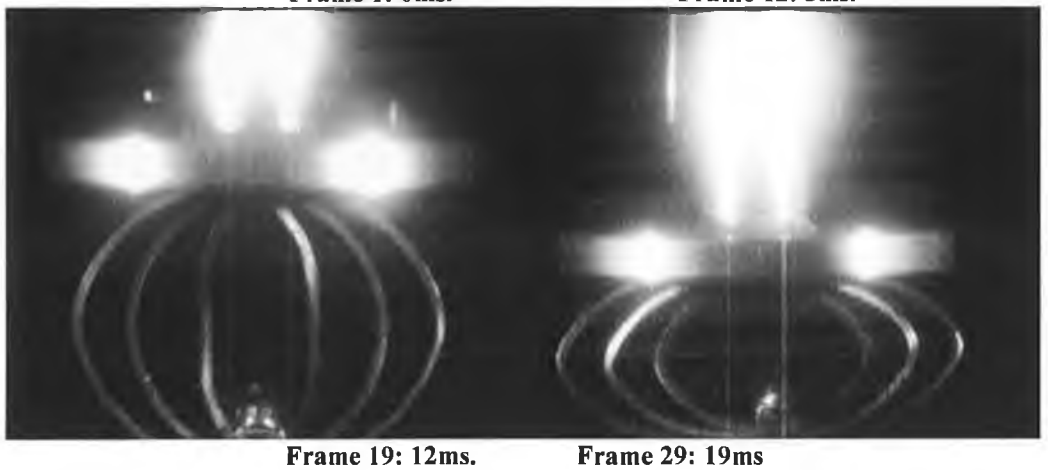

Frame 19: 12ms. **Frame 29: 19ms**

Figure 5-44: Dynamic displacement evolution of an OIPSS.

5.5.4 Evaluation of the OIPDS.

The output force-time response of an OIPDS (Oblong In-Plane Damped System) is shown in Figure 5-45. In an attempt to achieve a *monotonic* or rectangular force-deflection response than that exhibited by an OIPSS (Figure 5-40), two cylindrical spacers were used and inserted between the tubes as illustrated in Figure 5-49. This approach was also employed as in the quasi-static cases for this system. Upon observation of sample nine in Figure 5-46, it can be seen that symmetry was not achieved. Instead the spacers had a tendency to shift in the direction which offered the least resistance. It appears that the response is more sensitive to geometrical imperfections compared to its circular counterpart as noted in section 5.4.1. A possible reason for this increased sensitivity may be due to the fact that there is a greater chance of each tube deforming in an asymmetric manner due to the increased displacement stroke that must be undergone by the system. Also, due to the oblong shape of the tubes and the assemblage of the spacers with a steel dowel, it was difficult to achieve perfect symmetry before any loading was applied. This can also be regarded as a contributing factor in the observed behaviour of the system. The geometric softening behaviour of this system (see Figure 5-46) can also be explained using the concept of moment arms as previously described for the OIPSS section 5.4.2. Despite this mode of deformation behaviour, the rectangular shape force-deflection response was still maintained as noted in the quasi-static cases for this system.

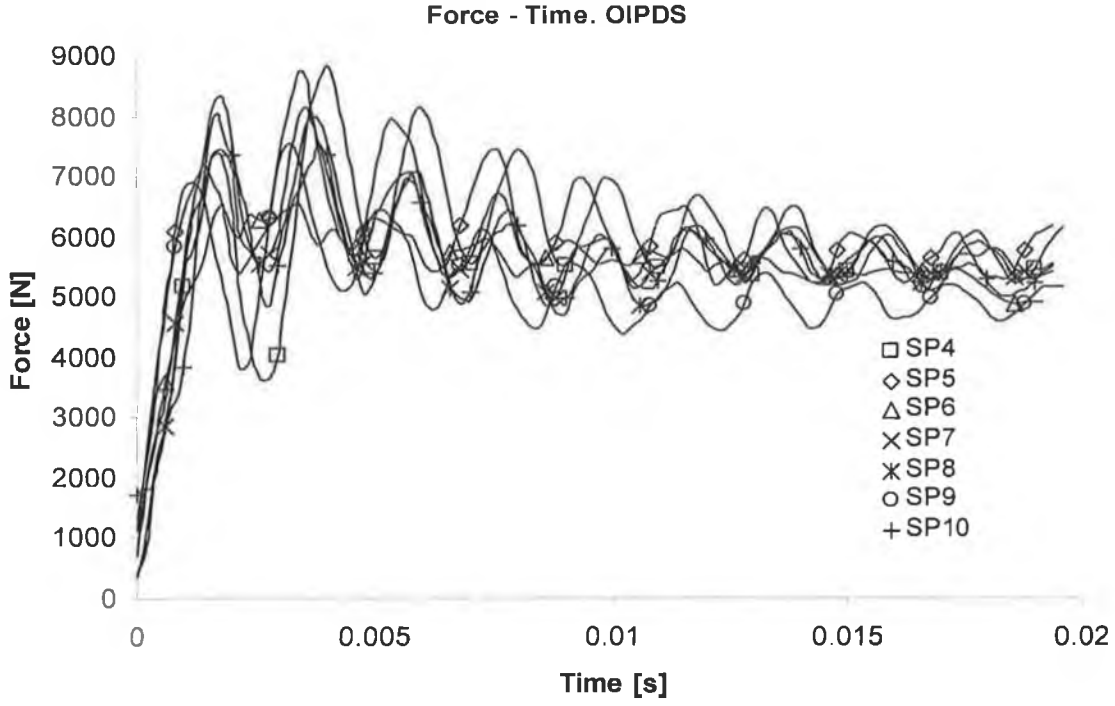

Figure 5-45: Dynamic force-time response of an OIPDS represented by seven samples.

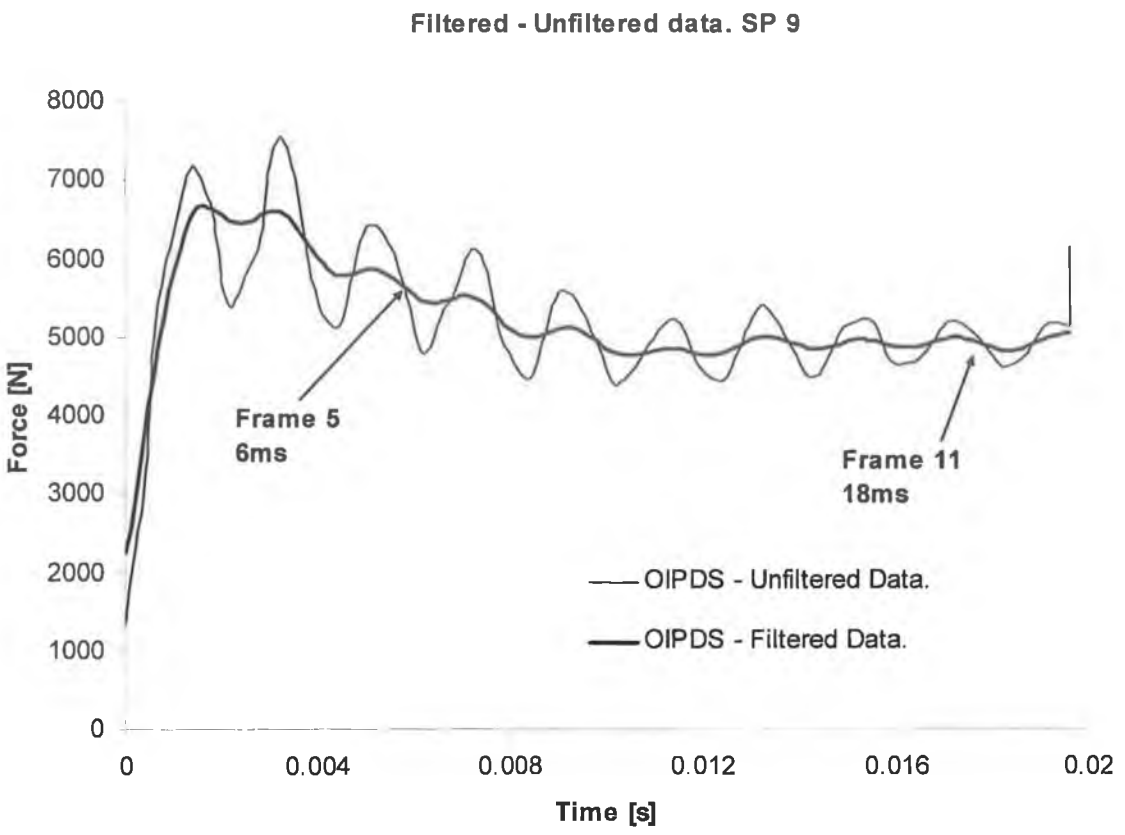

Figure 5-46: Sample nine of an OIPDS in its filtered and unfiltered state.

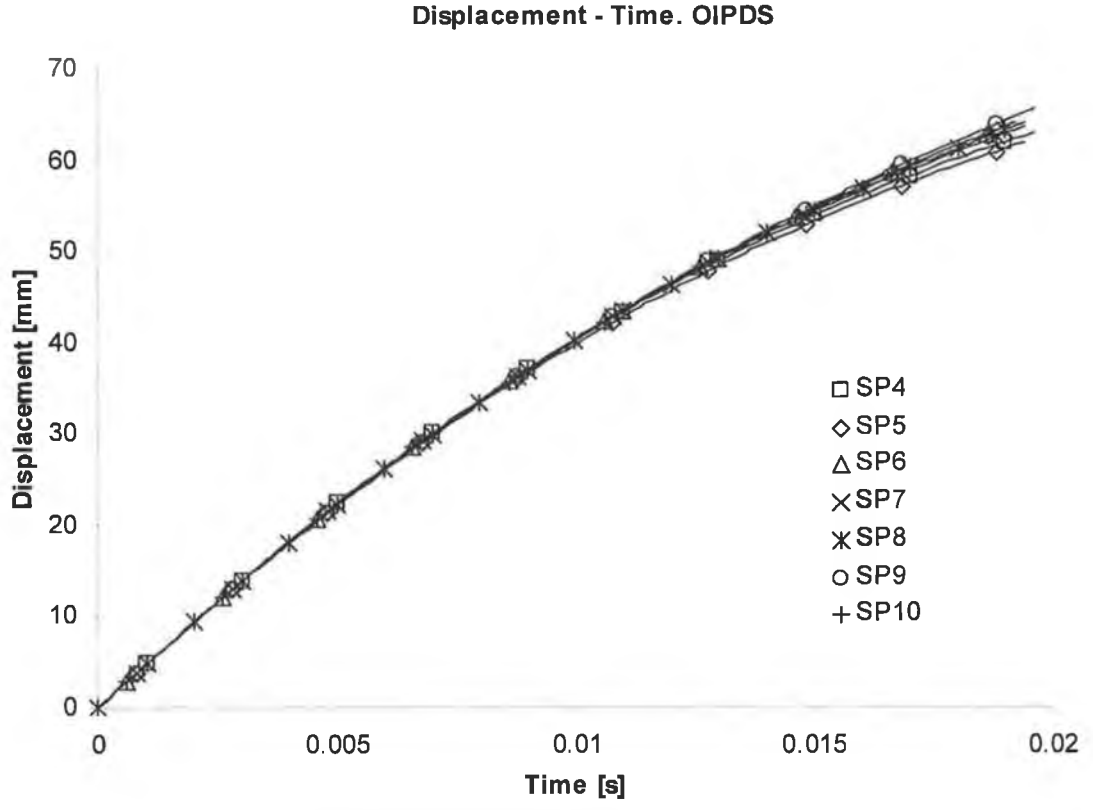

Figure 5-47: Displacement-time response of an OIPDS.

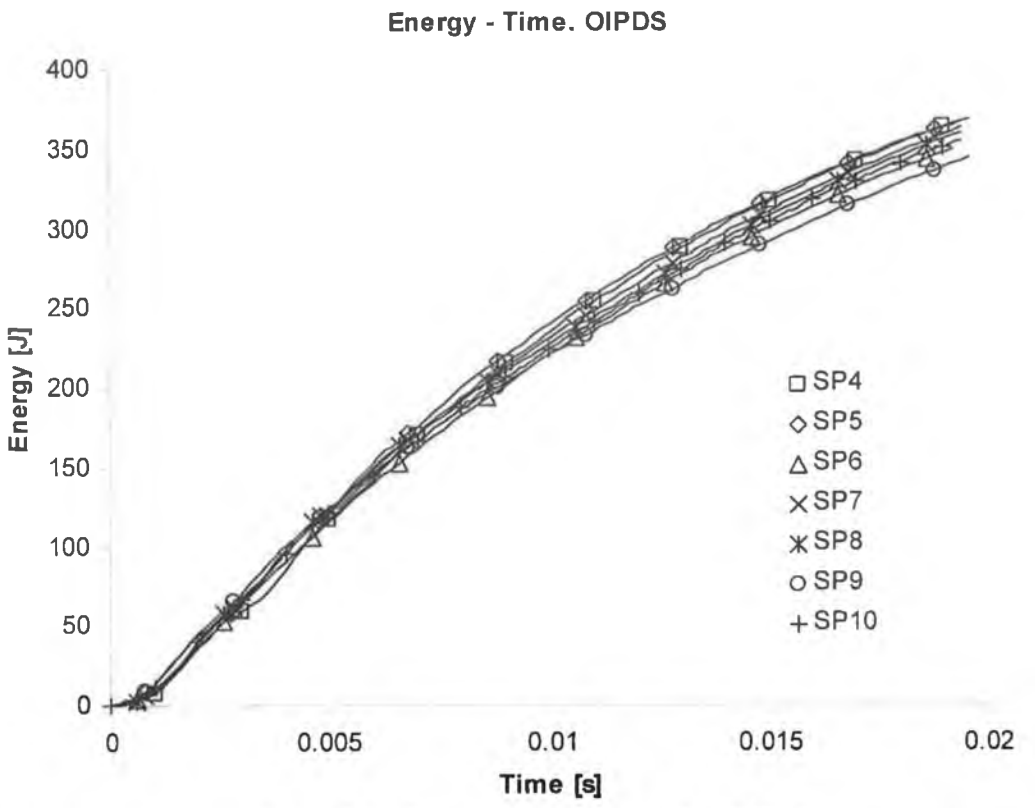

Figure 5-48: Energy-time response of an OIPDS.

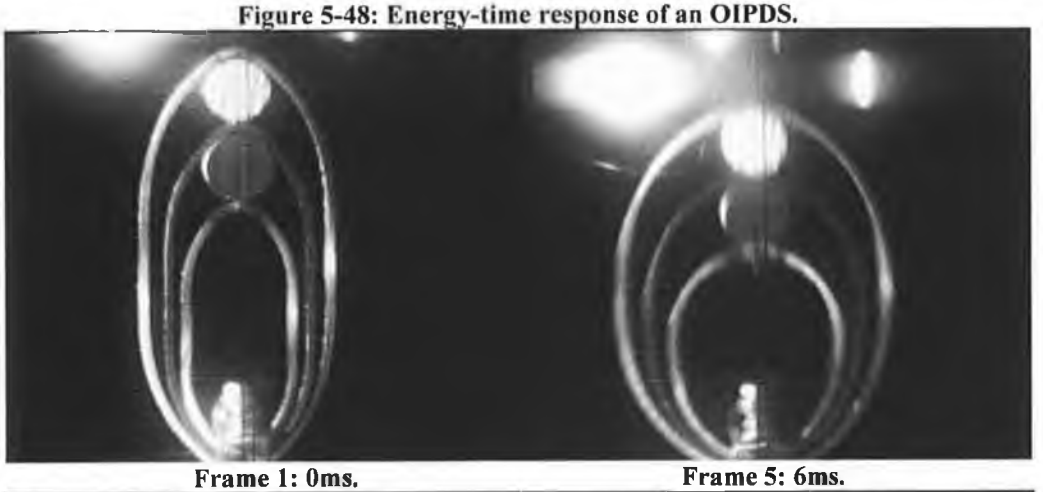

Frame 1: 0ms. **Frame 5: 6ms.**

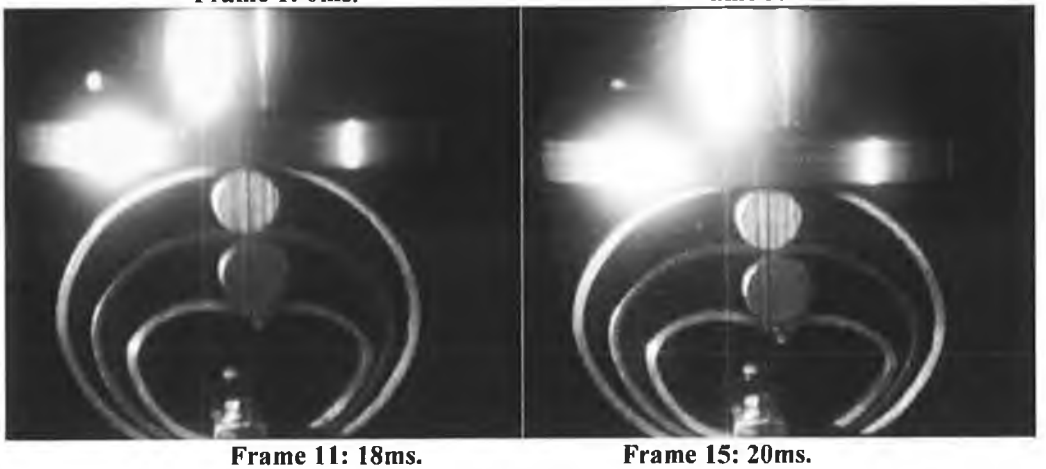

Frame 11: 18ms. **Frame 15: 20ms.**

Figure 5-49: Dynamic displacement evolution of an OIPDS.

5.6 Global Comparison of the Various Systems Analysed.

Figure 5-50 illustrates the global comparison of the different forms of the CIPSS compressed quasi-statically. It can be seen how the COPSS compressed under the three different indenters display similar modes of deformation in that the response is *monotonically* increasing. The SCIPDS represented by sample one and two display amore desirable response in that a rectangular mode of deformation is possible as shown in the early stages of deformation. Finally the SCIPSS compressed under a plate indenter illustrates a *non-monotonic* increase in force due to the absence of the cylindrical spacers. However, in the later stages of deformation the effect hardening is removed due to the presence of the slots.

Figure 5-51 offers a global comparison of the CIPSS and the CIPDS which were compressed quasi-statically and dynamically. For the CIPSS, it can be seen that there are variations in force magnitude for the quasi-static and dynamic cases. Also for this system, contact establishment between each tube occurs at different sages throughout the displacement stroke. It is not exactly know why this behaviour occurs but it should be noted that it is difficult to provide a direct comparison between the quasi-static and dynamic cases for the reason that an oscillation in force occurs from the time the striker hits the outer tubes and when this tube contacts the central tube. For the CIPDS, the force magnitude remains the same for the both the quasi-static and dynamic cases. Notice how the effect of introducing the cylindrical spacers for the CIPDS cause the force-deflection response to change significantly, resulting in a rectangular mode of deformation.

Finally Figure 5-52 illustrates the quasi-static and dynamic response of both the OIPSS and the OIPDS. Again it can be seen how contact establishment for the OIPSS occurs at different stages of the displacement stroke. For the OIPDS it can be seen the collapse load is the same for both the quasi-static and dynamic testing as noted above for the CIPDS. It should be noted that for both the dynamic cases of various systems analysed that the displacement stroke is smaller. This is due to the fact that the energy capacity of the ZWICK ROELL machine was not large enough to compress the systems to its full displacement stroke.

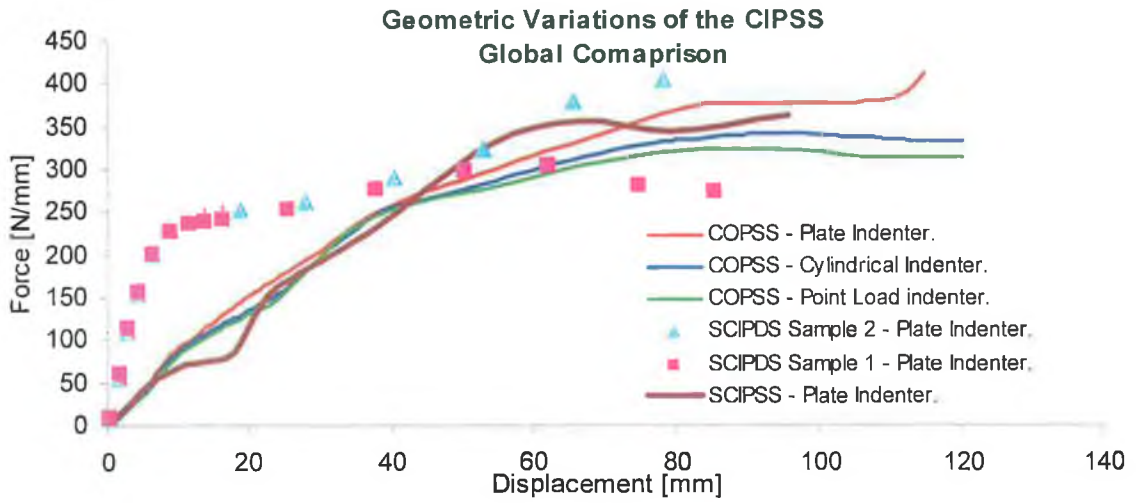

Figure 5-50: A global comparison of the force-deflection response for the various forms of the CIPSS.

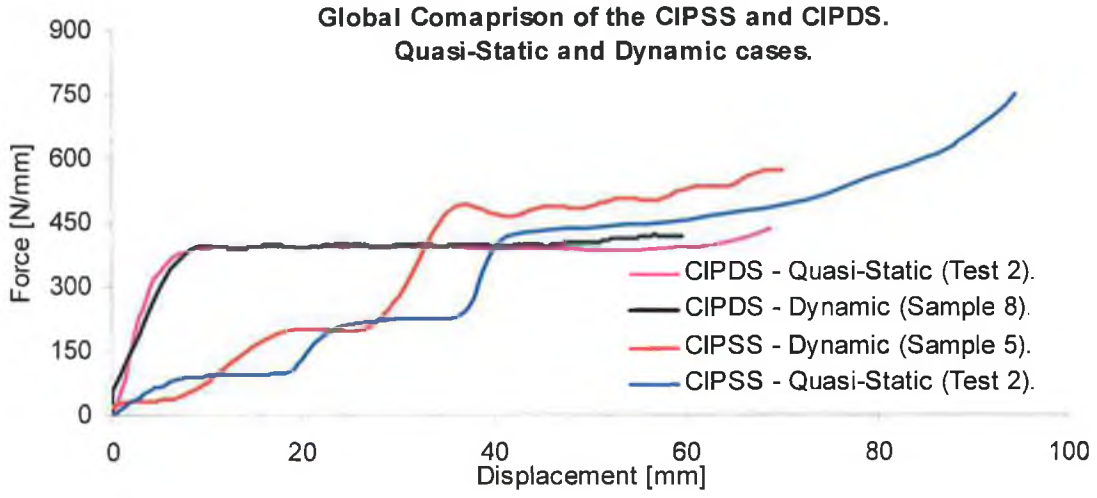

Figure 5-51: **A global comparison of the force-deflection of the CIPSS and the CIPDS [Quasi-Static and Dynamic cases].**

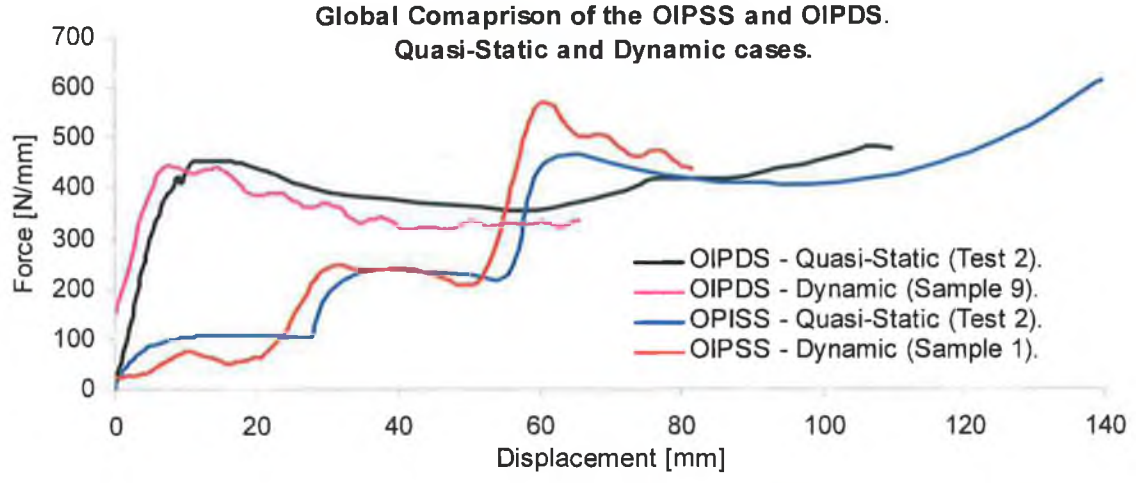

Figure 5-52: **A global comparison of the force-deflection of the OIPSS and the OIPDS [Quasi-Static and Dynamic cases].**

5.7 Summary of Chapter Five.

- Chapter five detailed an experimental investigation of In-Plane Systems and Out of-Plane Systems compressed laterally under quasi-static and dynamic loading conditions. An investigation was also made in relation to the slotted tube systems.
- In section 5.2, a detailed description was given on the lateral compression of CIPSS which is an energy absorber in its most basic form. This was to allow an understanding of the behaviour of subsequent modified systems analysed later in the chapter.
- A COPSS compressed under three different types of indenter was analysed in order to study the influence of indenter shape on the force-deflection response of the aforementioned energy absorbers.
- Three different slotted tube energy absorbers were also analysed with attention given to the behaviour of the slots and its effect on achieving a *monotonic* or rectangular force-deflection response.
- Section 5.4 detailed the response of three different absorbers, namely the CIPDS, OIPSS and the OIPDS under quasi-static lateral compression.
- Energy absorption characteristics as described in section 3.3.1 were applied to each absorber to describe their behaviour and to determine which system exhibited favourable responses based on their characteristics.
- Section 5.5 gave an account of the dynamic response of the nested systems analysed in section 5.4. Particular attention was given on the response of the optimised designs, namely the CIPDS and OIPDS, to examine how they responded dynamically and to determine whether they retained their rectangular shaped response as exhibited by their quasi-static counterparts.
- Finally, a global comparison of results between the various systems pertaining to section 5.3, 5.4 and 5.5 was illustrated in order to assist in the interpretation of results.

6 Specific Energy Maximization of Nested Systems.

6.1 Introduction.

The chapter is divided into three sections which detail the experimental analysis of a CIPSS (Circular In Plane Standard System) compressed under three different devices such as the rigid flat platen, cylindrical and point load indenter. The CIPSS was exposed to various external constraints during lateral compression in order to subject the system to greater volumetric deformation. The function of such constraints is to maximise the specific energy absorbing capacity of such energy absorbers. This is a requirement in the design of kinetic energy absorbers as outlined in section 1.6F. Hence this chapter examines the output response of such devices exposed to various external constraints and indenters.

6.2 Plate Indenter Compression.

6.2.1 CIPSS - Unconstrained.

Figure 6-1 shows the crush force and energy absorption response for a CIPSS with no external constraints imposed on it. Figure 6-2 depicts how the three tubes of varying diameter and each of length 60mm were placed within each other to form a nested system of eccentric configuration. Due to this arrangement, an initial spacing of 17mm and 21mm existed between the upper portions of the tubes. These two gaps allowed all three components to deform sequentially as loading proceeded, hence the reason for the *non-monotonic* increase in force throughout the deformation stroke as observed in Figure 6-1. As expected upon examination of this figure, an increase in force was observed at 17mm and 38mm which indicates contact has been established between each respective tube. Finally as the inner tube collapsed at approximately 42mm, the system containing the three tubes began to strain-harden to a maximum deflection of 116mm. The energy response was achieved by integrating the force over its corresponding deflection. The energy response became more linear once all tubes began to deform simultaneously. This energy response behaviour is pertinent to all subsequent nested systems analysed. As shown in Figure 6-2, the upper and lower halves of the inner tube were in the 'just touching' position. It was at this stage that the maximum displacement has occurred. It was possible to increase the stroke length, however this may be seen as an over loading or 'bottoming out' of the system and this is normally avoided.

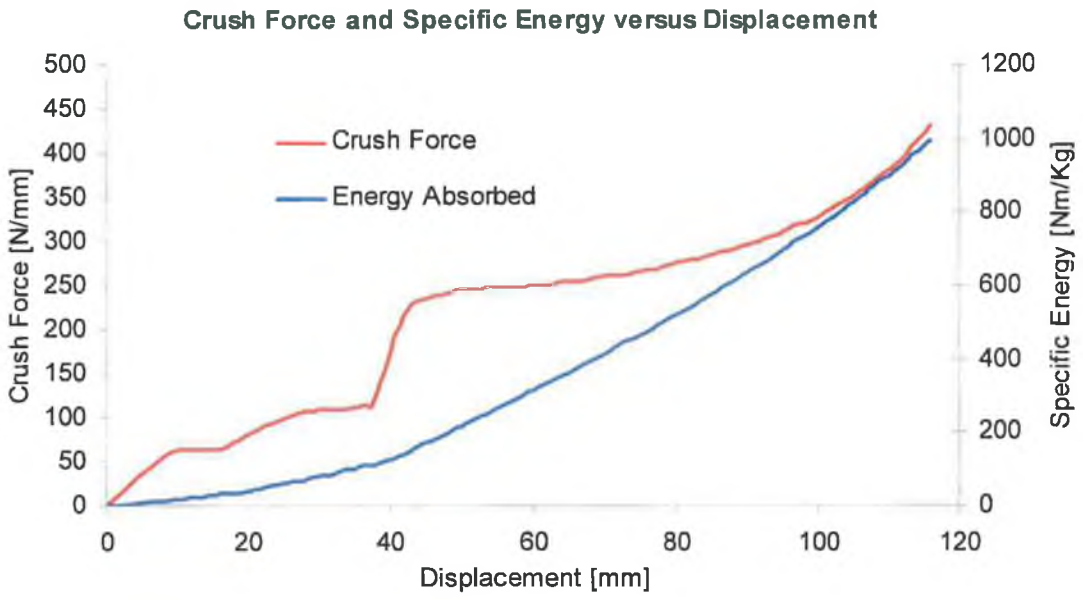

Figure 6-1: Force and specific energy response for a CIPSS with no constraints.

Figure 6-2: Initial and final stage of deflection for a CIPSS with no constraints.

6.2.2 CIPSS - Inclined Constraints.

Figure 6-3 presents the force- and energy-deflection response of a CIPSS subjected to inclined constraints. The external constraints as demonstrated by Reddy and Reid [62] served to increase the specific energy absorbing capacity of systems compressed under horizontal rigid platens. It should be noted that the authors applied the concept of external only to a single tube whereas in this work, it is applied to a nested system. Hence, it can be seen from Figure 6-3, that these constraints caused more volume of material to deform particularly for the outer and central tube. This results in a greater increase in force in contrast to an unconstrained CIPSS. However, it appears that, for this type of arrangement a maximum displacement of 95mm was reached. Any further crushing causes macroscopic fracture at the hinge points which would mark a decrease in force. It is common to design energy absorbers that undergo large plastic deformations without any incident of fracture or indeed 'bottoming out' of the structure. Figure 6-4 illustrates the initial and final stage of crushing for this energy absorber with inclined constraints.

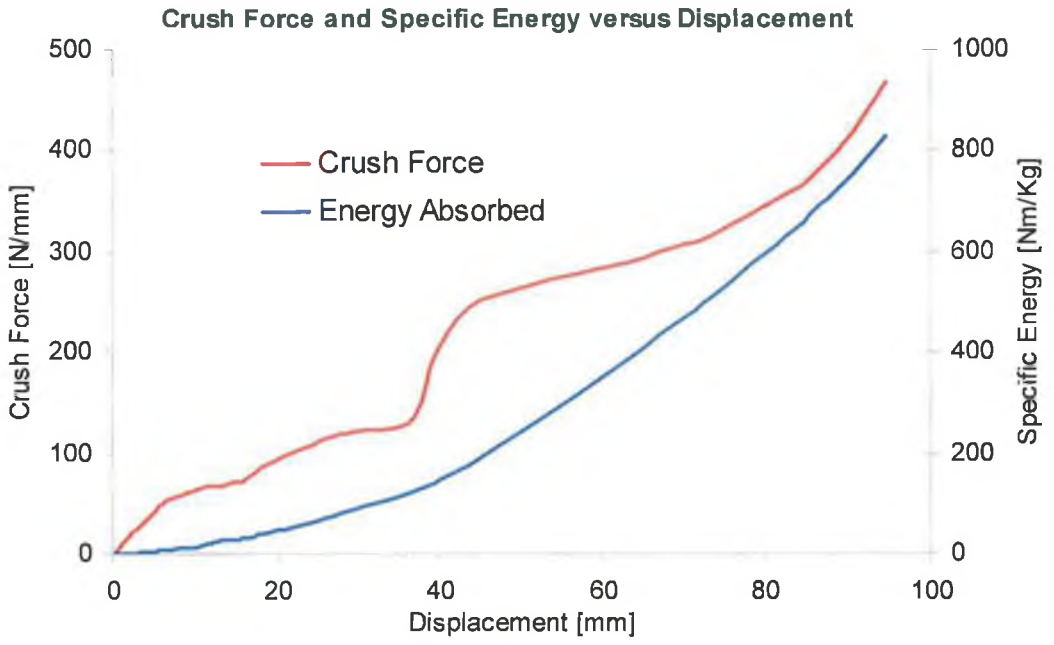

Figure 6-3: Force and specific energy response for a CIPSS with inclined constraints.

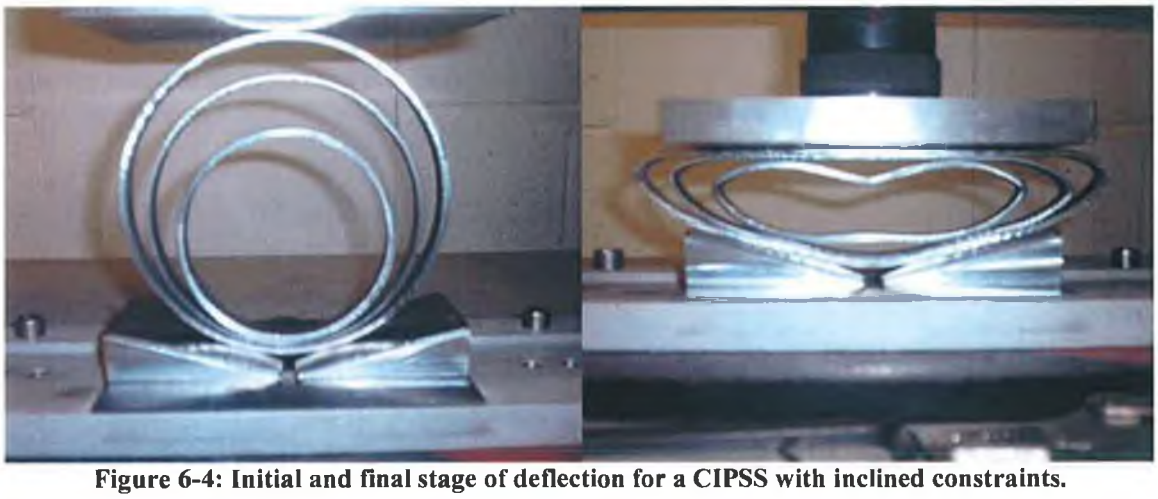

Figure 6-4: Initial and final stage of deflection for a CIPSS with inclined constraints.

6.2.3 CIPSS - Vertical Constraints.

Figure 6-5 depicts a graphical plot consisting of the crush force and specific energy absorption for a CIPSS compressed between rigid plates and vertical side constraints. Photographs consisting of the initial and final stages are displayed in Figure 6-6. It can be seen from this figure, that the introduction of sidewalls prevented the horizontal diameter of the outer tube from displacing outwards during compression. As a result, a greater volume of material was exposed to plastic deformation. This caused a greater an increase in the reactive force as shown in Figure 6-5. This increase in force was due to the stiffening of outer tube since it has conformed to the shape of the vertical side constraint while at the same time the central tube prevented it from collapsing inward.

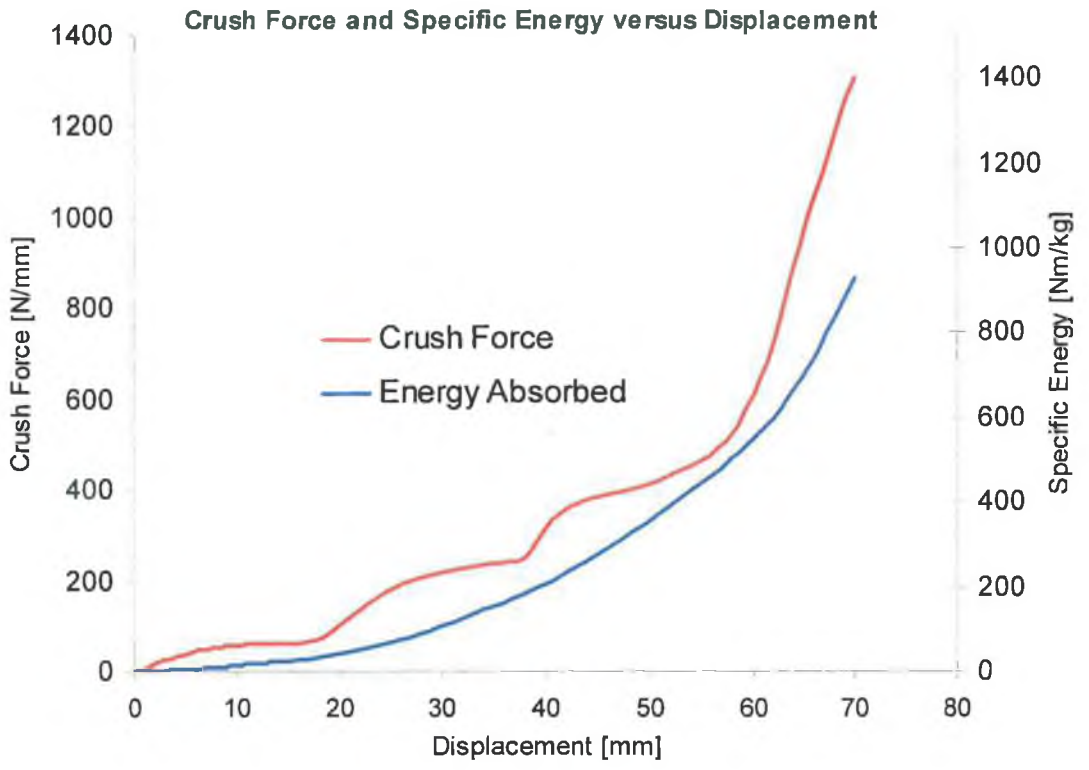

Figure 6-5: Force and specific energy response for a CIPSS with vertical constraints.

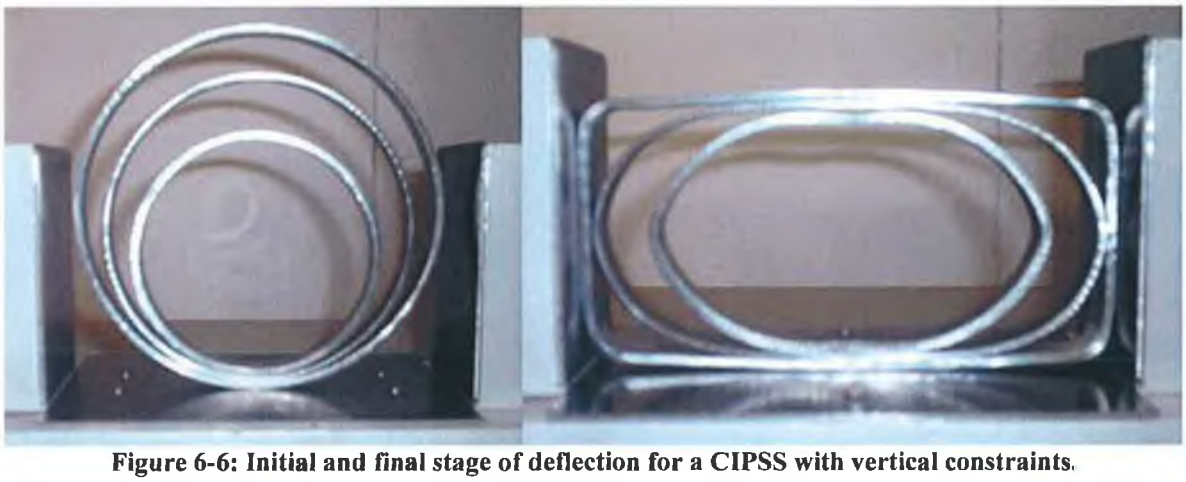

Figure 6-6: Initial and final stage of deflection for a CIPSS with vertical constraints.

6.2.4 CIPSS - Combined Constraints.

A crush force and specific energy response for a CIPSS compressed between rigid plates with both vertical and side constraints are shown in Figure 6-7. The resulting crush force has again increased as expected due to combined effects of the inclined and vertical constraints. A rapid increase in force occurs at approx 48mm and this was also due to the horizontal diameter of the outer tube restricted from deflecting laterally. Figure 6-8 depicts the various stages of compression for this particular system. It can be seen from the final stage of displacement that no further deflection was possible.

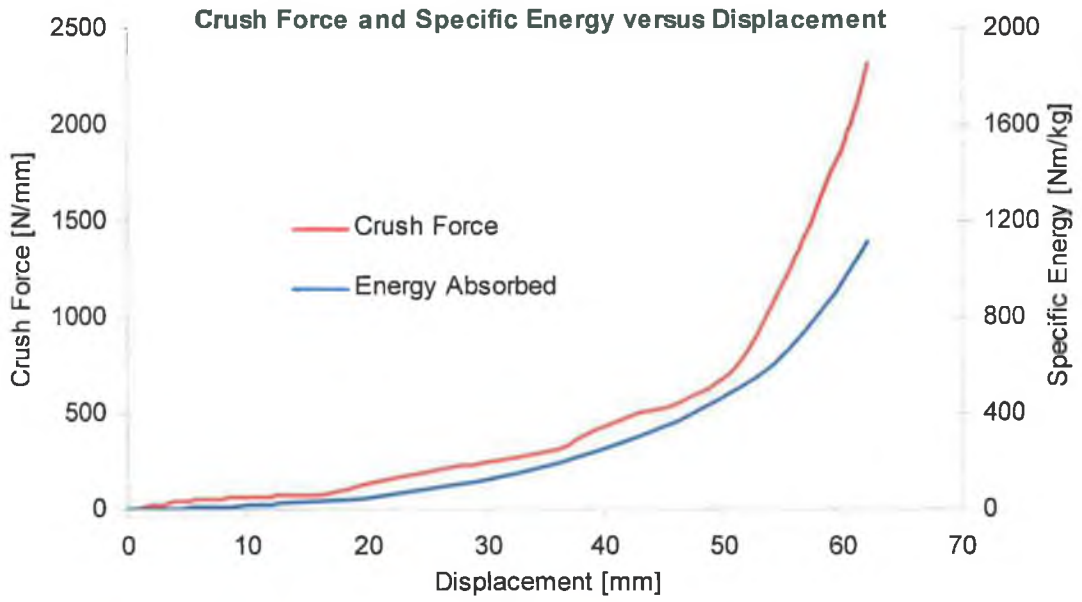

Figure 6-7: Force and specific energy response for a CIPSS with both constraints.

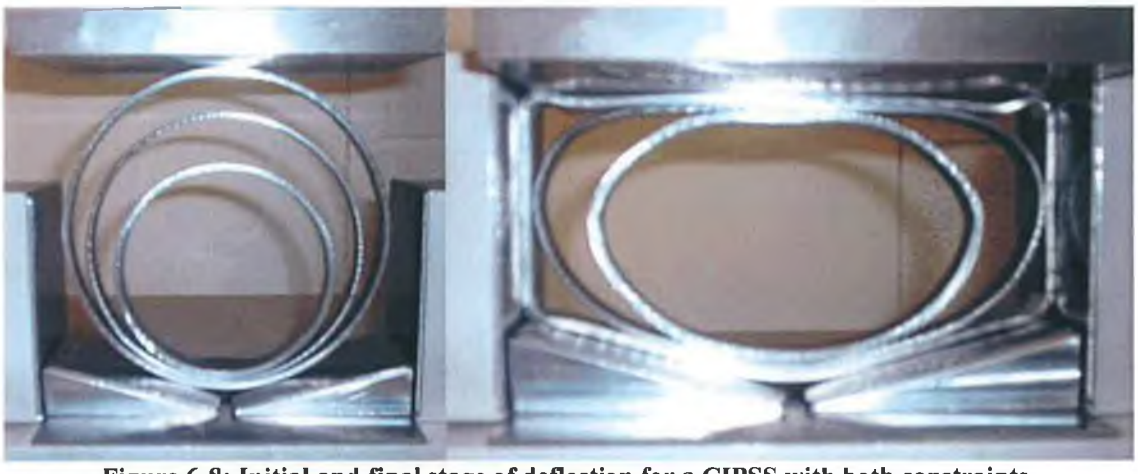

Figure 6-8: Initial and final stage of deflection for a CIPSS with both constraints.

6.3 Point Load Indenter Compression.

6.3.1 CIPSS – Unconstrained.

The corresponding force and energy response of an unconstrained CIPSS compressed with a point load indenter is depicted in Figure 6-9. Illustrations of the various stages of deflection are shown in Figure 6-10. From 45mm deflection, it can be seen that the whole system began to geometrically soften as opposed to strain hardening as observed with the compression of a CIPSS with a plate indenter. This was due to the concept of the moment arm increasing from the point of load of application as noted and analysed by Bell and Reid [49]. At approx 116mm deflection onwards there exist an increase in force; this was due to the adjacent faces of the indenter obstructing the outer tube as depicted in the photos of Figure 6-12.

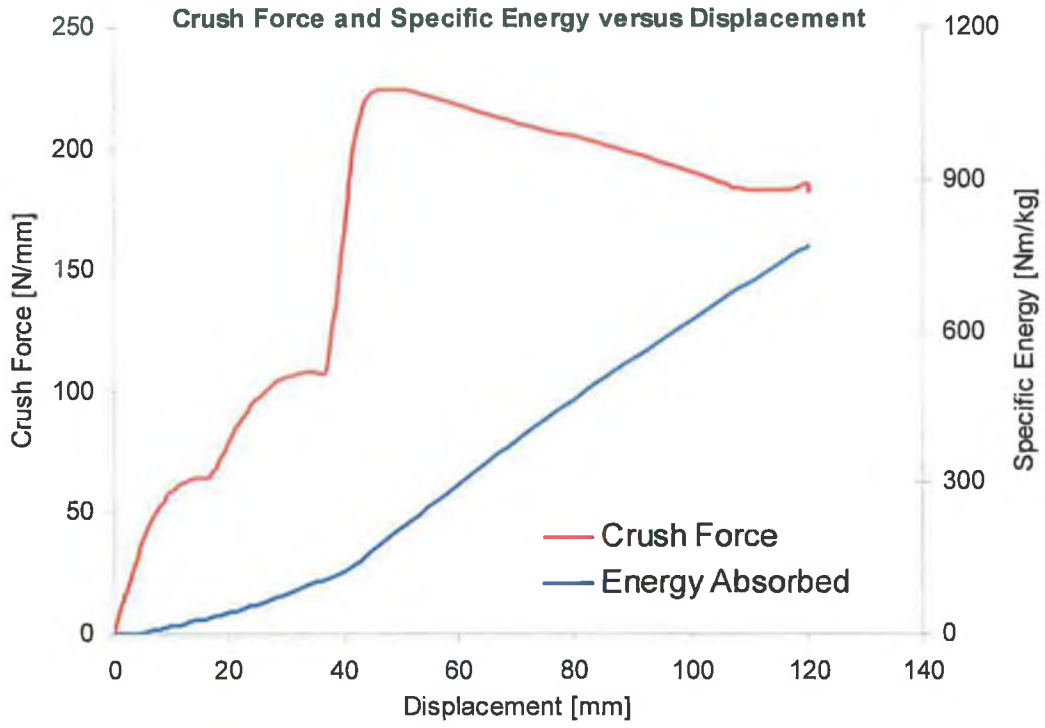

Figure 6-9: Force and specific energy response for an unconstrained CIPSS.

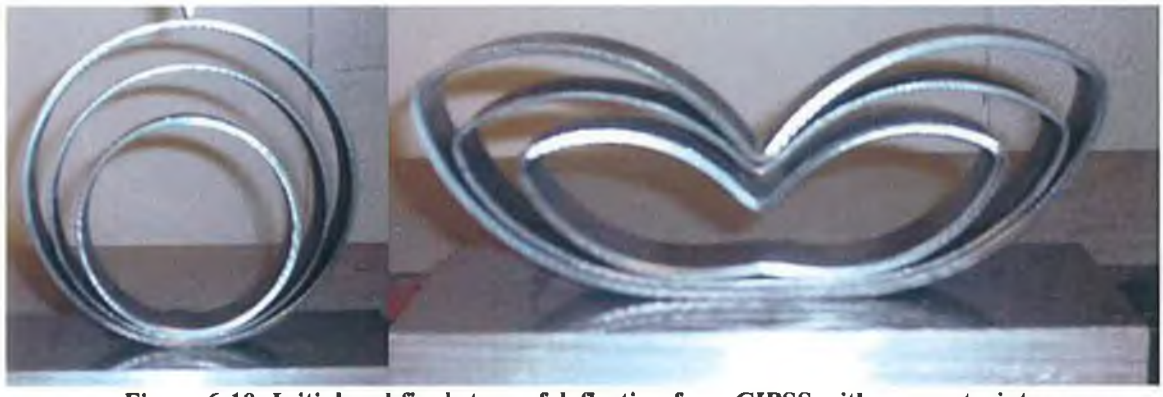

Figure 6-10: Initial and final stage of deflection for a CIPSS with no constraints.

6.3.2 CIPSS – Inclined Constraints.

Figure 6-11 offers the crush force and specific energy response of a CIPSS with fifteen degree inclined constraints. In comparison to the previous system, the resulting force has increased slightly due to introduction of such constraints. In the post collapse stages of the inner tube (at approximately 48mm) the system exhibited a softening characteristic for the remaining deflection. This behaviour was also due to the effect of increase in moment arm about the 2 horizontal hinge points. Compression of this system is illustrated in Figure 6-12. Notice how, for the final stage of deformation, the inclined constraints caused a greater interference of the adjacent sides of the indenter with the tube which resulted in a slight rise in force in the latter stages of deflection as shown in Figure 6-11.

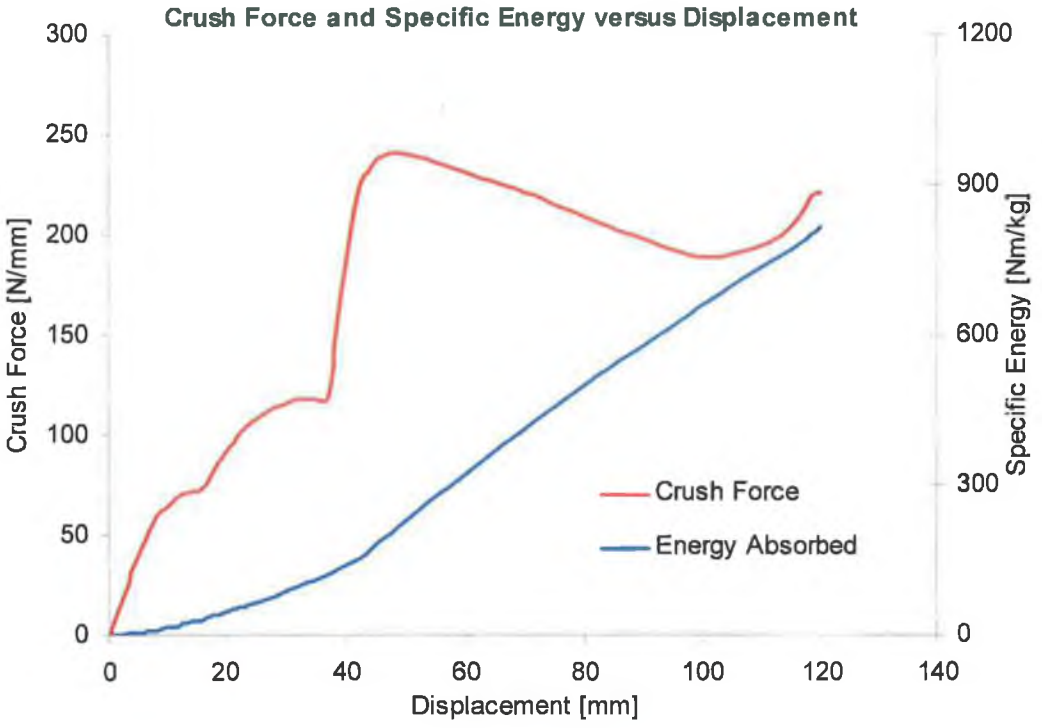

Figure 6-11: Force and specific energy response for a CIPSS with inclined constraints.

Figure 6-12: Initial and final stage of deflection for a CIPSS with inclined constraints.

6.3.3 CIPSS – Vertical Constraints.

Figure 6-13 and Figure 6-14 show the results of a CIPSS compressed with sidewalls present. Upon inspection of former figure, it can be seen how the central tube began to soften before it established contact with the inner tube. This was due to sufficient time for the central tubes to behave in this manner before contact was established with the inner tube. Once the collapse load was reached in the inner tube, the system geometrically softened for the remainder of deflection. Again a rise in force was observed due to presence of the indenter which obstructed the outer tube.

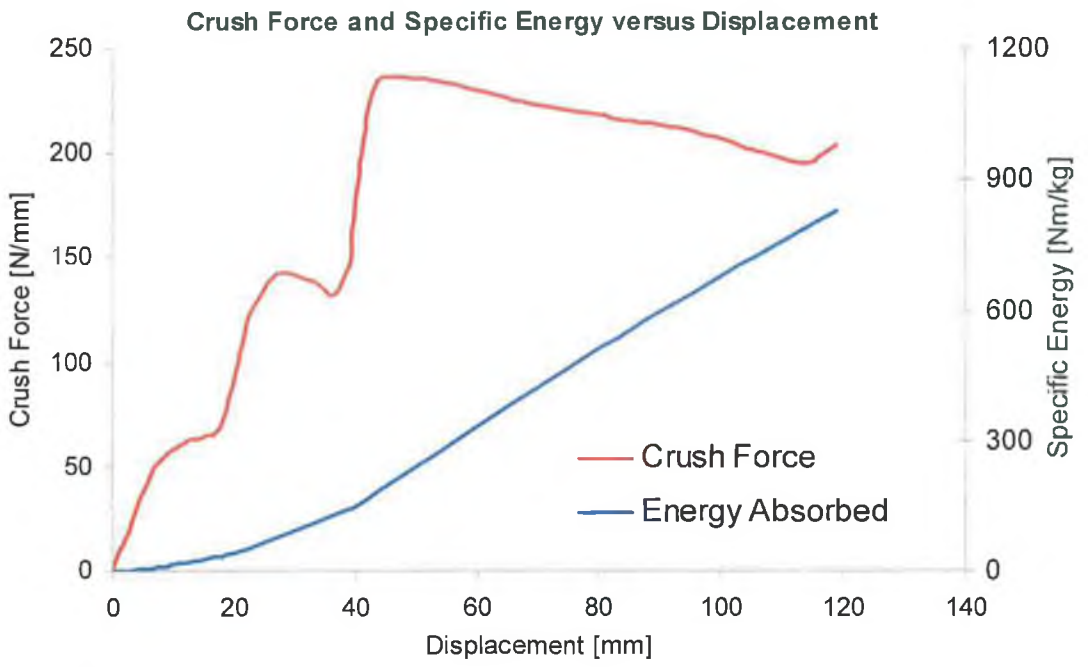

Figure 6-13: Force and specific energy response for a CIPSS with vertical constraints.

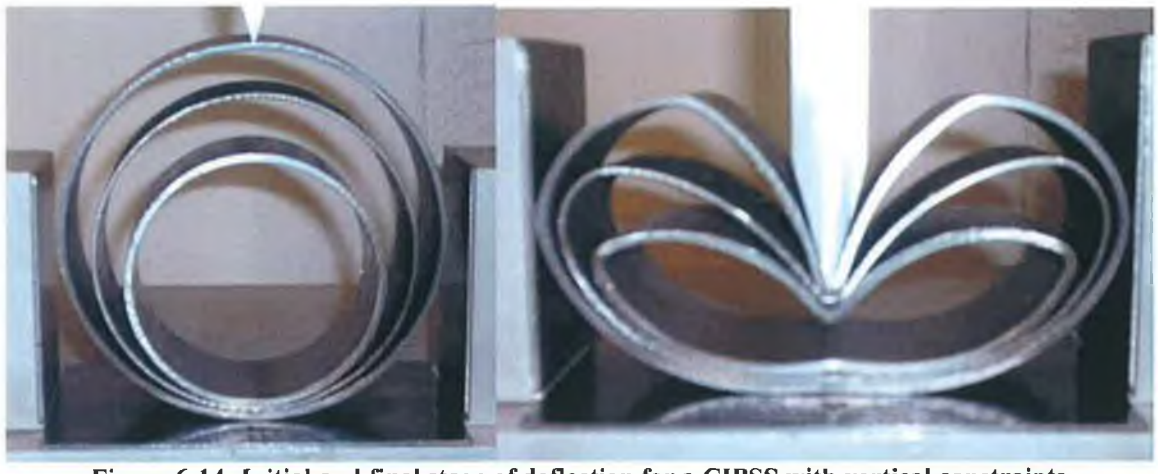

Figure 6-14: Initial and final stage of deflection for a CIPSS with vertical constraints.

6.3.4 CIPSS – Combined Constraints.

The final system compressed with a point load indenter consists of a CIPSS with both vertical and inclined constraints as shown in Figure 6-16. In Figure 6-15, the corresponding force and specific energy response for this system is displayed. At approximately 115mm deflection a rapid rise in force was observed. This was due to a combination of the inclined constraints and the indenter which exposed the outer tube to a greater volume of material deformation. However, as loading proceeded, the application of the point load caused the outer tube to move away from the sidewalls. Therefore, it can be seen that the effect of sidewall constraints in conjunction with a point load indenter is not as effective as in the case of a rigid flat platen.

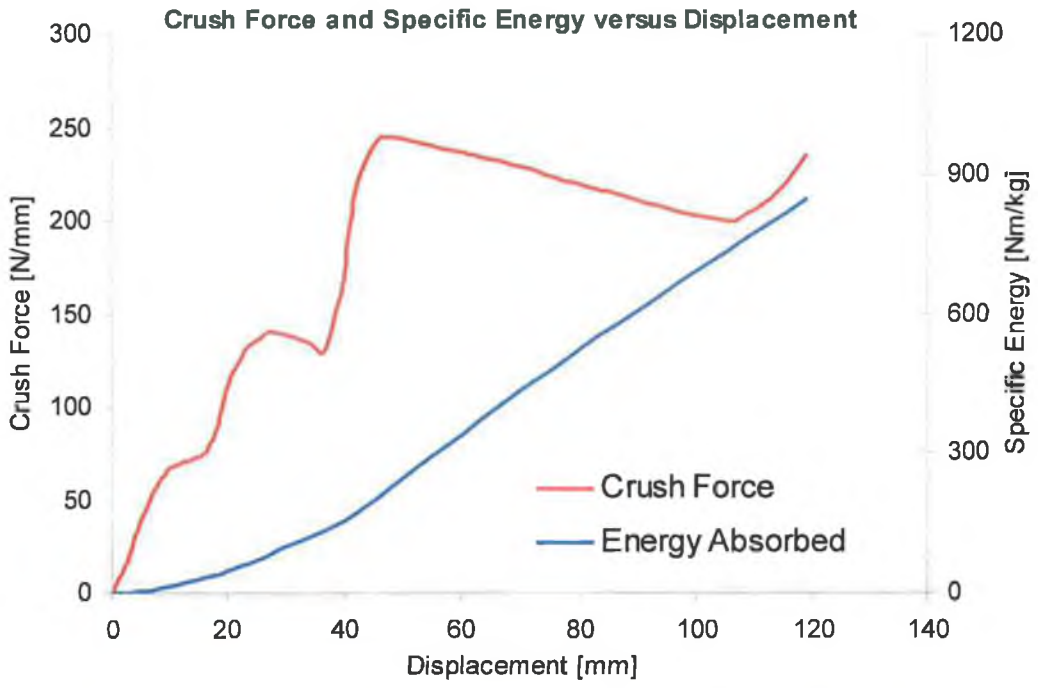

Figure 6-15: Force and specific energy response for a CIPSS with both constraints.

Figure 6-16: Initial and final stage of deflection for a CIPSS with both constraints.

6.4 Cylindrical indenter compression.

6.4.1 CIPSS – Unconstrained.

Figure 6-17 show the force and energy response for an unconstrained CIPSS compressed between a cylindrical indenter and a rigid platen. Figure 6-18 depicts the initial and final stages of compression for this particular system. At approximately 40mm deflection it can be seen that the system was still absorbing energy for the remainder of the stroke without any increase in resisting force. This section of the curve can be categorised as a *perfectly plastic* response since the system is neither strain-hardening nor strain softening. This is a very desirable feature in the design of energy absorbers as outlined in section 0.

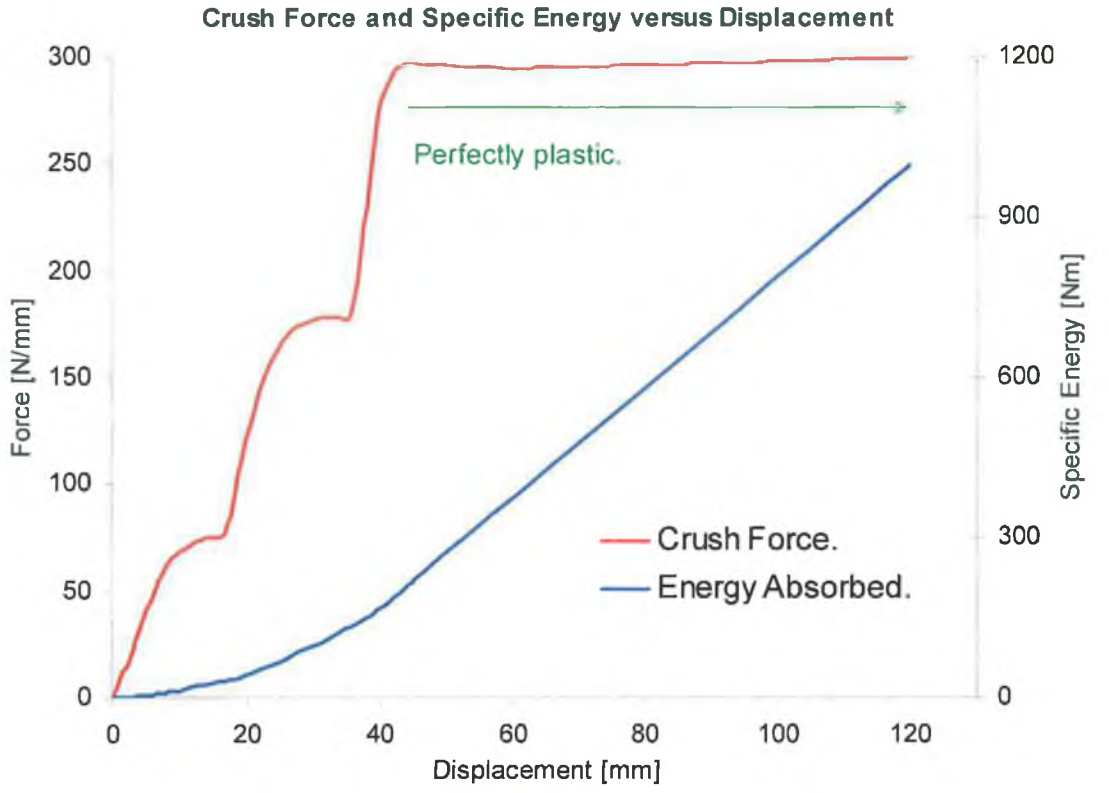

Figure 6-17: Force and specific energy response for an unconstrained CIPSS.

Figure 6-18: Initial and final stage of deflection for a CIPSS with no constraints.

6.4.2 CIPSS – Inclined Constraints.

Figure 6-19 illustrates the force-deflection response of a CIPSS with inclined constraints. The initial and final stages of deformation are depicted in Figure 6-20. The response was very similar in its mode of deformation and magnitude in comparison to the previous system analysed. From approximately 40mm the force remained constant and began to rise from approximately 100mm. This increase in force was due the inclined constraints causing the bottom segment of the outer tube to deform while at the same time the upper segment began to wrap around the cylindrical indenter to a small degree as illustrated in Figure 6-20.

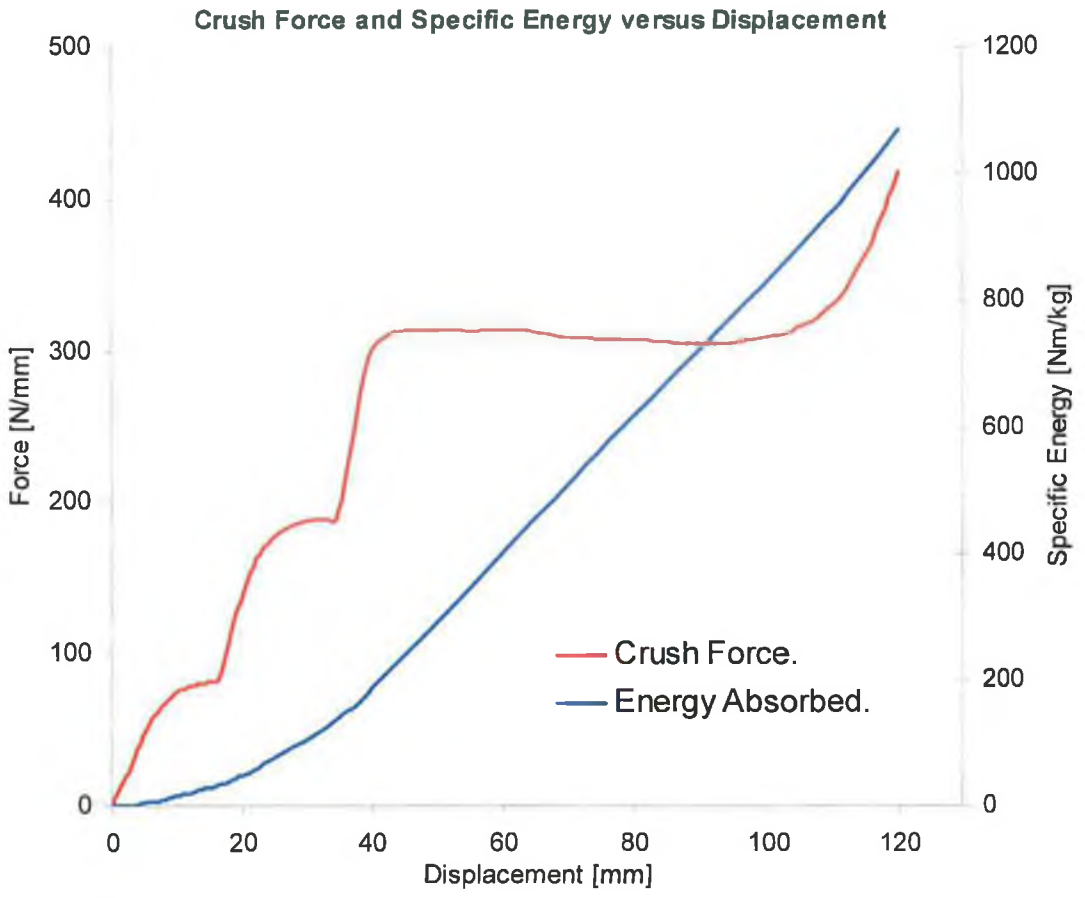

Figure 6-19: Force and specific energy response for a CIPSS with inclined constraints.

Figure 6-20: Initial and final stage of deflection for a CIPSS with inclined constraints.

6.4.3 CIPSS – Vertical Constraints.

Figure 6-21 show the force and energy response of a CIPSS compressed with vertically imposed side constraints. In contrast to the previous system, the mode of deformation has also changed, noticeably at approximately 40mm deflection. The system began to linearly strain harden for the final stroke of deflection. This strain-hardening was due to a combination of the horizontal diameter prevented from increasing and the outer tube which 'wrapped around' the cylindrical indenter as shown in Figure 6-22.

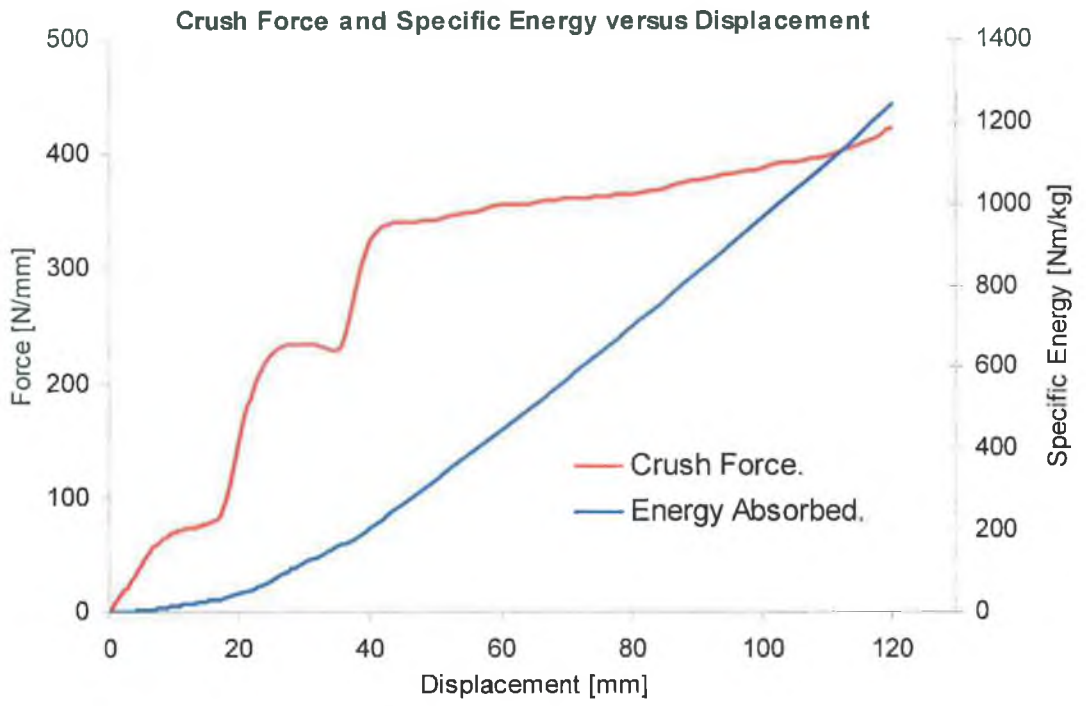

Figure 6-21: Force and specific energy response for a CIPSS with vertical constraints.

Figure 6-22: Initial and final stage of deflection for a CIPSS with vertical constraints.

6.4.4 CIPSS – Combined Constraints.

The experimental result for the compression of a CIPSS with a cylindrical indenter and externally imposed constraints is shown in Figure 6-23. At approximately the same deflection of 40mm as in the previous section, the system began to strain-harden. The increase in force observed at approximately 100mm deflection was due the existence of the inclined constraints. These constraints, having an angle of fifteen degrees, caused the lower or bottom regions of the system to deform more and therefore, as a consequence, a greater degree of 'wrap around' occurred on the indenter. The initial and final stages of compression are shown in Figure 6-24.

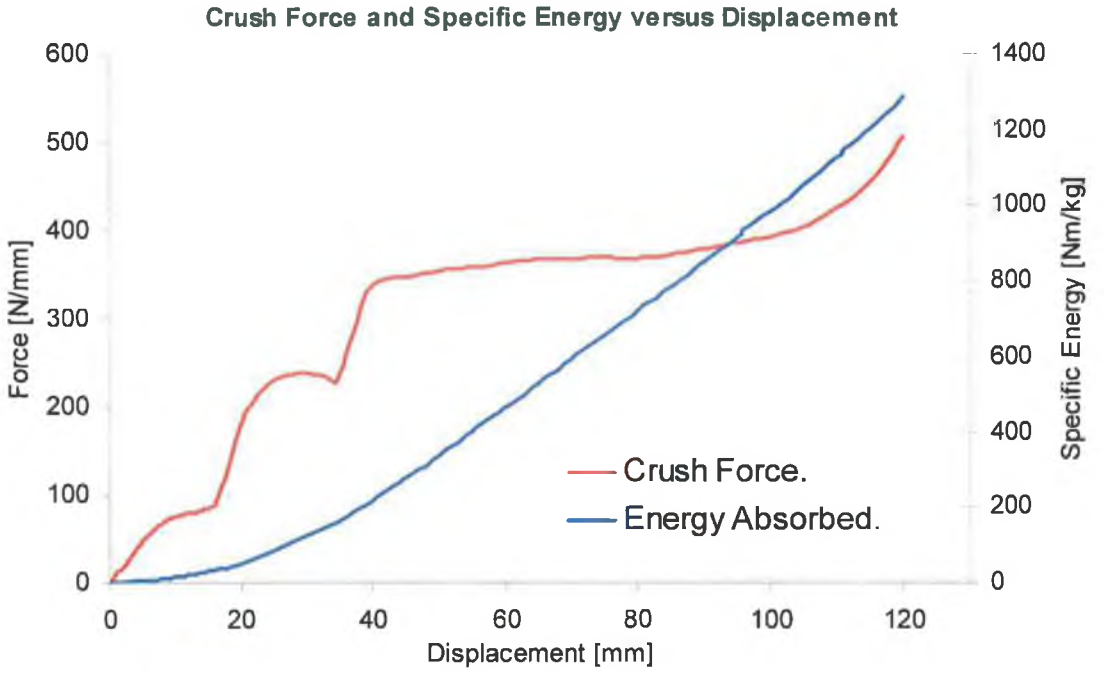

Figure 6-23: Force and specific energy response for a CIPSS with both constraints.

Figure 6-24: Initial and final stage of deflection for a CIPSS with both constraints.

6.5 Global Comparison / Analysis of the Energy absorption Characteristics.

Figure 6-25 depicts a force - deflection response for the CIPSS crushed with a flat platen under the various constraint conditions. Pointer A in this figure indicates the effect of adding an external constraint sequentially. As expected, the unconstrained system reached its full displacement stroke of 120mm, the system with inclined constraints reached a shorter distance of 95mm but absorbs a greater load and likewise for the system exposed to vertical constraints. Finally the system subjected to both constraints showed signs of a higher load but the shortest displacement stroke of 50mm was observed. This implies that the crush efficiency and overall energy absorption response (See section 3.3.1) for such systems compressed with a flat rigid platen greatly depend on the type of constraints applied, since this will inadvertently affect the magnitude of the displacement stroke.

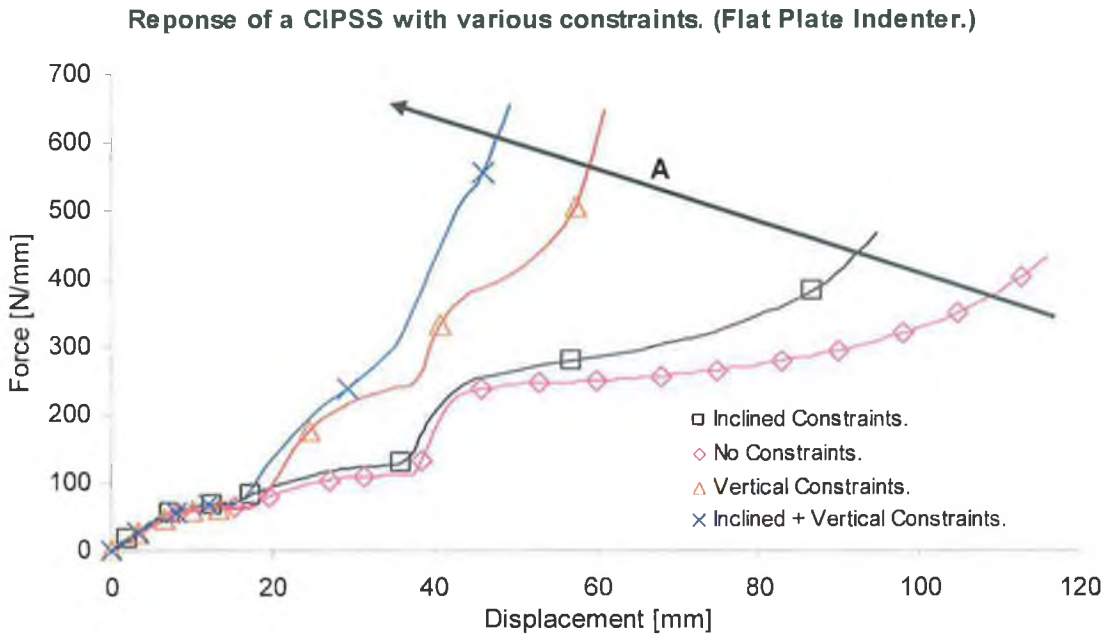

Figure 6-25: Global comparison of the CIPSS crushed under a flat rigid platen with different constraints.

Figure 6-26 displays a bar chart illustrating the various energy absorption characteristics of this system crushed under a rigid flat platen. In terms of crush efficiency, it can be seen that the efficiency reduced consecutively once an extra constraint was applied to the CIPSS under loading. For example, the CIPSS which was unconstrained experienced the highest efficiency of approximately 78% whilst the CIPSS subjected to both the inclined and sidewall constraint experienced the least efficiency of 40%. The very low efficiency for the latter system was due to the effect of 'locking'. This locking effect was due to nature of the inclined and sidewall constraints which prevented any further deformation possible within the system and hence the reason for a rapid rise in force as observed in Figure 6-5 and Figure 6-7. The energy efficiency of such systems also experienced a reduction in value for the obvious reason that the stroke length was very low. Concurrent to this, the peak load observed, occurred at the final stage of deflection as oppose to the initial stage, which will further reduce the energy efficiency. Since the weight effectiveness is the product of crush efficiency and specific energy absorption, it can be expected that this characteristic reduces progressively from an unconstrained CIPSS to a CIPSS subjected to both constraints. Notice however that the final system exposed to both constraints revealed a larger value than its counterpart with only sidewall constraints. This was due to the very large energy absorbed by this system.

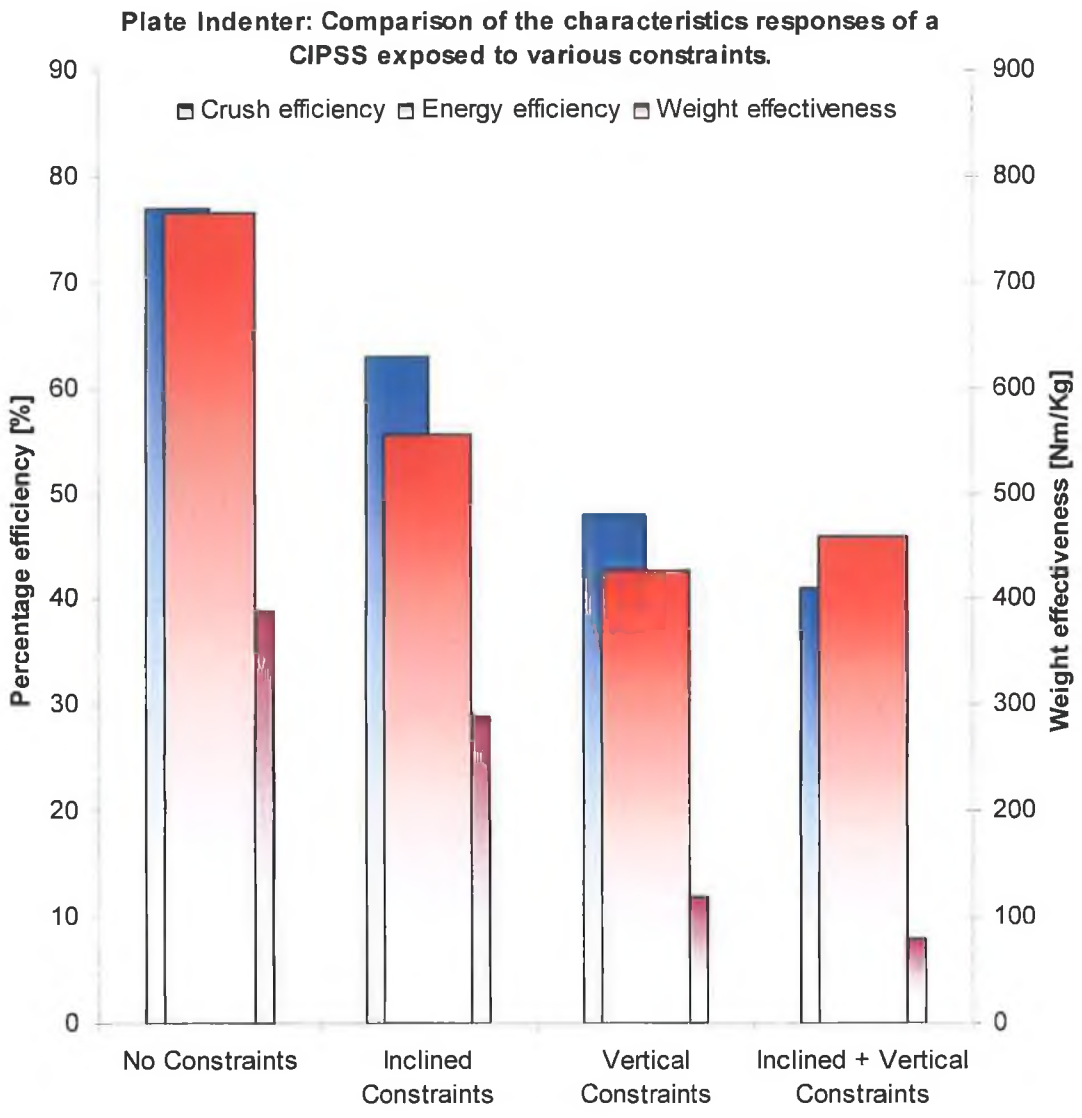

Figure 6-26: **A bar chart displaying the various responses of a CIPSS crushed under a flat plate indenter with different constraints.**

The force - deflection response of a CIPSS crushed under point load indenter is depicted in Figure 6-27. Immediately it can be seen that the full displacement of stroke of 120mm can be achieved for all for systems tested with the different constraints. Therefore a crush efficiency of 80% is possible for all four systems compressed under a point load indenter which is shown in Figure 6-28. Also shown in this figure is the energy efficiency which exhibit similar magnitudes ranging from 60% to 70% and which are higher than those compressed under a flat platen. The weight effectiveness for this particular system displayed an increasing trend in magnitude as the number of constraints was increased consecutively. It can be seen that the CIPSS compressed under a point load indenter exhibit more desirable energy absorption characteristics than its counterpart compressed under a rigid flat platen.

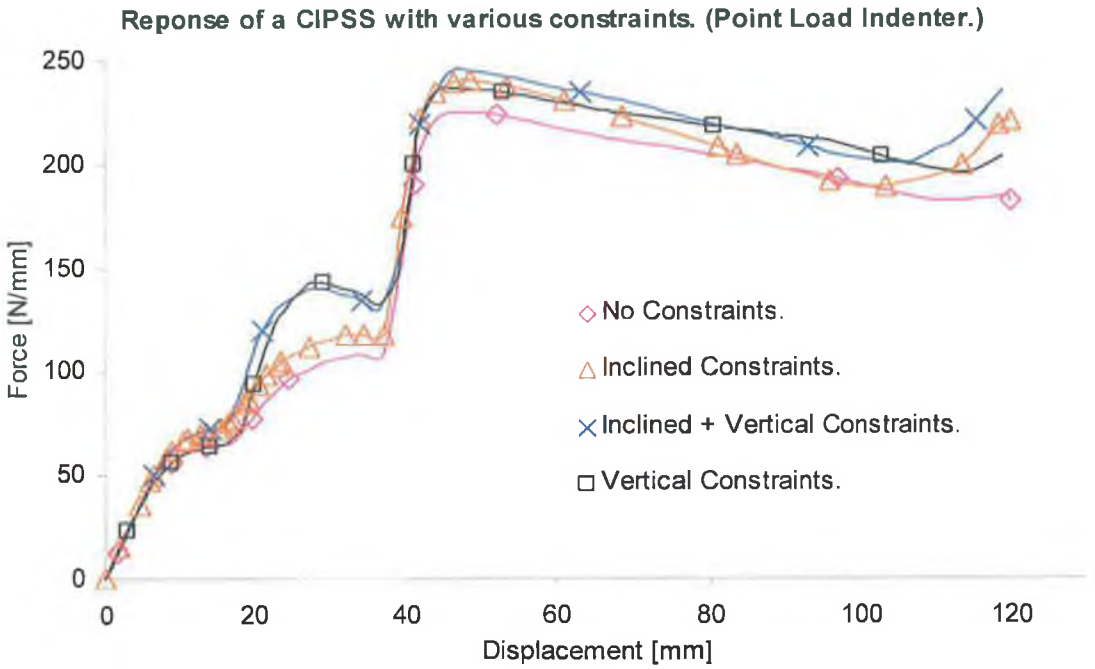

Figure 6-27: **Global comparison of CIPSS crushed under a point load indenter with different constraints.**

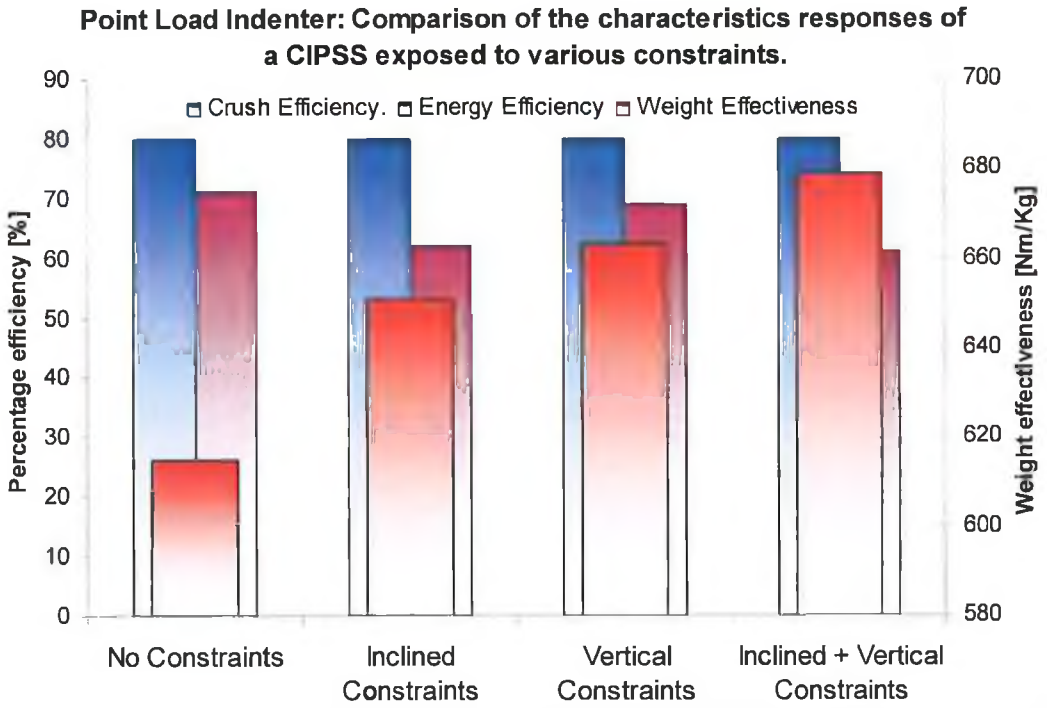

Figure 6-28: **A bar chart displaying the various responses of a CIPSS crushed under a point load indenter with different constraints.**

For a CIPSS crushed under a cylindrical indenter, a force - deflection response and a bar chart are displayed in Figure 6-29 and Figure 6-30 respectively. For this system, it was also possible to maintain a high crush efficiency of 80% since no locking occurred as observed for the systems subjected to rigid flat platen crushing. Also from this figure, notice the

collapse load has increased for the two systems subjected to both sidewall and inclined constraints respectively. In Figure 6-30, the energy efficiencies are somewhat lower than the preceding system, ranging from 55% to 75%. The unconstrained system exhibited the highest energy efficiency since its corresponding force was at a constant rate in contrast to those systems exposed to lateral constraints. The weight effectiveness exhibits positive results in that its magnitude increased as the number of constraints added was increased which is a desirable feature in the design of energy absorbers.

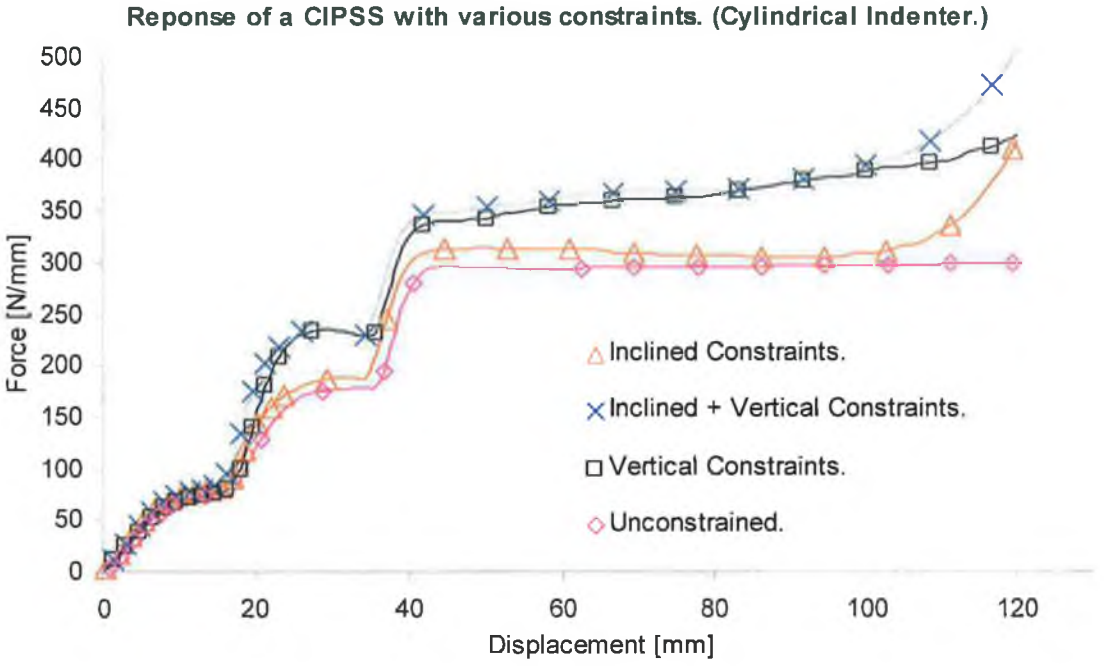

Figure 6-29: Global comparison of the CIPSS crushed under a cylindrical indenter with different constraints.

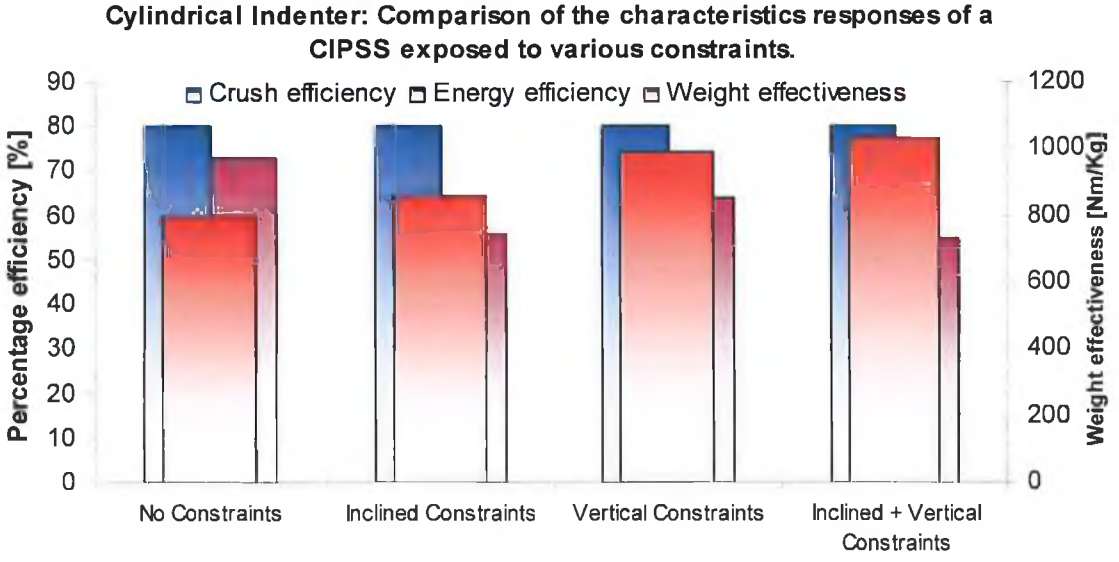

Figure 6-30: A bar chart displaying the various responses of a CIPSS crushed under a cylindrical indenter under different constraints.

6.6 Summary of Chapter Six.

- Chapter six analysed the response of nested systems such as the CIPSS subjected to lateral compression by various indenters and exposed to various external constraints. The effect of the interaction between these indenters and the various constraints on each energy absorber was analysed.
- In order to assist in analysing the response of such devices, energy absorption characteristic as a performance tool was applied to illustrate which devices exhibited the most desirable responses. Characteristics such as the crush efficiency, energy efficiency and weight effectiveness were employed to describe the behaviour of such devices.
- It was found that for the four systems compressed under a plate indenter, the crush efficiency, energy efficiency and weight effectiveness reduced consecutively as the number of constraints was added.
- For the systems compressed under both a point load and cylindrical indenter, it was found that both the crush efficiency and the weight effectiveness increased consecutively as the number of constraints were added. The energy efficiency of the systems crushed under these two indenters varied due to the shape of their force-deflection response.

7 Finite Element Analysis and Results.

7.1 Introduction.

This chapter details a numerical analysis of the various energy absorbers already experimentally analysed. More specifically, it is divided into two sections with section 7.6 concerned with the response optimisation of nested systems. Section 7.9 is concerned with the specific energy maximisation of nested systems. Prior to this, a description is given on the numerical procedure employed to simulate the various devices under both quasi-static and dynamic loading conditions.

7.2 Quasi - Static Analysis: Numerical Procedure.

ANSYS, an implicit finite element code was used to simulate the quasi - static loading of the selected energy absorbers. Since the loading rate was in the static range and no dynamic effects were present, the implicit version of the code was deemed a suitable choice. Elements used were three-dimensional eight node brick elements which have large strain, large deflection and plasticity capabilities (See Figure 7-1a). The numerical models contain three non-linear phenomena and are as follows: Material non-linearity in which a bilinear isotropic hardening material model was used to capture the strain hardening effects in the plastic stages of deformation. The yield stress and plastic modulus values were taken from sample dog bone specimens as outlined in section 4.5. Figure 7-1b illustrates the bilinear stress-strain curve used to model elastic and plastic stages of material deformation of the mild steel tubes. It should be noted that a bilinear material model was commonly used by various researchers, Ruan et al [93], Wu and Carney [75], Jing and Barton [43], Kadaras and Lu [53], Reid and Harrigan [33, 34]. Good agreement was found by the researchers between the numerical results and those obtained by experiments.

The second non-linearity being the contact interaction between each respective tube. An augmented Lagrangian penalty method was used to define the contact algorithm in order to capture the models changing contact status throughout the deformation stroke (See section 3.2.5). This was achieved using surface to surface contact groups with each group defined by the relevant adjacent surfaces that establish contact during the compression process. The various indenters used to compress the nested systems were defined as rigid bodies and constrained to translate vertically over a predefined displacement. This predefined displacement was applied by means of a pilot node. This pilot node was also used to accumulate the corresponding reactive force from each node of each element created due to the applied displacement. The energy absorbers were modelled as one quarter models with

symmetry constraints invoked along the appropriate symmetry planes. Resulting reactive forces of each model were scaled by a factor of four for analysis and for comparison against experimentally observed values. The third non-linearity being large strain-large deformation, this feature must be included due to the large displacements that are applied. An arbitrary solution time of 1 was assigned to all models with a typical time step size of 0.005. This low value was used in order to ensure that nonlinear solution converges due to the path dependant plasticity material model involved. A maximum and minimum time step of 0.02 and 0.001 was defined respectively for the upper and lower limits of the solution time step.

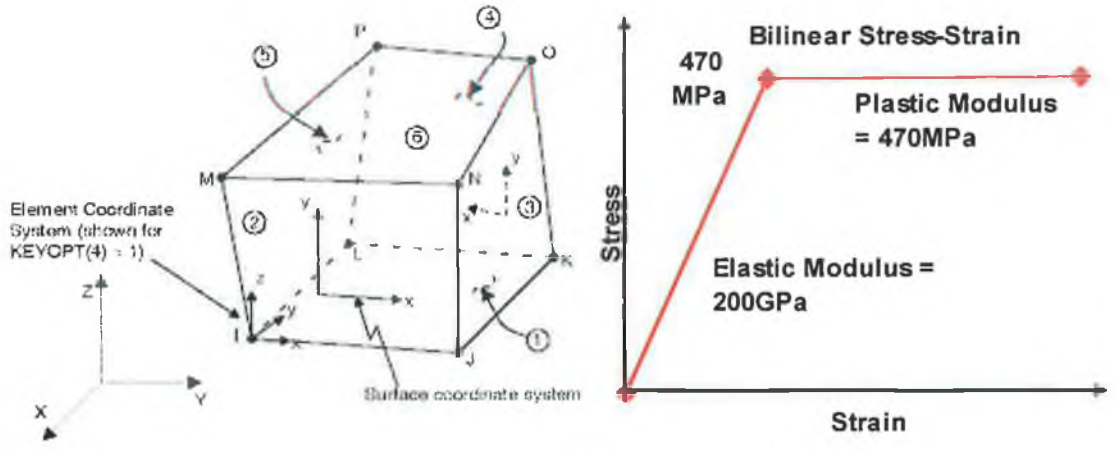

(a) (b)

Figure 7-1: (a) Solid45 brick element used to discretize the quasi –static models [85]. (b) Bilinear stress-strain curve used to represent the material behaviour of mild steel.

7.3 Geometry Creation of the Oblong Tubes.

The geometry contour of each of the oblong tubes was obtained by applying the appropriate loading and boundary conditions as observed in experiment during the preparation stages. Prescribed vertical displacements of 50mm, 40mm and 30mm were applied to the outer, central and inner tubes respectively using three individual pilot nodes as shown in Figure 7-2 which illustrates the initial and final stages of tensile displacement for each of the tubes. When the full displacement was applied, each individual tube was unloaded until the force ramped back to zero as shown in Figure 7-3. This was done in order to take into account the final state of deformation due the elastic spring back which occurs when the tensile load was removed. The final geometry profile was updated from the deformed mesh using update geometry capabilities in ANSYS. The new oblong shaped geometry for each tube was discretized with the same mesh density as their circular counterparts in order to maintain consistent modelling and meshing practice.

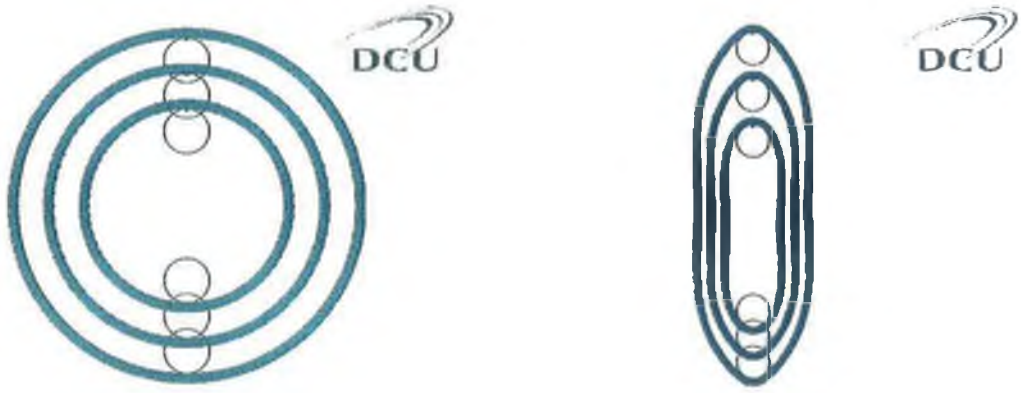

Figure 7-2: Initial and final stage of displacement using the tension method as produced by ANSYS.

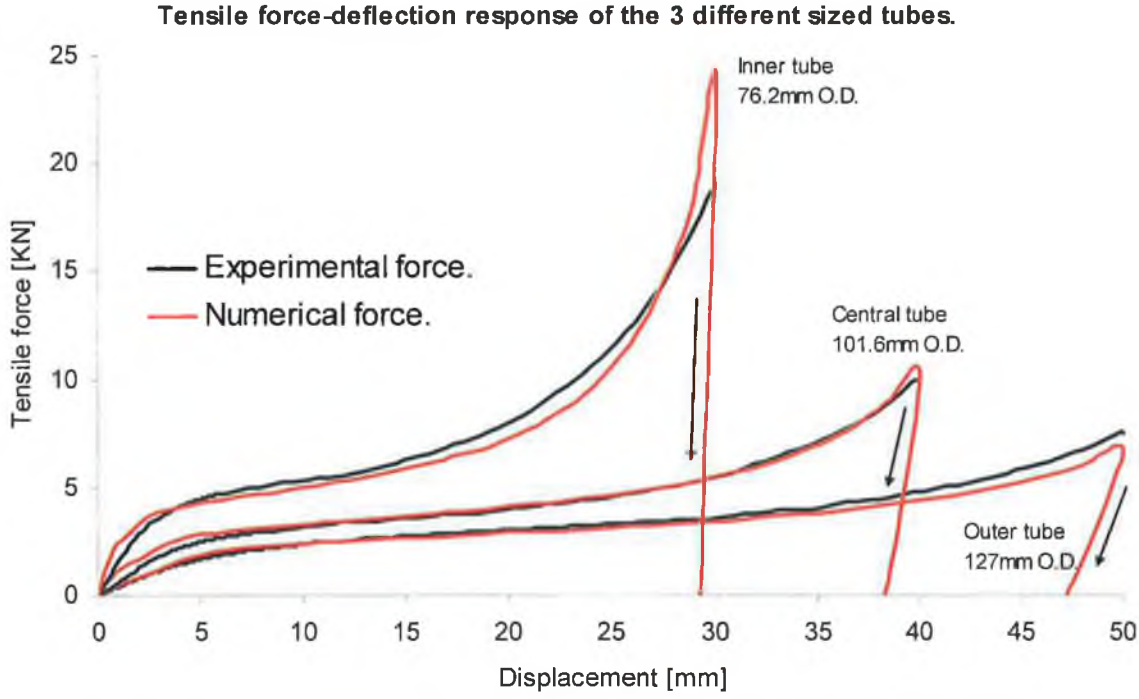

Figure 7-3: Force deflection response of the three tubes [Loading and unloading].

7.4 Dynamic Analysis: Numerical Procedure.

The explicit non linear finite element code LS-DYNA was used to predict the response of the selected energy absorbers subjected to a free falling impinging mass. Two element formulations was used, namely the brick and shell element, in order to provide a comparison of results at a later stage. The complete model consisted principally of the striker, the assemblage of tubes and the base. These three components in each system were modelled with an explicit structural solid (See Figure 7-4) consisting of eight nodes having translations, velocities and accelerations in the x, y and z directions at each node. The element continuum is of a Lagrangian formulation, and by default, uses one point integration with viscous hourglass control if necessary. The striker was modelled as a rigid entity with translational displacement permitted in the vertical y direction, this impact

velocity was defined via the *BOUNDARY_PRESCRIBED_MOTION_RIGID card in LS-DYNA. For each of the various absorbers analysed experimentally, an average velocity time curve was obtained and applied to the striker through this control card. (See Figure 4-6). All other rotations and translations on this striker were fixed. In the material model associated with the striker, the mass density was increased to represent the total mass of both the carriage and the striker and was applied using the *MAT_RIGID card. The base was modelled as rigid with all rotations and translations defined as fixed entities. The tubes contained within the various energy absorbers were discretized by fully integrated solid elements. These elements perform better where element distortions are large but are about four times more costly. No hourglass control is needed as there are no zero-energy modes [86]. This feature was activated via the *SECTION_SOLID control card. Figure 7-5 depicts the time step size required to solve the OIPDS under the prescribed dynamic loading conditions using brick elements. This is shown for the three different element mesh densities of three, five and six elements through the thickness of each tube respectively. The time step size is automatically determined by the LS-DYNA program once the solution time is defined through the *CONTROL_TERMINATION card. The *CONTROL_ENERGY card was activated in order to examine the energy balance of the brick models as detailed in section 3.3.4.

The OIPDS was also modelled with shell elements (Figure 7-4) in order to make a comparison of results against the system represented by brick elements. This shell model was represented by the Belytschko-Tsay shell element with five integration points defined through the thickness of each tube. The shell thickness and the number of integrations were defined through the *SHELL_SECTION card. All shell elements include membrane, bending and shear deformation capabilities. Since the shell elements are defined by a mid – plane, it is very important that appropriate gaps between the shells are modelled in the finite element geometry in order to account for the shell thickness dimensions. If this is not adhered to, initial penetrations will occur in the contact surfaces resulting in an incorrect solution of the problem. Symmetry conditions were invoked along the appropriate symmetry planes via the *BOUNDARY_SPC_SET card in order to reduce CPU time. The striker was also modelled as a rigid entity using brick elements as described in the preceding paragraph. The shell element formulation is quite suited to model bending dominated problems. In addition to this, the solution time using the shell element formulation is considerably less than that when using the brick element formulation as shown in Figure 7-6 when compared with Figure 7-5. The disadvantage with using brick

elements is that at large deformations, the brick will be become highly distorted particularly in the regions of the hinges within the plastic zone and therefore, it may not capture the bending stress accurately throughout the model.

The contact algorithm used to simulate contact between the respective components (striker, tubes and base) for both the brick and shell element models was based on the 'Automatic Surface to Surface Contact' in which contact was established when a surface of one body penetrates the surface of another body. This contact algorithm was defined using the *CONTACT_AUTOMATIC_SURFACE_TO_SURFACE card. A static coefficient of friction value of 0.2 was assigned to the contact pairs to prevent lateral movement between the respective tubes [34].

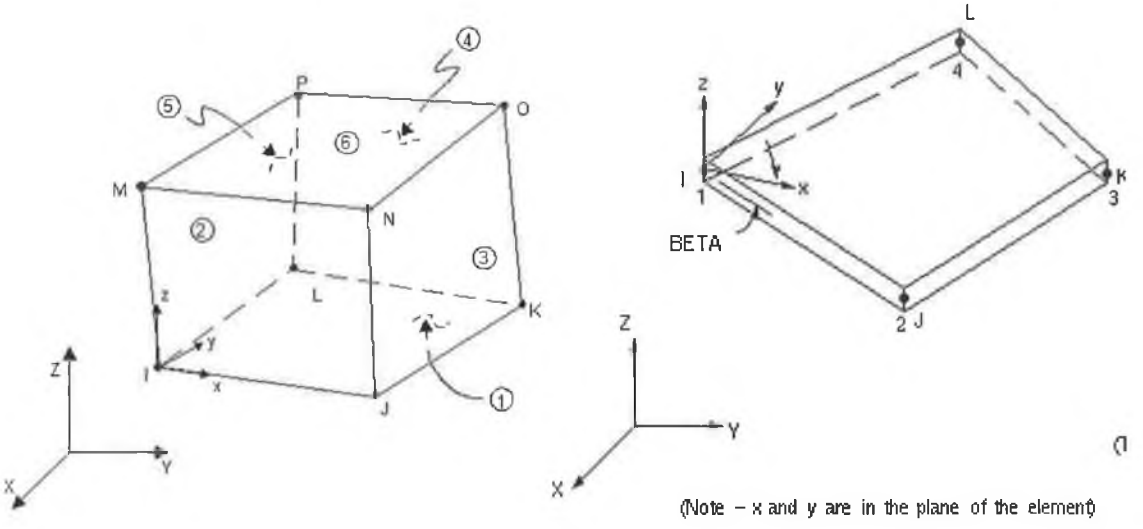

Figure 7-4: The explicit 8 node brick and 4 node shell element used for the dynamic analysis. [85]

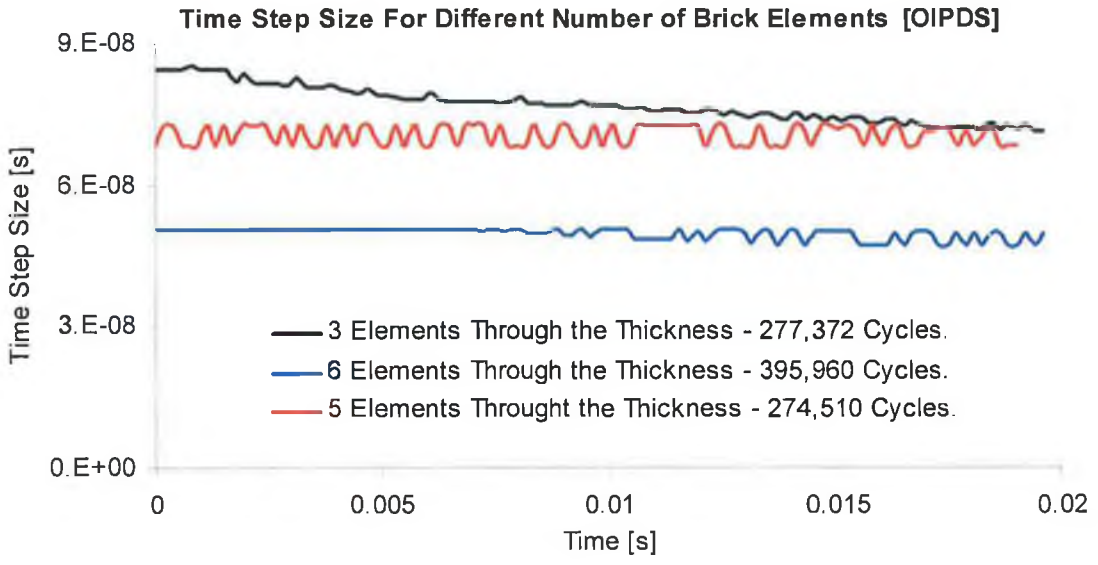

Figure 7-5: A plot illustrating the time step size for the different number of brick elements through the thickness of each tube. [OIPDS]

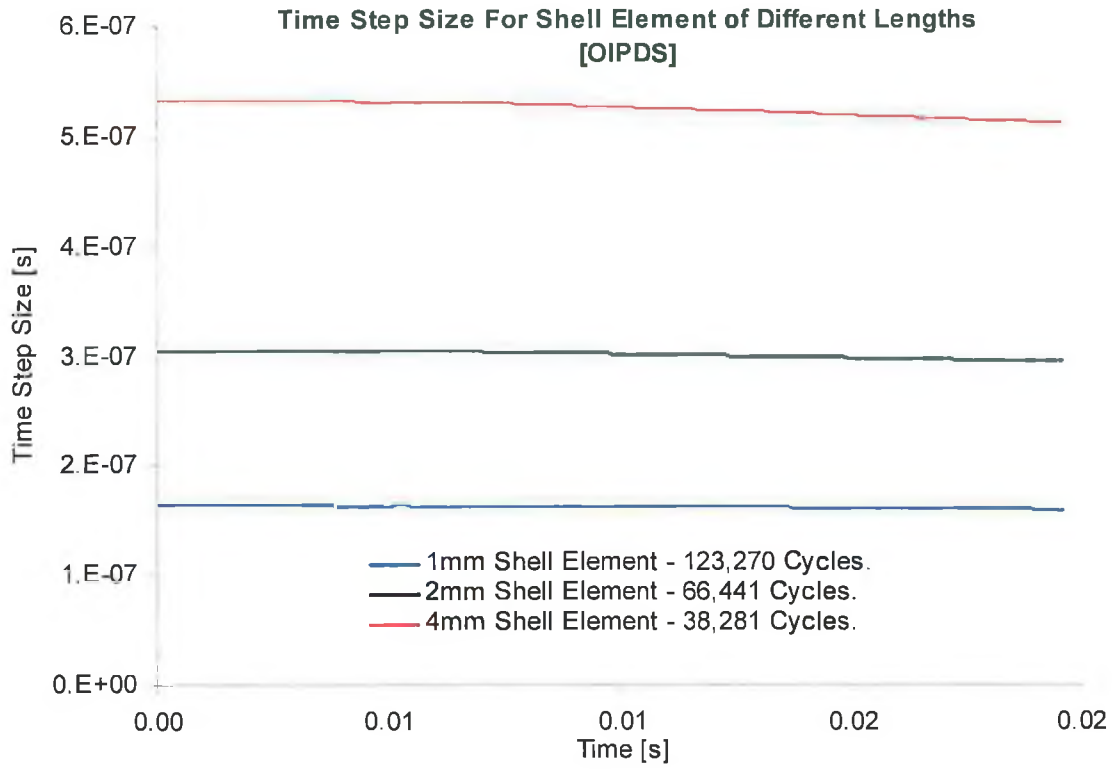

Figure 7-6: **A plot illustrating the time step size for the different number of shell elements through the thickness of each tube. [OIPDS]**

7.5 Mesh Convergence.

Figure 7-7 illustrates the convergence plot of three different mesh densities for the CIPDS. It can be seen that a convergence solution was achieved when three or five elements were used to mesh the thickness of the tubes within the CIPDS. The corresponding force convergence plot for this particular system is shown in Figure 7-8. Hence both the CIPSS and the CIPDS consisted of a mesh density involving three elements through the thickness of each tube as represented by the inlay in the same figure.

Figure 7-9. illustrates the convergence plot of three different mesh densities for the OIPDS. It can be seen that a convergence solution was achieved when five or six brick elements were used to mesh the thickness of the tubes. Hence, all subsequent models involving brick elements consisted of a mesh density involving five bricks through the thickness of each tube. Accordingly, a force - time plot of the OIPDS illustrating the response for three, five and six elements through the thickness of each tube is shown in Figure 7-10.

For the shell models, a convergence study was also undertaken with Figure 7-11 illustrating the force - time response of three different mesh densities. Three simulations with a shell element length of 4mm, 2mm and 1mm were conducted.

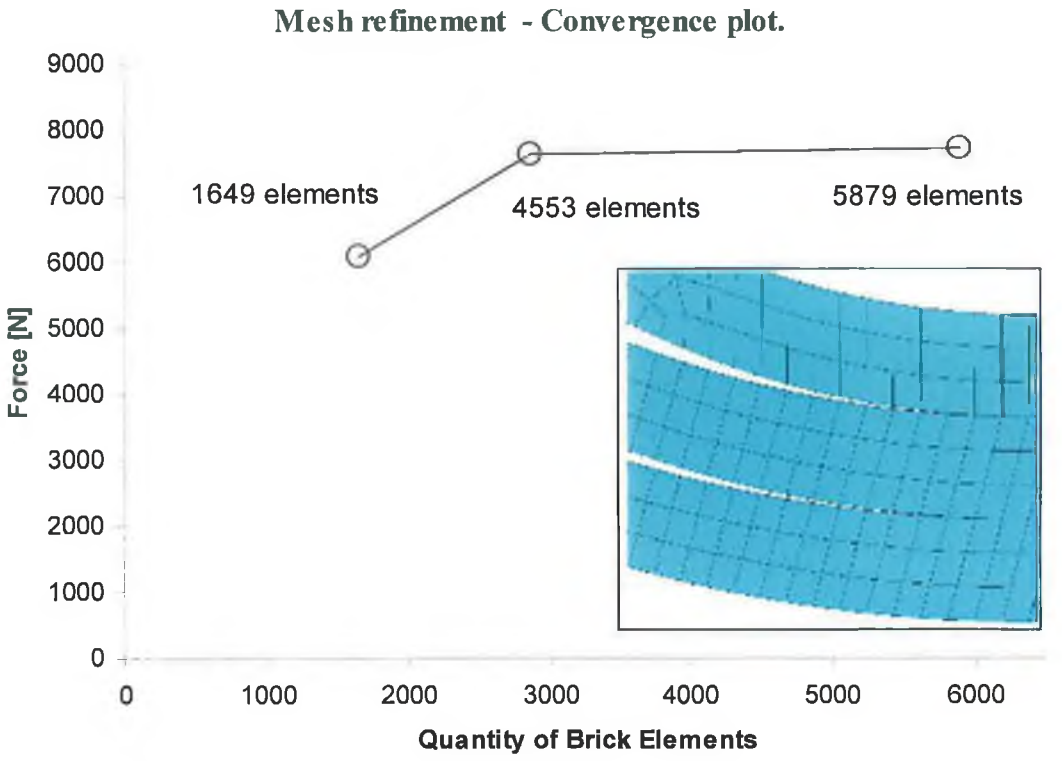

Figure 7-7: A force convergence plot of three different mesh densities for the CIPDS.

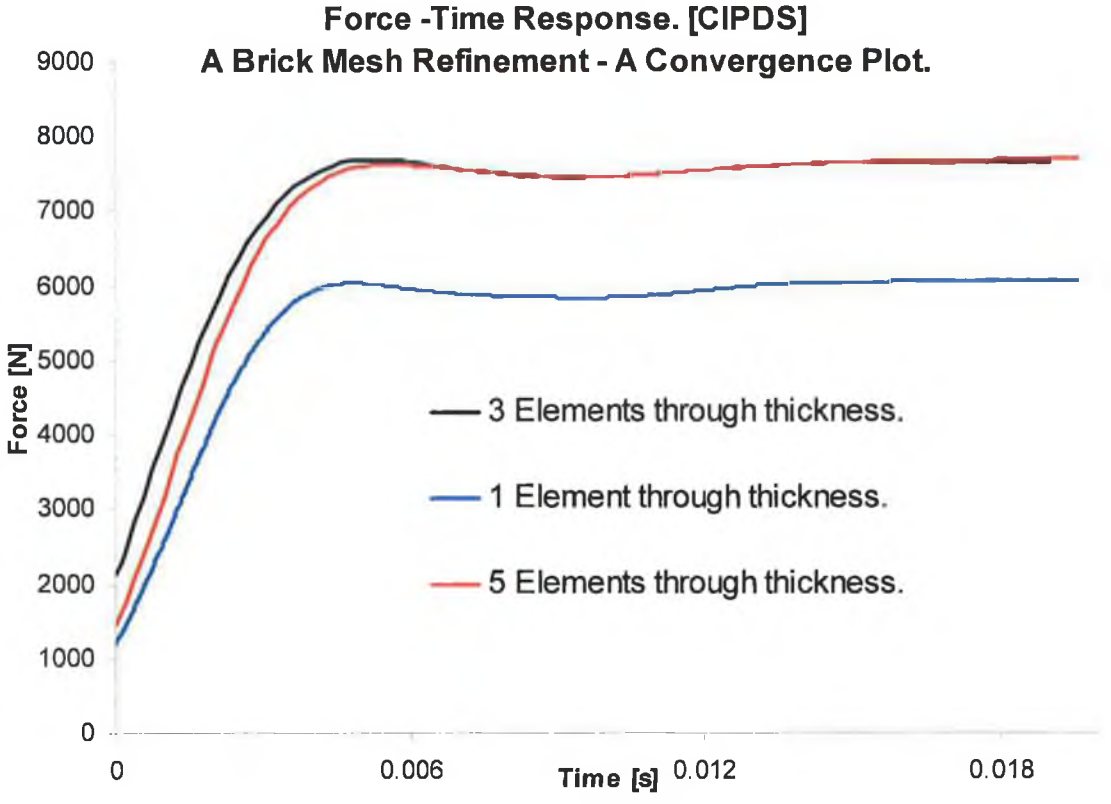

Figure 7-8: **A force-time convergence plot of the CIPDS analysed with 1, 3 and 5 brick elements through the thickness of each tube.**

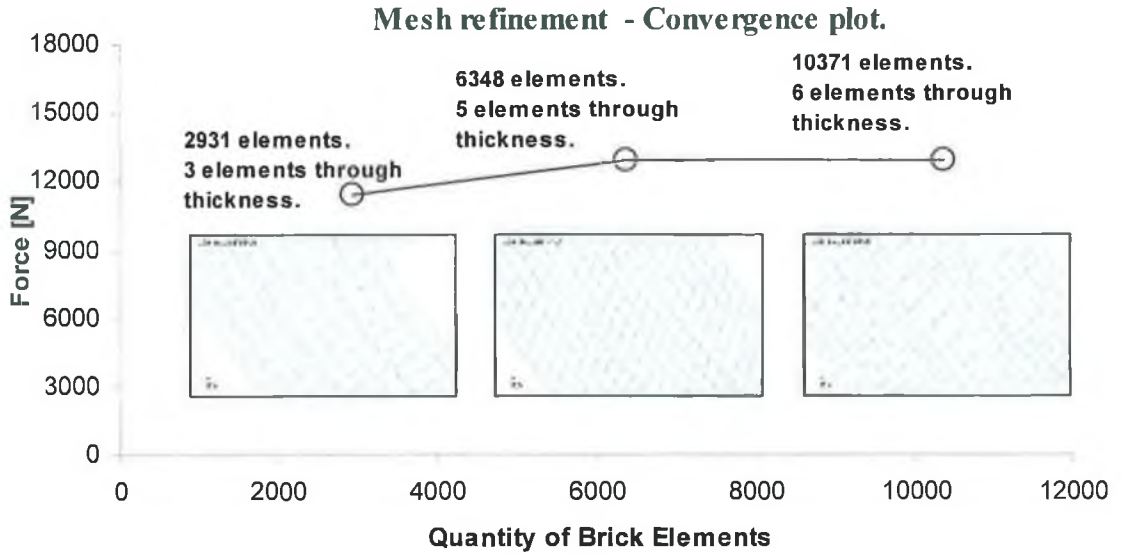

Figure 7-9: **A convergence plot illustrating the number of brick elements for each of the three different mesh densities pertaining to the OIPDS.**

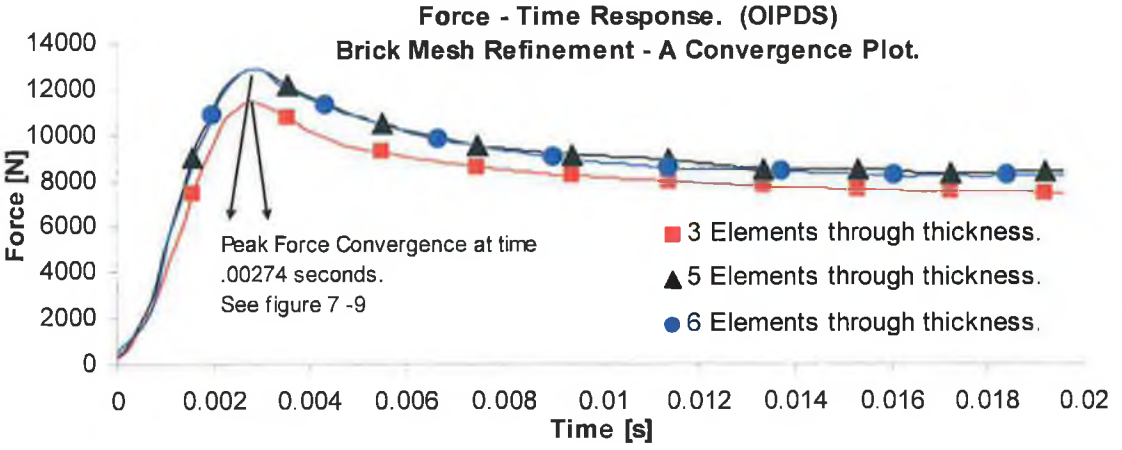

Figure 7-10: **A force-time convergence plot of the OIPDS analysed with 3, 5 and 6 brick elements through the thickness of each tube.**

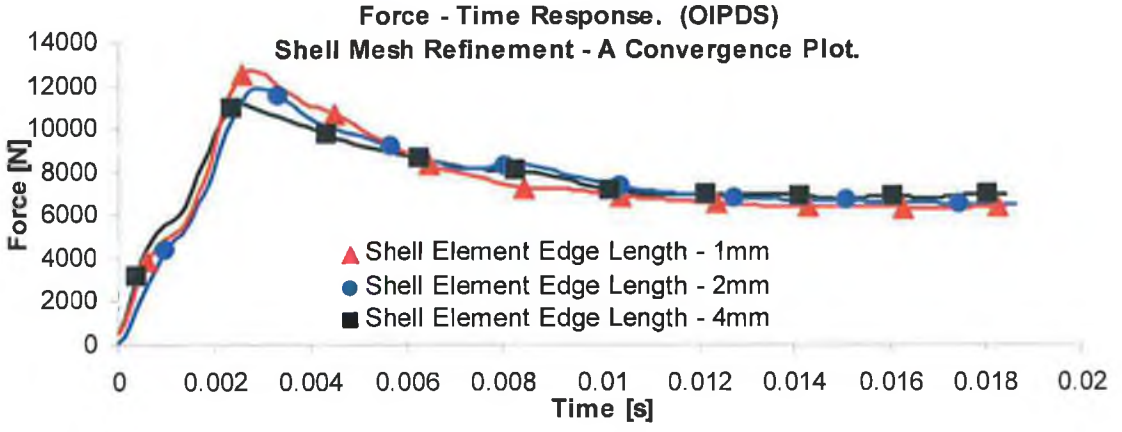

Figure 7-11: **A force - time convergence plot of the OIPDS analysed with five integration points through the thickness of each tube.**

7.6 Numerical Results: Response Optimisation of Nested Systems.

Section 7.6 details the comparison of results between the finite element method and those obtained from experimental techniques as described in chapter 5.

7.6.1 Geometric Variations of the CIPSS.

7.6.2 A COPSS Crushed under a Plate Indenter.

Figure 7-13 show the numerical and experimental results for a COPSS compressed with a flat plate indenter. It can be see that there was reasonable agreement between the two methods. The numerical method slightly under predicted the force at approximately 6mm with an over prediction in the final stages of deformation. In terms of the energy response, excellent correlation was found with only a difference of 3% between the two methods. Figure 7-14 illustrates the boundary conditions applied to the one quarter symmetry model. Also shown are the contact pairs, with the contact normals facing each other, used to capture the contact interaction between the adjacent surfaces of each tube. Finally, Figure 7-15 depicts the Von Mises plastic strain history of three selected nodes, each node been located at the uppermost region of each tube and at the intersection of the symmetry planes as shown in the first picture in Figure 7-12. It should be noted that the same location of nodes is employed for subsequent models analysed in this chapter.

By examining this figure, it can be seen that the outer tube in the region defined by the outer node experienced an increase in plastic strain until contact was established with the central tube. From this point onwards, the strain became constant whilst concurrently; the central node in the central tube began to rise until contact was established with the inner tube. Similarly, this node experienced a constant strain, whilst inner node remained constant for up to 85mm deflection before beginning to increase again for the remainder of the stroke. This increase in strain was due to increased bending and separation of the upper hinge of the inner tube from the central tube.

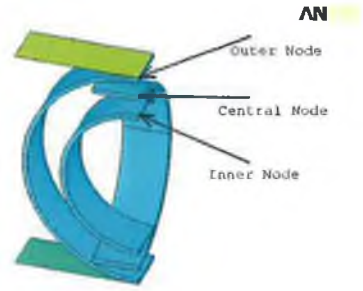

Figure 7-12: Location of the nodes for analyzing the strain evolution throughout the displacement stroke.

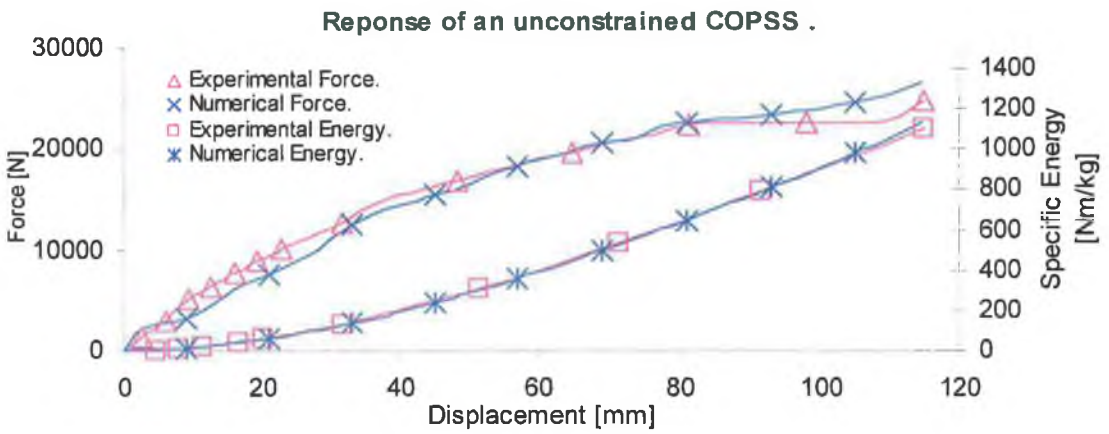

Figure 7-13: **Comparison of results between the numerical and experimental methods for a COPSS crushed under a flat plate indenter.**

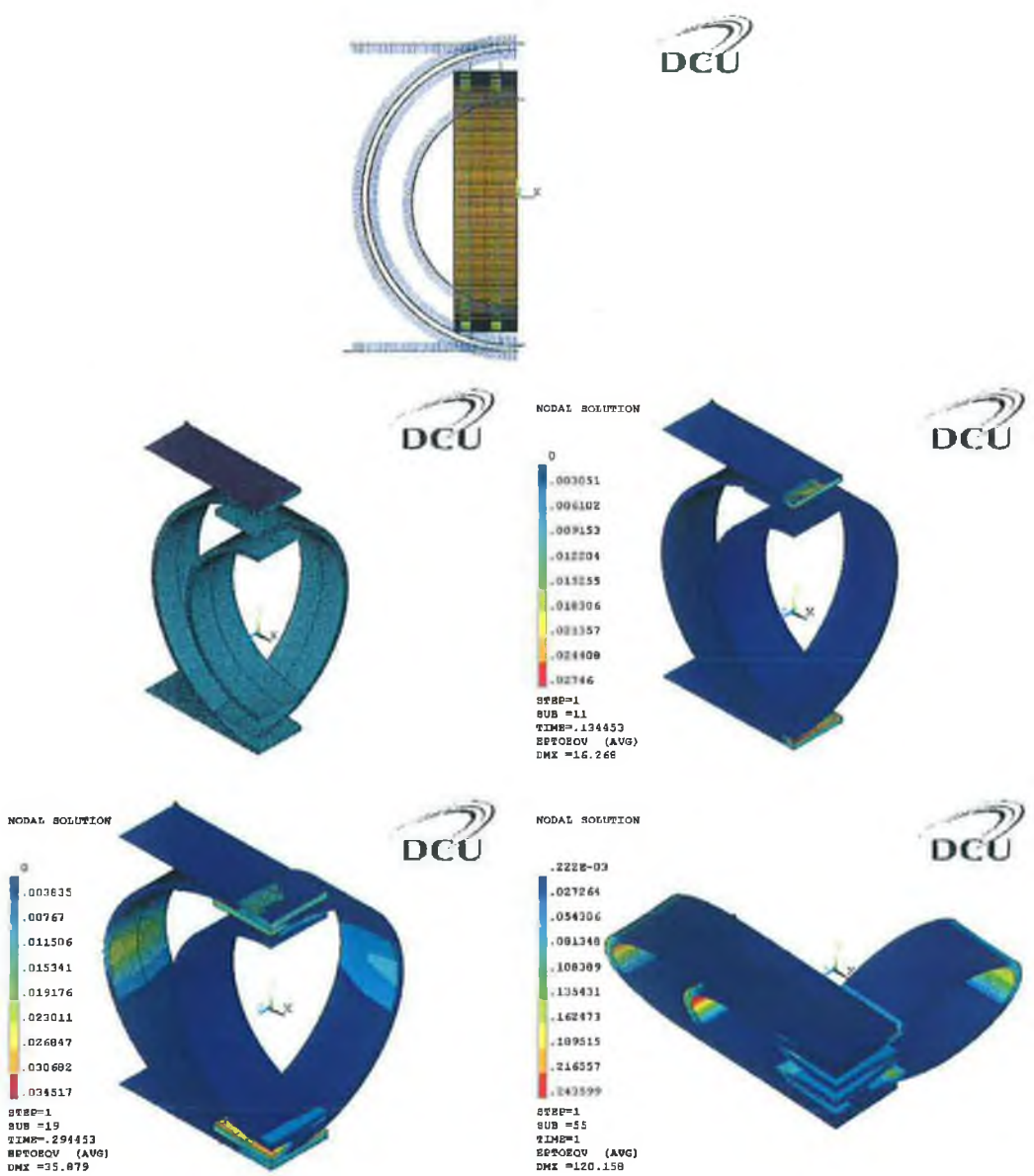

Figure 7-14: **Illustration of the boundary, contact definitions and a spatial plot of the Von Mises total strain.**

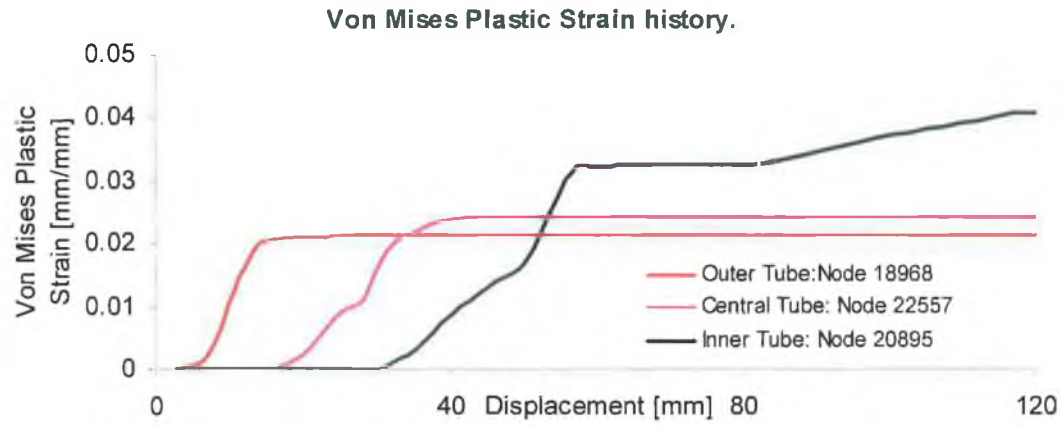

Figure 7-15: **Plastic strain history at three selected nodes for a COPSS crushed under a flat plate indenter.**

7.6.3 A COPSS Crushed under a Point Load Indenter.

Figure 7-16 shows the numerical and experimental response for a COPSS compressed with a point-load indenter. For up to 30mm deflection, the numerically predicted result was in good agreement in terms of magnitude followed by a slight over prediction for the remaining deflection. In terms of the energy response, a value of 2% was observed between the numerical and experimental method. Figure 7-17b illustrates the Von Mises plastic strain history at three selected nodes for this particular system. The node presenting the region of the outer tube began to increase in strain from approximately 35mm displacement; this was due to the point load indenter used to compress the system which caused increased bending to develop in the contact region of this point load indenter.

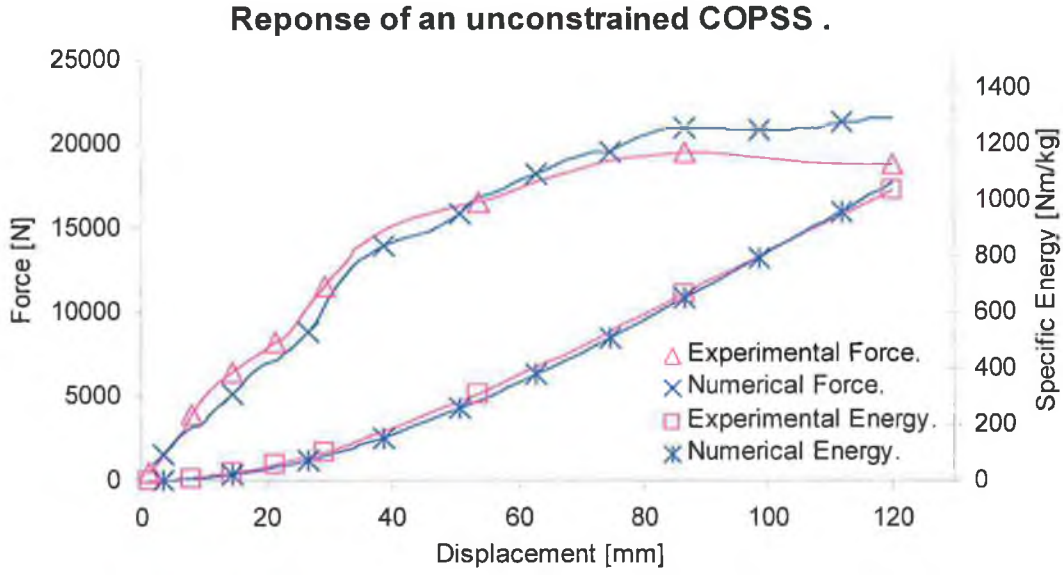

Figure 7-16: **Comparison of results between the numerical and experimental methods for a COPSS crushed under a point load indenter.**

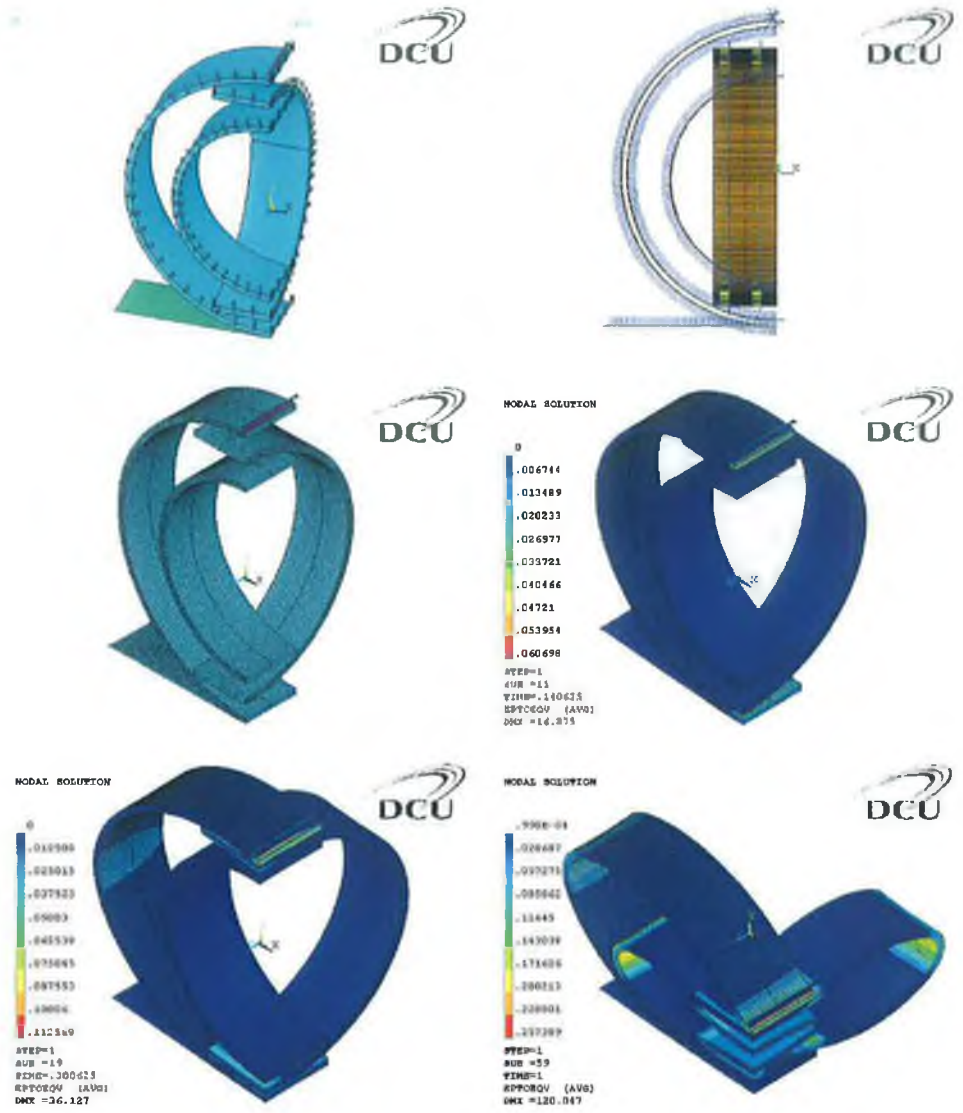

(a)

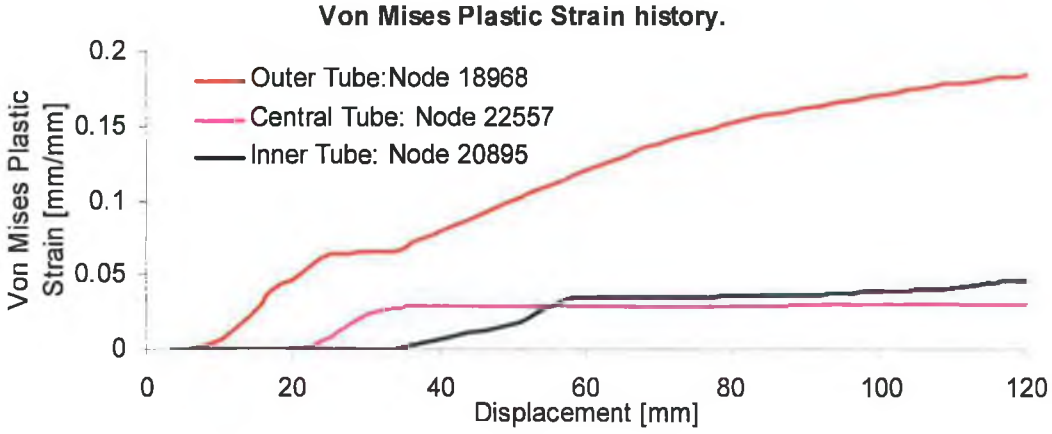

(b)

Figure 7-17 **(a) Illustration of the boundary and contact definitions with a Von Mises total strain plot for a COPSS.**
(b) Von Mises Plastic strain history at three selected nodes for a COPSS crushed under a point load indenter.

7.6.4 A COPSS Crushed under a Cylindrical Indenter.

Figure 7-18 displays the numerical and experimental results for the compression of COPSS with a cylindrical indenter. As observed in the previous two systems, there was a slight under prediction of the force from approximately 6mm deflection with an over prediction occurring in the final stages. Despite this, there is a good correlation between the two methods in terms of the deformation mode and for the total energy absorbed, in which a difference of 1% was observed. Figure 7-19a illustrates the boundary and contact definitions for this particular model in conjunction with the Von Mises total strain evolution at various stages of deflection. Figure 7-19b offer a Von Mises plastic strain history plot, it can be seen that the response of each node was similar to that of a COPSS compressed under a plate indenter.

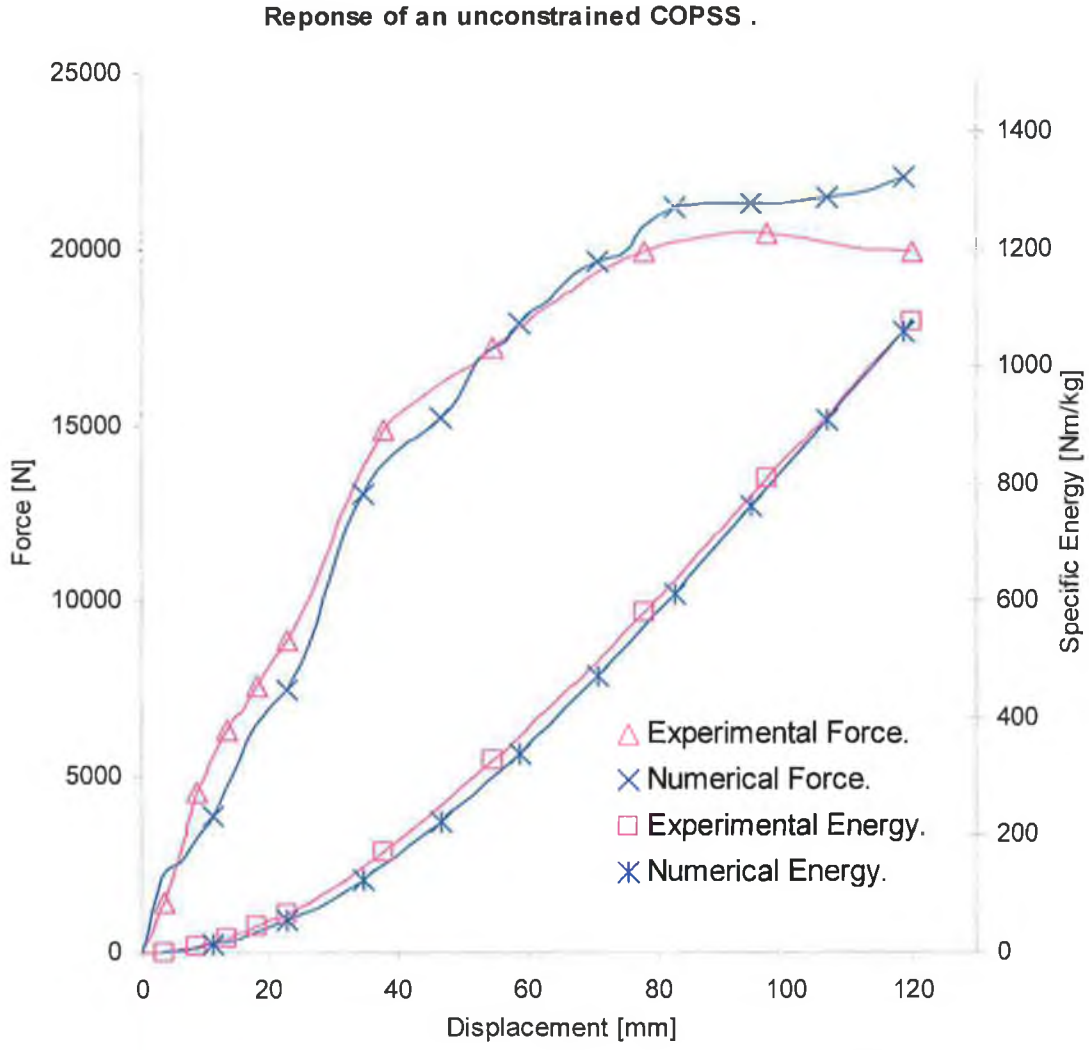

Figure 7-18: Comparison of results between the numerical and experimental methods for a COPSS crushed under a cylindrical indenter.

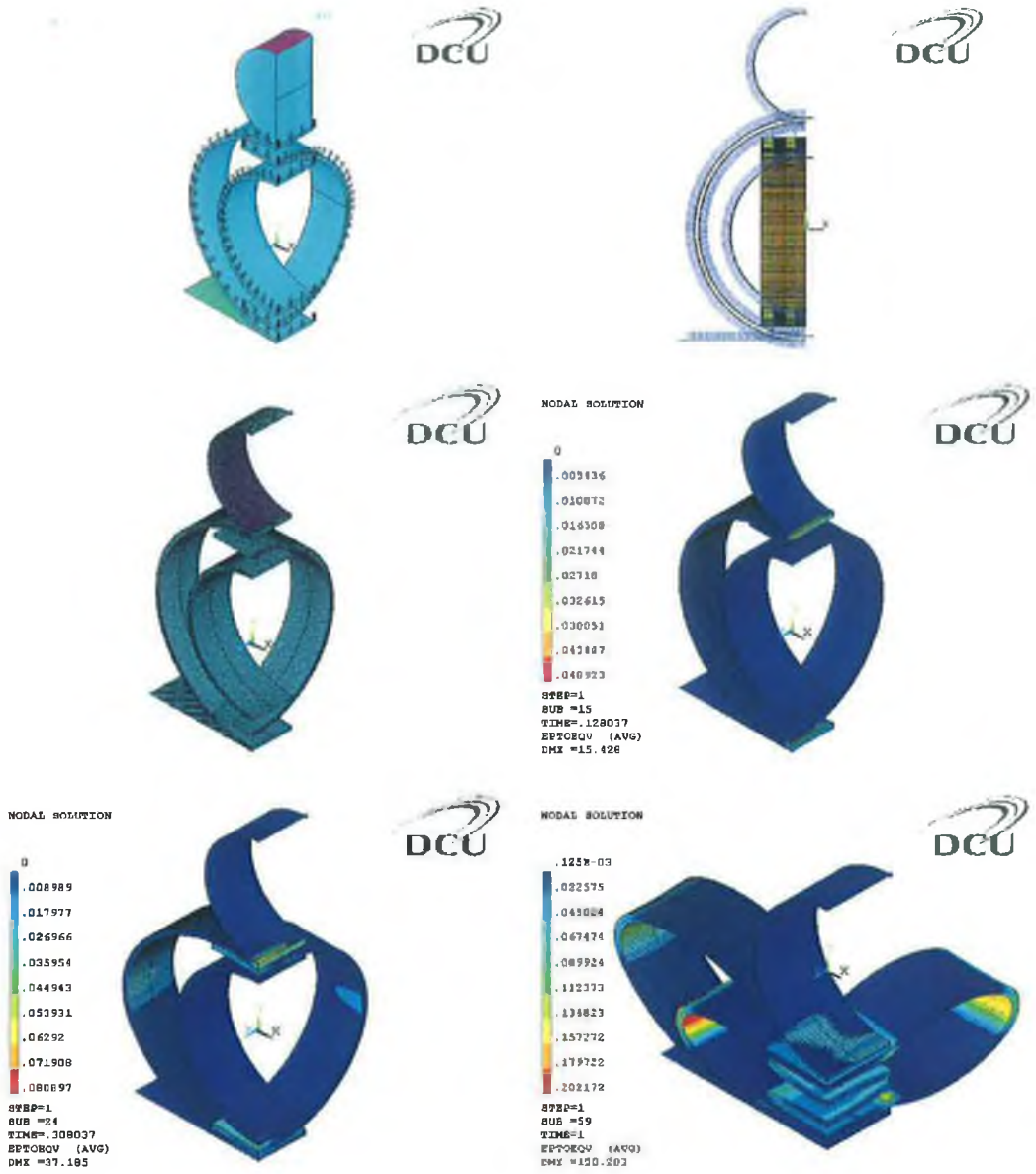

(a)

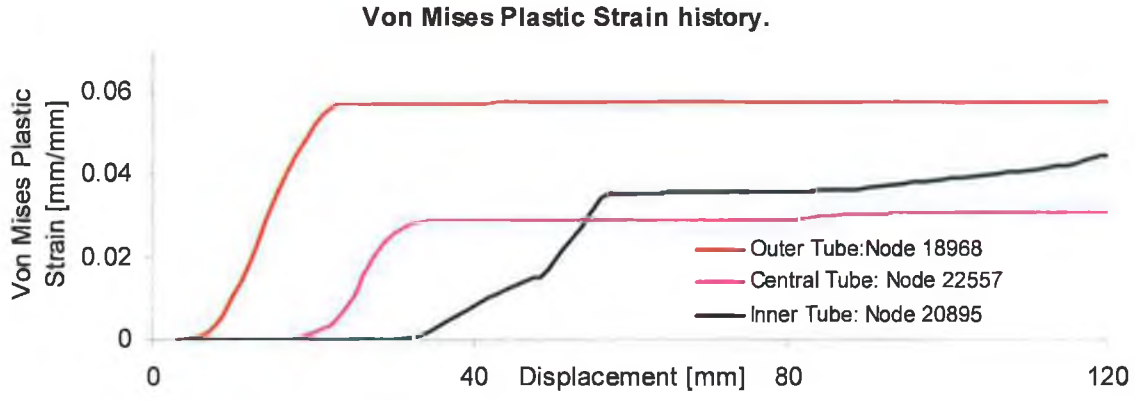

(b)

Figure 7-19: **(a) Illustration of the boundary and contact definitions with a Von Mises total strain spatial plot for a COPSS.**
(b). Plastic strain history at three selected nodes for a COPSS crushed under a cylindrical indenter.

7.6.5 A SCIPSS Crushed under a Plate Indenter.

It can be seen in Figure 7-20 that the numerical response correlated very well with that of experiment, with only a slight under-prediction in the collapse load of each tube and an over-prediction in the final stages of deformation. The resulting difference in the energy absorbed between the numerical code and that of experiment was approximately 3%. Figure 7-21a illustrates the symmetry boundary conditions applied to the model along with the contacts pairs defined in order to capture the changing contact status. Figure 7-21b depicts a force-time graph illustrating the solution history of the numerical model during the compression process. Bisection is a feature used by the ANSYS program to recover from convergence failure due to the number of equilibrium iterations being exceeded during solution. This bisection function cuts the prescribed time step in half and automatically recovers from the last converged substep until convergence is achieved before progressing onto the next substep. The graph indicates the number of bisections which occurred during the compression stroke. It can be seen that bisection of the allocated time step inevitably occurs when contact was established between the tubes at the two stages of deflection.

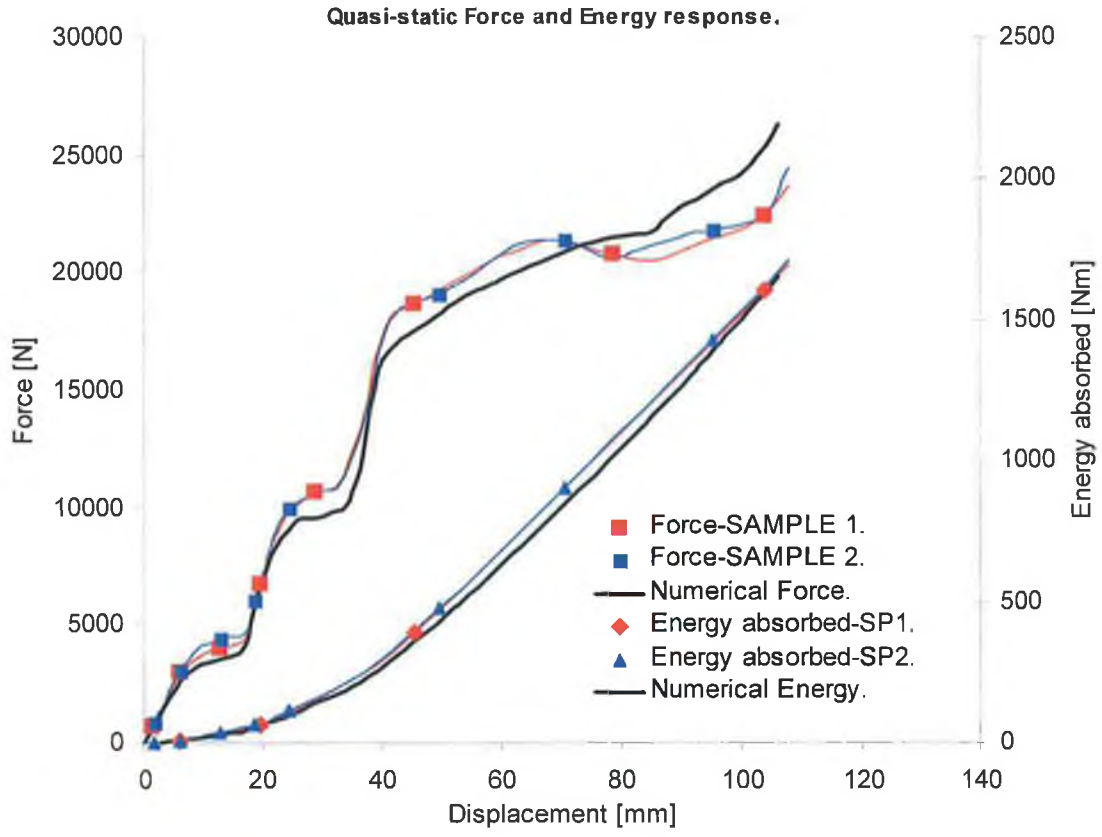

Figure 7-20: Force- and energy-deflection response for a SCIPSS compressed under a flat plate.

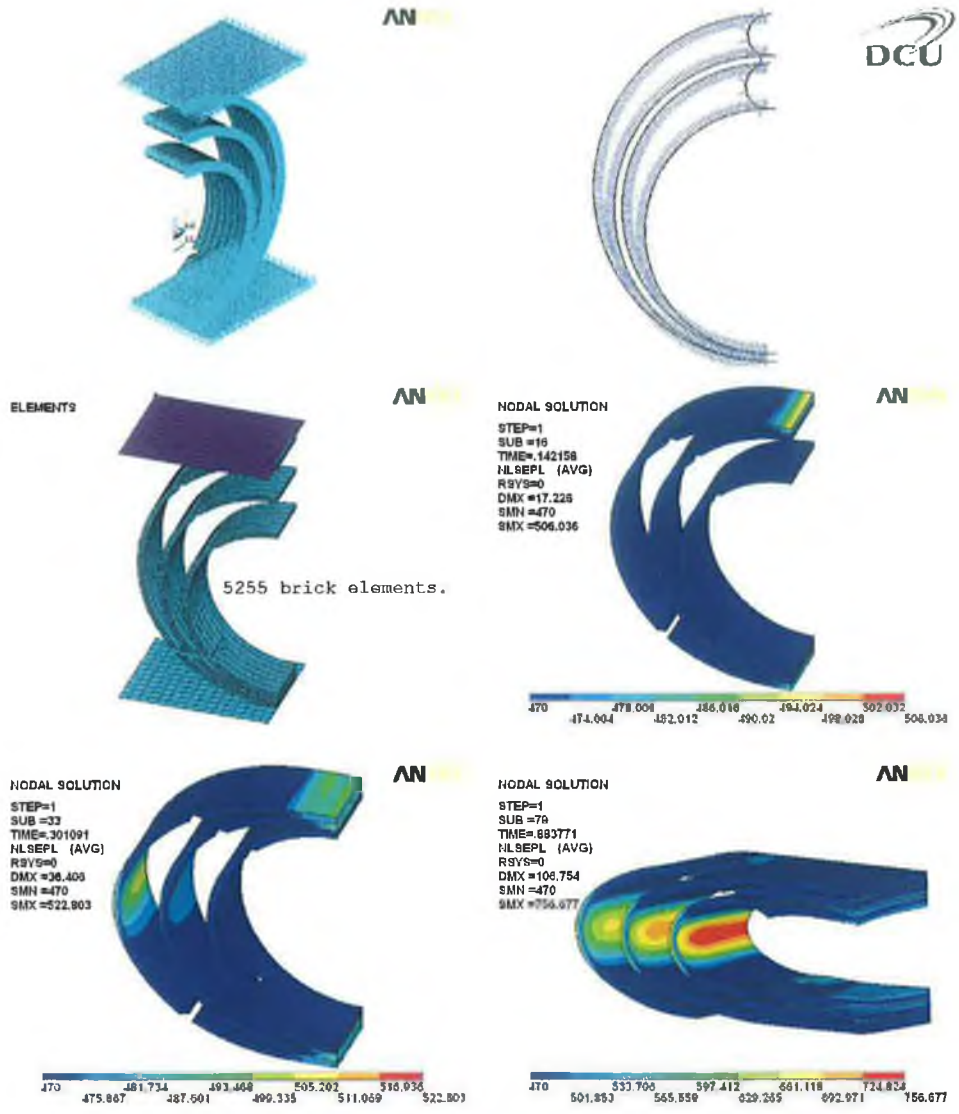

(a)

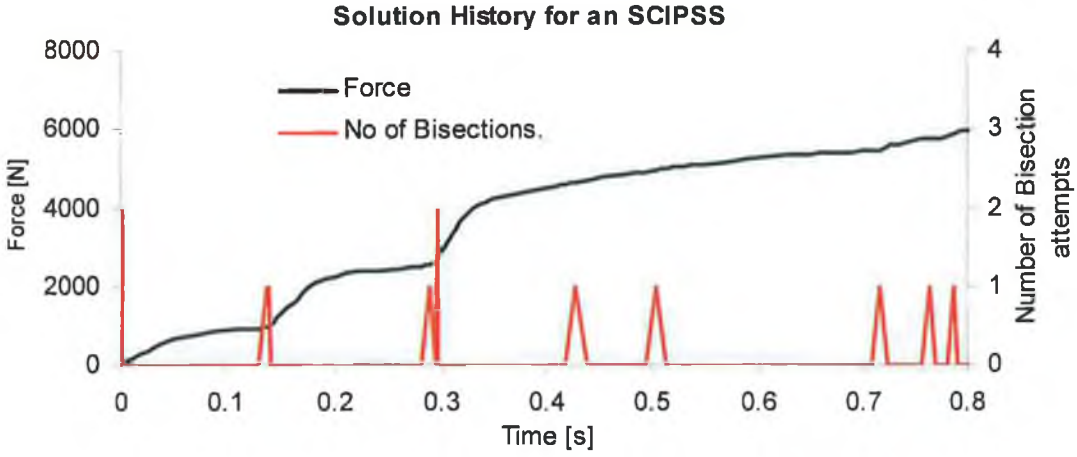

Figure 7-21: **(a) Illustration of the boundary and contact definitions with an equivalent stress spatial plot for a SCIPSS.**
(b) Force-time response illustrating the number of bisections that occurred in order to achieve convergence.

7.6.6 A SCOPSS Crushed under a Plate Indenter.

Figure 7-22 presents a comparison of the numerical and experimental response of a SCOPSS compress under a flat rigid plate. The numerical code predicted the force-deflection response very well for up to a displacement stroke of approximately 60mm. From therein, no strain softening occurred, instead, the force remained constant for a period of time before it began to increase again. During the early stages of compression, the maximum strains where located in the vicinity of the slots, however, as loading proceeded, the large strains spread over a larger plastic zone with the highest strains located at the four quadrant points of each tube. This was due to the increased bending which becomes concentrated in this region. This resulted in the observed rise in force for the remaining displacement stroke. It can be seen that there are variations in the mode of deformation between the three samples. The difference in the total energy absorbed between the three samples and that predicted by the numerical code ranges from 4% to 14%. Figure 7-23b presents the solution history for this system. It can be seen that bisection occurred at a number of stages throughout the displacement stroke.

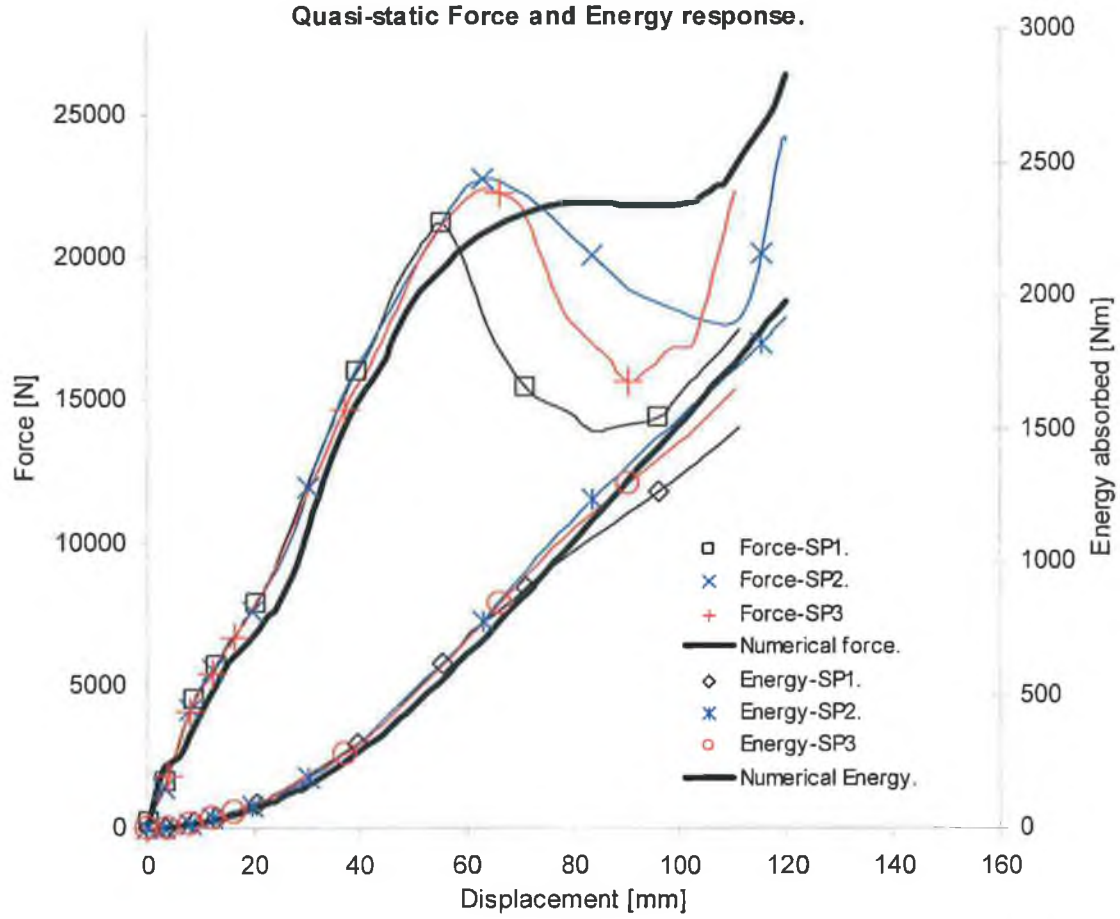

Figure 7-22: Force- and energy-deflection response for a SCOPSS compressed under a flat plate.

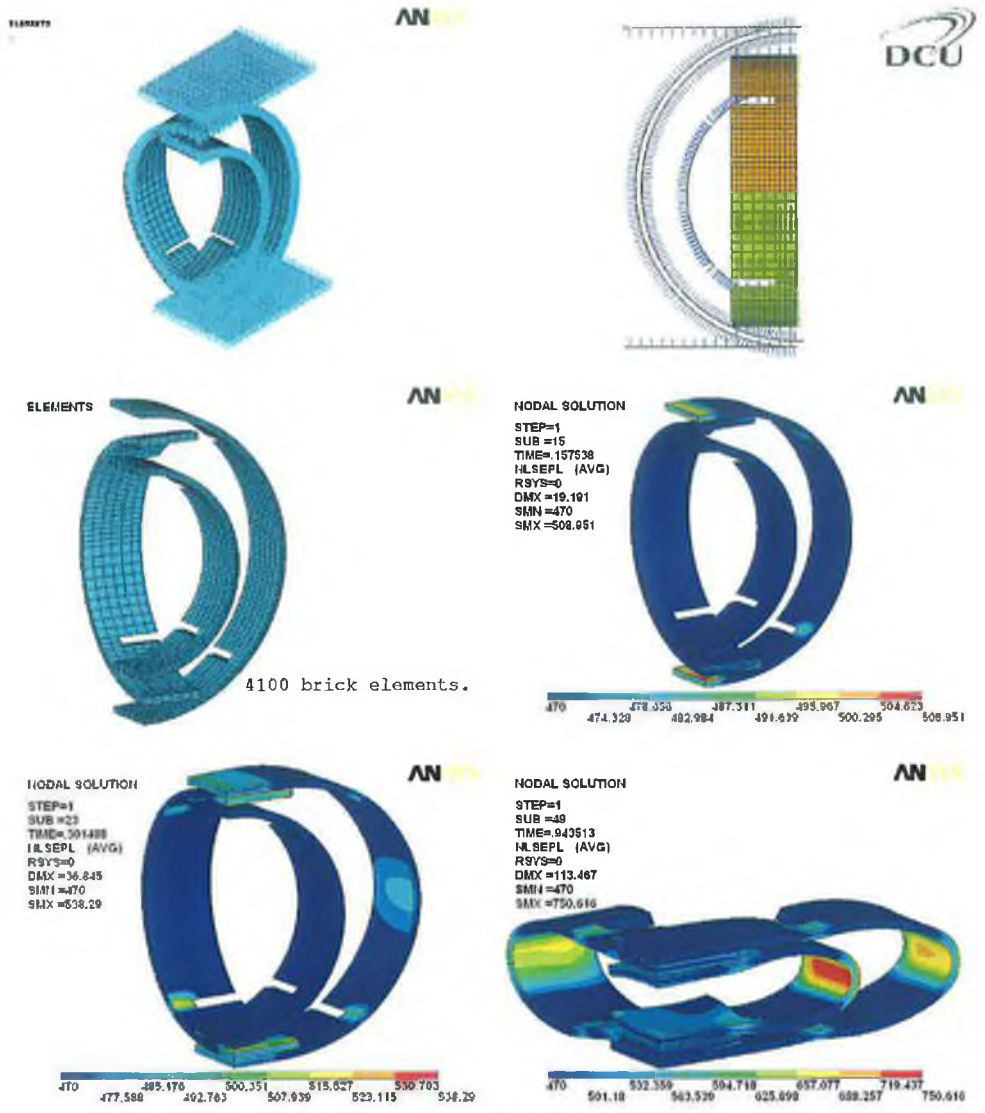

(a)

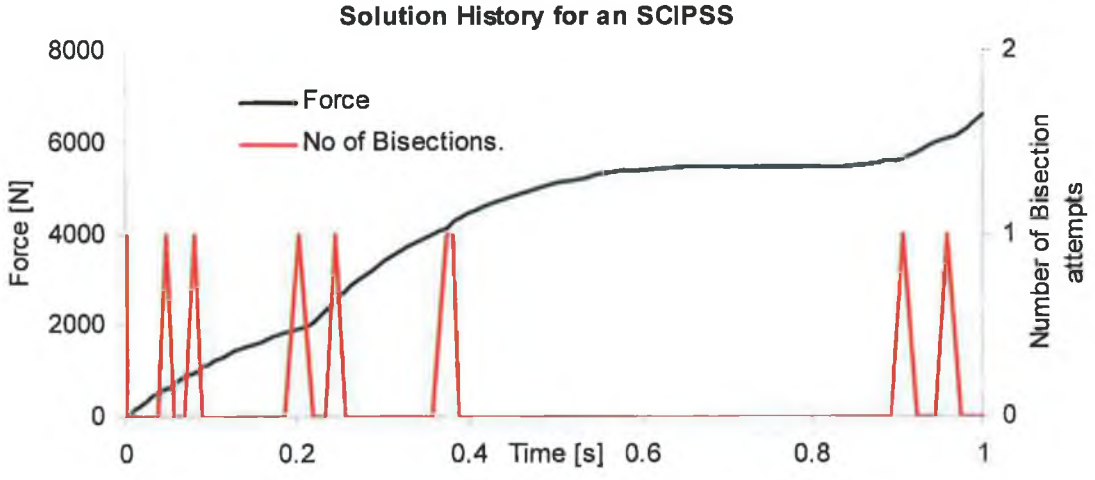

(b)

Figure 7-23: **(a) Illustration of the boundary and contact definitions with an equivalent stress spatial plot for a SCOPSS.**
(b) Force-time response illustrating the number of bisections that occurred in order to achieve convergence.

7.6.7 A SCIPDS Crushed under a Plate Indenter.

As shown in Figure 7-24, it can be seen that there was an excellent correlation between that of experiment and the numerical code in predicting a large part of the force-deflection response of this particular system. In the later stages of deflection, sample one appeared to behave inconsistently in that the force tends to rise whilst sample two tends to drop in force. The resulting difference between the two methods for the amount of energy absorbed was 7% for sample one and 5% for sample two. Figure 7-25 depicts the boundary conditions applied to the one quarter model in addition to the contact pairs used to capture the contact status during the deformation process. Also shown in this figure, is the equivalent stress represented as a spatial plot for the complete deformation process.

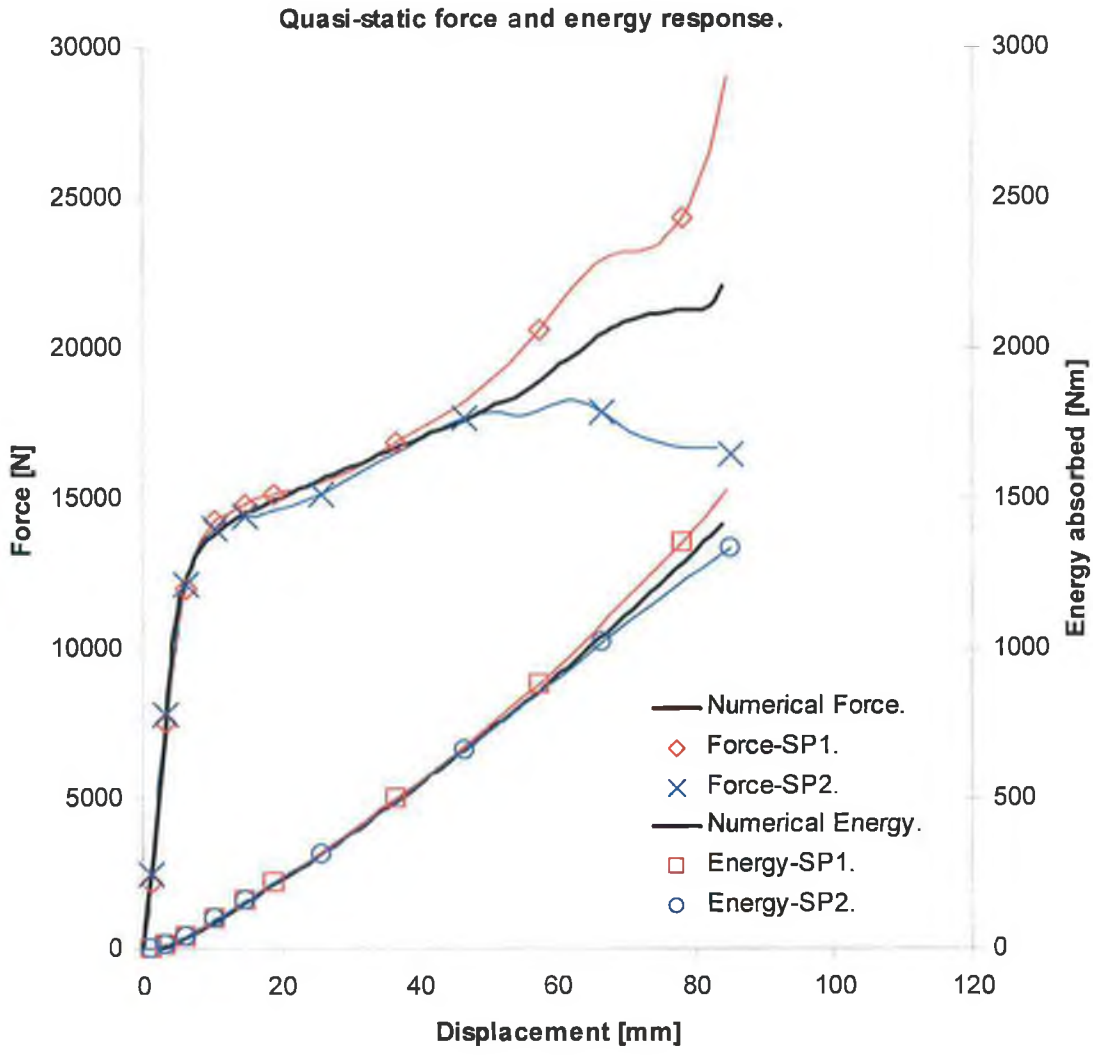

Figure 7-24: Force- and energy-deflection response for a SCIPDS compressed under a flat plate.

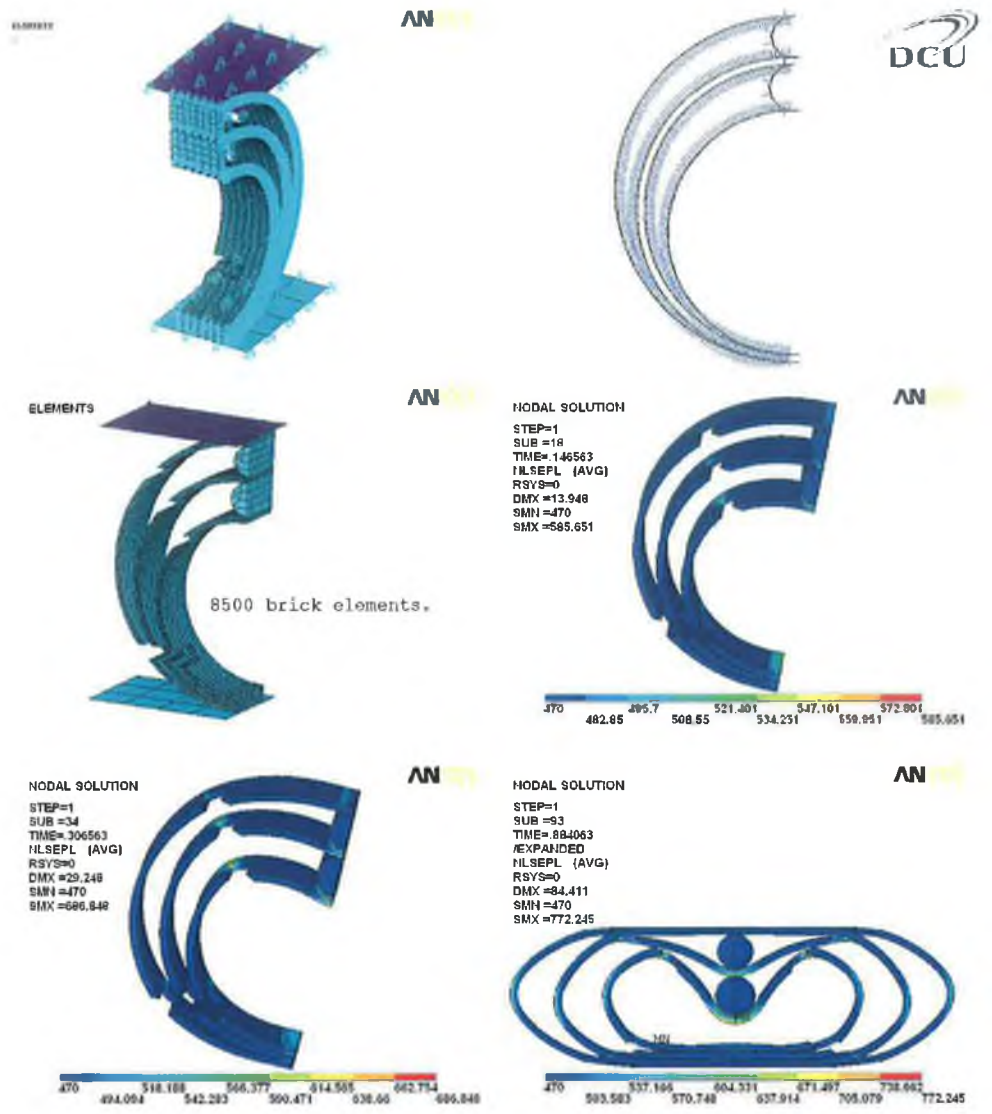

Figure 7-25: **Illustration of the boundary and contact definitions with an equivalent stress plot for a SCIPDS.**

7.6.8 A SCIPDS Crushed under a Cylindrical Indenter.

Figure 7-26 illustrates a global comparison of the numerical results for the various forms of energy absorbers analysed. As previously observed in the preceding paragraphs, there was reasonably good correlation between the numerical and experimental methods for the various systems analysed. Therefore, in view of this, another SCIPDS was developed numerically and its force-deflection response was obtained as shown in Figure 7-26. This system was crushed under the action of a cylindrical indenter, the displacement plots of which are shown in shown in Figure 7-27. This system provided a further desirable force-deflection response than its counterpart crushed under a plate indenter, since less strain hardening occurred and the force was approximately rectangular which is ideal in the design of energy absorbing devices.

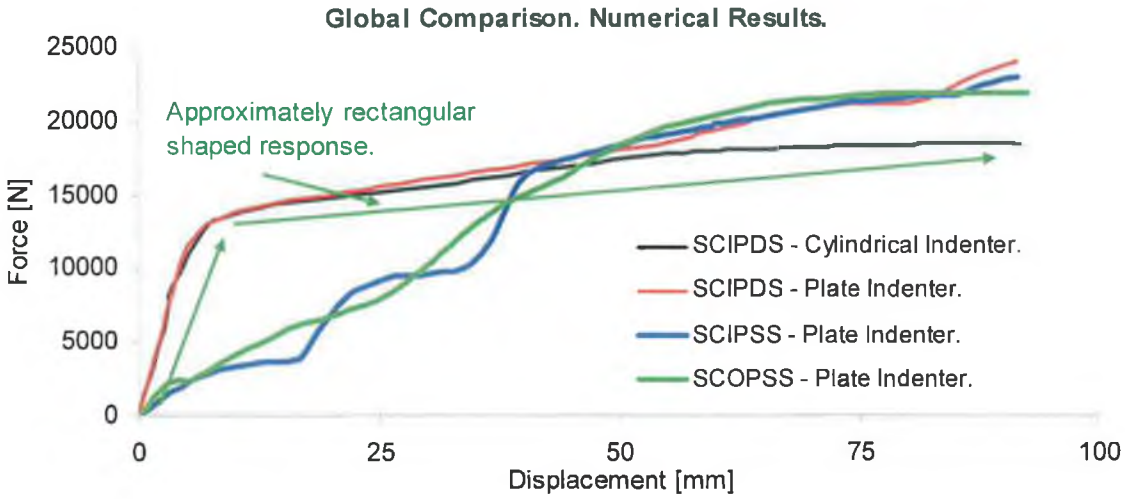

Figure 7-26: Global comparison of the various energy absorbers analysed.

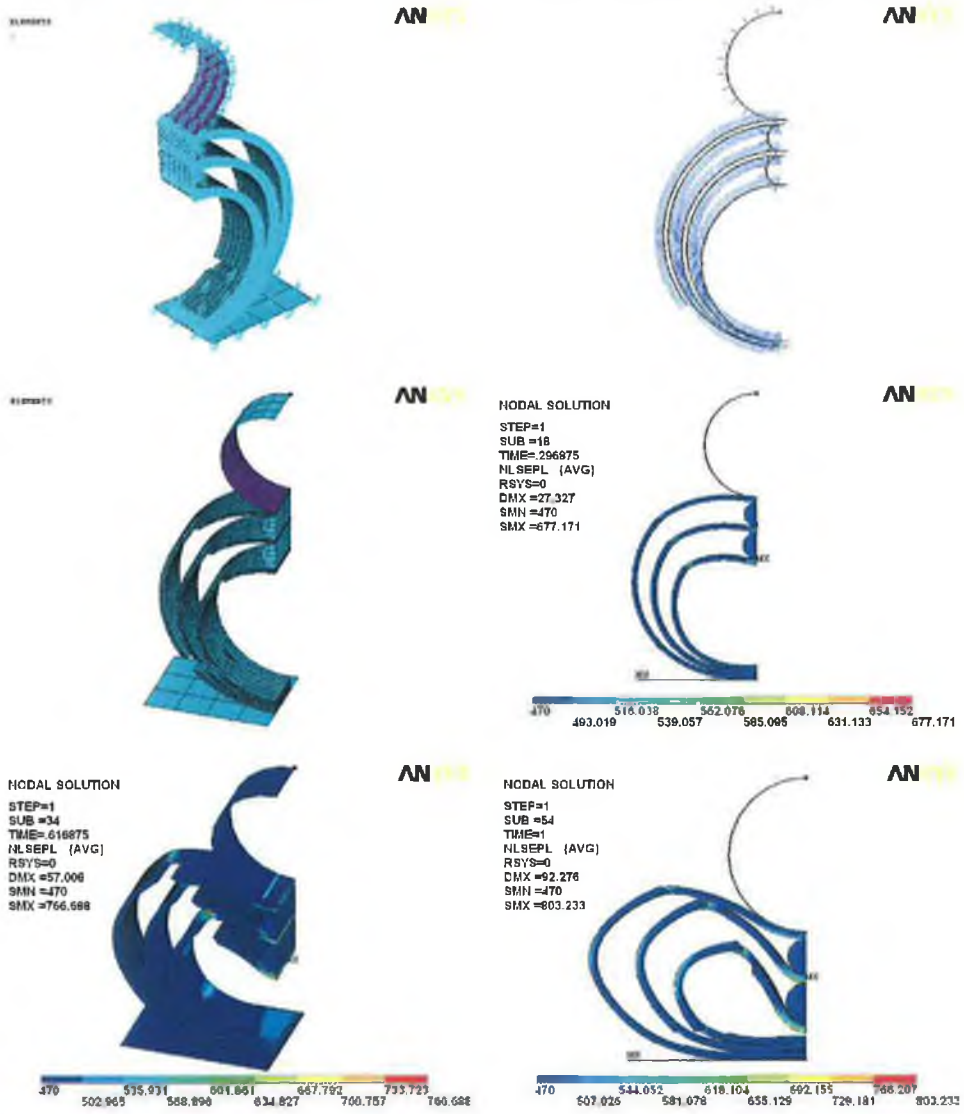

Figure 7-27: **Illustration of the boundary and contact definitions with an equivalent stress plot for a SCIPDS crushed under a cylindrical indenter.**

7.7 Quasi-Static Analysis of the CIPSS, CIPDS, OIPSS and the OIPDS.

7.7.1 Analysis of the CIPSS.

The numerical and experimental force- and energy-deflection response of a CIPSS is shown in Figure 7-28. A slight under prediction of the collapse load was observed for each of the three tubes followed by a slight over estimation from approximately 70mm of displacement. In terms of the energy absorption response, a difference of 3% was observed between the two methods. Figure 7-29 depicts the solution history for this particular system, it can be seen that bisection of the time step occurred twice as each tube established contact during the compression process. Also, in the final stages of compression, a single bisection occurred frequently due to the rapid rise in force. This may be due to the high strain that occurs at the hinges points due to the intense bending of each tube in the later stages of deflection.

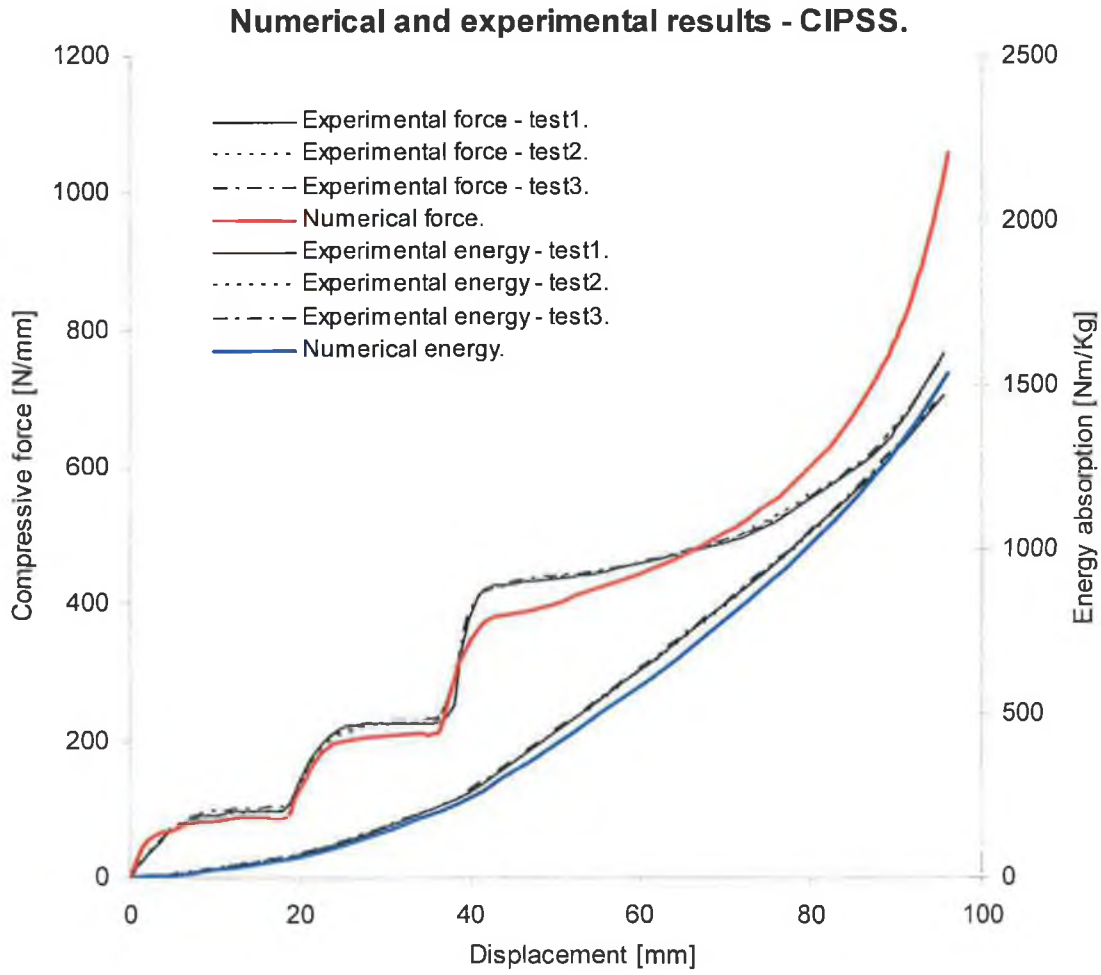

Figure 7-28: Experimental and numerical comparison of a CIPSS crushed under a flat plate indenter.

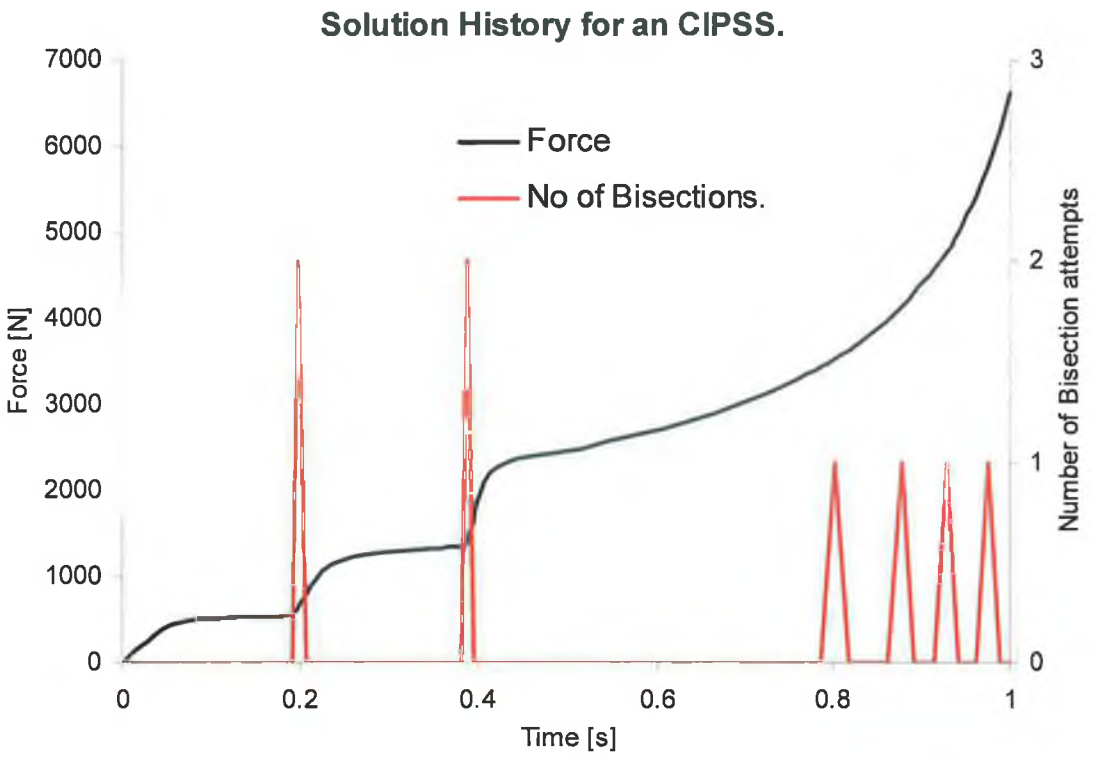

Figure 7-29: Force-time graph illustrating the bisection history for a CIPSS.

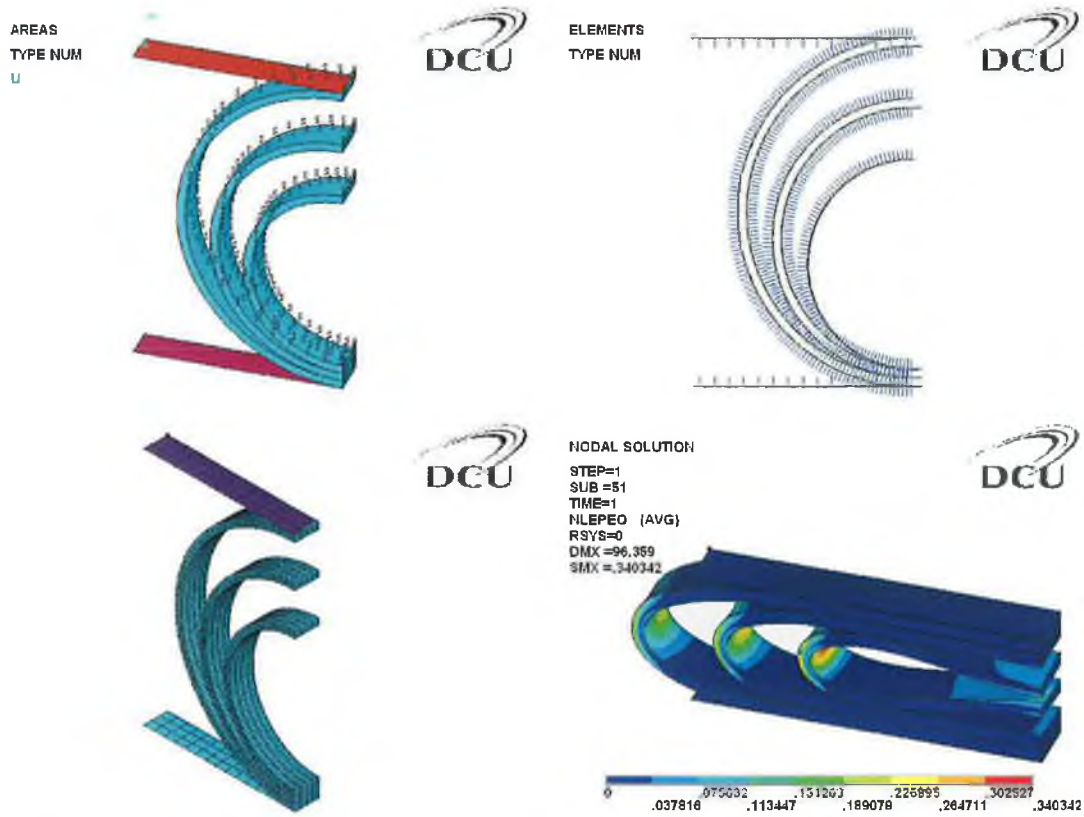

Figure 7-30: Illustration of the boundary and contact definitions with an equivalent plastic strain spatial plot for a CIPSS crushed under a plate indenter.

7.7.2 Analysis of the CIPDS.

The numerical response of a CIPDS is illustrated in Figure 7-31 with graphical plots displayed in Figure 7-33. Again, it can be seen that a slight under prediction occurs at the collapse stage of compression for each tube with an over prediction observed during the latter stages of compression. A linear strain hardening response by the numerical method was observed for the remainder of the displacement stroke. For the energy response, a difference of less than 1% was observed between the two methods. Figure 7-32 depicts the solution history for this system, only a single bisection occurred at the collapse stage of this system during the compression process indicating an easily converged solution. Figure 7-33 illustrates the symmetry conditions applied to the model along with the contact pairs defined to capture the contact behaviour of the system.

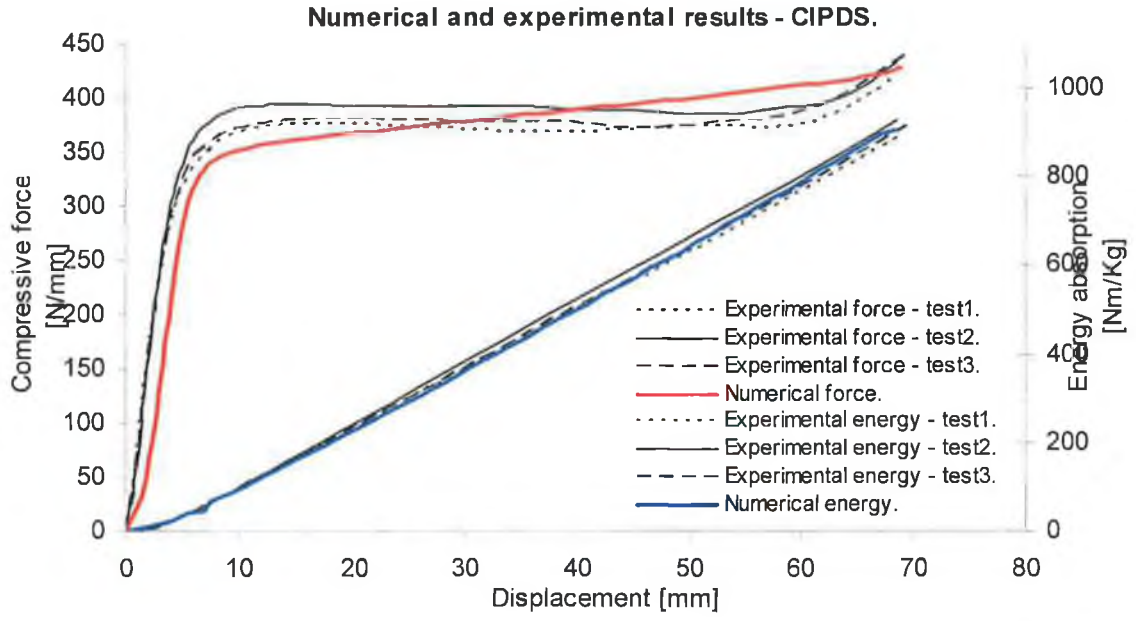

Figure 7-31: Experimental and numerical comparison of the CIPDS crushed under a flat plate indenter.

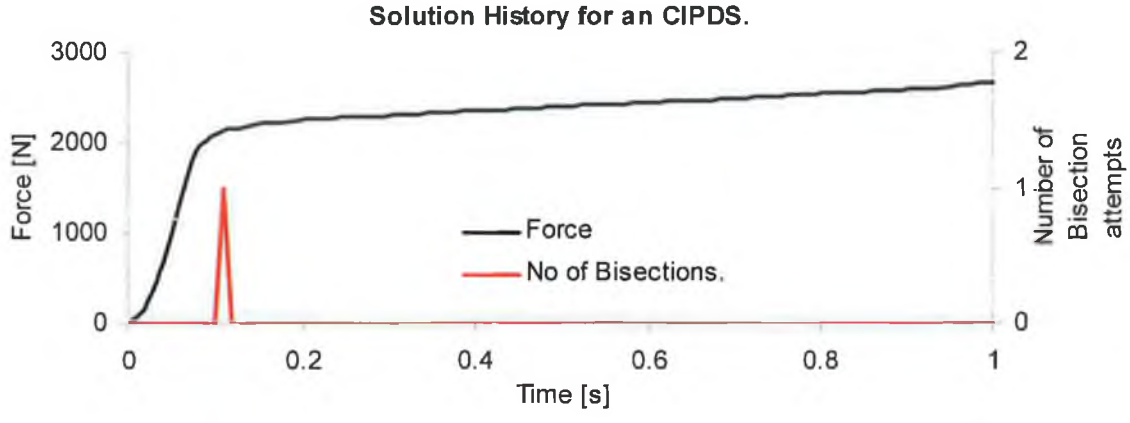

Figure 7-32: Force-time graph illustrating the bisection history for a CIPDS.

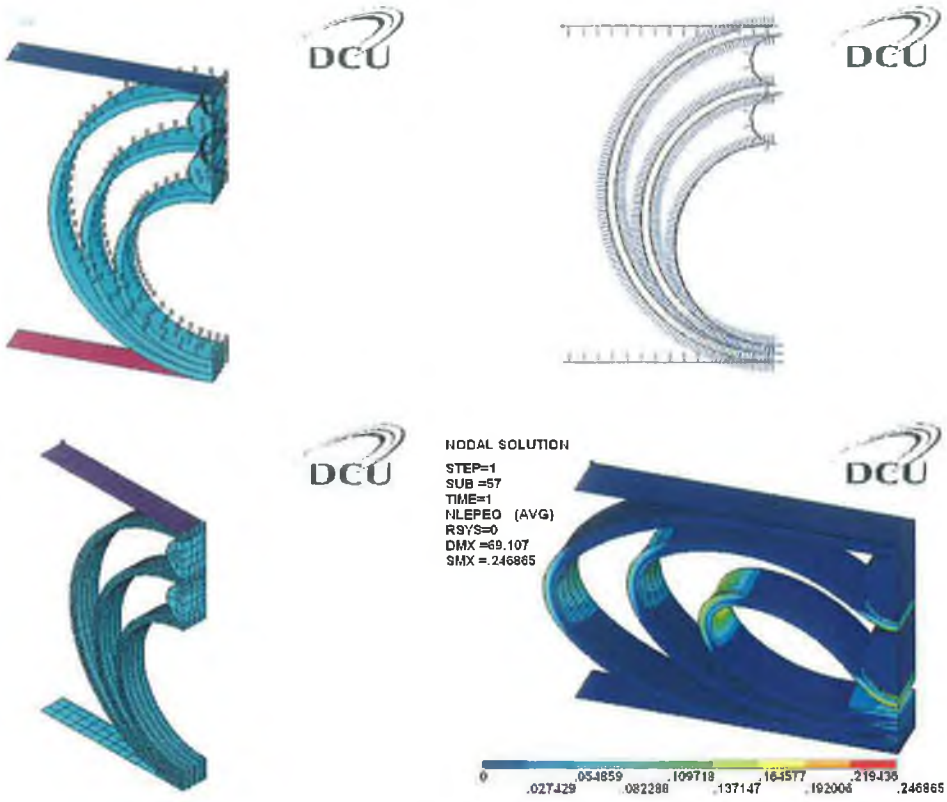

Figure 7-33: **Illustration of the boundary and contact definitions with an equivalent plastic strain spatial plot for a CIPDS crushed under a plate indenter.**

7.7.3 Analysis of the OIPSS.

Figure 7-34 and Figure 7-35 depicts the numerical response for an OIPSS using both the compression and tension method respectively. Upon examination of the OIPSS constructed using the former method, the collapse load was over predicted by the numerical code for the complete displacement stroke. For the OIPSS created using the tension method, an even greater over estimation was observed for the collapse load of each tube. For this particular absorber, from approximately 65mm displacement, a good correlation was seen between the actual and numerical response in predicting the geometrical softening process. For the OIPSS created using the tension method, a difference of 8% was found and a difference of 15% for the OIPSS generated using the compression method. Figure 7-36 depicts the bisection history for this particular system. It can be seen that there was some difficulty in the numerical code achieving convergence during the collapse stage of each tube. Three bisections occurred twice during contact stage between the respective tubes. Figure 7-37 illustrates the symmetry conditions applied to the model along with the contact pairs defined to capture the contact behaviour of the system.

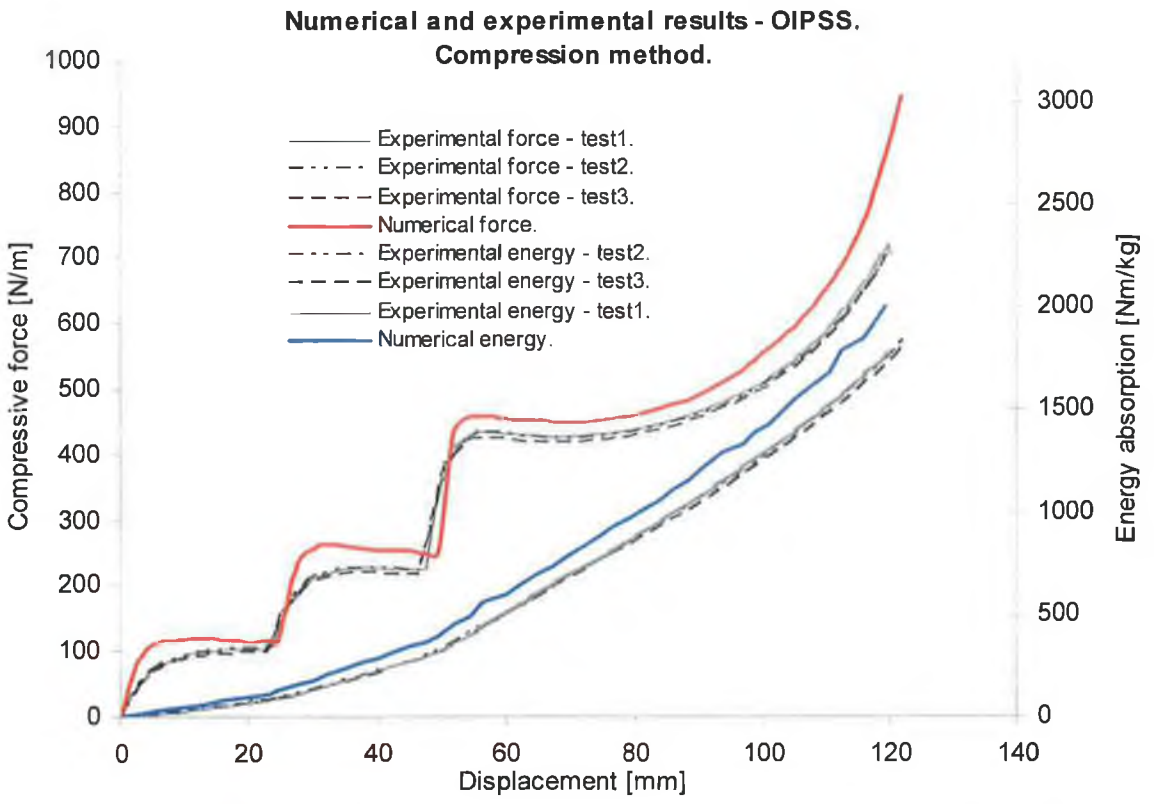

Figure 7-34: Experimental and numerical comparison of the OIPSS. [Compression method]

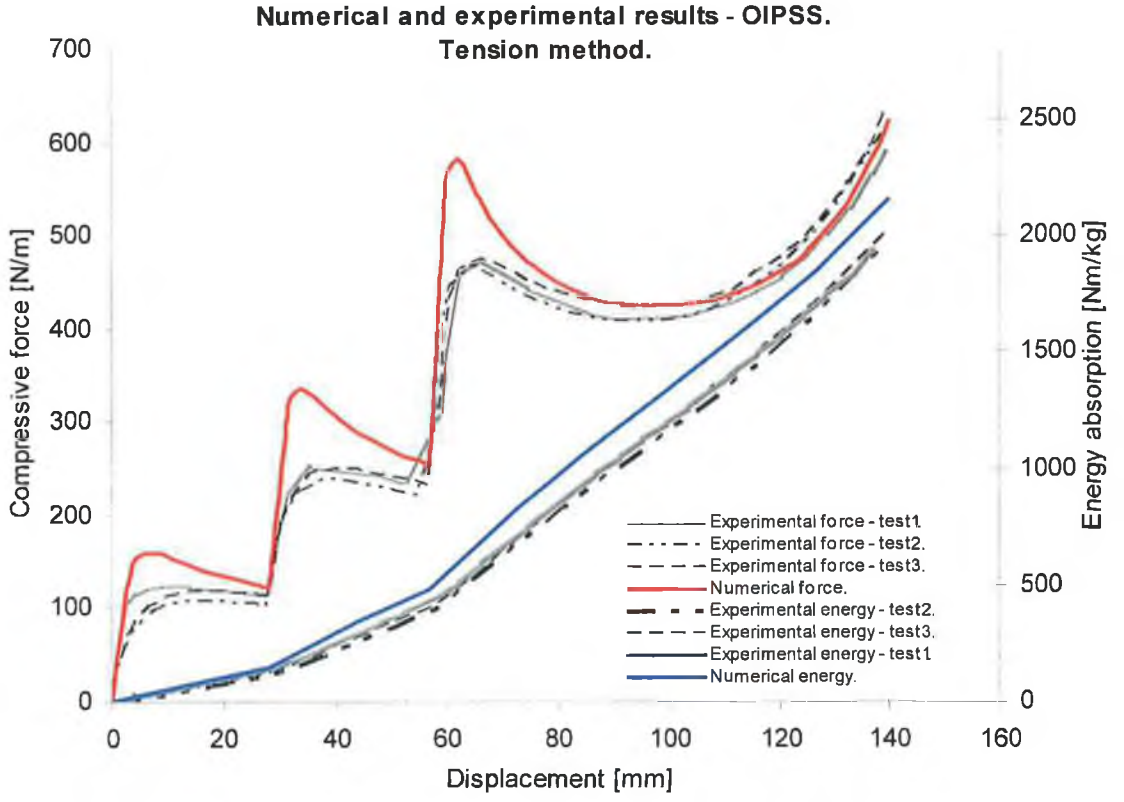

Figure 7-35: Experimental and numerical comparison of the OIPSS. [Tension method]

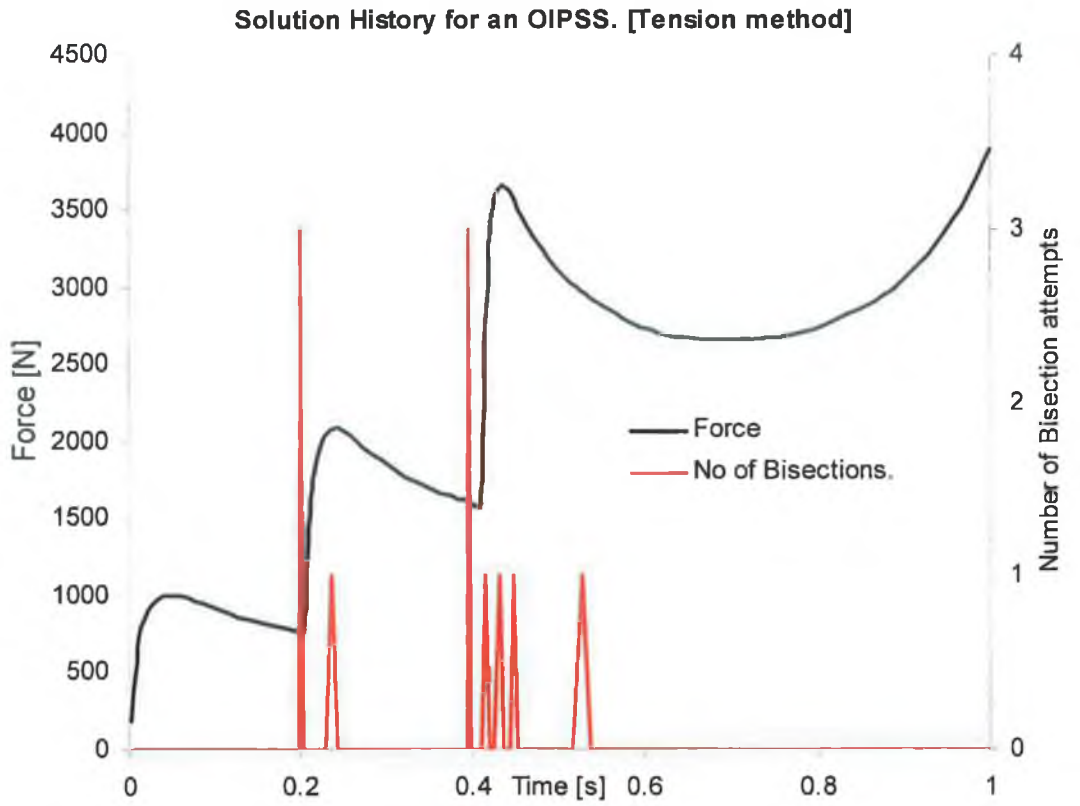

Figure 7-36: Force-time graph depicting the bisection history of the OIPSS. [Tension Method]

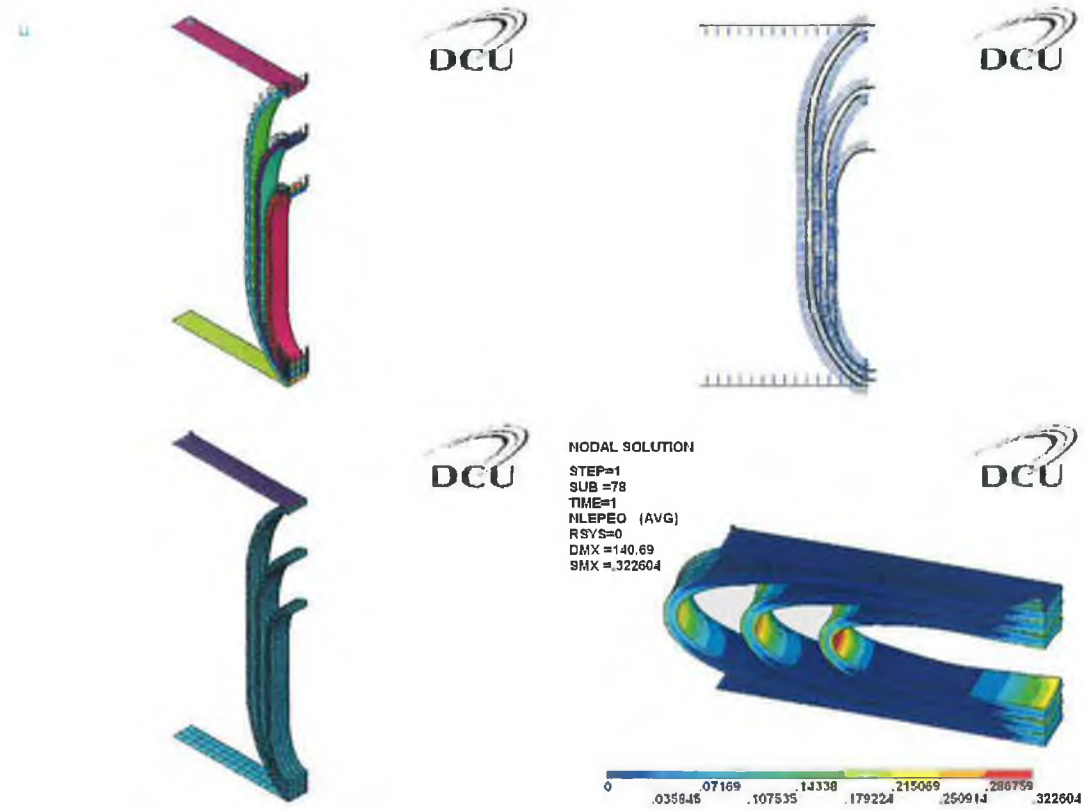

Figure 7-37: **Illustration of the boundary and contact definitions with an equivalent plastic strain spatial plot for a OIPSS crushed under a plate indenter.**

7.7.4 Analysis of the OIPDS.

Figure 7-38 depicts the numerical and experimental comparison of an OIPDS subjected to lateral crushing. As in the previous two systems analysed, an over prediction in force in the collapse stage of compression was noticed. From therein, a geometrical softening characteristic was observed for the remainder of the displacement. In terms of energy absorption response, a difference of 10% was observed between the numerical and experimental methods. The bisection history of this system is displayed in Figure 7-39; it can be that there was some difficulty in achieving convergence in this model during the collapse stage of compression in which a total of four bisections occurred followed by two bisections in the latter stages of compression. Figure 7-40 illustrates the symmetry conditions applied to the model along with the contact pairs defined to capture the contact behaviour of the system.

The reason for the over-prediction observed in the oblong tube energy absorbers appears to stem from the difficulty of the numerical code to accurately capture the behaviour of the hinge points (collapse points) in order for the tubes to collapse plastically. By examining the initial stages of displacement in Figure 7-40, one could visualise each tube within this oblong shaped absorber to consist of two arcs at the top and bottom joined together by two separate columns. In doing so there is the possibility that the numerical code predicts the plastic collapse hinges to occur elsewhere, possibly in the regions of point A , B and C (See the illustration in Figure 7-40) due to the fact that the central portion of the tube is acting like a column.

This 'column effect' is known experimentally to strengthen the load capacity of an elliptical tube due to its stiffness when compressed between rigid platens [**76**].Therefore, in view of this, when this energy absorber was subjected to a compressive force, a rapid increase in force was observed due to this 'column effect'. There remains the possibly of the explicit code's difficulty in predicting where the plastic hinge zone in each column should occur at the appropriate stage of deflection. By examining Figure 7-38, it can be seen that once the collapse load was reached, the force dropped rapidly to a more reasonable level of force magnitude indicating a more accurate correlation by the numerical code with that of experiments.

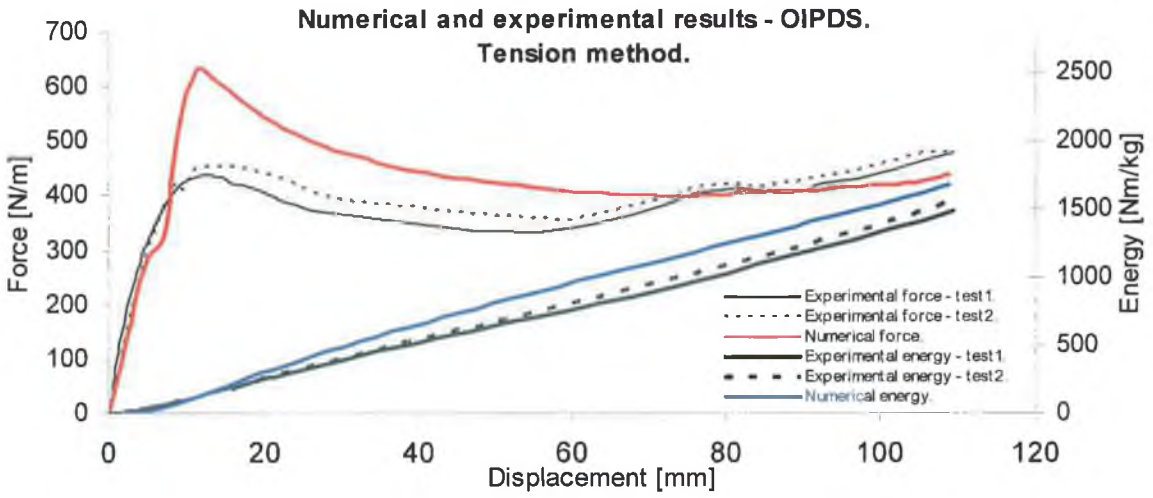

Figure 7-38: Experimental and numerical comparison of the OIPDS. [Tension method]

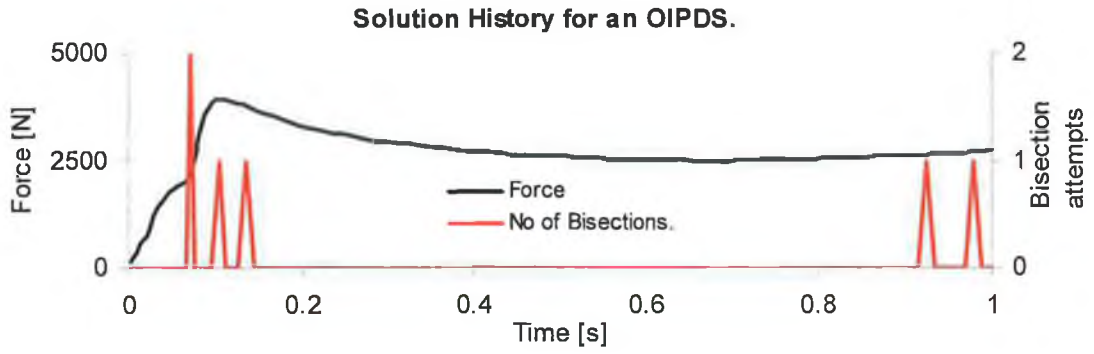

Figure 7-39: Force-time graph depicting the bisection history of the EIPDS.

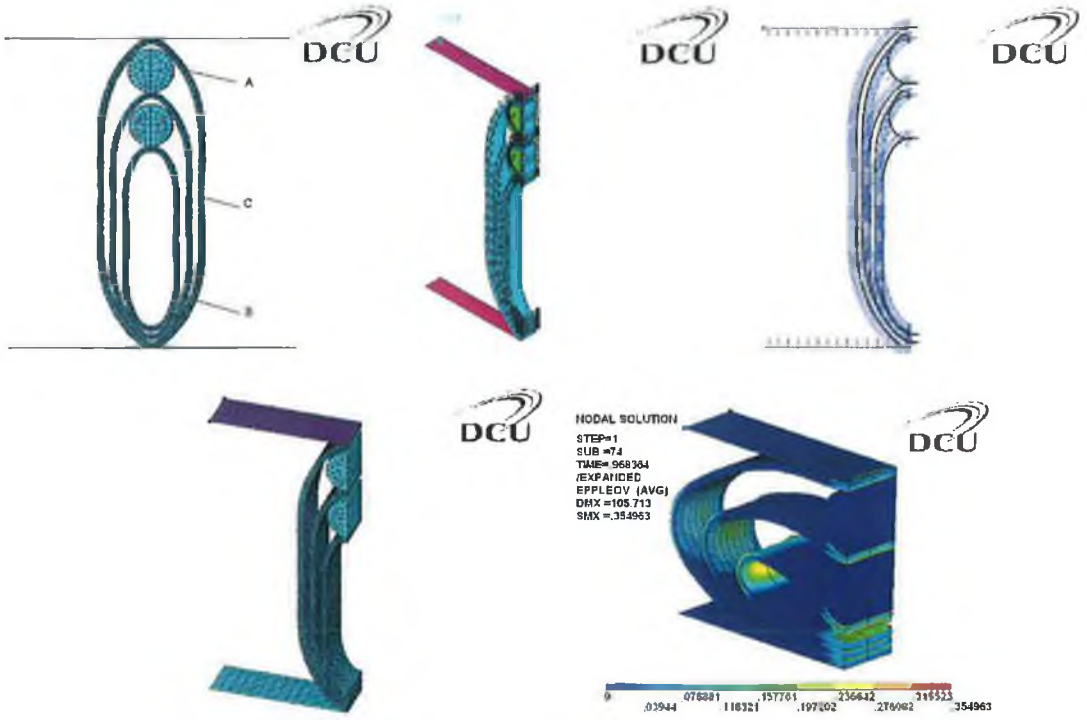

Figure 7-40: Initial and final stages of displacement of an OIPDS as produced by ANSYS.

7.8 Dynamic Analysis of the IPSS and IPDS Energy Absorbers.

7.8.1 Evaluation of the CIPSS.

Figure 7-41 and Figure 7-42 presents the force - and energy - time responses for a CIPSS simulated using the explicit numerical method and its comparison to that of experiments. Upon examination of Figure 7-41, it appears that contact between each of the respective tubes was predicted to occur at slightly different times by both the experimental and numerical methods. For example, the time of contact between the outer tube and central tubes predicted by the numerical method occurs at approximately 4ms as opposed to a shorter time of 3ms observed in experiments. For contact between the central tube and the inner tube, values of approximately 6ms and 8ms are depicted by the experimental and numerical methods, respectively. The energy time response appears to display good agreement between both methods. The evolution displacement plots extracted from the numerical method are displayed in Figure 7-45. It appears that one can be confident that the deformation mode response is in good agreement with that of experiments (Figure 5-34). The displacement - time curve shows good agreement between the two methods which is to be expected since an average velocity time curve pertinent to each absorber was applied to the striker. Figure 7-44 illustrates the numerical energy balance for this model, it can be seen that the total energy and the external work are equal, indicating the absence of any numerical modelling errors as outlined in section 3.3.4.

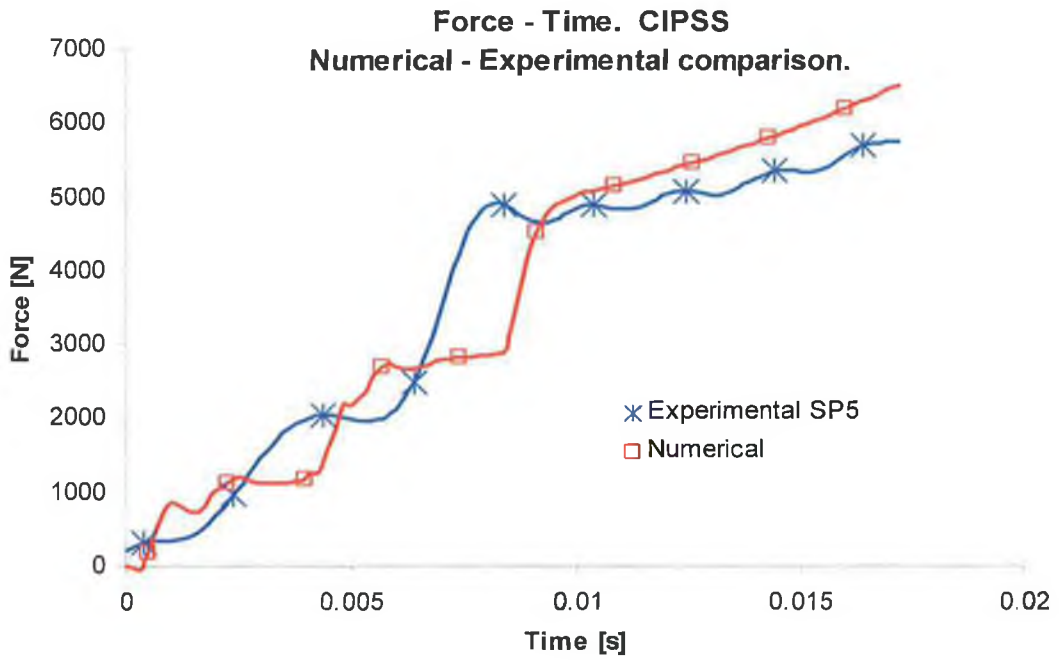

Figure 7-41: Force-time curve for a CIPSS.

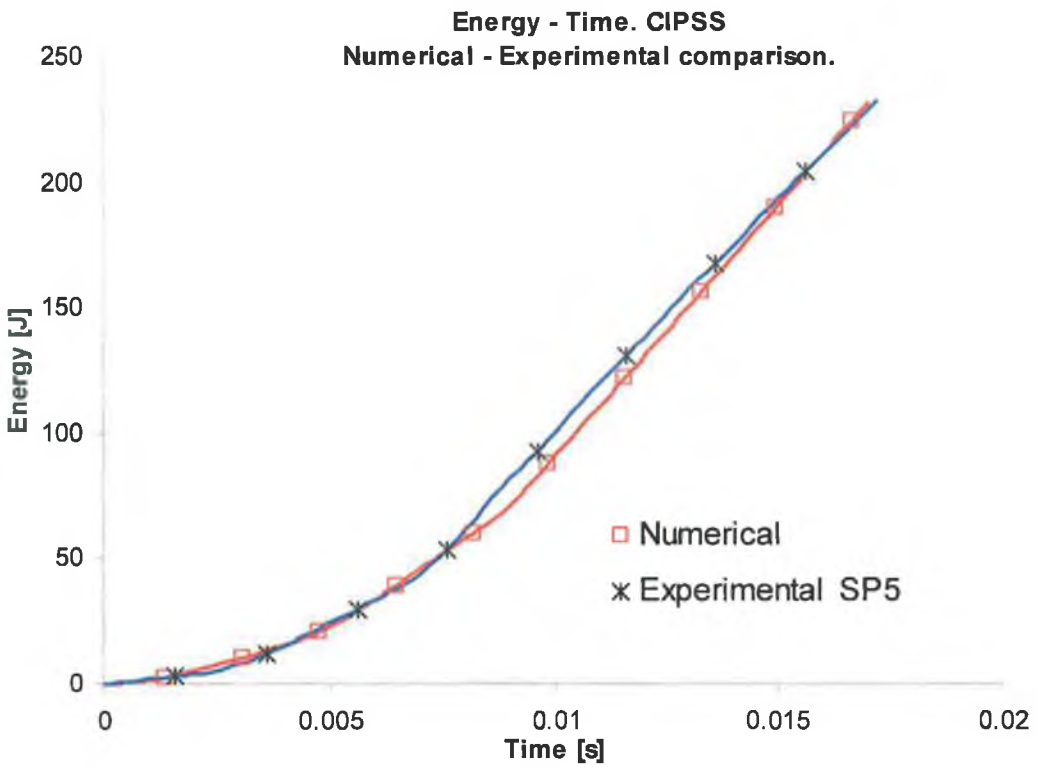

Figure 7-42: Energy-time response for a CIPSS.

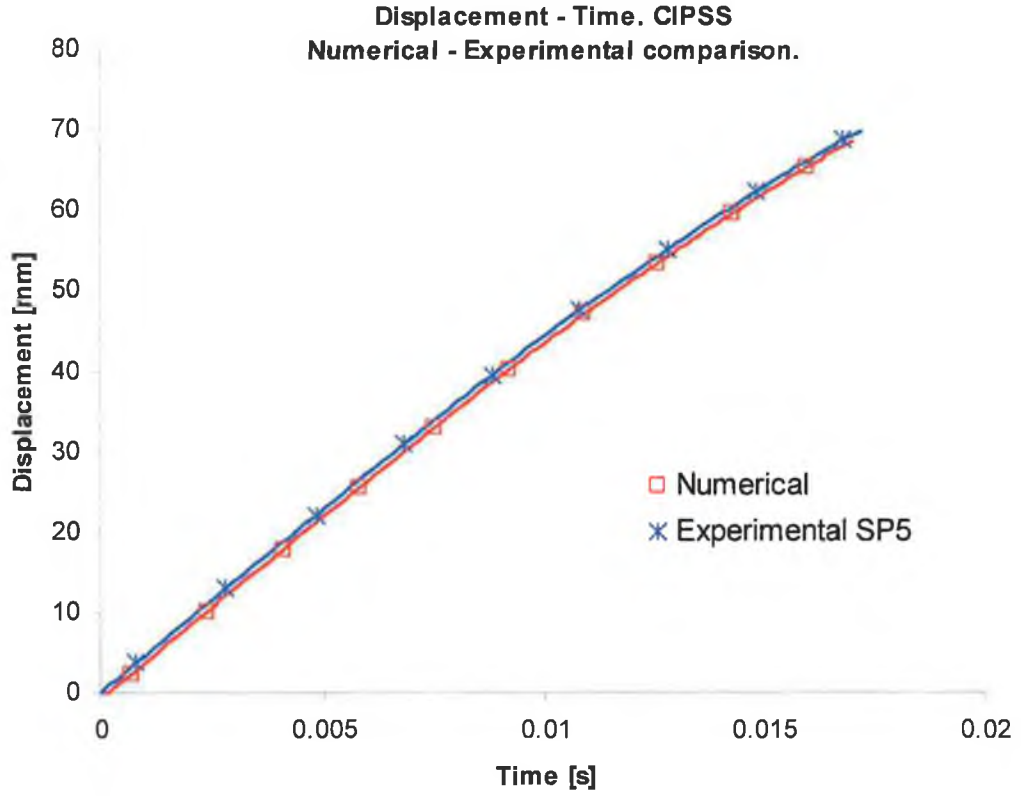

Figure 7-43: Displacement-time curve for a CIPSS.

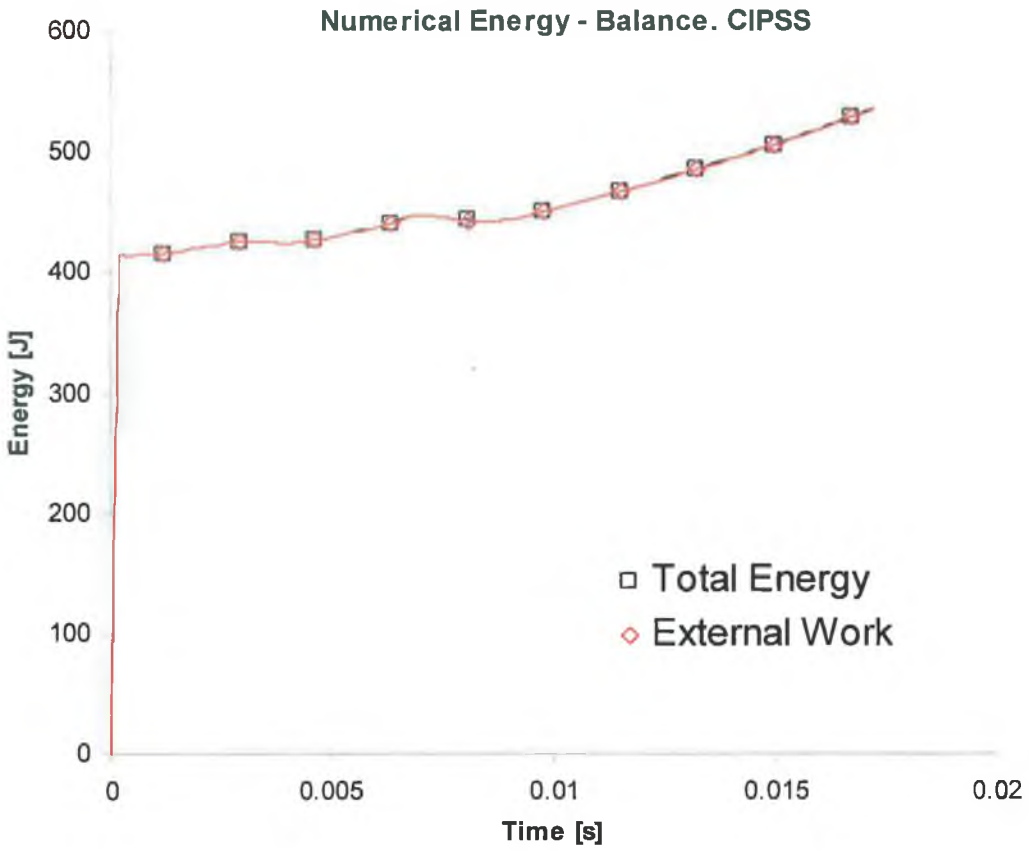

Figure 7-44: Numerical energy balance for a CIPSS.

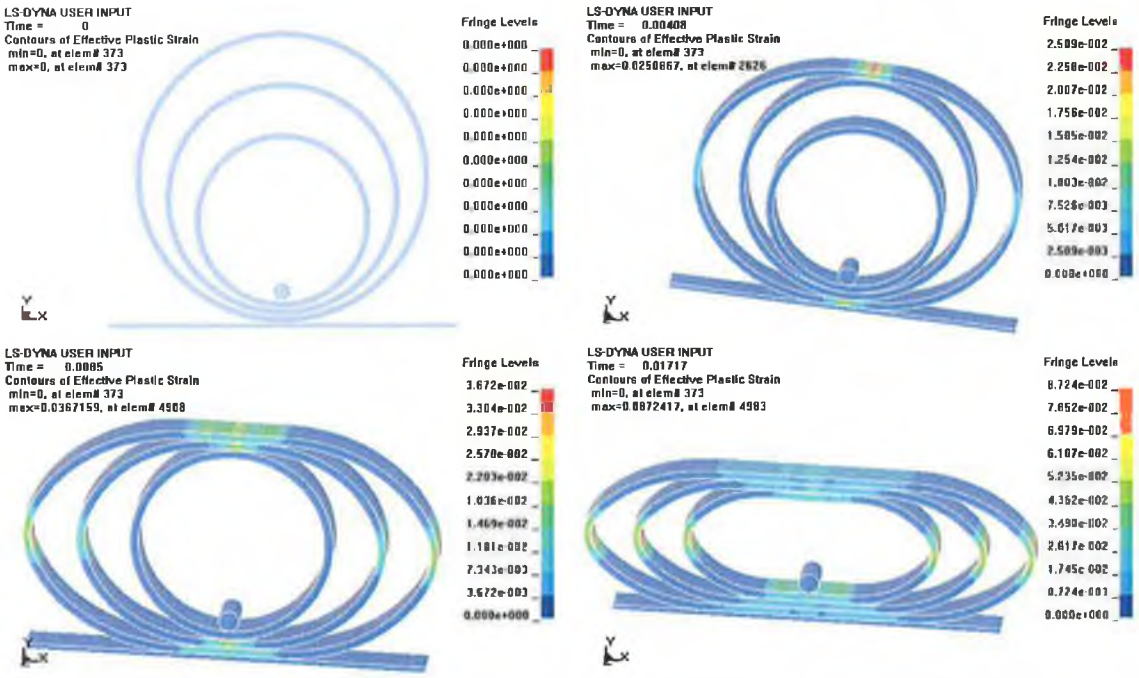

Figure 7-45: Effective plastic strain evolution of a CIPSS under dynamic lateral loading.

7.8.2 Evaluation of the CIPDS [Brick Element Model].

Figure 7-46 and Figure 7-47 depicts the force - and energy - time response of a CIPDS. There appears to be a significant over prediction in force magnitude displayed by the numerical method. A 15% over prediction in energy absorption was observed for this energy absorber. In order to assist in this explanation for discrepancy of results, Figure 7-52 was created. Upon analysis of the CIPDS from this figure, it can be seen from an experimental point of view that both the static and dynamic cases exhibit similar force deflection response in terms of magnitude. This would indicate that for the given velocity applied to the striker, that the strain rate sensitivity is not a significant factor in the deformation response of this particular system. Also, with the advantage of using the numerical model to demonstrate the effect of strain rate insensitivity by excluding the strain rate parameters, it can be seen that numerical results agree favourably with both the static and dynamic experimental cases. This would appear to signify that the values of D and q used in the Cowper-Symonds relation may not be valid in this particular application of energy absorbers since an obvious large increase in the dynamic yield stress is evident using the specified strain rate parameters. The usual constants of $40.4s^{-1}$ and 5 for D and q are normally used by researchers; however, it was found that substitution of these values into the Cowper-Symond relation yields an even larger value of yield stress than the constants of $6844s^{-1}$ and 3.91 used in the current material model. The over prediction in dynamic yield stress using the constants of $6844s^{-1}$ and 3.91 was also reported by Colokoglu and Reddy [30]. It was stated that these constants were not valid for the strain levels experienced in the work and that more appropriate values pertaining to strain levels of 10% would produce better results.

The constants of $40.4s^{-1}$ and 5 have also have been used by Harrigan et al [34] to predict the dynamic force magnitude for the internal inversion of mild steel tubes. It was found that the dynamic load conditions greatly over-predicted those that were recorded experimentally. It appears that the constants only apply to applications involving small strains (5%) and not to large strains that are encountered in the internal inversion of mild steel tubes. Large strains also exist in the lateral compression of the aforementioned tube systems. Hence, it was stated by the authors [94] that more research needs to be conducted in this area in terms of obtaining experimental data pertaining to material strain rate sensitivity of mild steel. Such experimental data needs to be collected in the form of a range of constants which represent the behaviour of mild steel at different strain rates and

strain levels. Figure 7-51 illustrates the Von Mises temporal variation of the peak response within the CIPSS and the CIPDS. A peak stress of 650MPa and 710MPa was observed for these two energy absorbers respectively from the numerical model. Figure 7-47, 7-48 and 7-49 illustrates results for the energy – time, displacement – time and numerical energy balance for this system respectively.

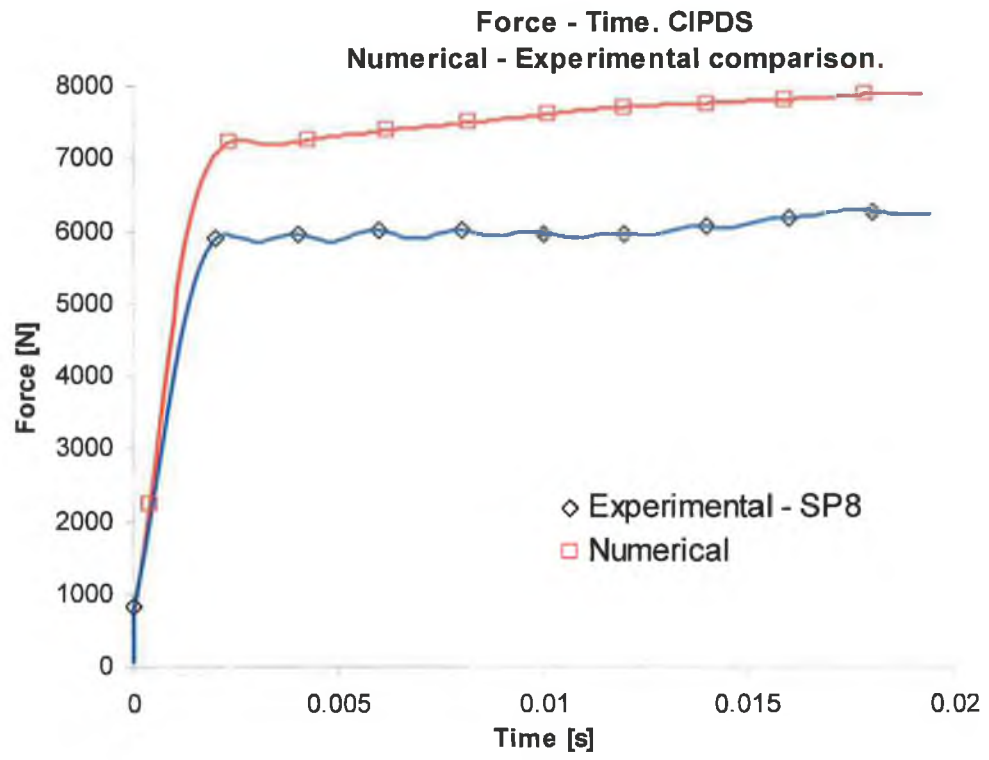

Figure 7-46: Force-time curve for a CIPDS.

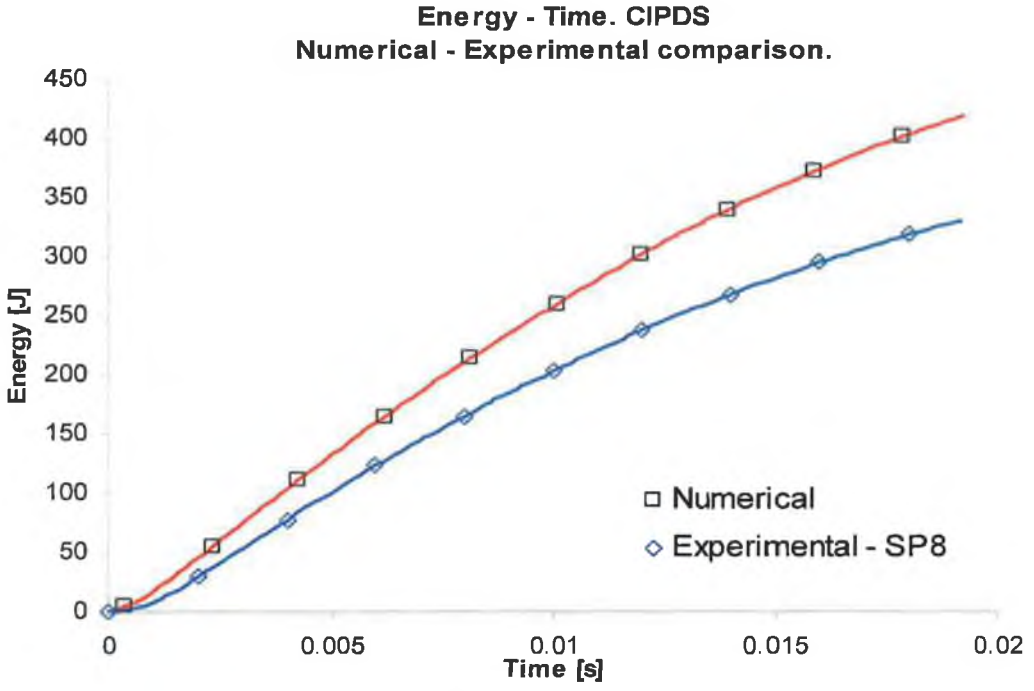

Figure 7-47: Energy-time curve for a CIPDS.

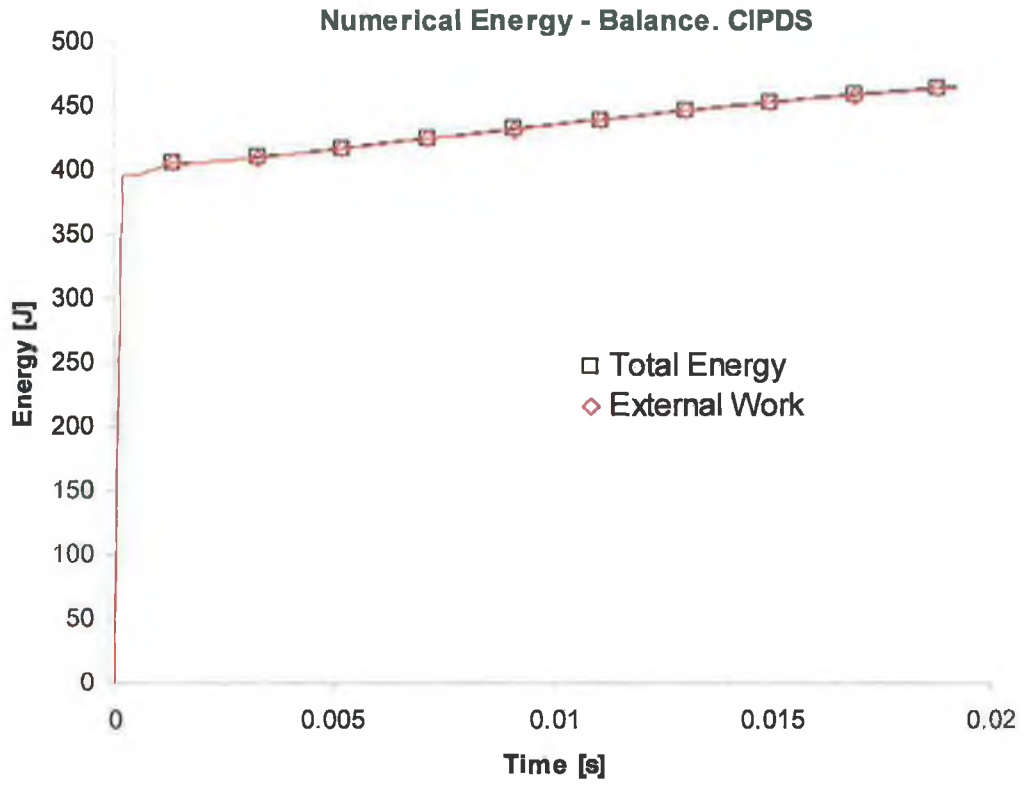

Figure 7-48: Numerical energy balance for a CIPDS.

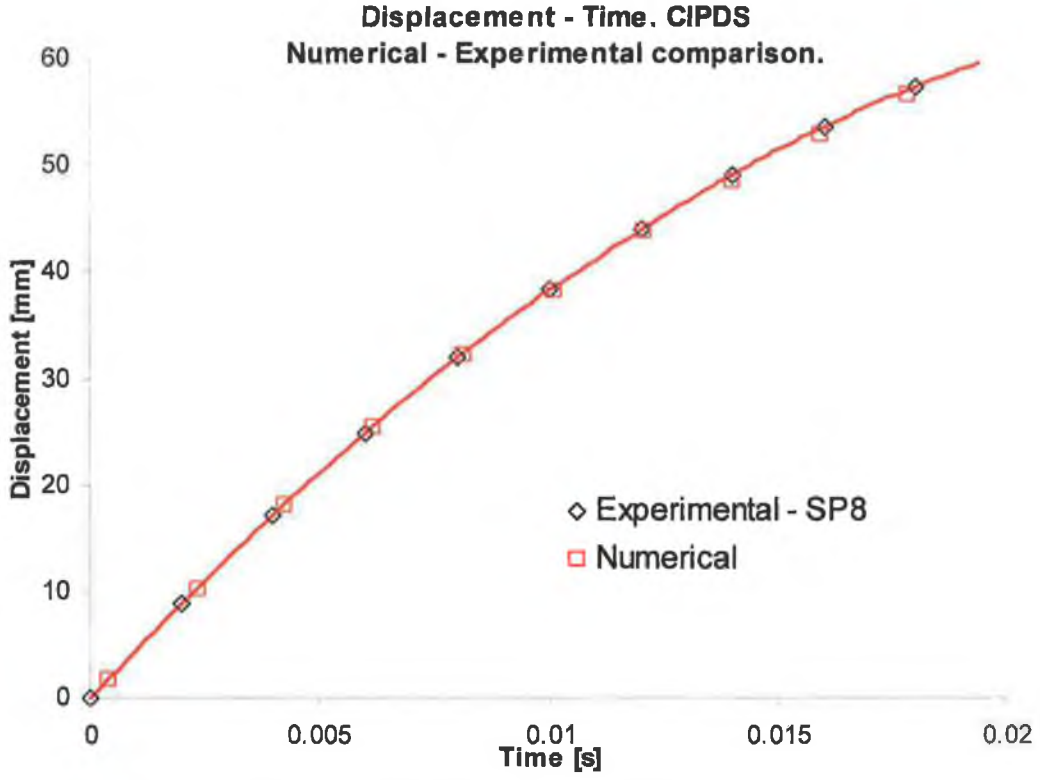

Figure 7-49: Displacement-time curve for a CIPDS.

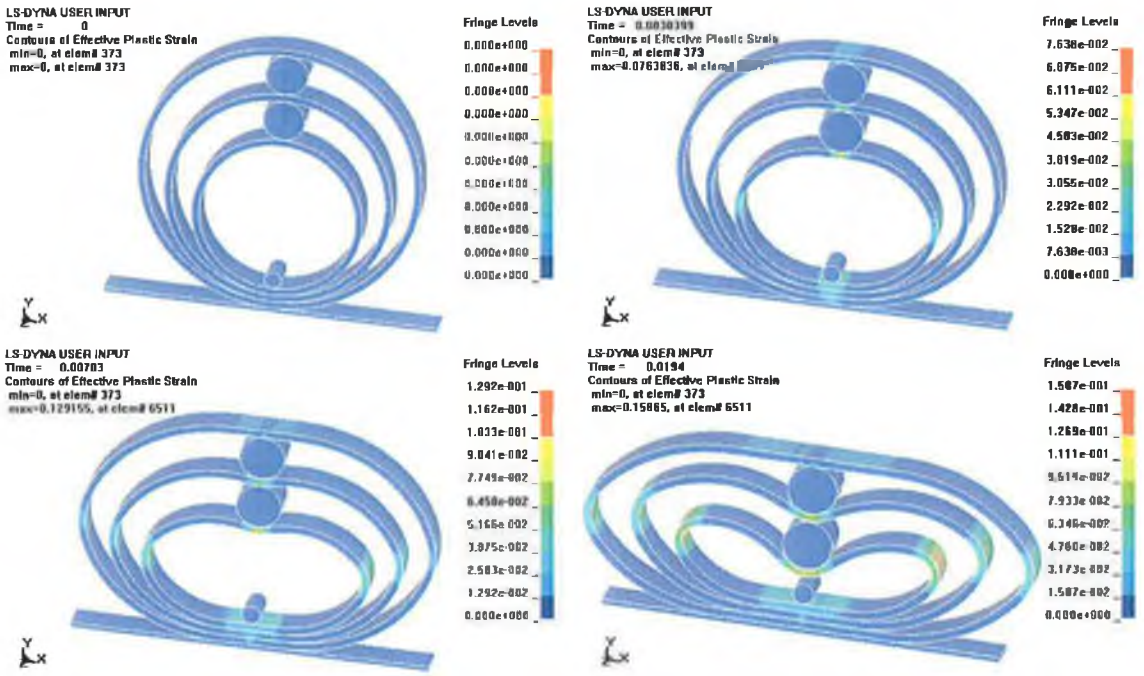

Figure 7-50: Effective plastic strain evolution of a CIPDS under dynamic lateral loading.

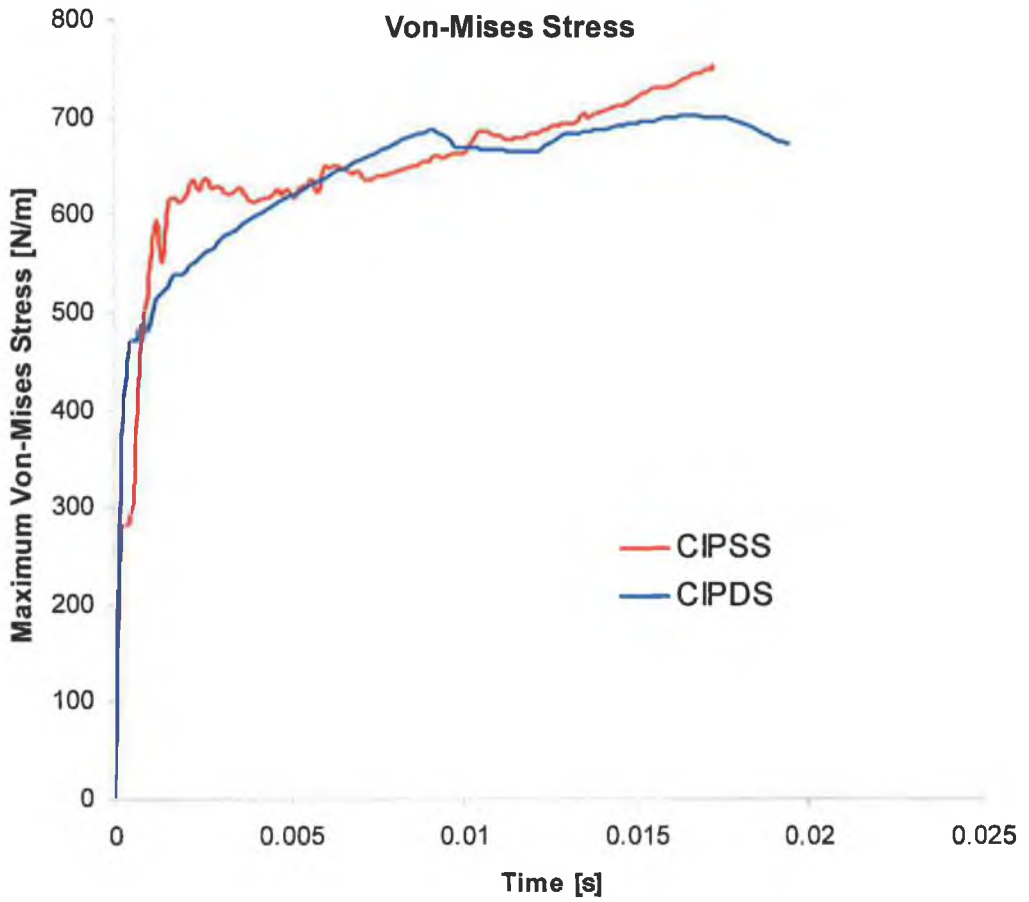

Figure 7-51: A temporal plot of the Maximum Von Mises stress for both the CIPSS and CIPDS.

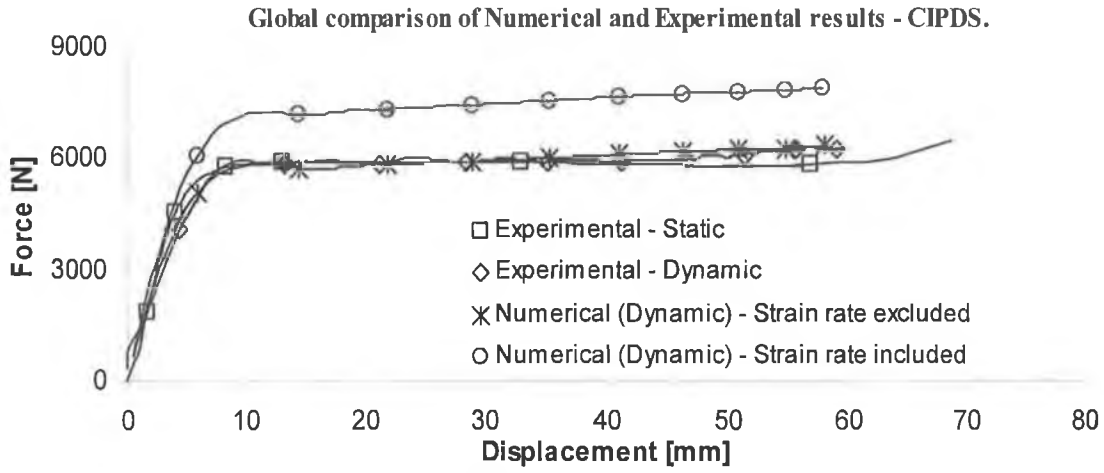

Figure 7-52: Comparison of results for a CIPDS - Static and dynamic cases.

7.8.3 Evaluation of the OIPSS and the OIPDS [Brick Element Model].

For the OIPSS and OIPDS, the force and energy responses are over-predicted by the numerical code. Values of 32% and 40% in the over estimation of energy absorption are observed as shown in Figure 7-53 and Figure 7-58 respectively. Figure 7-54, 7 – 55 and Figure 7-56 illustrates plots of the energy – time, displacement – time and numerical energy balance for OIPSS respectively. There appears to be two reasons for the over-prediction in results illustrated by the numerical method. In order to assist in this explanation for discrepancy of results, Figure 7-64 was created. Upon analysis of the OIPDS in this figure, it can be seen from an experimental point of view that both the static and dynamic cases exhibit similar force deflection response in terms of magnitude. This would indicate for the given velocity applied to the striker, the strain rate sensitivity is not a significant factor in the deformation response of this particular system. This behaviour was also noted by Zhao and Fang [48] in which they reported that the same deformation response existed between that quasi-static and dynamic cases. They concluded that the striker velocity was low enough such that strain rate effects were not significant. Shrive and Andrews [65] also noted a similar response characteristic of a tube system subjected to lateral impact loading. From a numerical standpoint, in which the effects of strain rate were both included and excluded, it can be seen that the force magnitude was over-predicted in both cases.

The first reason for the over-prediction in force, with the aid of examining the strain rate sensitive numerical response from Figure 7-64, appears to be due to the values of D and q used in the Cowper-Symonds relation as outlined in the previous section in relation to the CIPDS. These values may not be valid in this particular application since an obvious large

increase in the dynamic yield stress is evident using the specified strain rate parameters, where in fact, both the experimental static and dynamic results show similar forces of magnitude.

The second reason for the over-prediction appears to be in the difficulty of the numerical code to accurately predict where the horizontal hinge points (collapse points) within the plastic zone should occur in order for the tubes to collapse plastically; this reason was explained in section 7.7.4. By examining Figure 7-58, it can be seen that once the collapse load was reached, the force dropped rapidly to a more reasonable level of force magnitude. As already explained in the same section, this behaviour was due to the geometrical softening that occurs since the moment arm has increased due the application of the load which can be approximated as a point load. Therefore the force required to continue the deformation is reduced. Figure 7-63 illustrates the Von Mises stress time response of the OIPSS and the OIPDS in which peak stress between 700MPa and 800MPa was observed.

It should be noted that at significantly higher impact velocities, the CIPSS, CIPDS, OIPSS and the OIPDS will experience greater inertial effects depending on the magnitude of the impact velocity. Hence, the mode of deformation may be different in addition to the force magnitude. It is known that at the high velocity impact lateral loading of tubes or rings may lead to localised deformation as a result of inertial effects due to the structural shock wave propagating through the structure [69].

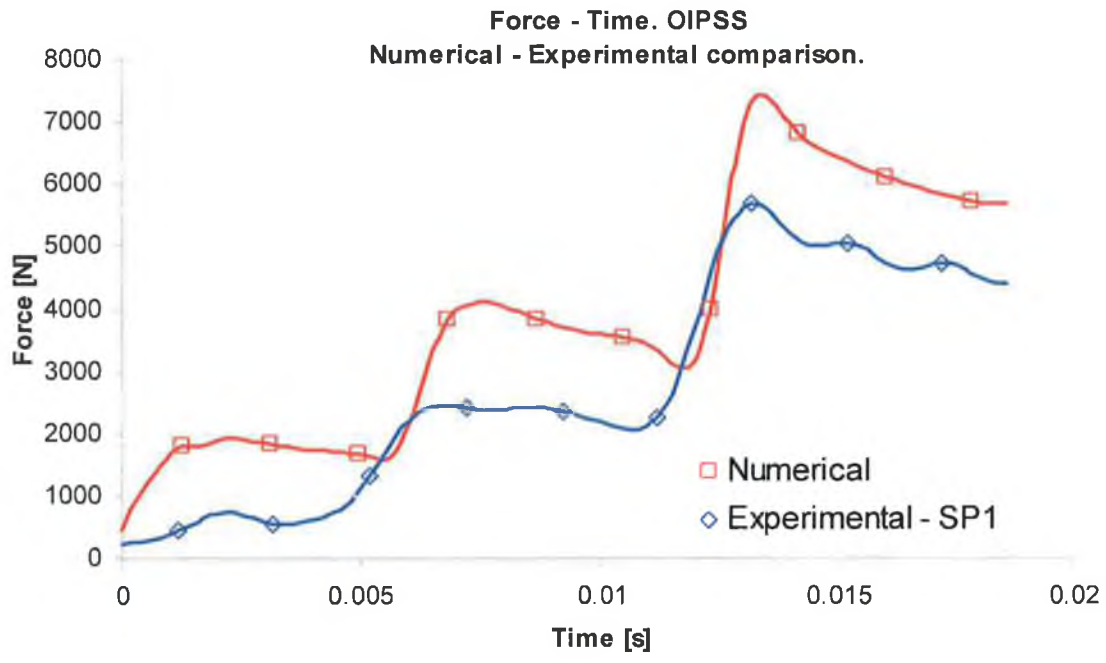

Figure 7-53: Force-time response of an OIPSS.

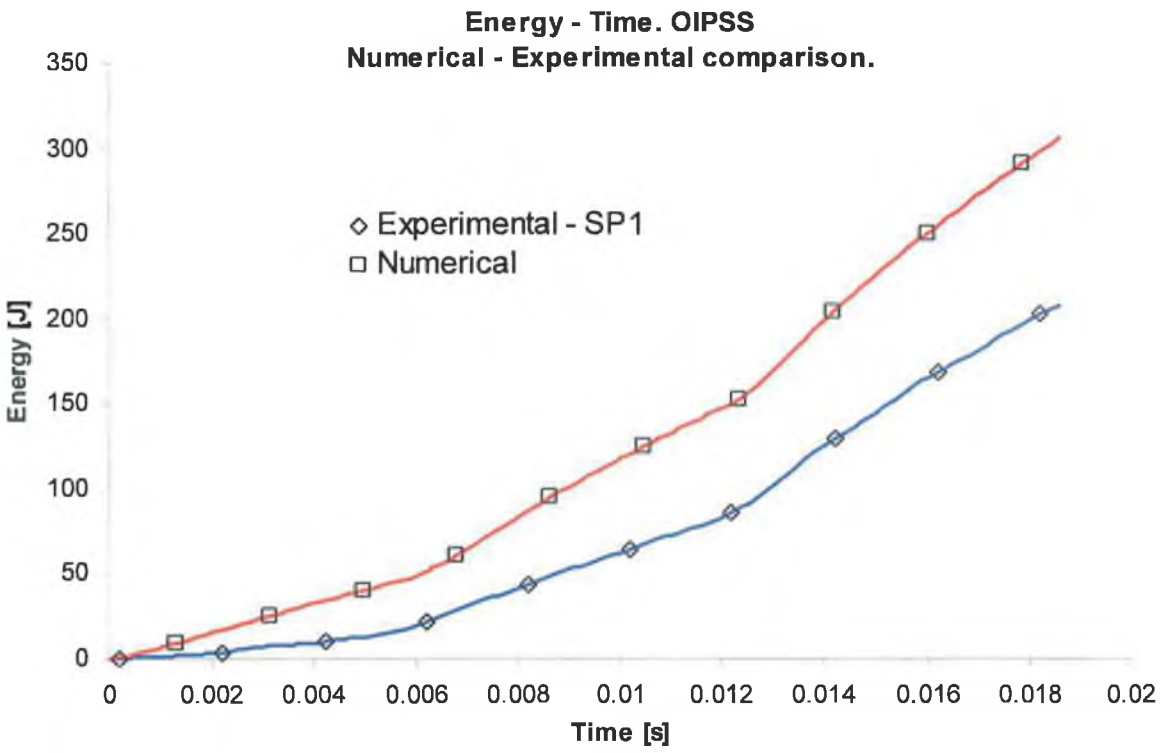

Figure 7-54: Energy-time response of an OIPSS.

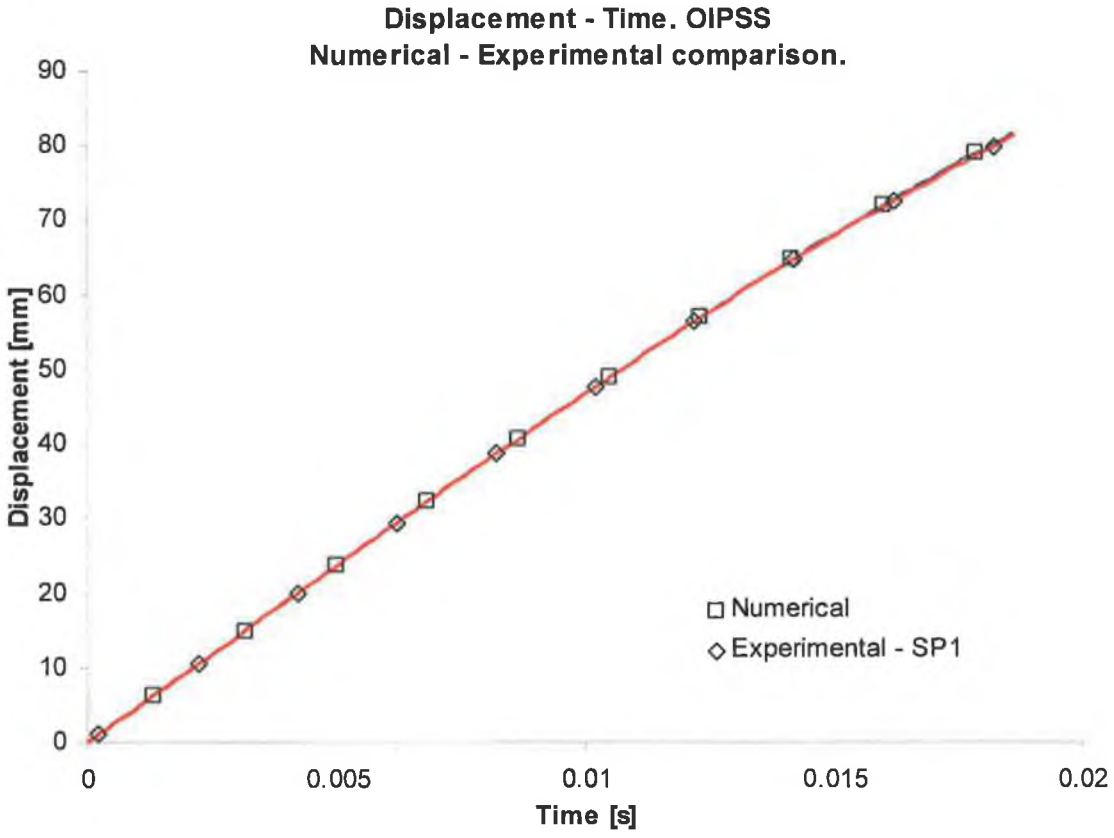

Figure 7-55: Displacement-time response of an OIPSS.

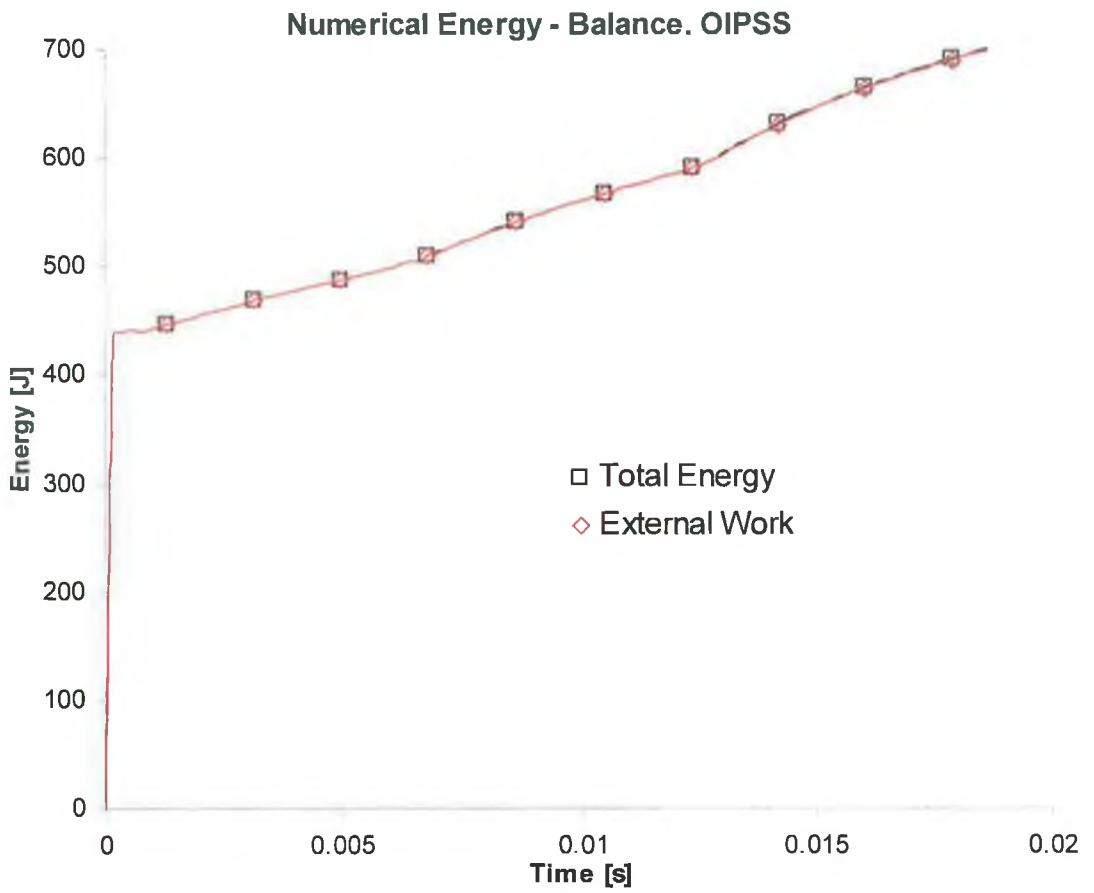

Figure 7-56: A numerical energy balance for an OIPSS.

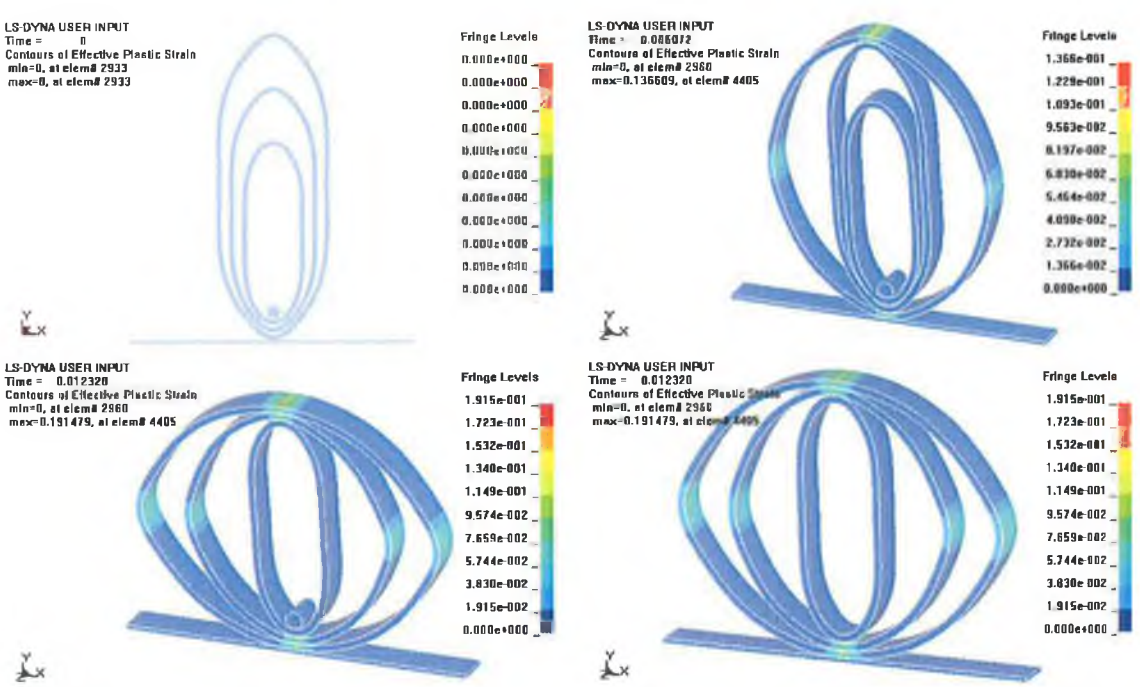

Figure 7-57: Effective plastic strain evolution of an OIPSS subjected to dynamic lateral loading.

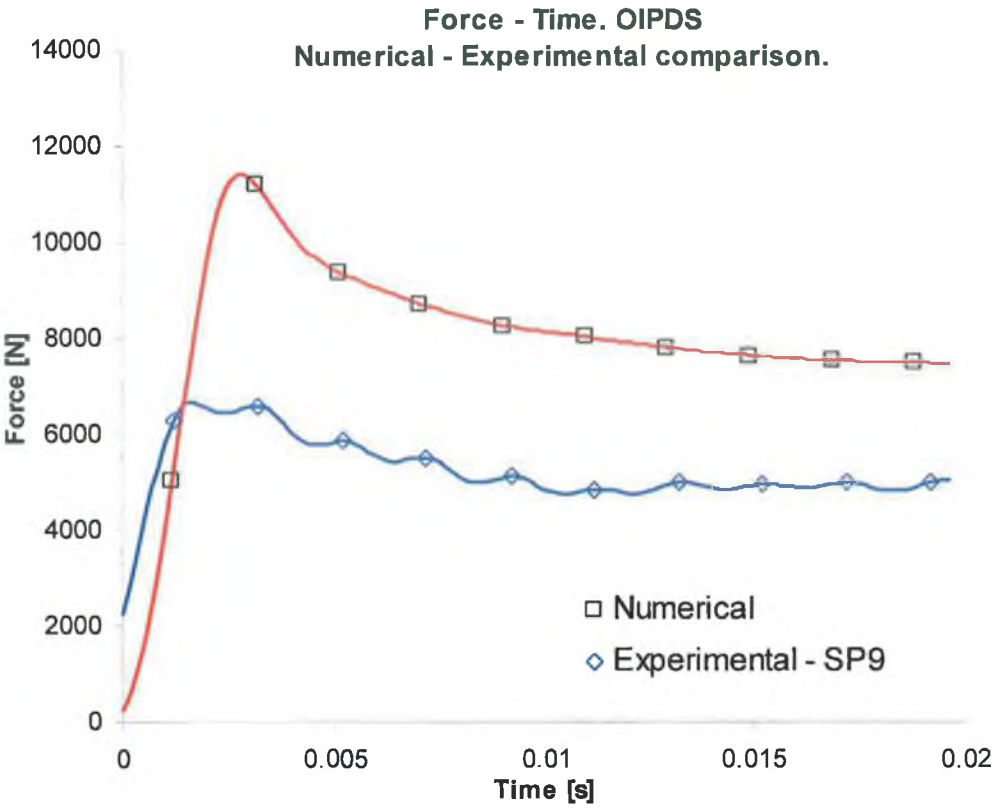

Figure 7-58: Force-time plot of an OIPDS.

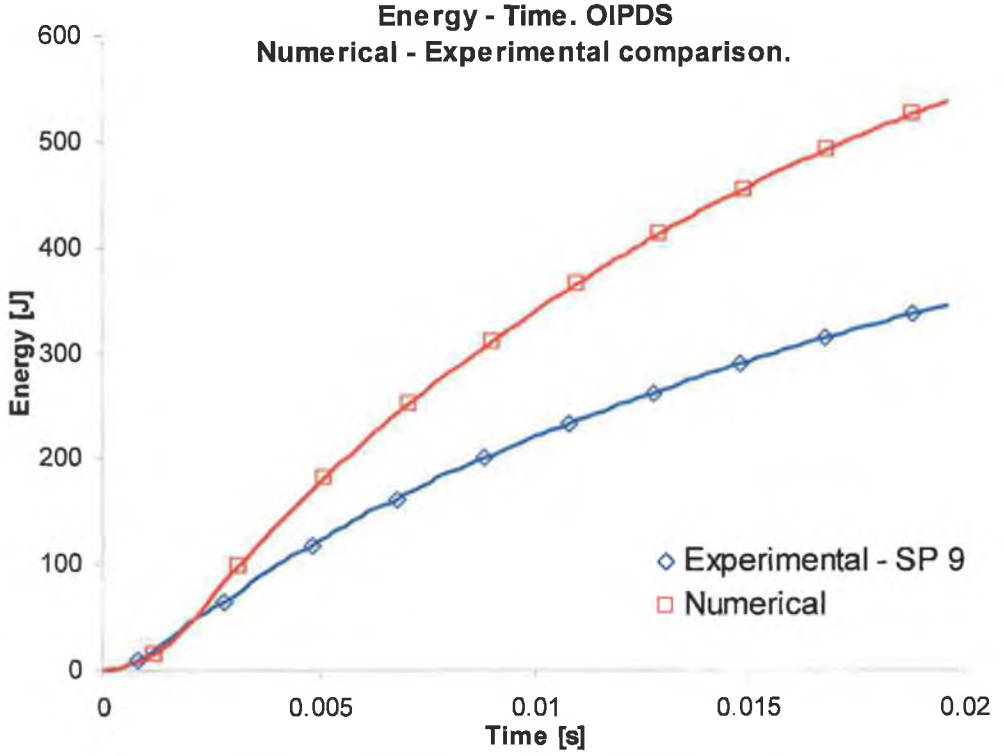

Figure 7-59: Energy-time response of an OIPDS.

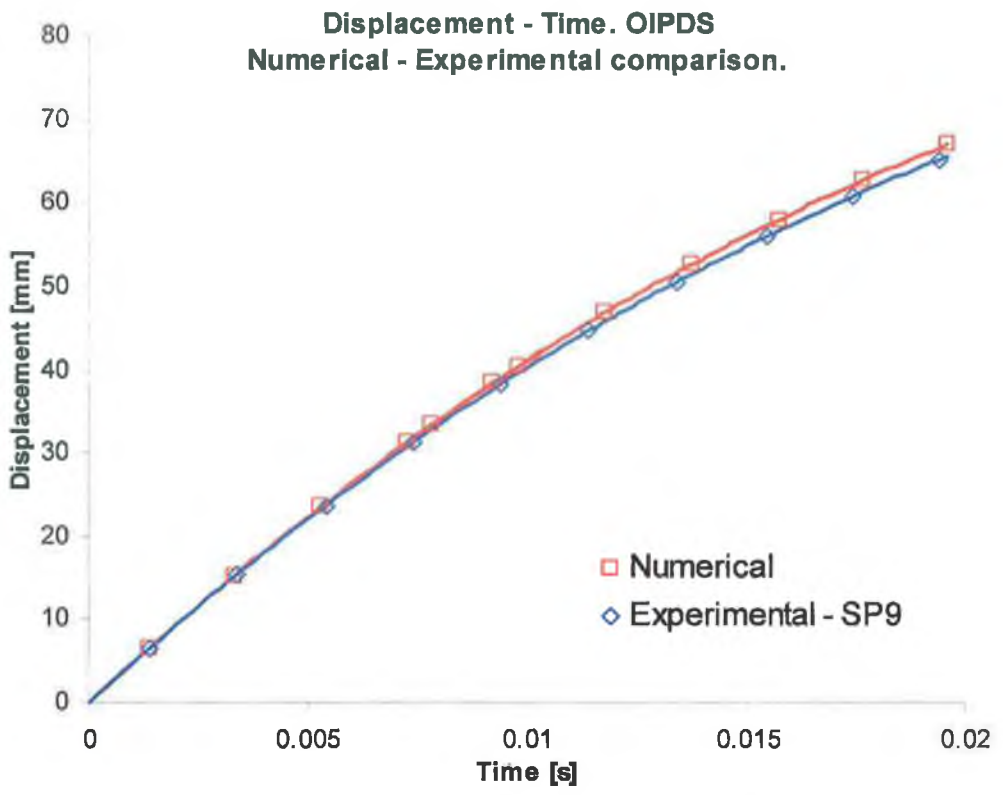

Figure 7-60: Displacement-time response of an OIPDS.

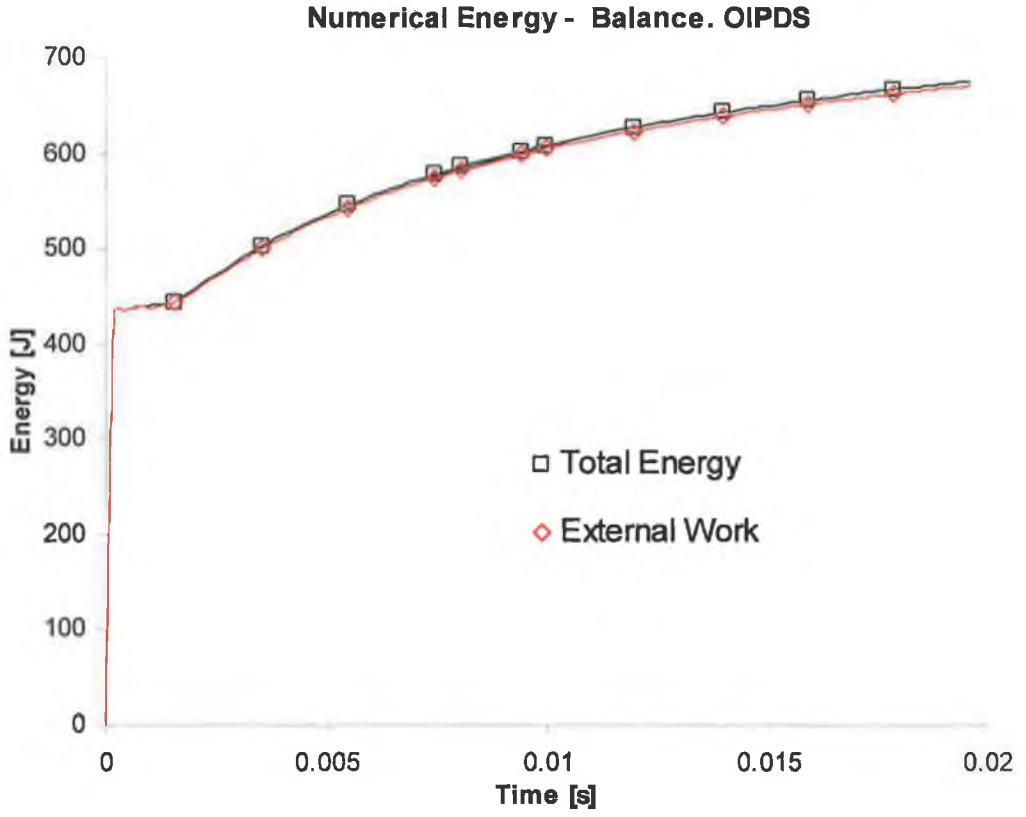

Figure 7-61: A Numerical energy balance of an OIPDS.

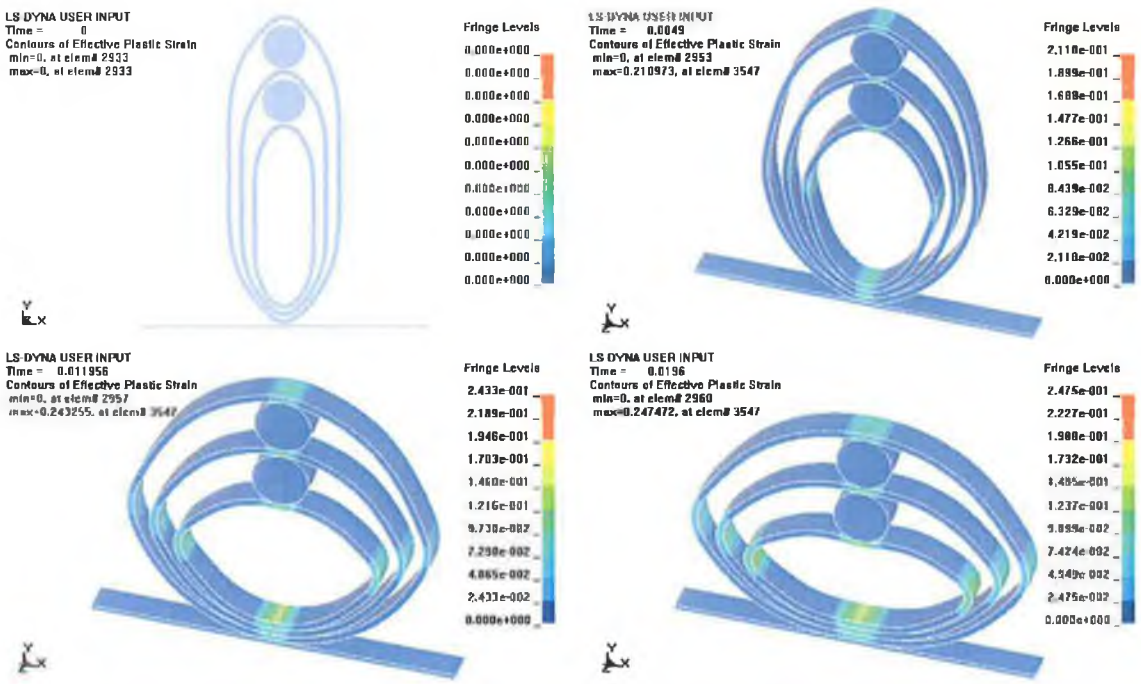

Figure 7-62: Effective plastic strain evolution o an OIPDS subjected to dynamic lateral loading.

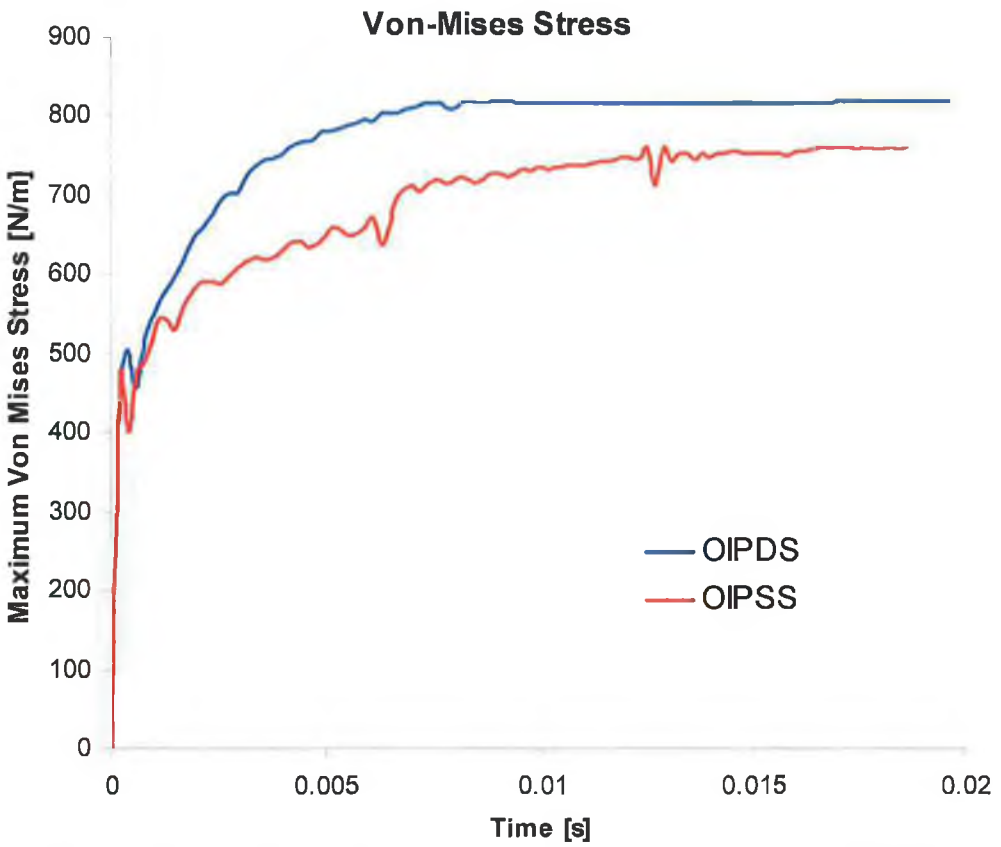

Figure 7-63: A temporal plot of the Maximum Von Mises stress for both the OIPSS and OIPDS.

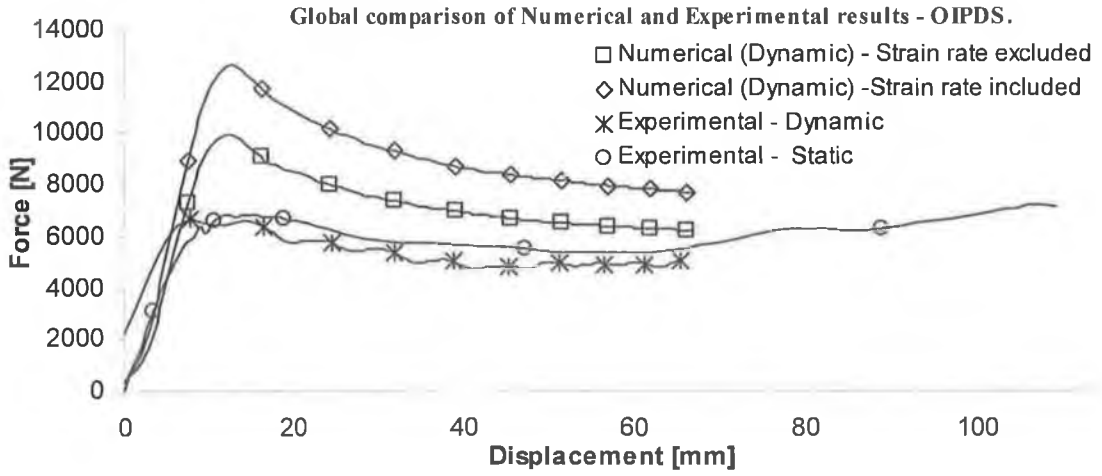

Figure 7-64: Comparison of results for an OIPDS - Static and dynamic cases.

7.8.4 Evaluation of the OIPDS. (Shell Element Model)

Figure 7-65 illustrates a comparison of results between the shell element model and the actual experimentally observed force-deflection response. The same procedure as described in 7.8.3 was employed in which the OIPDS was simulated with and without the strain-rate effects. It can be seen that with the inclusion of strain rate effects, the collapse load appears to be well over predicted and it should be noted that the magnitude of force is similar to that of its brick element counterpart. However, in the post collapse stages, the force reduces considerably indicating the ability of the shell element to more accurately predict the force due to this bending dominated mode of deformation. For the shell model and excluding the effects of strain rates sensitivity, it can be seen that there is quite a good correlation between the numerical and experimental result. The collapse load is still over estimated although the magnitude is considerably less than its corresponding brick model counterpart as shown in Figure 7-64. It appears that the shell element model also has difficulty to correctly predict the collapse load for this OIPDS: it may be due to the straight portion of the oblong tubes acting as columns as outlined in section 7.7.4. The displacement evolution for this shell element model is displayed in Figure 7-66. For an interesting comparison, Figure 7-67 is displayed which offers a comparison of results between the shell and brick element formulations and that of experiment. It can be seen that the shell element formulation is the better one to use since it is quite suited to model bending dominated problems. In addition to this, the solution time using the shell element formulation is considerably less than that when using the brick element formulation.

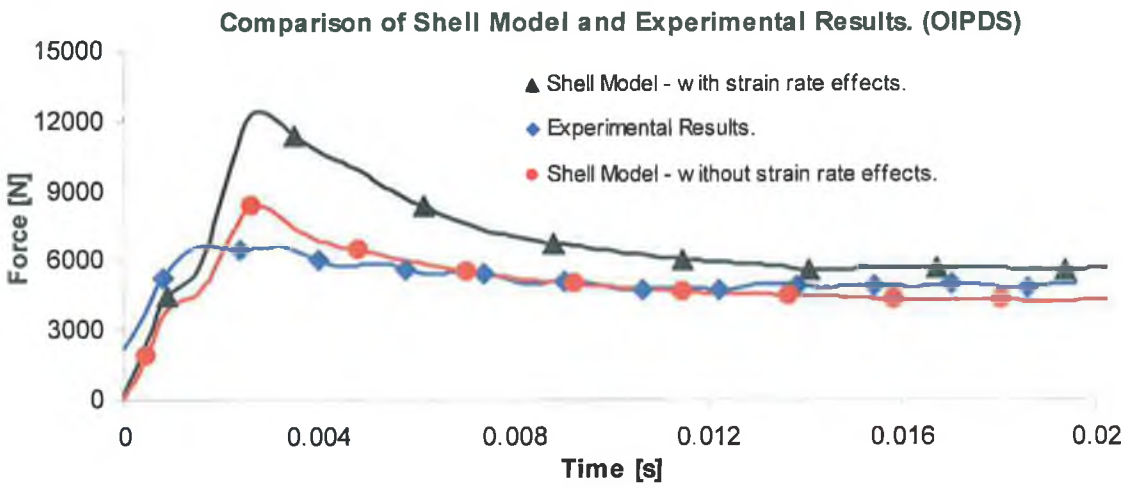

Figure 7-65: A force – time plot comparing the brick and shell model against the actual observed result for an OIPDS.

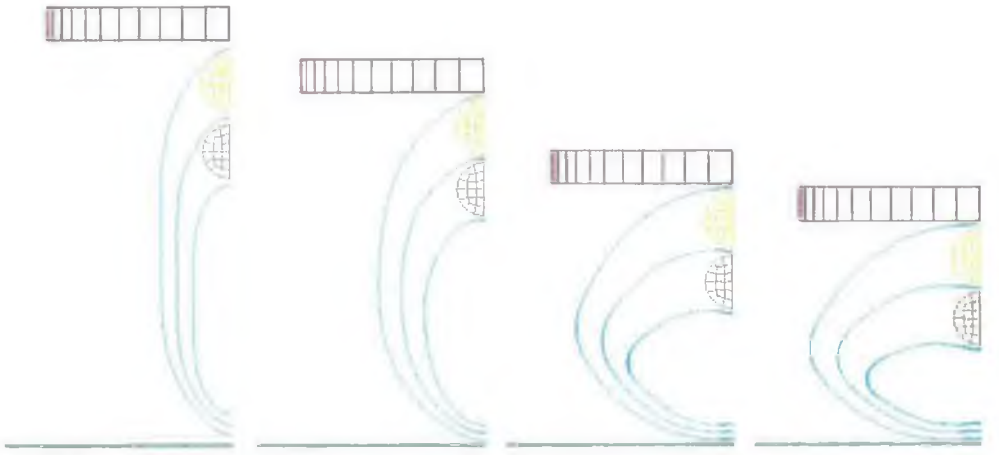

Figure 7-66: A numerical plot of the displacement evolution for a shell modelled OIPDS.

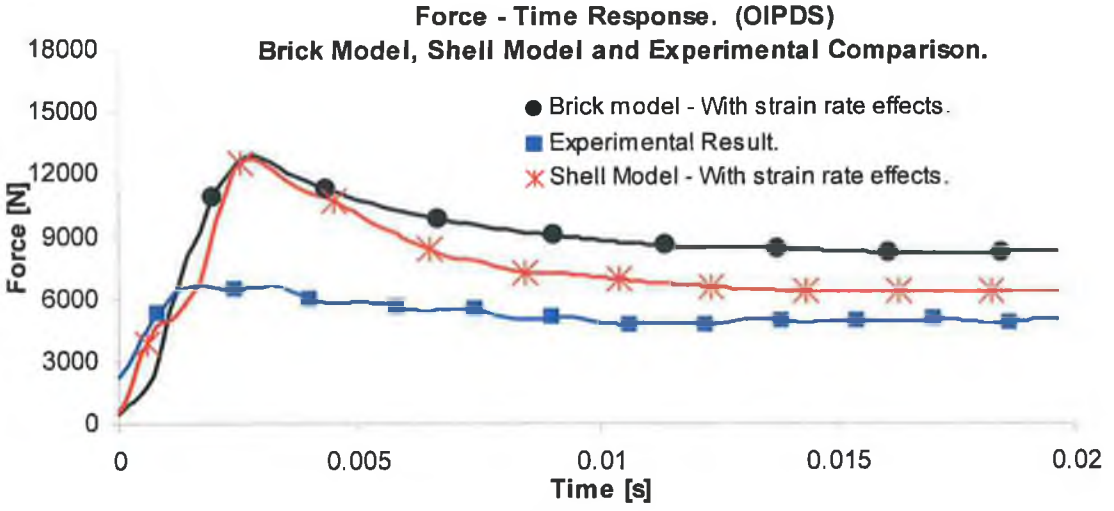

Figure 7-67: A force – time plot comparing the brick and shell model against the actual observed result for an OIPDS.

7.9 Numerical Results: Specific Energy Maximization of Nested Systems.

The following numerical models are based on the CIPSS subjected to the various forms of external constraints and loaded quasi – statically as described and analysed in chapter six. A comparison of results is made between the numerical and experimental methods by examining the force and energy - deflection responses. The various graphical plots such as boundary (symmetry) conditions are displayed in addition to the contact normals of the associated contact pairs. An illustration of the Von Mises total strain plots at various stages of the crushing process is also depicted. Finally, the Von Mises plastic strain history of a selected node from each model is illustrated.

7.10 Plate Indenter Compression.

7.10.1 CIPSS - Inclined Constraints.

Figure 7-68 illustrates two graphical plots depicting the boundary conditions applied to the one quarter model and the orientation of the contact normals for each of the contact pairs. Two contact pairs were used to model the contact interaction between the three tubes. The third contact pair represented the horizontal rigid platen and the outer tube whilst the final pair modelled the interaction of the inclined constraint with the outer tube. The same contact modelling procedure was also applied to all subsequent systems analysed in this section. A comparison of results between the two methods for a CIPSS subjected to inclined constraints is depicted in Figure 7-69. It can be seen that the numerical method is in very good agreement with the experimental method in predicting the force - deflection response with a difference of 4% between the two methods. Only a slight under prediction was observed for the collapse load of each tube, at approximately 38mm, the final strain hardening response been reasonably well predicted by the numerical code.

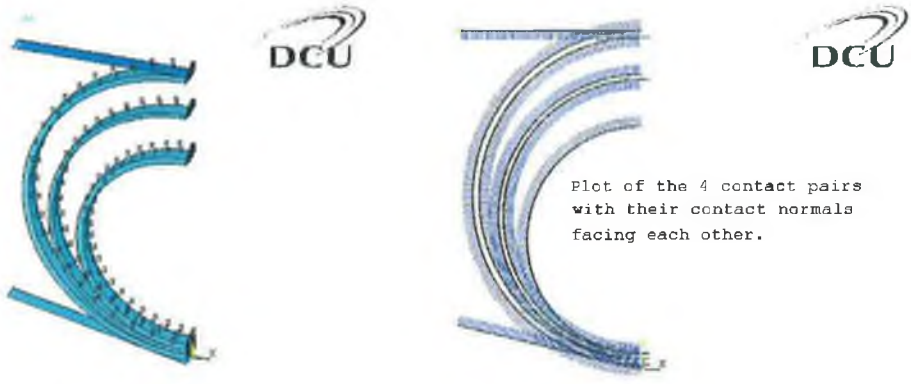

Figure 7-68: A graphical plot of the boundary conditions and contact pairs for a CIPSS with inclined constraints.

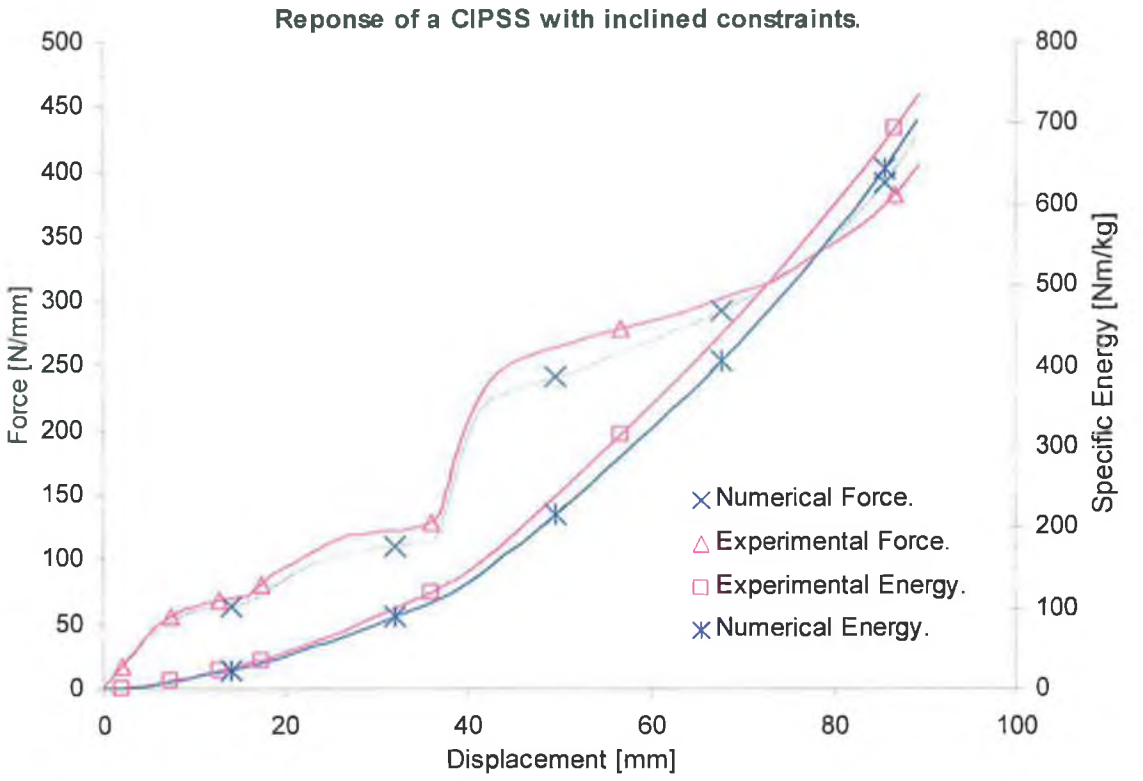

Figure 7-69: Comparison of results between the numerical and experimental methods for a CIPSS subjected to inclined constraints.

Figure 7-70 displays the Von Mises total strain plots at the various evolution stages for this system. As expected, when each tube was loaded, the higher levels of strain were located within the plastic bending zone of each tube. Under the standard case of a system compressed between two rigid flat platens, there will also exist a hinge point at the upper and lower most regions of each tube under loading. For this case however, due to the presence of inclined constraints, the higher levels of strain existed only at three locations as shown in the final displacement of the same figure. Three nodes were used to capture the Von Mises plastic strain history throughout the deformation process as shown in Figure 7-71. Each node was selected from the upper most and central region of each tube, i.e., the upper most region at the intersection of the two symmetry planes as shown in Figure 7-12. By examining this figure with the aid of arrows A and B, it can be seen that the outer tube in the region defined by node 1926 experienced an increased in plastic strain until contact was established with the central tube. From this point onwards, the strain becomes constant whilst concurrently; node 3474 in the central tube begins to rise until contact is established with the inner tube. Similarly, this node experiences a constant strain whilst node 621 increases for the remainder for the displacement stroke. This continual increase in strain at this node was due to increased bending at this region.

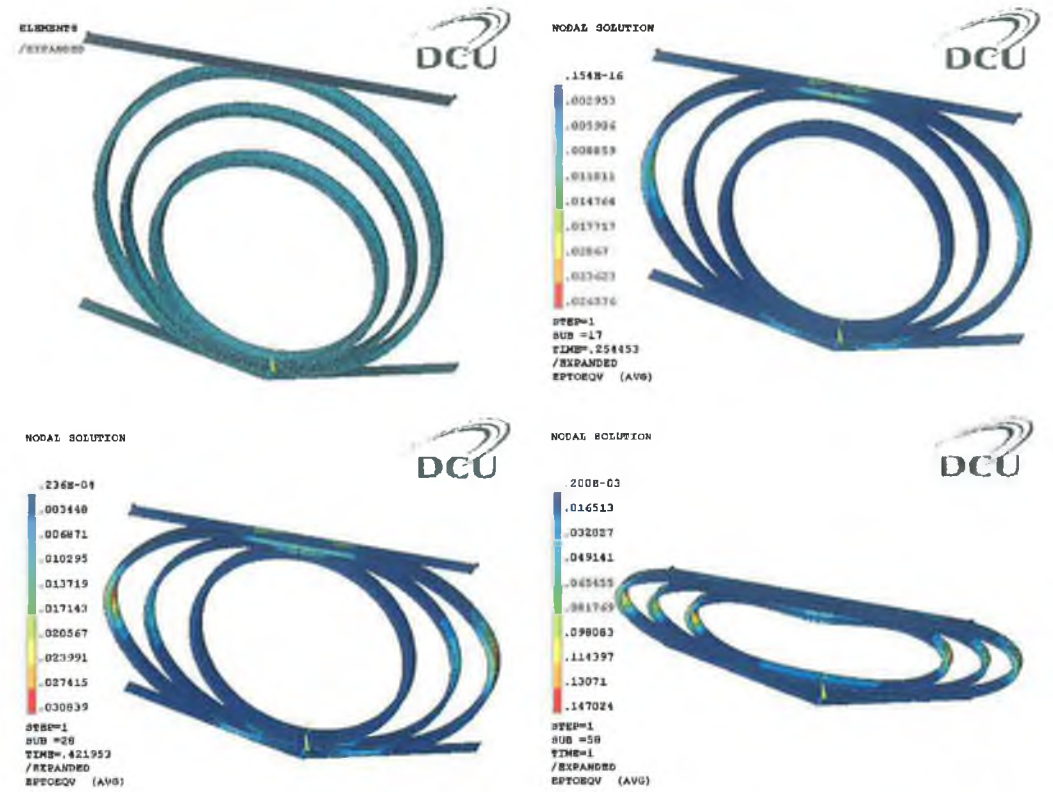

Figure 7-70: Von Mises total strain contour plot for a CIPSS with inclined constraints.

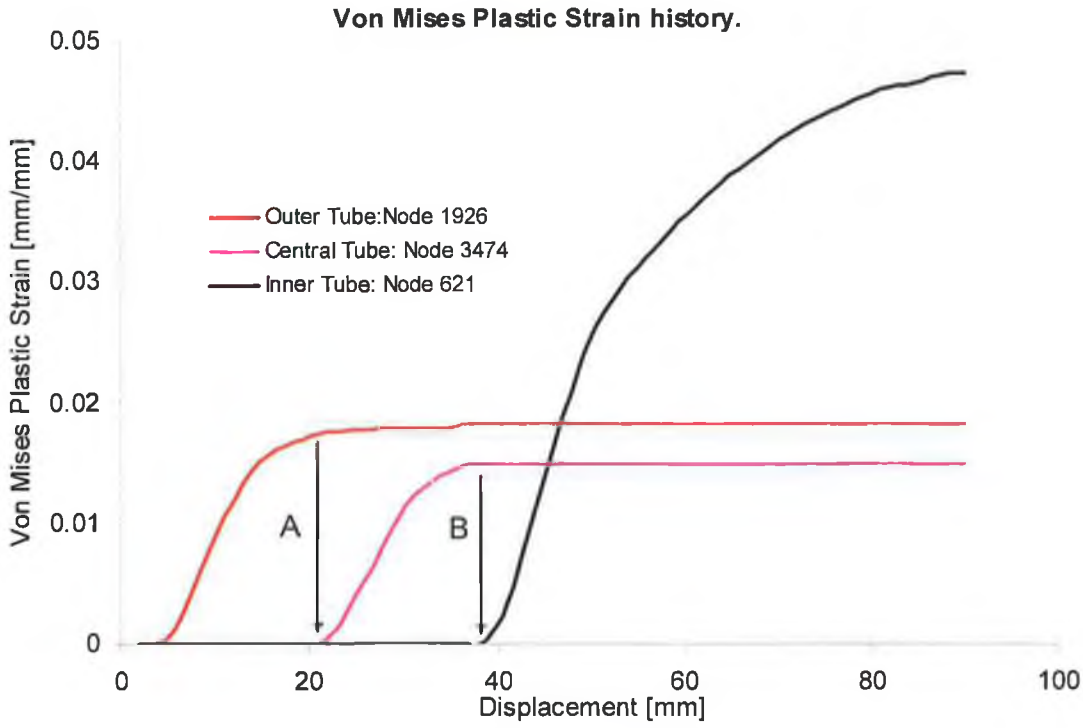

Figure 7-71: Plastic strain history of a CIPSS subjected to inclined constraints.

7.10.2 CIPSS - Vertical Constraints.

The force-deflection response for a CIPSS subjected to sidewall constraints is depicted in Figure 7-72. The numerical method predicts the response extremely well and hence only a difference of 3% in specific energy absorption between both methods for this particular system. Figure 7-73 presents a graphical plot of the Von Mises total strain experienced by this system throughout the displacement stroke. Initially, before the sidewall restricted movement of the outer tube, the initial positions of the plastic bending zone locations were at both the horizontal and top-bottom sections. However, once contact was established between this tube and the sidewalls, the final position of the hinges moved to a location close to the sidewalls as shown in the final displacement plot of Figure 7-73. It was at this stage the system was in a 'locked' condition and hence the resulting force began to rise rapidly. Figure 7-74 depicts a Von Mises plastic strain history of three selected nodes from each tube. A similar behaviour was observed as in the previous system. The outer tube in the region of node 1926 experienced an increase in plastic strain until contact was established with the central tube. Accordingly, the region of node 3474 of the central tube experienced an increase in strain whilst the plastic strain of outer tube remained constant. Finally, the third selected node of the inner tube experienced an increase in plastic strain for the remainder of the displacement stroke due to the bending and separation of this section of the inner tube away from the central tube.

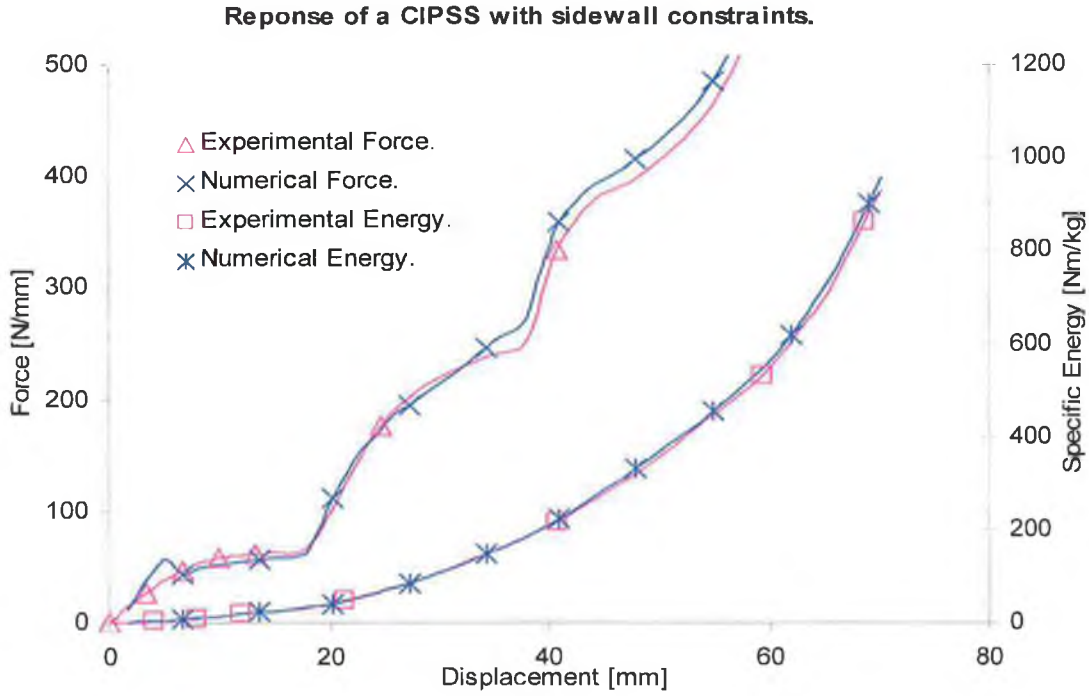

Figure 7-72: **Comparison of results between the numerical and experimental methods for a CIPSS subjected to sidewall constraints.**

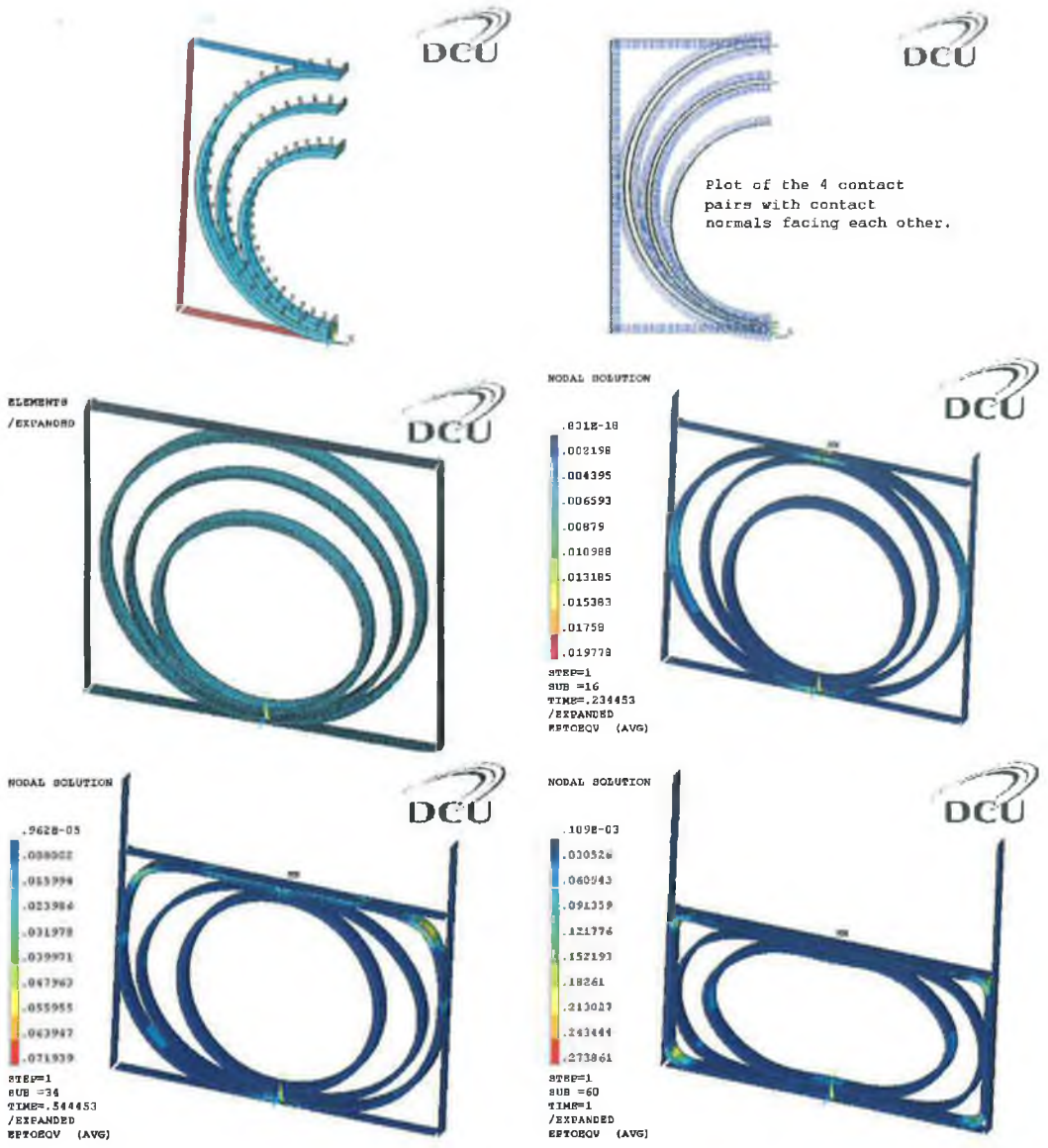

Figure 7-73: **Illustration of the boundary and contact definitions with a total Von Mises total strain plot for a CIPSS with sidewall constraints.**

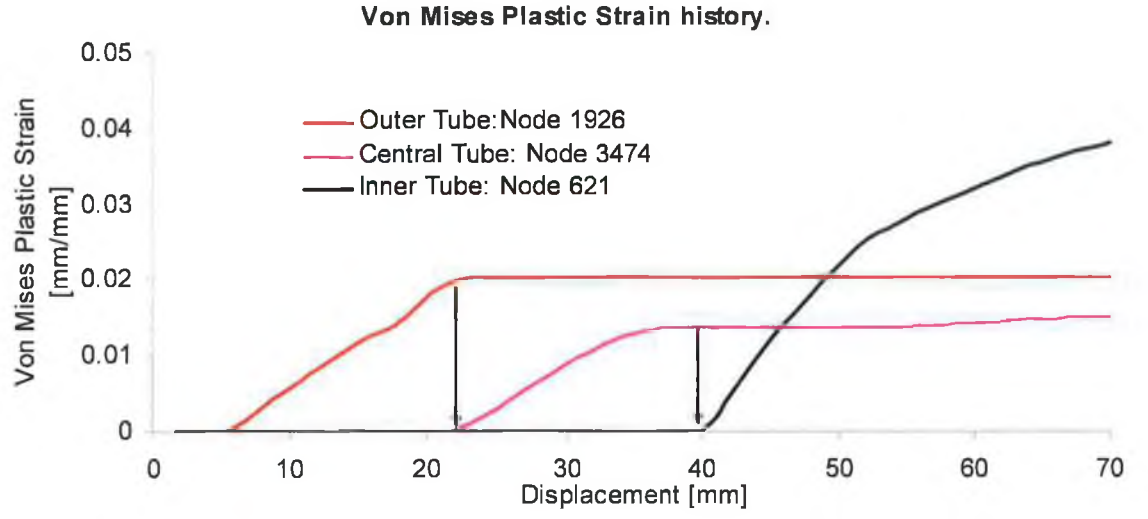

Figure 7-74: Plastic strain history at three selected nodes for a CIPSS subjected to sidewall constraints.

7.10.3 CIPSS - Combined Constraints.

Figure 7-75 offers the force- and energy-deflection response of a CIPSS subjected to both types of constraints. Again, a very good response was predicted by the numerical method. A final value of 2% was reported in terms of over prediction the specific energy response by the numerical method. The Von Mises total strain evolution plots for this system are displayed in Figure 7-76. Again a similar situation was observed with regard the plastic bending zone. Initially located at the horizontal quadrants of the outer tube, the hinges have shifted to a position close to the vertical rigid walls.

Figure 7-77 depicts the Von Mises plastic strain history of this system represented by the same three nodes. Again, it can be seen from this figure that once contact was established between each respective tube, the strain remained constant for the remainder of the stroke. At the same time, the region in the vicinity of the selected node for the inner tube experienced an increasing value in strain for the final displacement stroke.

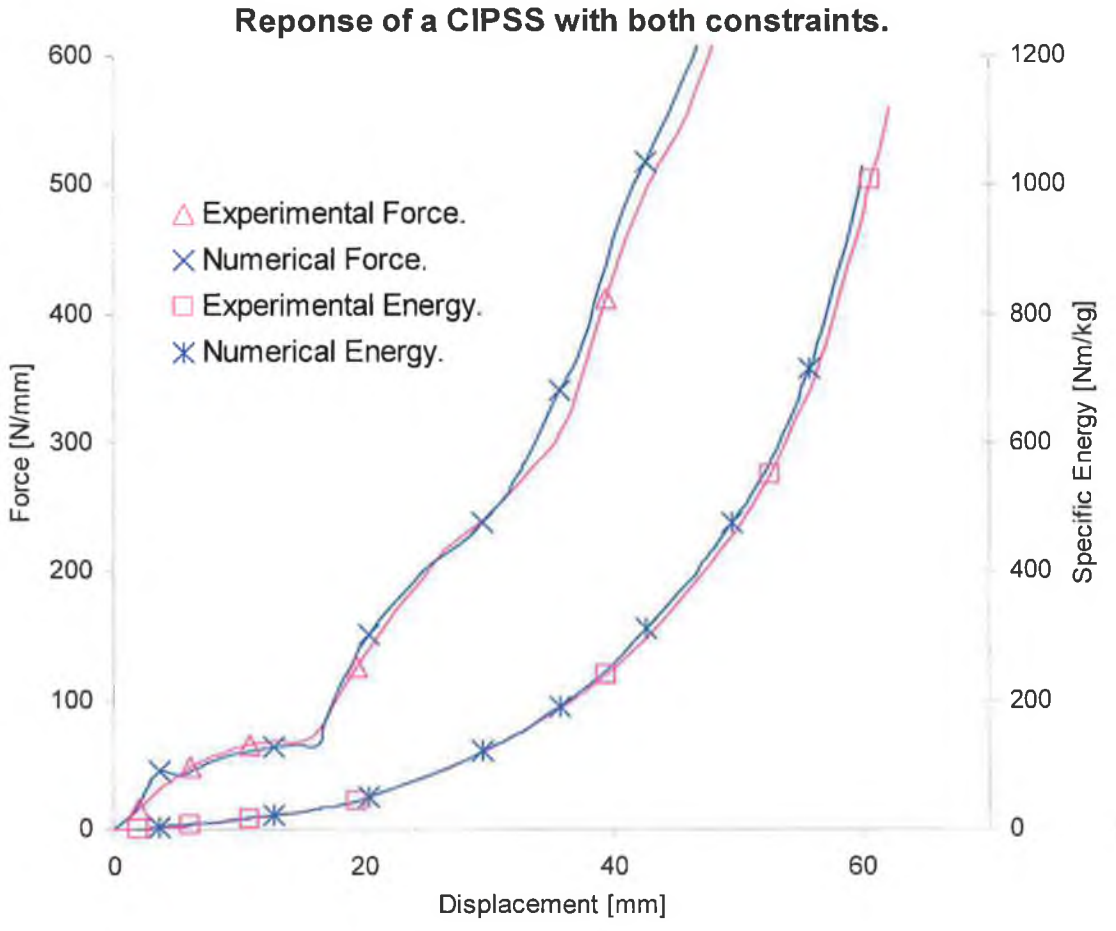

Figure 7-75: **Comparison of results between the numerical and experimental methods for a CIPSS subjected to combined constraints.**

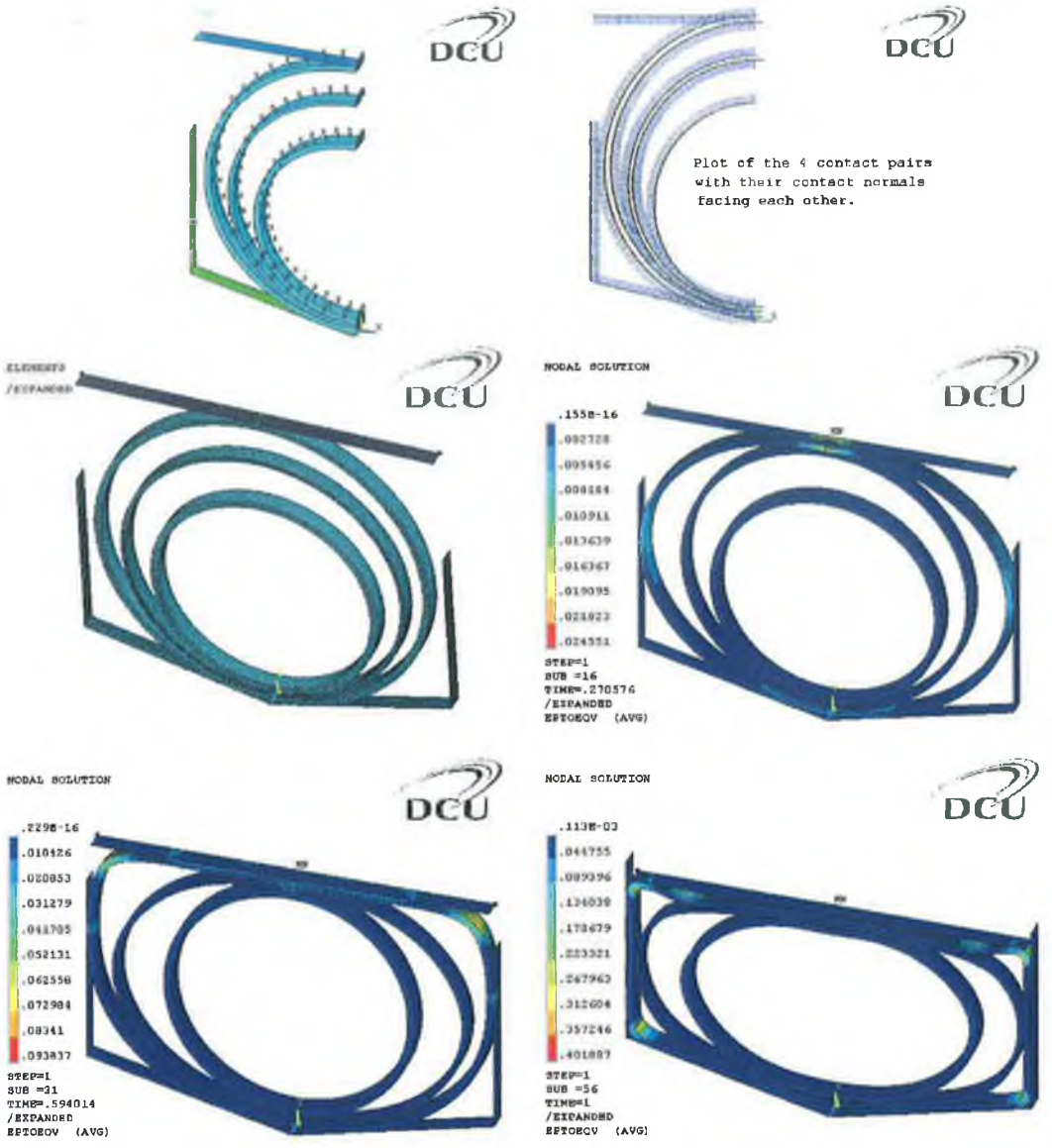

Figure 7-76: **Illustration of the boundary and contact definitions with a total Von Mises total strain plot for a CIPSS with both constraints.**

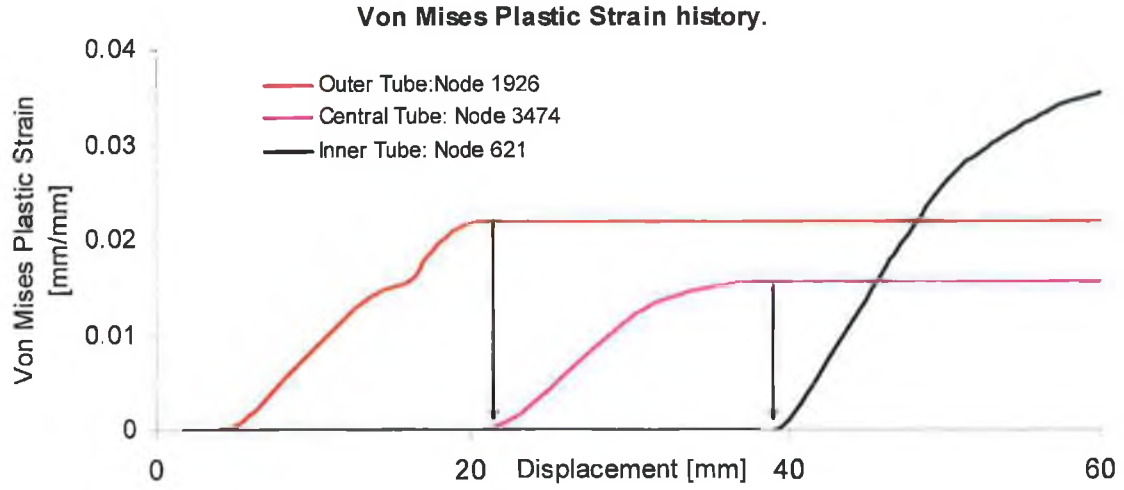

Figure 7-77: Plastic strain history at three selected nodes for a CIPSS subjected to both constraints.

7.10.4 CIPDS - Combined Constraints.

Figure 7-78 depicts a numerical comparison of results between a CIPDS and a CIPSS subjected to combined constraints under the action of a plate indenter. It can be seen that the CIPDS absorbs more energy in the earlier stages of deflection due to the presence of the spacers inserted between the tubes. The CIPDS absorbed 26% more energy than its CIPSS counterpart; this was due to the fact that the former system was absorbing more energy in the earlier stages of deflection as shown in Figure 7-78. The boundary conditions and contact pair definitions are depicted in Figure 7-79 along with the displacement evolutions for the complete stroke. A Von Mises plastic strain history of the three selected nodes is depicted in Figure 7-80. It can be seen that the node on the outer tube remains relatively constant for the entire stroke whilst the nodes on the remaining tubes experience an increase in strain. This is due to the fact that the plastic bending zone in the vicinity of these two node experiences a greater strain in contrast to the node on the outer tube.

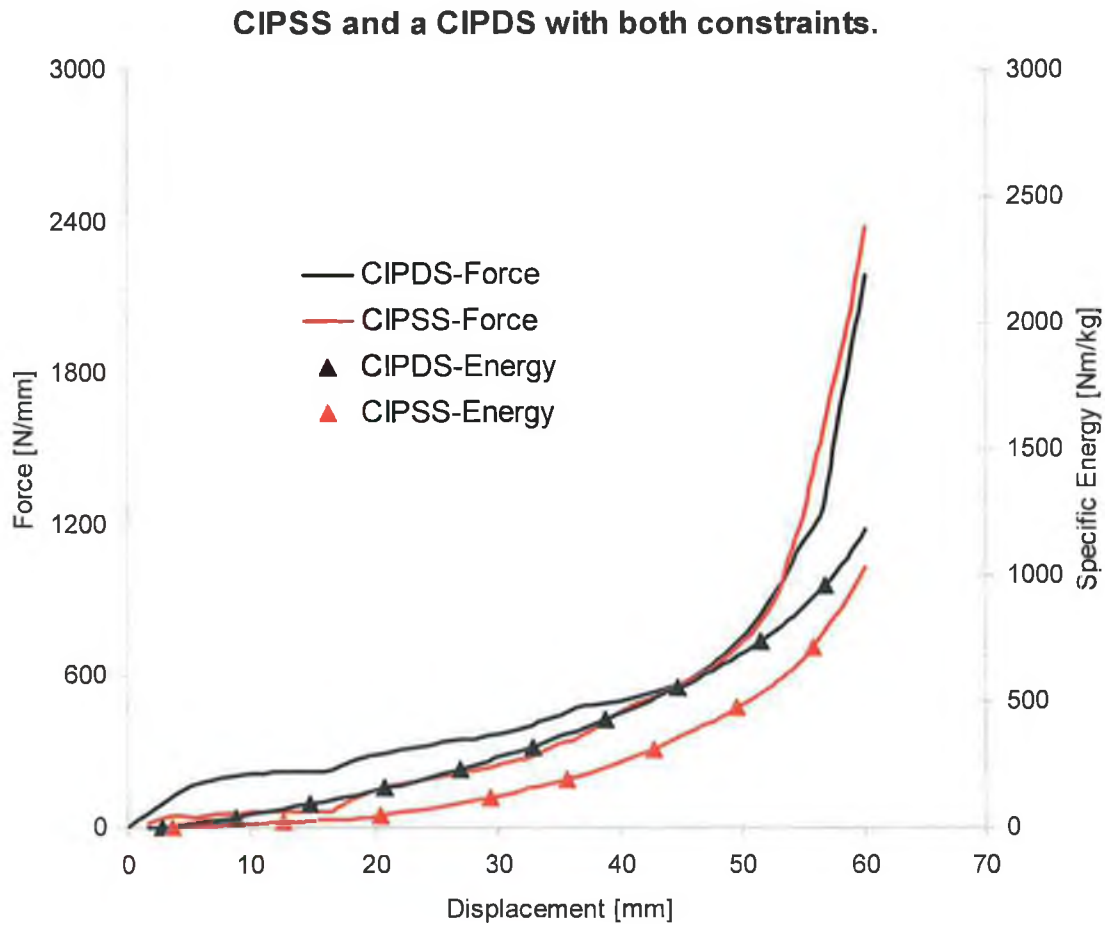

Figure 7-78: Force-deflection response of a CIPDS subjected to combined constraints.

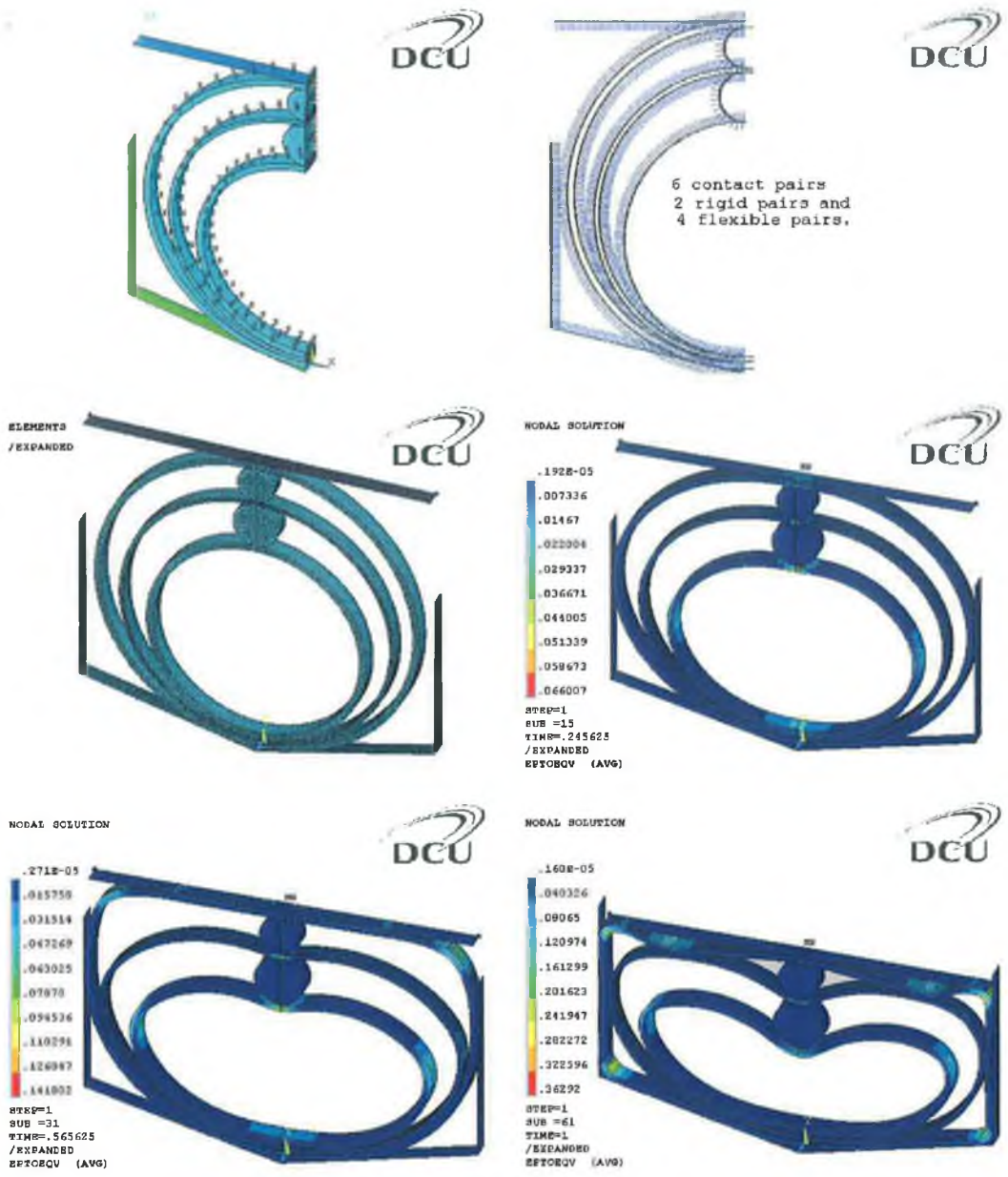

Figure 7-79: **Illustration of the boundary and contact definitions with a total Von Mises plastic strain plot for a CIPSS with both constraints.**

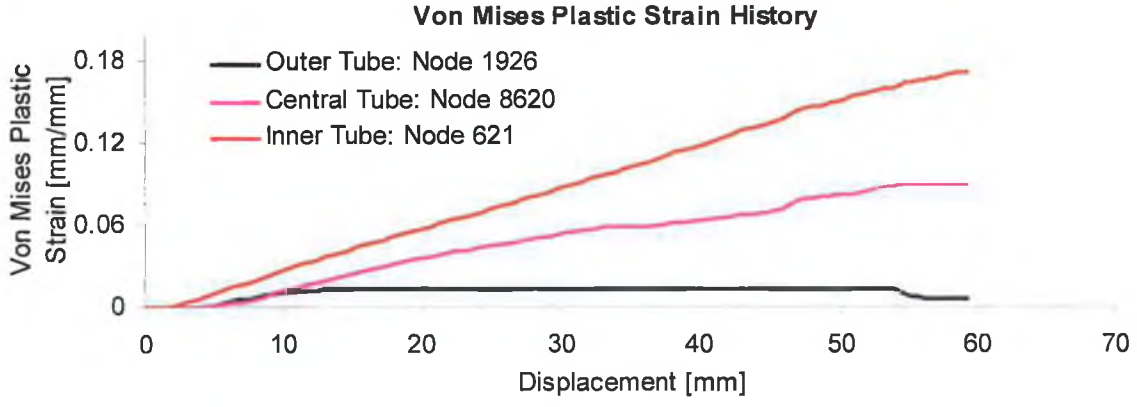

Figure 7-80: Plastic strain history at three selected nodes for a CIPDS subjected to both constraints.

7.11 Point Load Indenter.

7.11.1 CIPSS - Inclined Constraints.

Figure 7-81 illustrates a comparison of results for the response of a CIPSS subjected to inclined constraints under the crushing of a point load indenter. The numerical method has slightly under - predicted the collapse load of each tube followed by a slightly softening in force for the remaining deflection. However, in terms of energy absorption, a difference of 2% exists between the numerical and experimental methods. The displacement plots consisting of the Von Mises total strain gradients are depicted in Figure 7-82. As shown in the final stages of displacement, it can be seen how the greatest plastic strain occurred in the region of the horizontal quadrants and in the upper most section of all three tubes.

The Von Mises total strain history of the identical three selected nodes is displayed in Figure 7-83. The behaviour of these three nodes is different from the previous three systems compressed under a flat rigid platen. Since the nature of the application load is in the form of a point load indenter, the plastic strain in the vicinity of the three selected nodes will increase for the full displacement stroke. This is due to the fact that bending in this plastic zone region of each tube becomes concentrated resulting in an increase in plastic strain within these regions. Figure 7-84 depicts the bisection history of this system, it can be seen that three bisections occurred during contact between the central and inner tube.

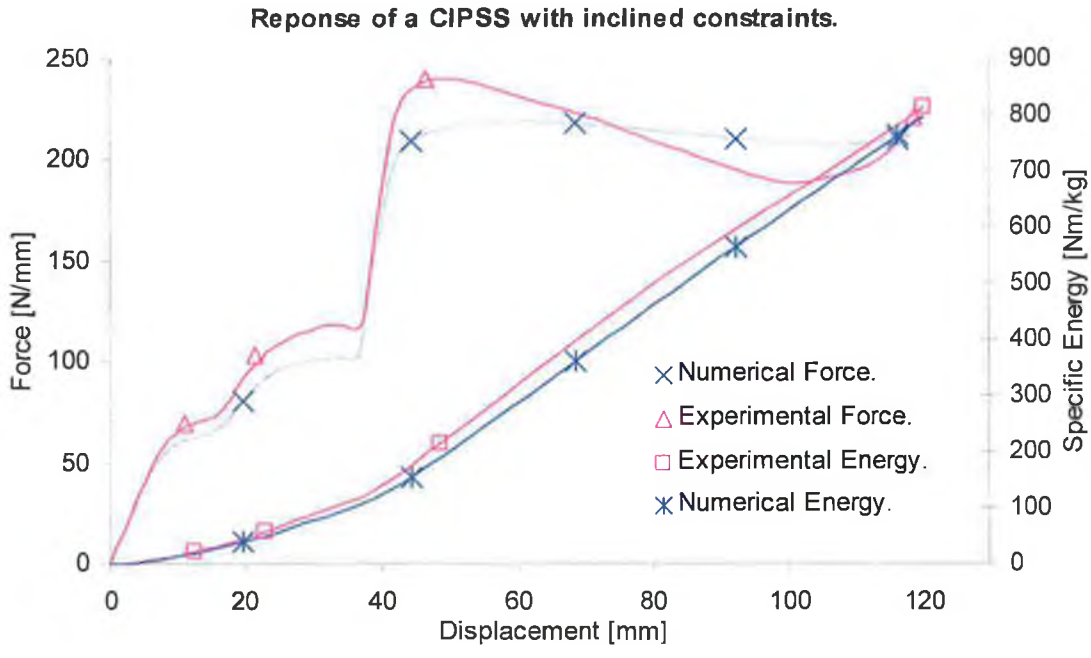

Figure 7-81: **Comparison of results between the numerical and experimental methods for a CIPSS subjected to inclined constraints.**

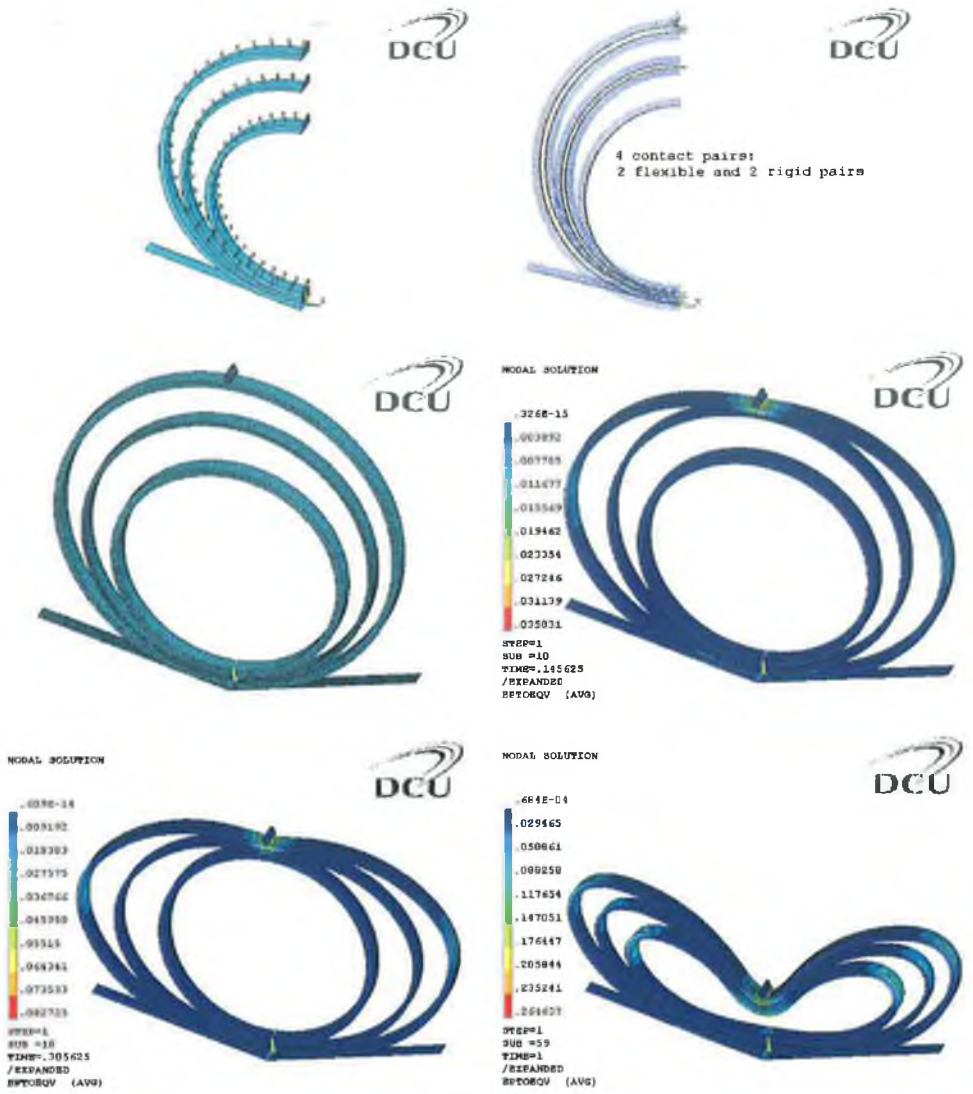

Figure 7-82: **Illustration of the boundary and contact definitions with a total Von Mises total strain plot for a CIPSS with inclined constraints.**

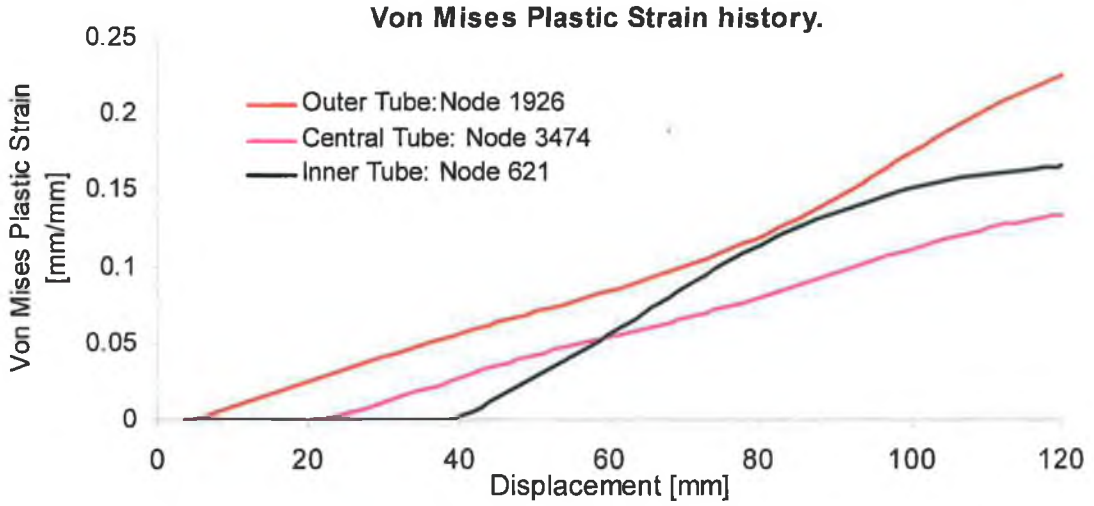

Figure 7-83: Plastic strain history at three selected nodes for a CIPSS subjected to inclined constraints.

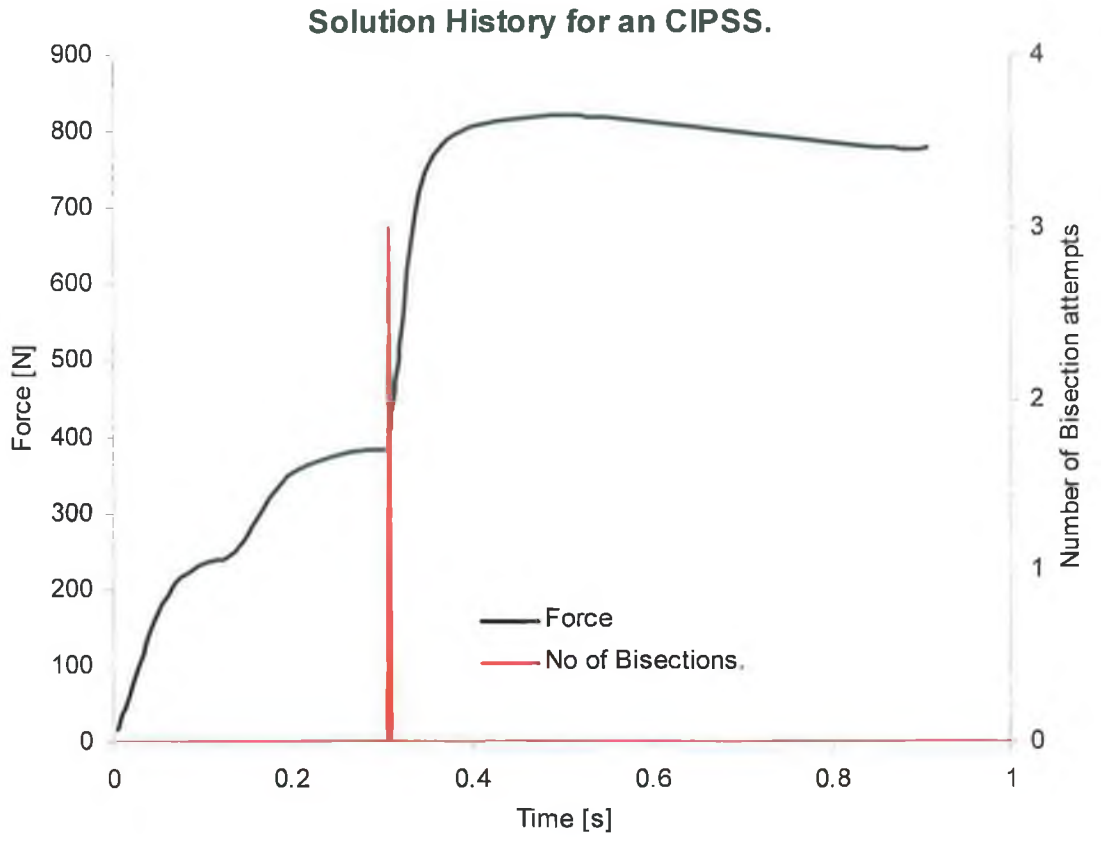

Figure 7-84: Force-time graph depicting the bisection history of the CIPSS with inclined constraints.

7.11.2 CIPSS - Vertical Constraints.

Figure 7-85 shows the outcome of results from both the numerical and experimental methods for a CIPSS subjected to vertical constraints. Again the force - deflection response predicted by the numerical method is in good agreement with that of experiments with only a slight under – prediction in the collapse load of each tube. The force appears to remain almost constant in the post collapse stage of crushing. In terms of the total specific energy absorbed, the numerical method over predicts the experimental value by 2%.

The Von Mises plastic strain history for this system is depicted in Figure 7-86. As expected, an increase in the plastic strain for the full displacement in the regions of the selected nodes is observed. Note for the outer tube at approximately 18mm defection that node 1926 began to experience an increase rate of plastic strain. This behaviour was due to the outer tube establishing contact with the sidewalls which generated increased bending in this region resulting in the observed increase in strain from 18mm. Figure 7-87 offers a Von Mises total strain plot at the various stages of displacement for this particular system.

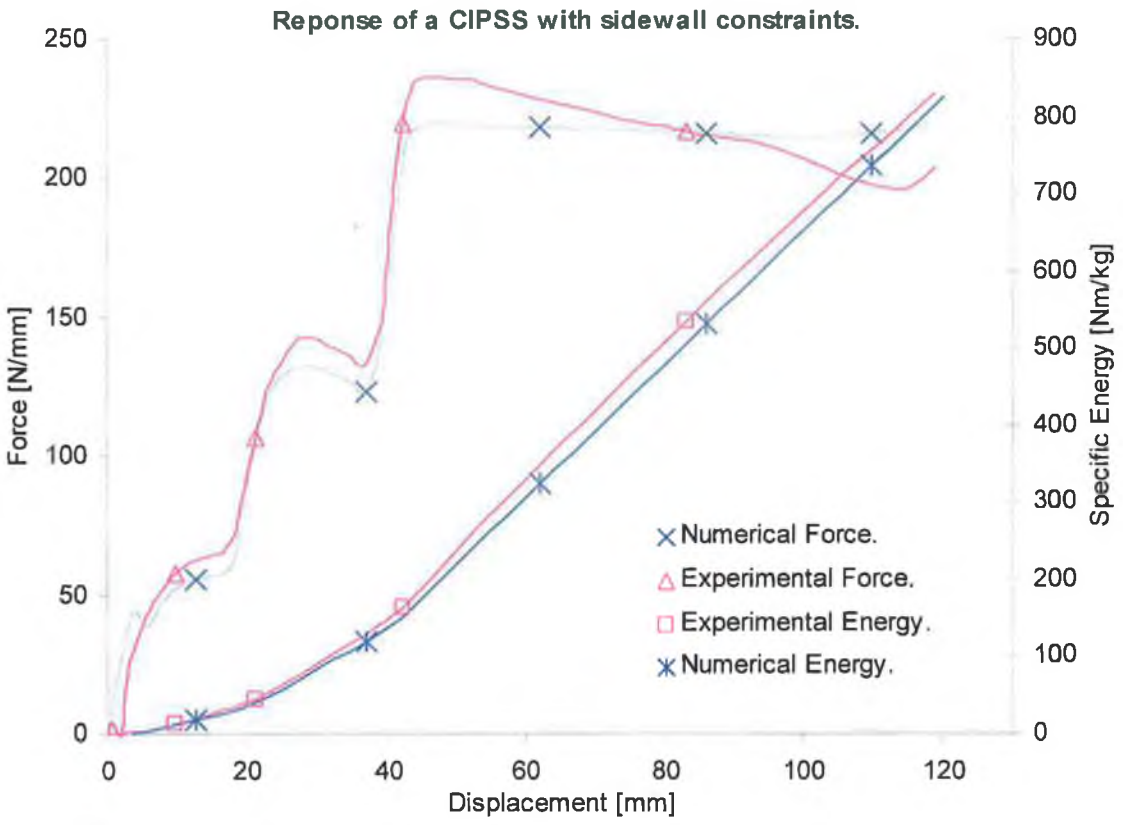

Figure 7-85: **Comparison of results between the numerical and experimental methods for a CIPSS subjected to sidewall constraints.**

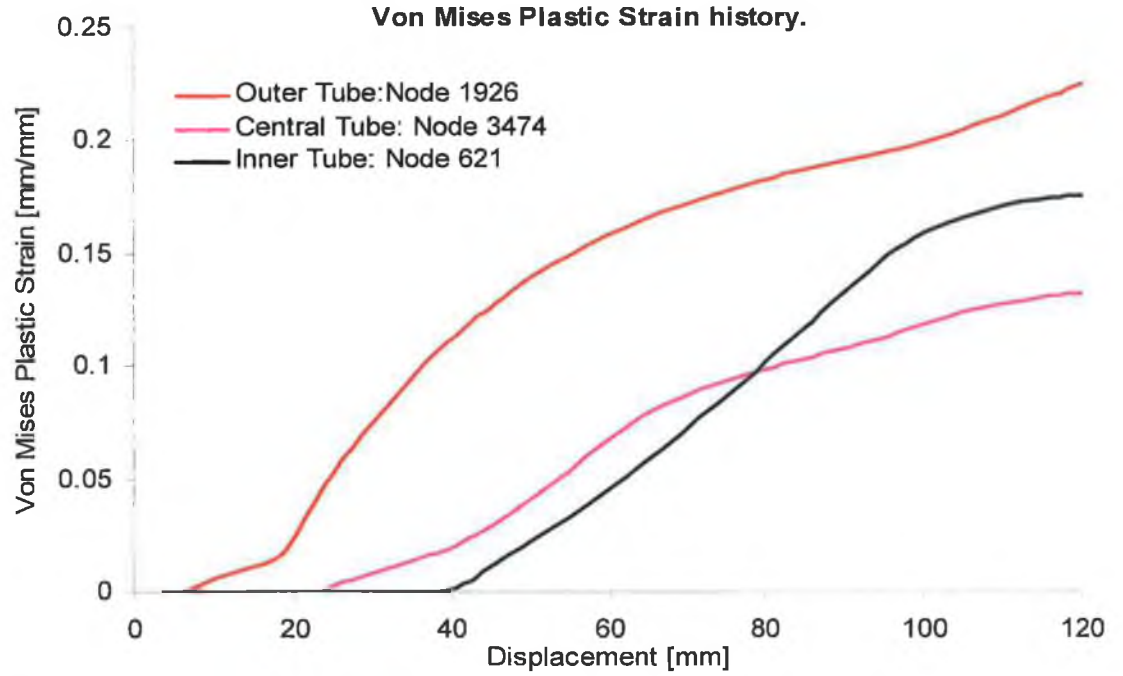

Figure 7-86: Plastic strain history at 3 selected nodes for a CIPSS subjected to sidewall constraints.

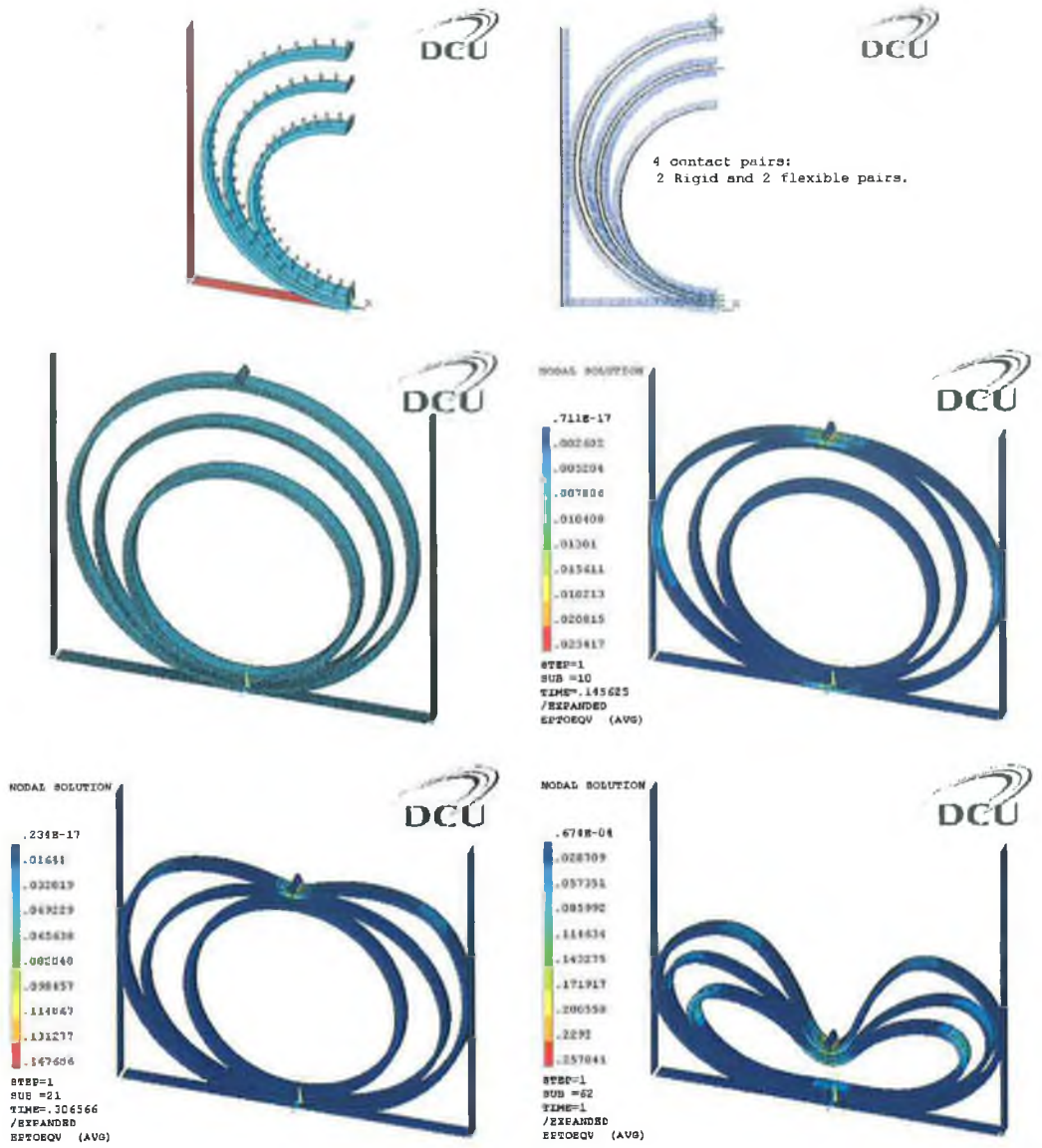

Figure 7-87: **Illustration of the boundary and contact definitions with a Von Mises total strain plot for a CIPSS with sidewall constraints.**

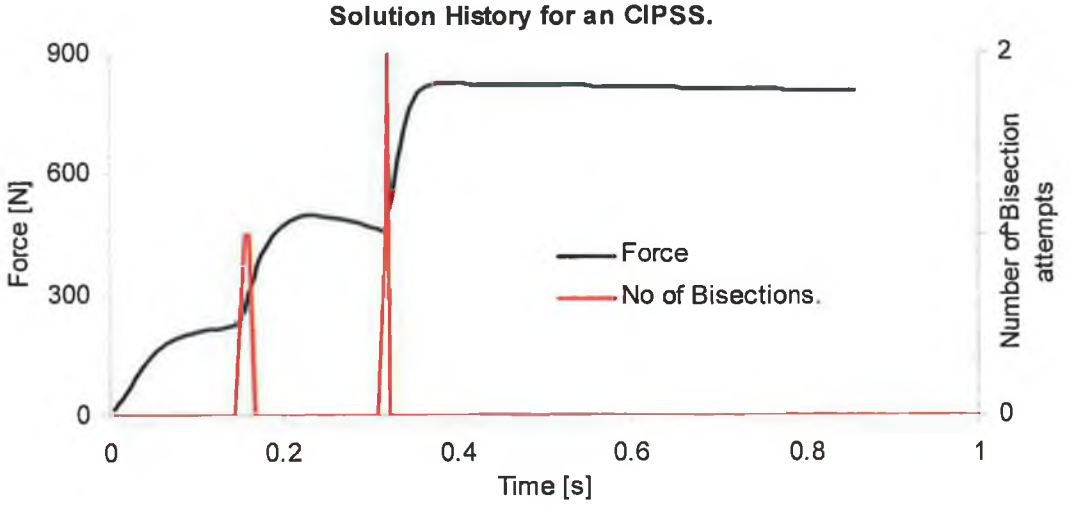

Figure 7-88: Force-time graph depicting the bisection history of the CIPSS with side constraints.

7.11.3 CIPSS - Combined Constraints.

A similar prediction in the force – deflection response by the numerical method for this system is offered in Figure 7-89. A small under prediction in the collapse load was observed whilst in the post collapse stages the force remained constant as opposed to a softening stage as observed in experiments.

Figure 7-90 and Figure 7-91 shows the various stages of displacement and the Von Mises plastic strain history of the three selected nodes respectively. It can be seen that the nodes behaved in a same manner as the previous two systems in that an increase in plastic strain occurred throughout the deformation stroke. Again it can be seen that node experienced an increase in plastic strain as soon as contact was established between the outer tube and the sidewall.

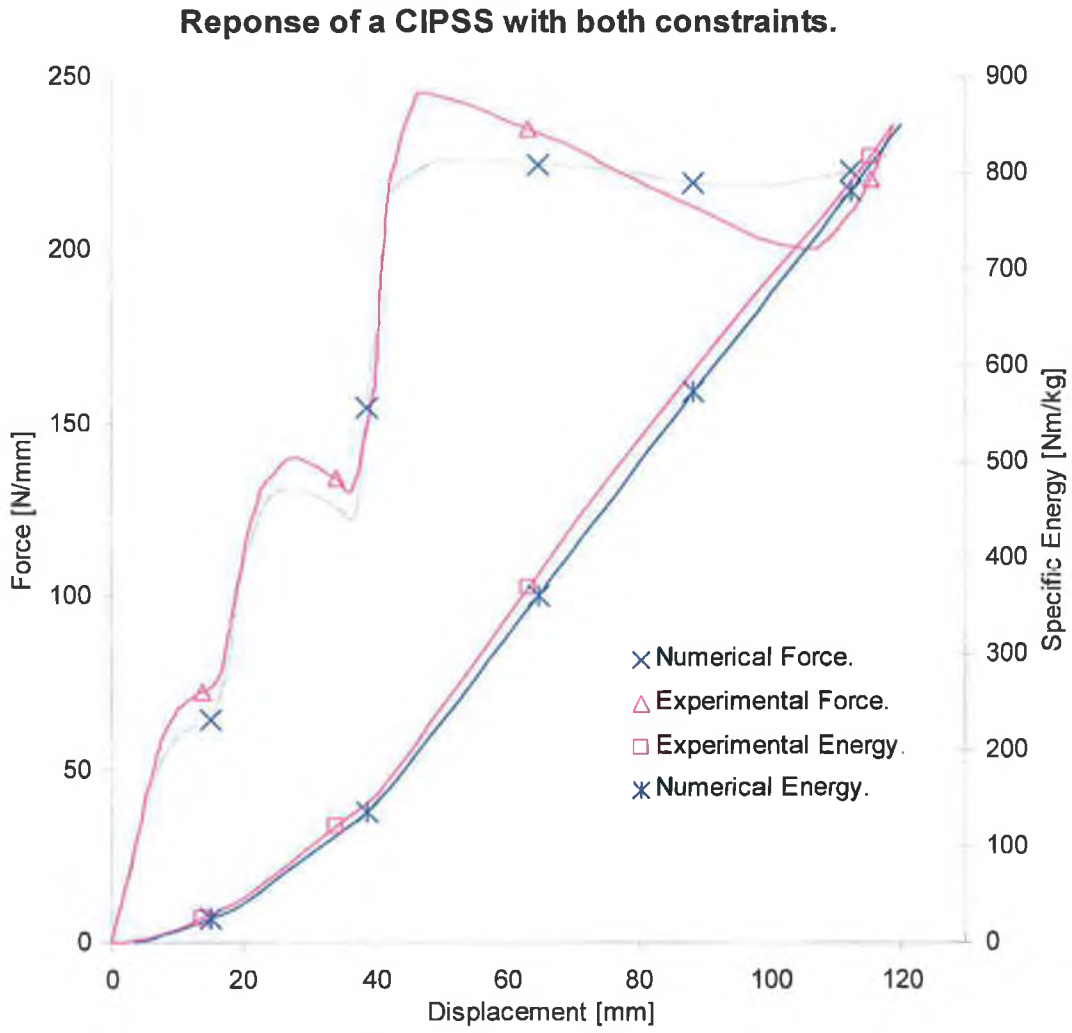

Figure 7-89: Comparison of results between the numerical and experimental methods for a CIPSS subjected to both constraints.

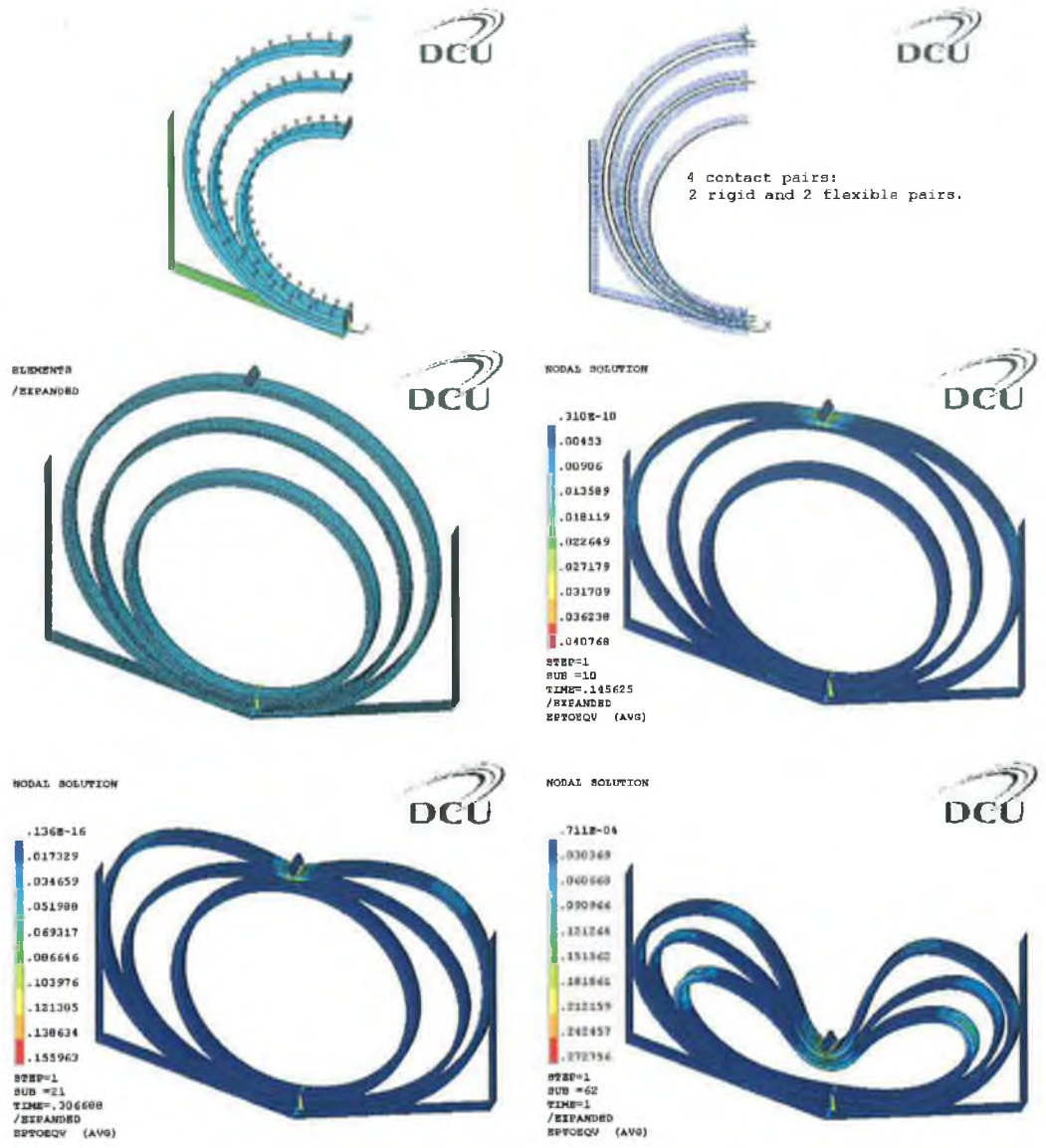

Figure 7-90: **Illustration of the boundary and contact definitions with a total Von Mises total strain plot for a CIPSS with combined constraints.**

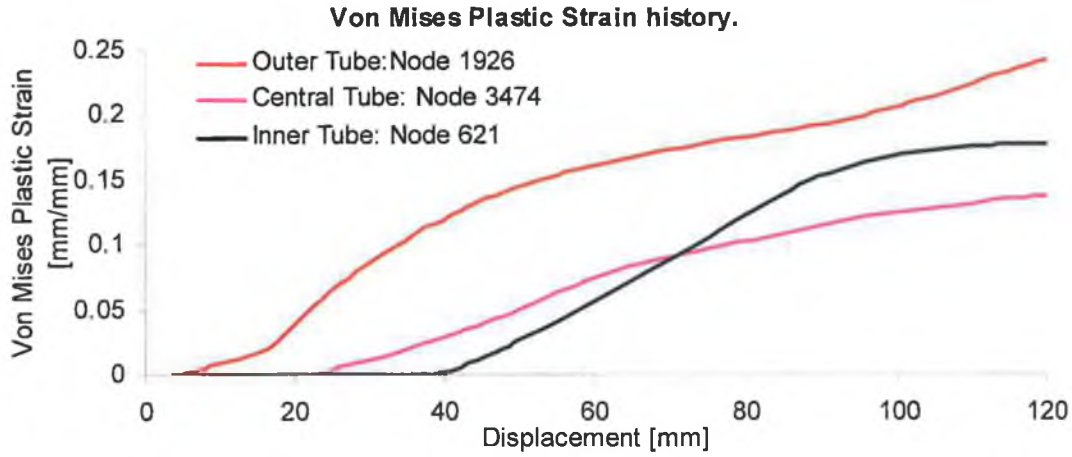

Figure 7-91: **Plastic strain history at three selected nodes for a CIPSS subjected to combined constraints.**

7.11.4 CIPDS - Combined Constraints.

Figure 7-92 illustrates a comparison of results using the numerical method for both the CIPSS and the CIPDS subjected to a point load indenter and combined constraints. It can be seen how the CIPDS exhibits a more desirable response in that the response is rectangular in shape. At 43mm deflection the CIPDS has absorbed 55% more energy than its CIPSS counterpart; this is due to the fact that the system is more efficient in absorbing energy since the three tubes are being displaced synchronously. It can be seen however that the total displacement stroke for the CIPDS is 100mm as opposed to 120mm for the CIPSS; this was expected since the presence of the dampers will compromise the final length of the displacement stroke. Despite this, the CIPDS absorbed approximately 5% more energy. Figure 7-93 and Figure 7-94 depict the various stages of displacement and the plastic strain history of the three selected nodes respectively. A dynamic simulation was also prepared for the CIPDS subjected to the combined constraints and a point load indenter as shown in Figure 7-95. It can be seen that the mode of response is very similar to the static case, however the magnitude of force is a lot higher. As explained in section 7.8.2 with the aid of Figure 7-52 and Figure 7-64, the numerical code had a tendency to over-predict the magnitude of force for the dynamic response of the CIPDS and the OPIDS. Therefore, it can be assumed that the same behaviour was observed for the CIPDS compressed dynamically under the action of a point load indenter. Figure 7-96 illustrated the various stages of evolution for this particular system.

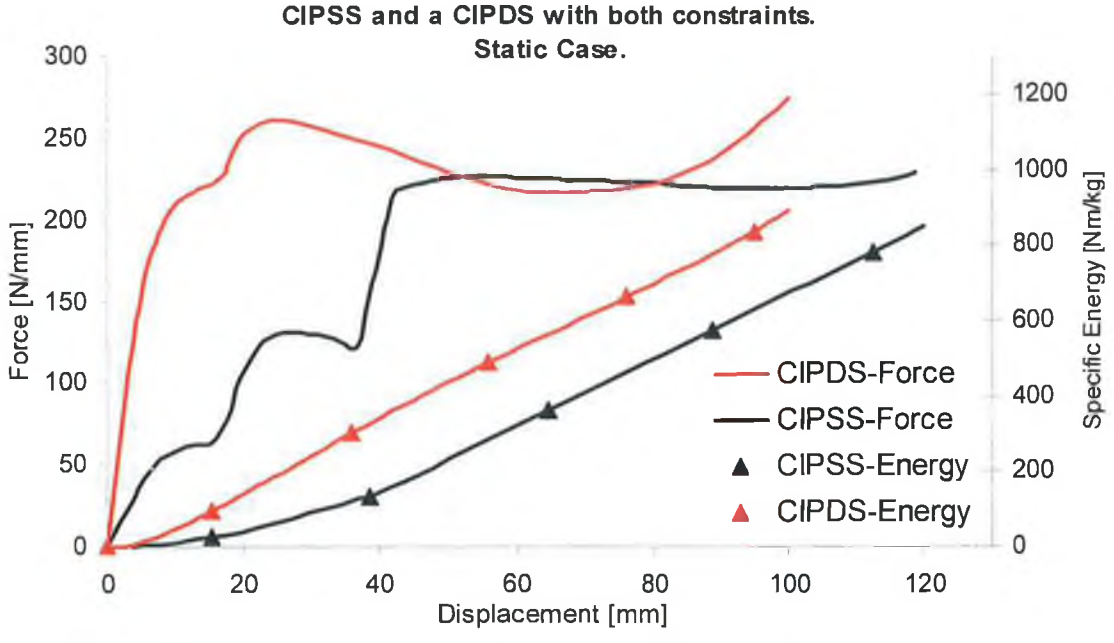

Figure 7-92: **Comparison of results for a CIPSS and a CIPDS compressed under a point load indenter and exposed to combined constraints.**

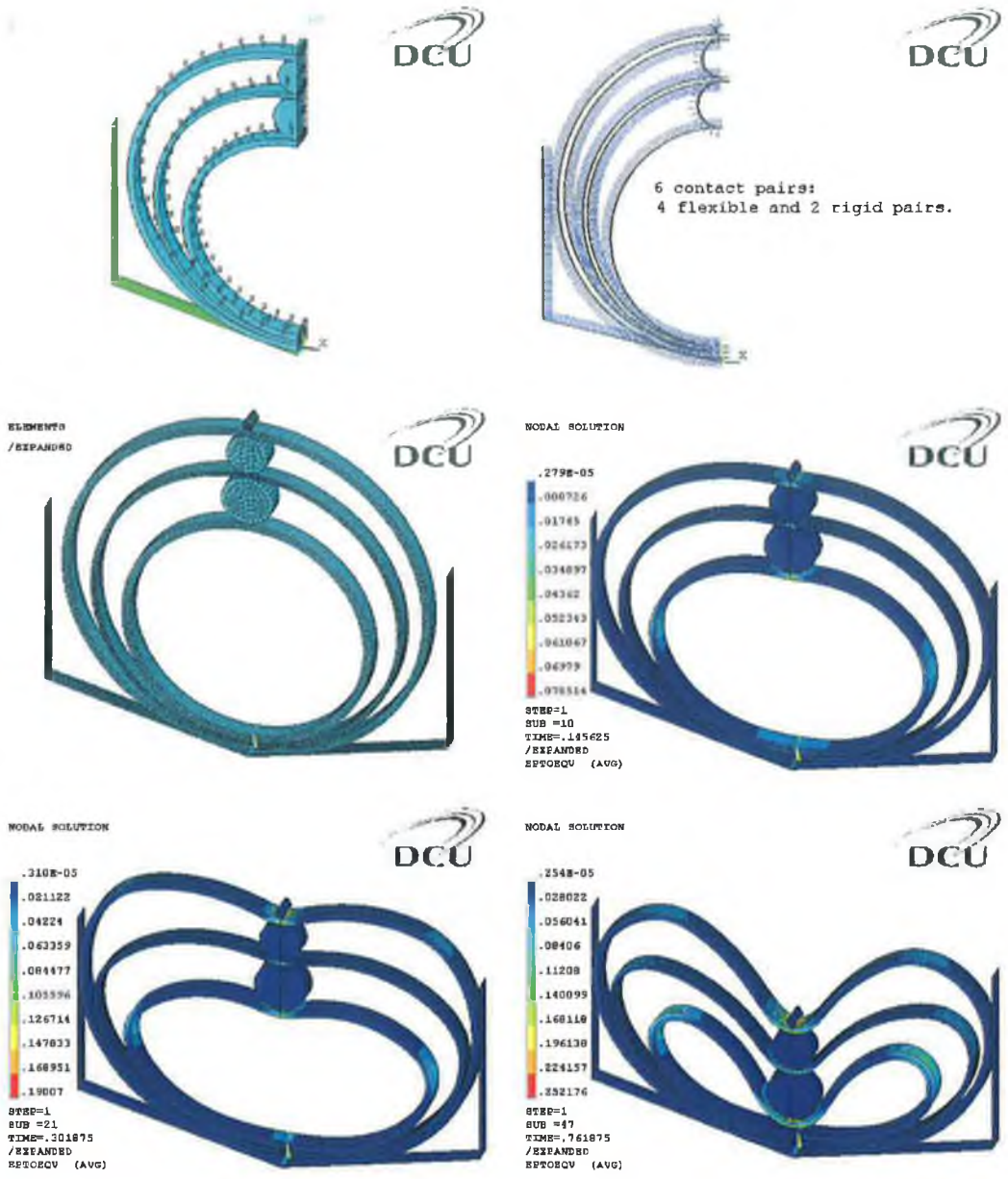

Figure 7-93: **Illustration of the boundary and contact definitions with a Von Mises total strain plot for a CIPDS with both constraints.**

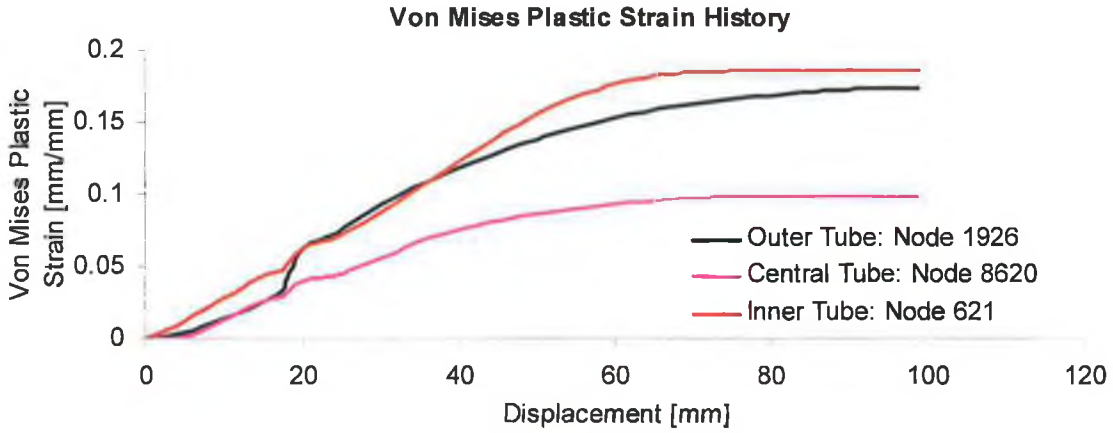

Figure 7-94: **Plastic strain history at three selected nodes for a CIPDS subjected to combined constraints.**

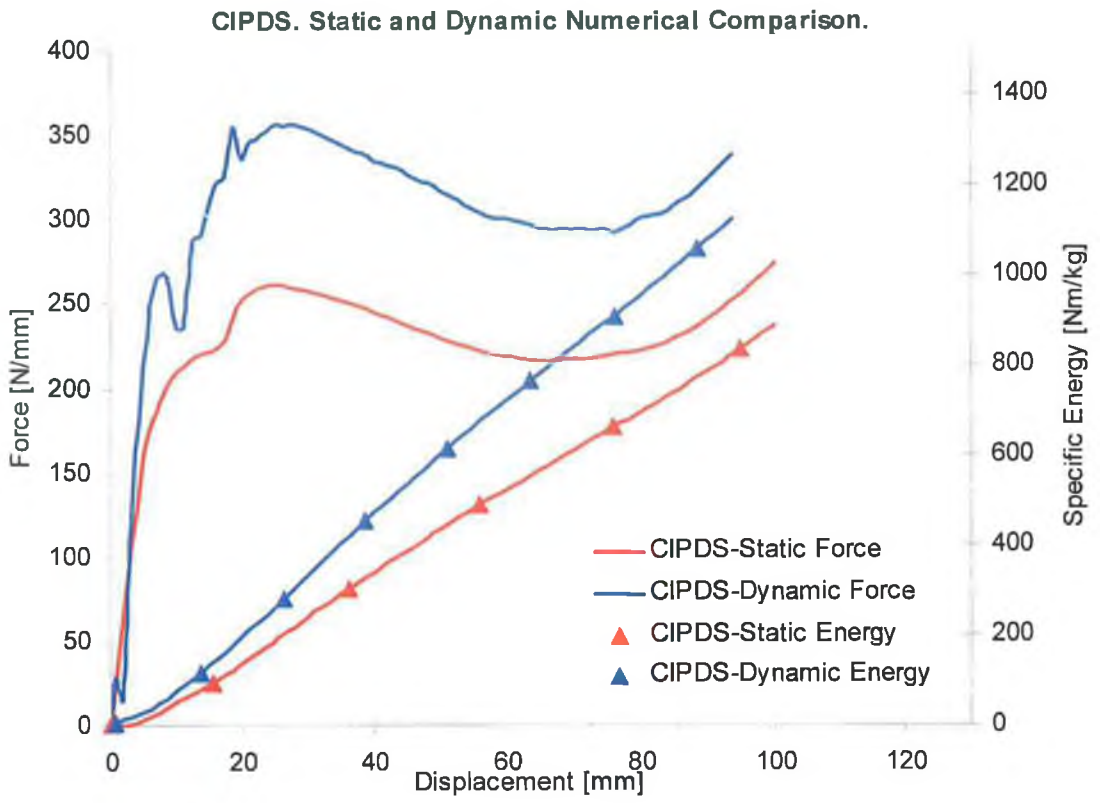

Figure 7-95: **Static and Dynamic numerical response for a CIPDS compressed with a point load indenter.**

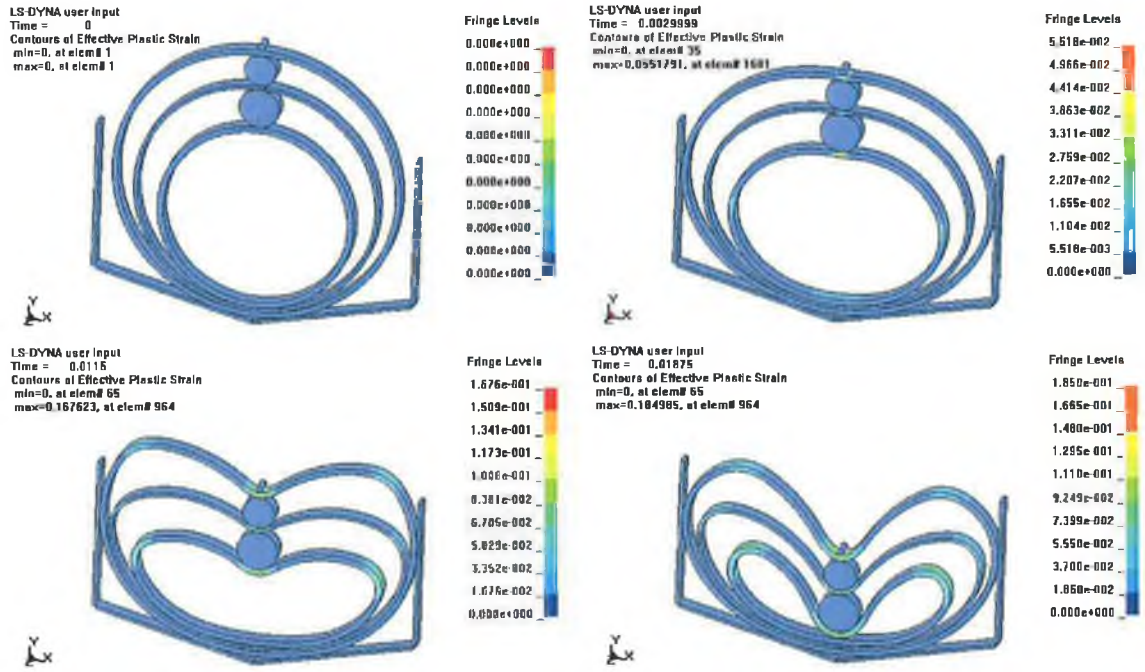

Figure 7-96: Effective plastic strain evolution of a CIPDS subjected to dynamic lateral loading.

7.12 Cylindrical Indenter.

7.12.1 CIPSS - Inclined Constraints.

For a CIPSS compressed under the action of a cylindrical indenter and exposed to inclined constraints, the corresponding force – deflection response is illustrated in Figure 7-97. Again, an under prediction in force by the numerical method was observed. However, more importantly is the amount of energy absorption as predicted by the numerical method in which a small under prediction of 7% was observed. Figure 7-98 illustrates the Von Mises total strain displacement plots. The plastic strain history from three selected nodes is displayed in Figure 7-99. Since a cylindrical indenter is the intermediate condition between the limiting cases of a point load indenter and a flat plate indenter, it can be expected that firstly, the rate of increase in plastic strain will be less than of a CIPSS crushed under a point load indenter and secondly, the plastic strain in these regions will eventually be evenly distributed and become constant as in the case of a flat plate indenter.

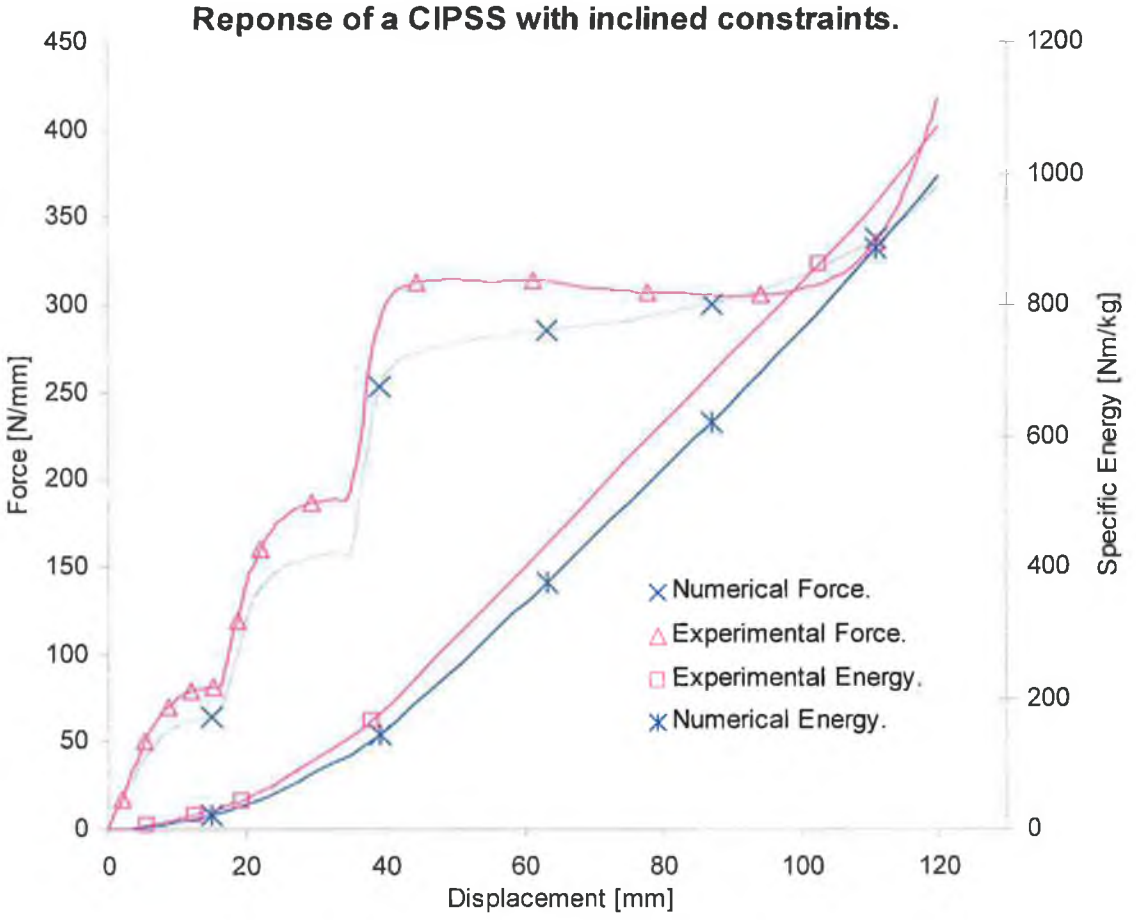

Figure 7-97: Comparison of results between the numerical and experimental methods for a CIPSS subjected to inclined constraints.

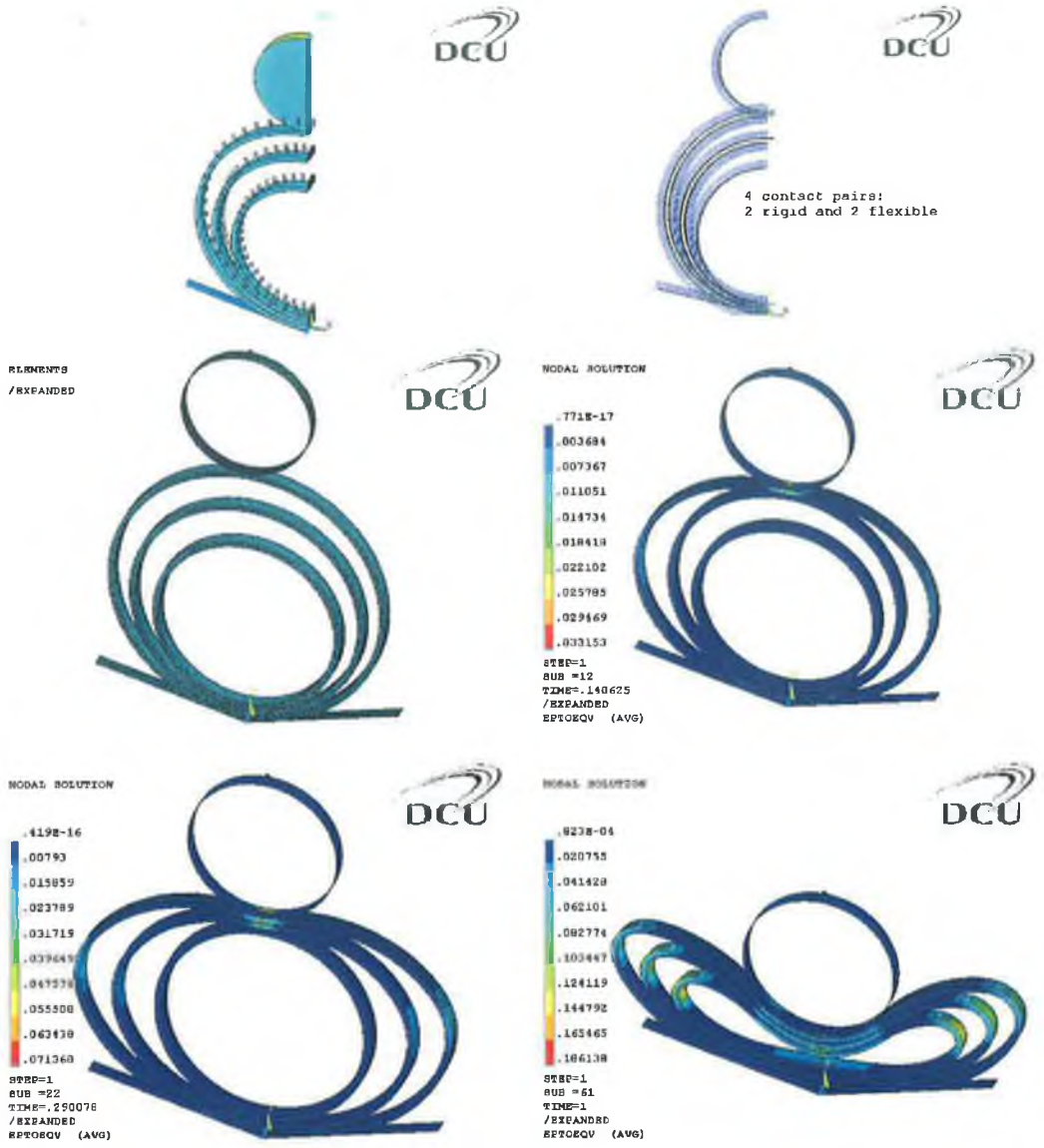

Figure 7-98: **Illustration of the boundary and contact definitions with a total Von Mises plastic strain plot for a CIPSS with inclined constraints.**

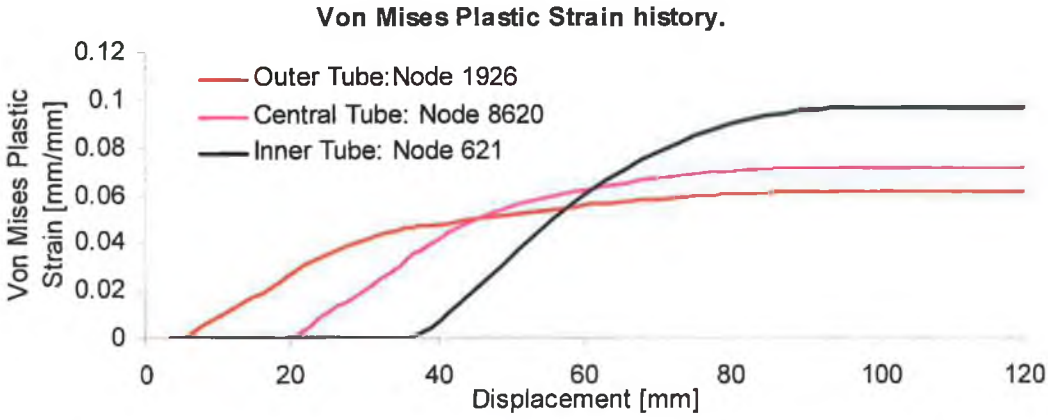

Figure 7-99: Plastic strain history at three selected nodes for a CIPSS subjected to inclined constraints.

7.12.2 CIPSS - Vertical Constraints.

Figure 7-100 illustrates a CIPSS compressed under the action of a cylindrical indenter and with sidewall constraints, it appears that a greater under prediction in force is observed for the full displacement stroke, however a reasonable correlation was found in which the post collapse response predicted by the numerical method increased at the same rate as that detected in experiments. A difference of 12% exists between the numerical and experimental methods for the final specific energy absorbed. The displacement evolution of this system illustrating the Von Mises total strain is displayed in Figure 7-101. Note in the final displacement plot, the location of the plastic hinges near the cylindrical indenter. Figure 7-102 displays the Von Mises total strain history for this system subjected to sidewall constraints. As mentioned previously, node 1926 underwent a greater increase in plastic strain at approximately 18mm due to the outer tube making contact with the sidewall and therefore increasing the amount of plastic bending. It appears that the plastic strain became constant at an early stage of deflection in the region of this node. This behaviour is similar to that observed by a CIPSS compressed under the action of a flat plate indenter.

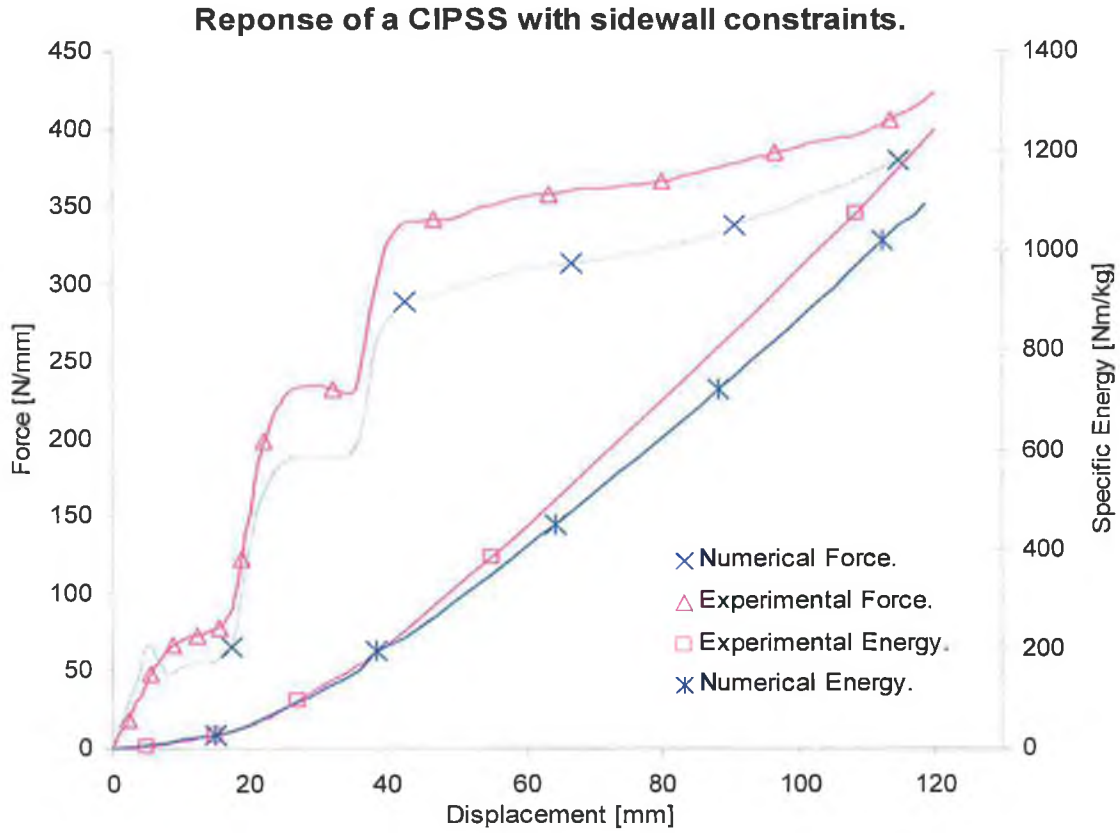

Figure 7-100: Comparison of results between the numerical and experimental methods for a CIPSS subjected to sidewall constraints.

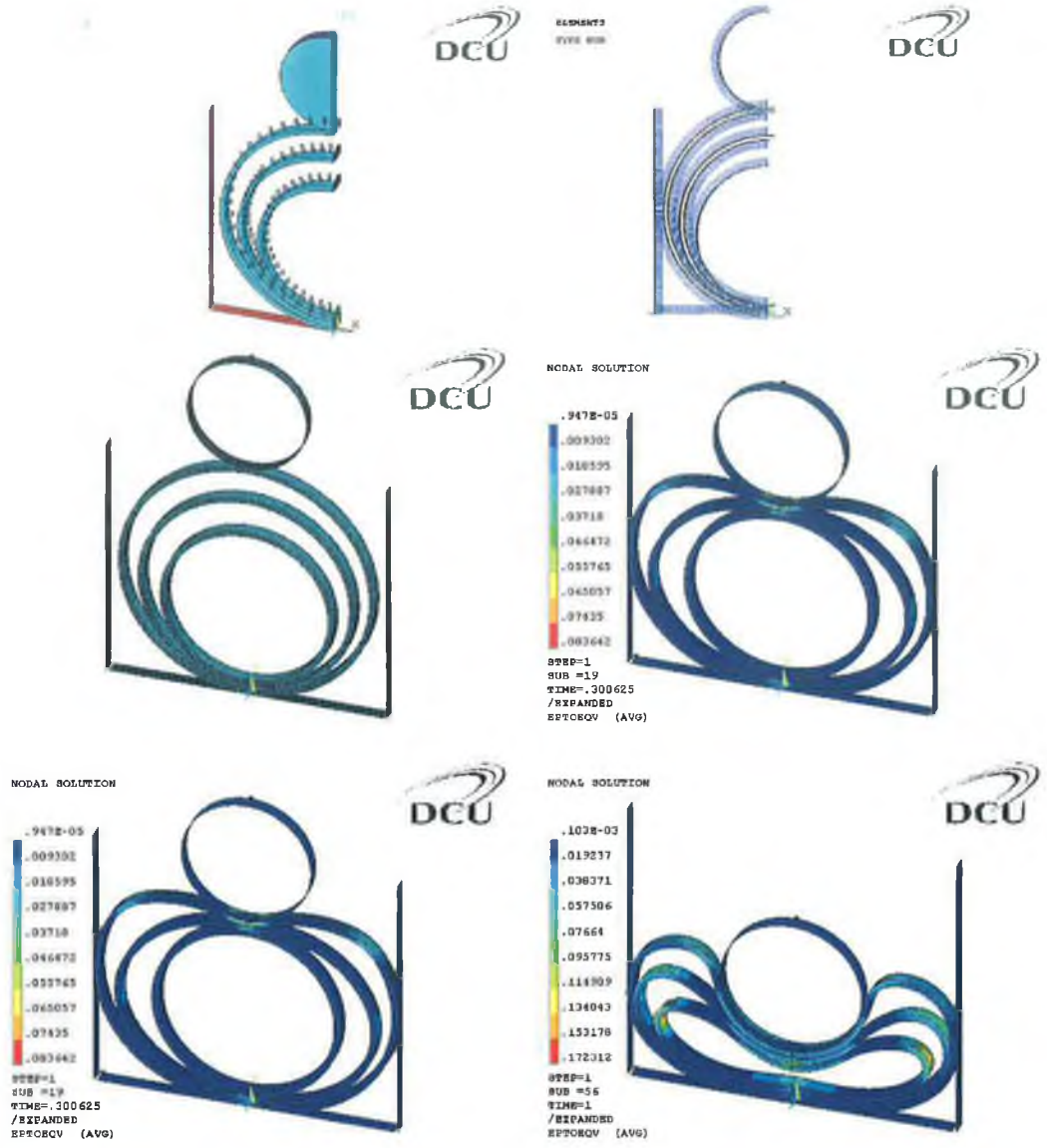

Figure 7-101: **Illustration of the boundary and contact definitions with a total Von Mises plastic strain plot for a CIPSS with sidewall constraints.**

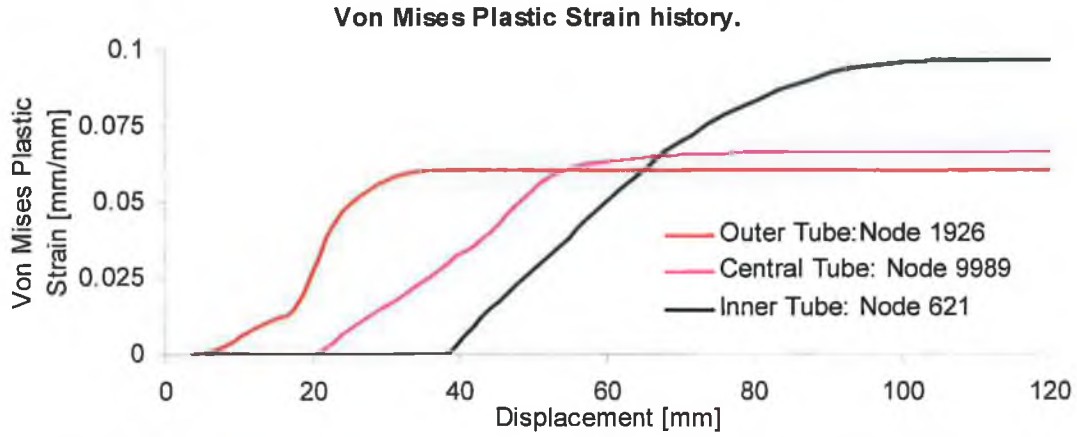

Figure 7-102: Plastic strain history at three selected nodes for a CIPSS subjected to sidewall constraints.

7.12.3 CIPSS - Combined Constraints.

Figure 7-103 depicts the numerical and experimental response of a CIPSS subjected to a cylindrical indenter and combined constraints. An under prediction in force was observed for this particular system. However, the mode of deformation is very similar to that observed in experiment. A difference of 11% was observed between the numerical and experimental methods in predicting the final energy absorption value. The boundary conditions and contact definitions in addition to the Von Mises total strain displacement evolution of this system is depicted in Figure 7-104. Figure 7-105 depicts a similar plastic strain history of the three selected nodes as in the previous system.

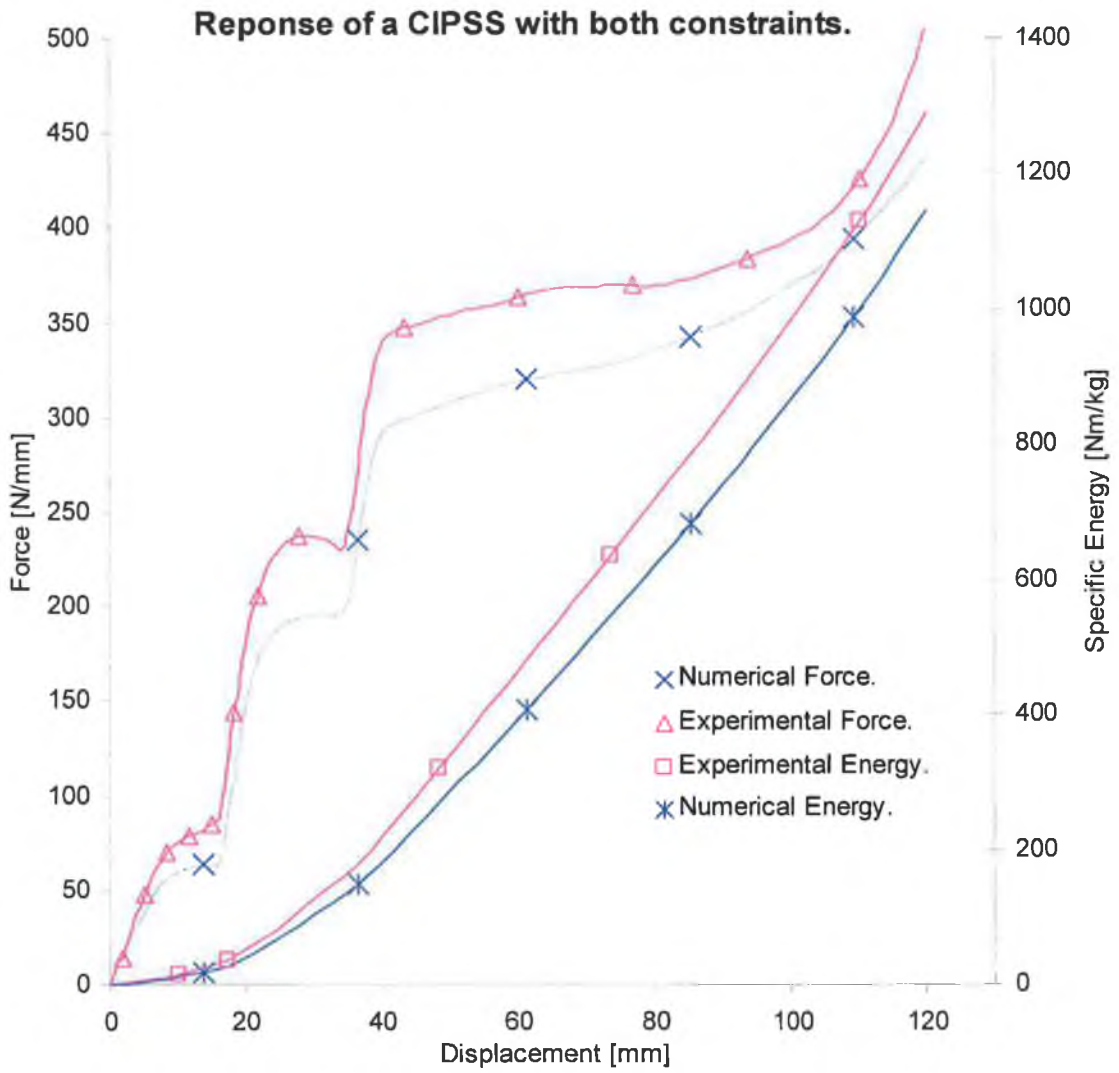

Figure 7-103: Comparison of results between the numerical and experimental methods for a CIPSS subjected to both constraints.

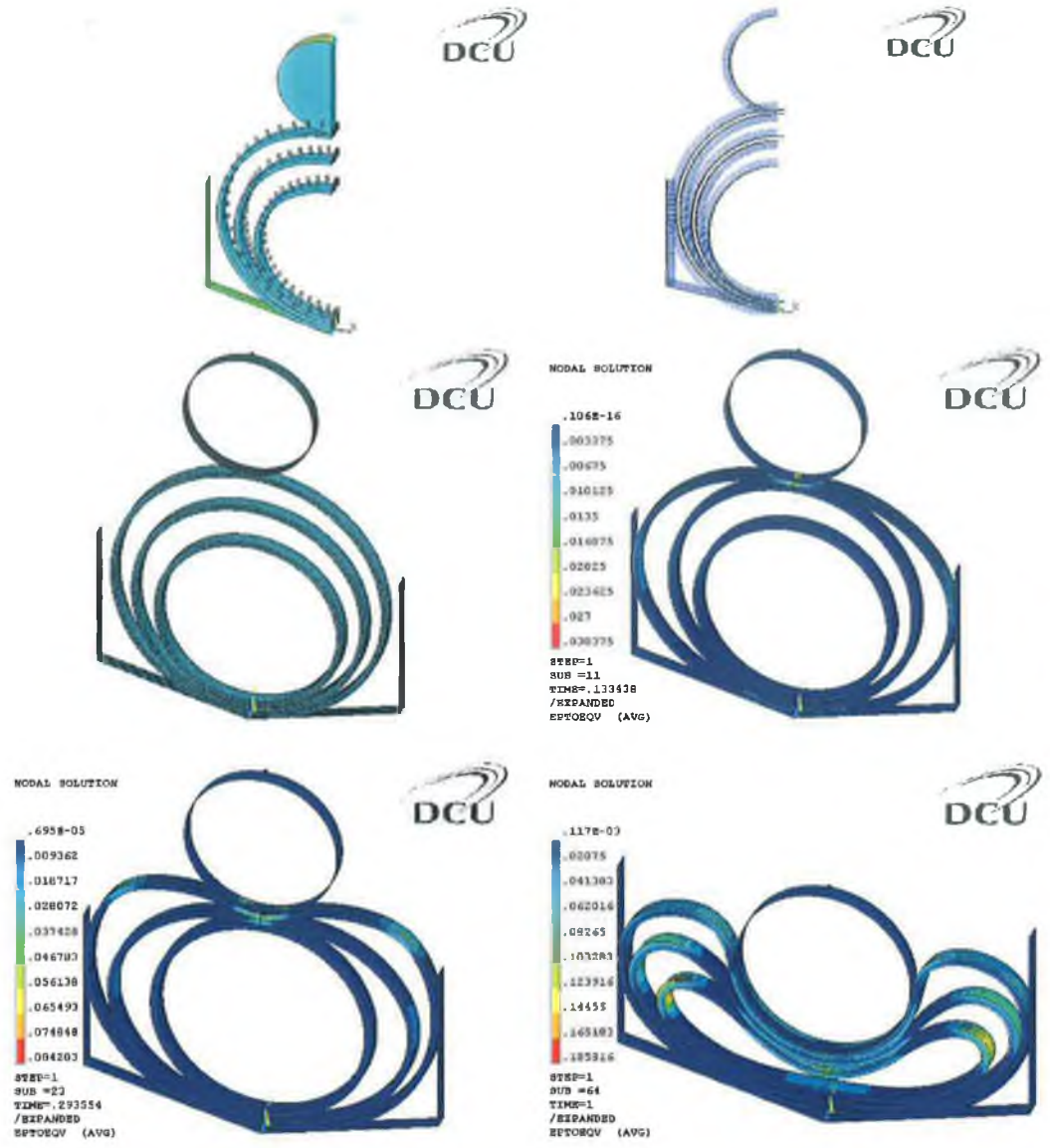

Figure 7-104: **Illustration of the boundary and contact definitions with a Von Mises total strain plot for a CIPSS with both constraints.**

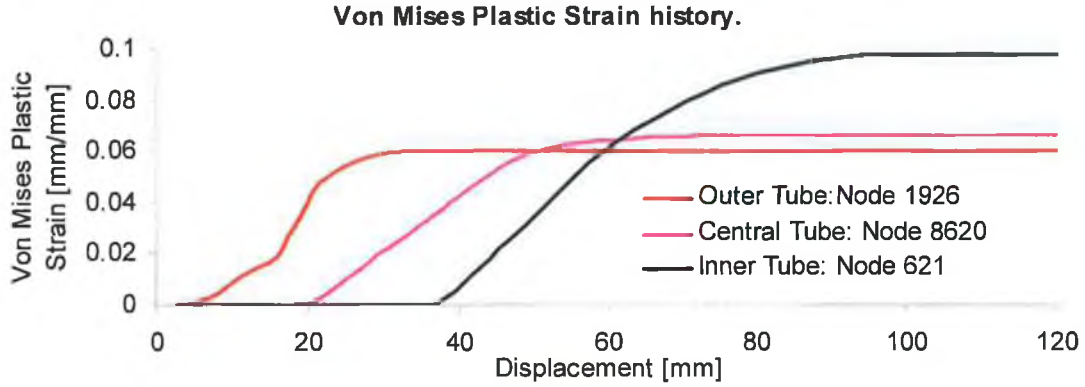

Figure 7-105: Plastic strain history at 3 selected nodes for a CIPSS subjected to combined constraints.

7.12.4 CIPDS - Combined Constraints.

Figure 7-106 depicts a numerical comparison of a CIPSS and a CIPDS compressed under the action of a cylindrical indenter and exposed to combined constraints. It can be seen that a more desirable response is exhibited by the CIPDS due to its rectangular shaped behaviour. In contrast to the CIPDS compressed with a point load indenter which absorbed more energy than its CIPSS counterpart (See Figure 7-92), this system absorbs less energy. This was due to the fact that for the CIPSS case (See Figure 7-104), the outer tube wrapped around the cylindrical indenter to large extent which therefore caused an increase in energy absorption. The resulting difference in the amount of energy absorption between the two systems was approximately 11%. Figure 7-107 and Figure 7-108 depict the various stages of displacement and the plastic strain history of the three selected nodes respectively. A dynamic simulation was also prepared for the CIPDS subjected to the combined constraints and a cylindrical indenter as shown in Figure 7-109.A similar over prediction in response in the force was also observed by the numerical code for this particular system and is also due to the strain rate parameters used in the material model. It can be seen however, that the deformation mode is similar to its quasi static case. The various stages of evolution for this system CIPDS is depicted in Figure 7-110.

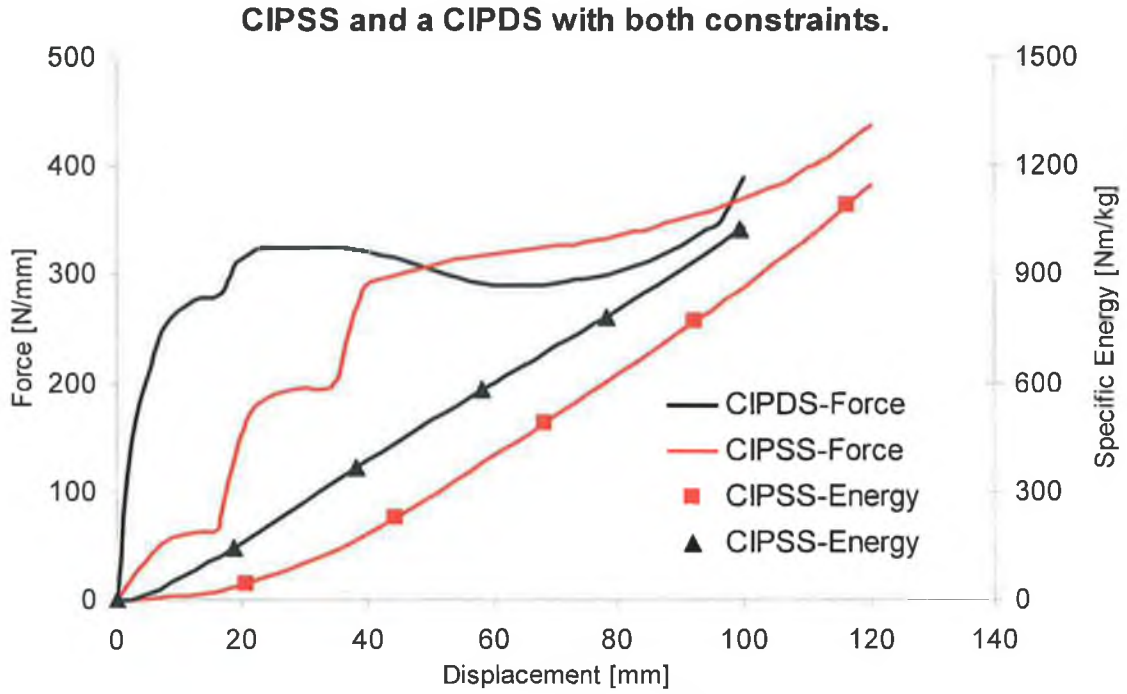

Figure 7-106: Comparison of results for a CIPSS and a CIPDS compressed under a cylindrical indenter and exposed to combined constraints.

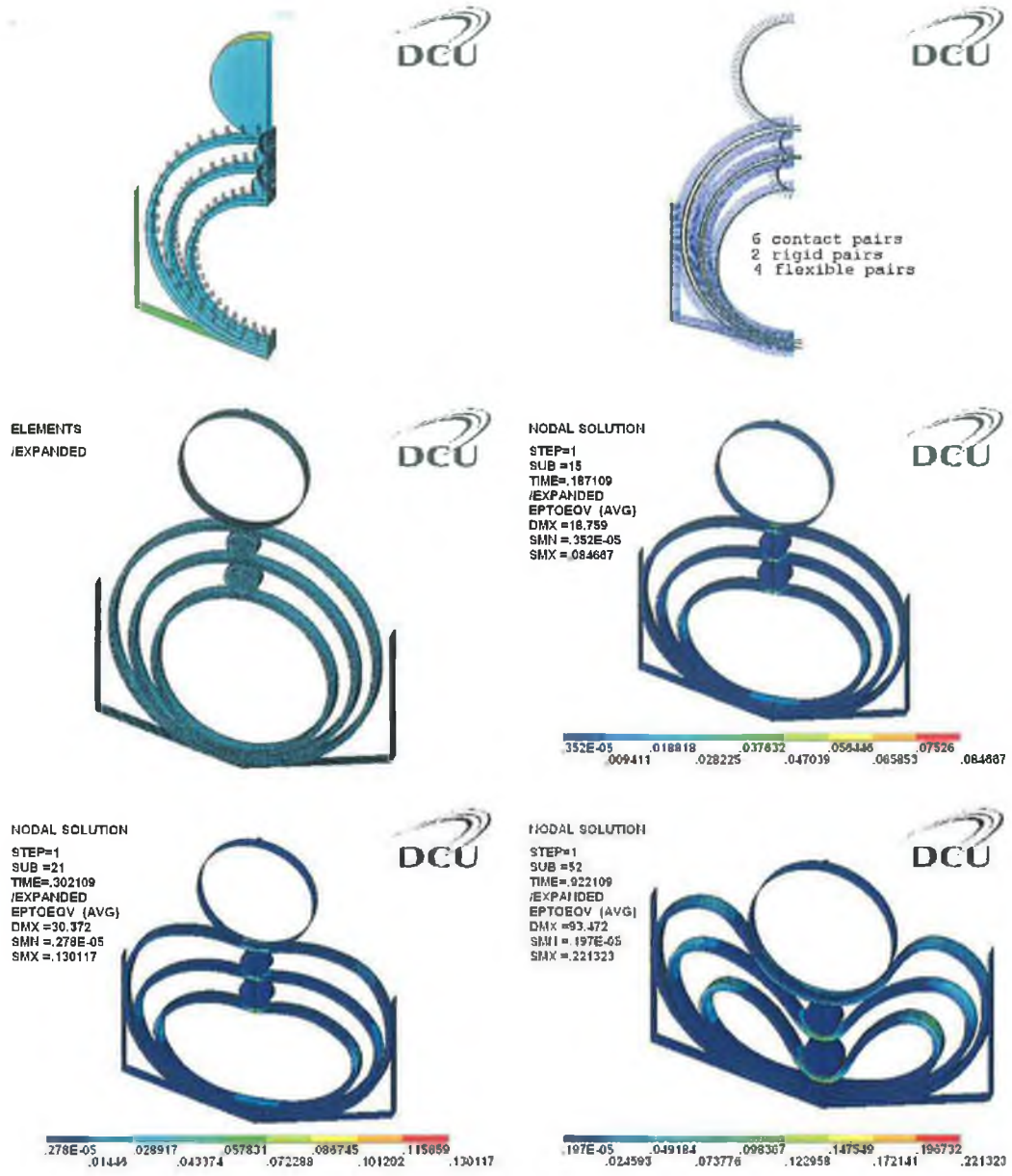

Figure 7-107: **Illustration of the boundary and contact definitions with a Von Mises total strain plot for a CIPDS with both constraints.**

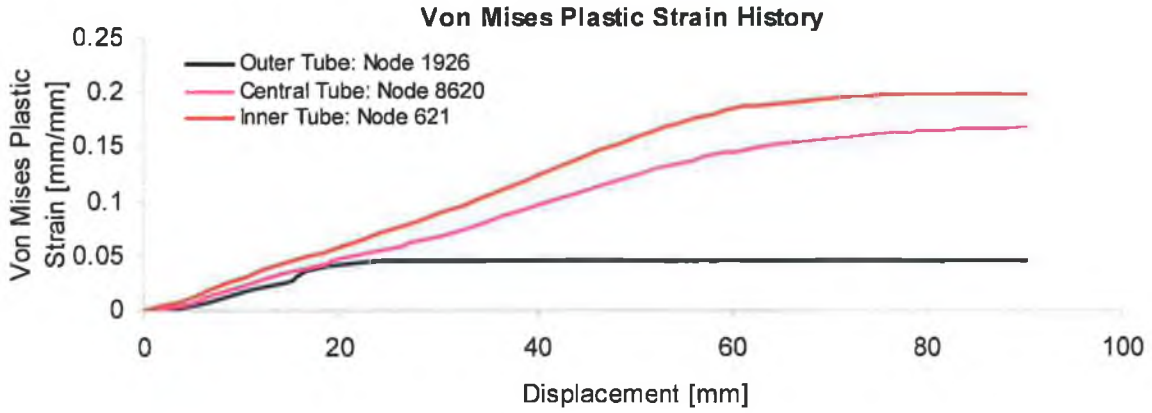

Figure 7-108: **Plastic strain history at three selected nodes for a CIPDS subjected to combined constraints.**

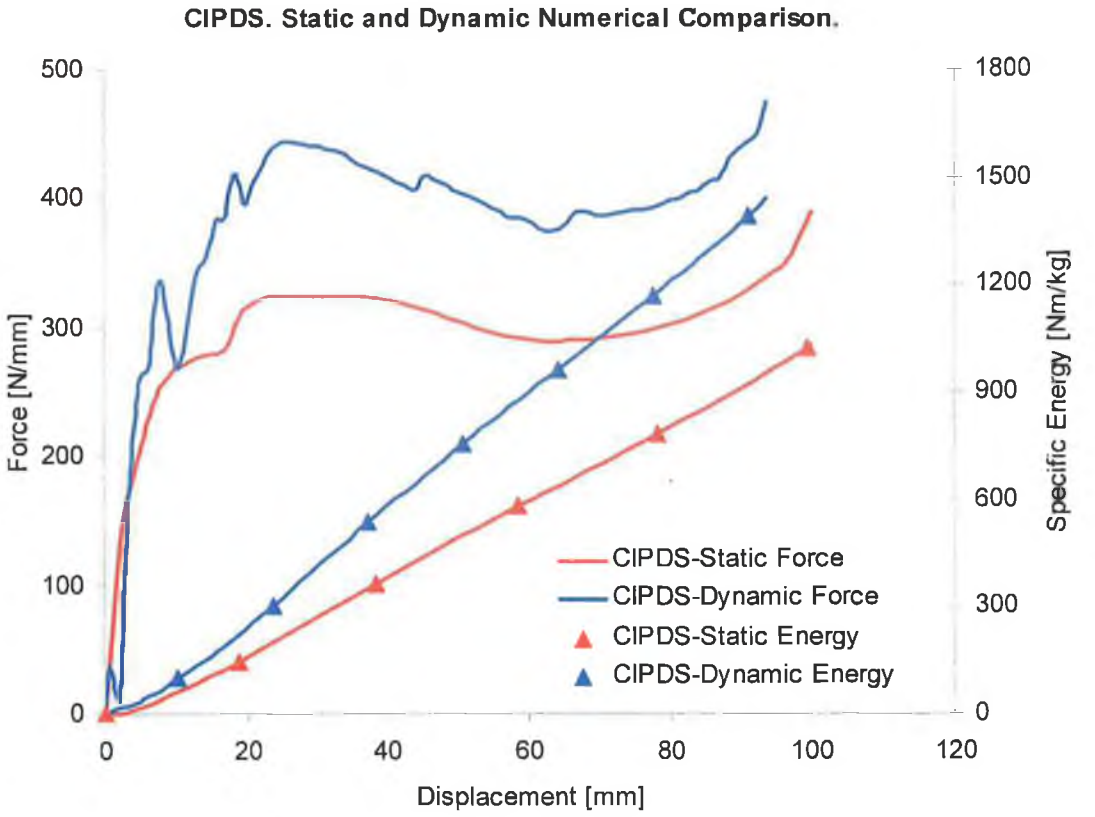

Figure 7-109: Static and Dynamic numerical response for a CIPDS compressed with a cylindrical indenter.

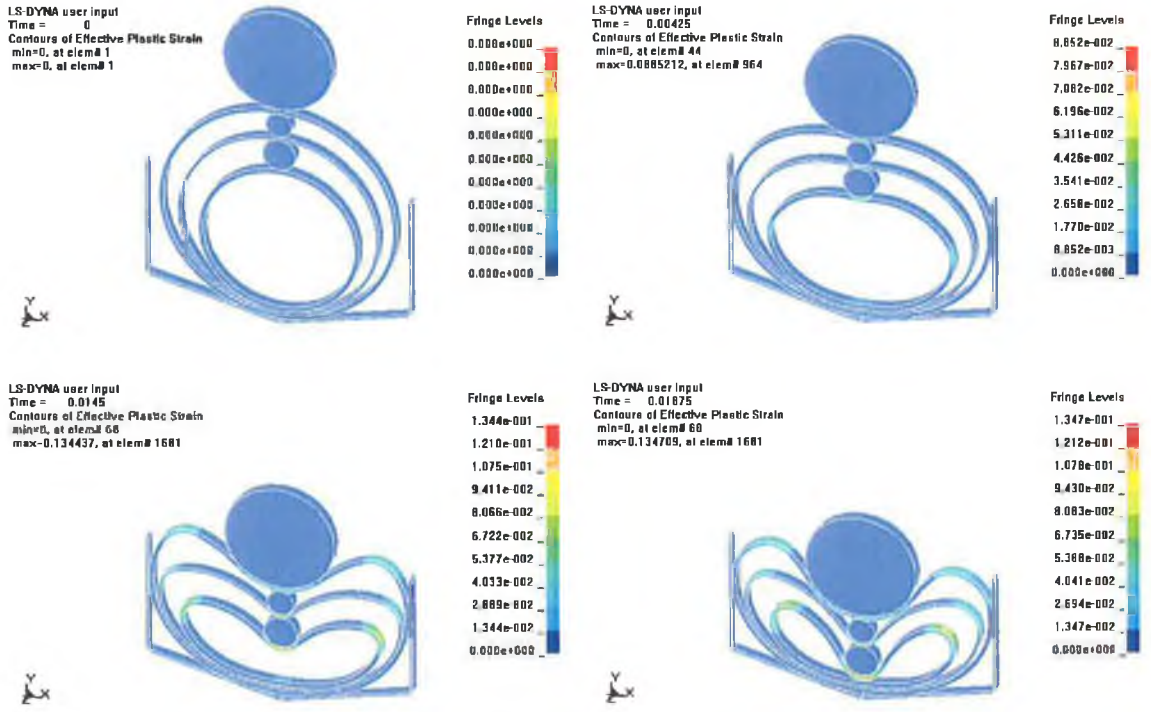

Figure 7-110: Effective plastic strain evolution of a CIPDS subjected to dynamic lateral loading.

7.13 Summary of Chapter Seven.

- A description was given on the numerical procedures taken in both ANSYS and LS-DYNA for the simulation of the various energy absorbers.
- An account was given on the procedure taken within ANSYS for the creation of the oblong tubes. This was achieved by applying a tensile force to each tube and updating the newly formed geometry before being discretized with elements.
- A mesh convergence test was analysed for both the brick element and the shell element in order to ensure that an appropriate density of elements was applied to the model to ensure reliable results.
- A comparison of results between the experimental and numerical methods was offered for each of the various energy absorbers analysed. The results were divided into two sections with the first section pertaining to chapter five and the second chapter related to chapter six.
- The chapter was divided into three sections with the first section concerned with the geometric variations of the CIPSS. It was found that very good agreement existed between the numerical and experimental methods. However, it was noticed that large deviations in results occurred fro the SCOPSS and the SCIPDS crushed under a plate indenter in the later stages of displacement. This was due to the fact that the slots present in the tubes caused the system to deform asymmetrically as a result of geometric imperfections.
- The second section was concerned with the quasi- static and dynamic analysis of the IPSS and the IPDS. Again, very good agreement was found between the both methods indicating the validity of the numerical models with the exception of the OIPSS and the OIPDS. Both the implicit and explicit numerical methods had difficulty in accurately predicting the collapse load of each tube.
- The third section was concerned with the specific energy maximisation of nested system compressed quasi – statically. Excellent agreement was found between the two methods. This ensured that results obtained from further simulations not validated experimentally can be viewed with confidence.

8 Discussion of Results.

8.1 Response Optimisation of Nested Systems.

As previously mentioned in chapter one, the response optimisation of nested metallic systems is based on one of the design principles of kinetic energy absorbers which state that the resisting force should ideally remain constant during the complete displacement stroke. In an attempt to achieve this particular form of response, three different design concepts were simulated using the finite element method and validated using experimental techniques and are outlined in the following sections.

8.1.1 Out of Plane Standard Systems. (OPSS)

The first concept was based on a modified form of the CIPSS, namely the COPSS. This system exhibited an improved response in that the abrupt increase in force observed by the CIPSS was eliminated, thereby producing a *monotonically increasing* response. This was due to the fact that as the tubes were rotated, the resulting spaces between the tubes were not eliminated. Therefore upon loading, the tubes began to compress in a synchronous manner. It should be noted that the COPSS maintains its energy absorbing capacity despite its different mode of deformation which is desirable. The application of the various indenters to compress the nested systems resulted in a very similar force-deflection response; the only difference being the magnitude of force which varied slightly for each indenter. A simple method in optimising the response of a COPSS by applying Pythagoras's theorem was proposed. This optimisation involves eliminating the gaps or spaces that exist between each tube, since it is these gaps that cause fluctuations in force as the three tubes establish contact with each other. This method can help the design engineer to select tubes of a certain diameter and thickness so that all tubes are just touching before crushing is initiated. In doing so, minimum fluctuations in force can be achieved. Good correlation of results between the both the numerical and experimental methods indicate that the various finite element models can successfully simulate the response of such energy absorbers.

8.1.2 Slotted Tube Systems.

The concept of slotted tube systems such as the SCIPSS, the SCIPDS (crushed under both the plate and cylindrical indenter) and the SCOPSS was introduced. It was discovered that the compression of a SCIPSS exhibited a *non-monotonically increasing* force whilst the compression of a SCOPSS illustrated a *monotonically increasing* force.

It was found that the compression of a SCIPDS under a flat plate indenter did not produce a reasonably rectangular shaped response, since there was a continual increase in force for the entire displacement stroke. This was due to the interaction of the slots with the plate indenter. In the initial stages of deflection as loading proceeded, the tubes collapsed in the region of the slots as expected. However as deformation ensued, the hinge points or the kinks in tube generated due to the presence of the slots became in contact with the surrounding tube resulting in a continual increase in force. This increase in force was due the presence of a shorter moment arm as a result of using a plate indenter. It should be recalled that the compression of a tube with a plate indenter caused the resulting force to increase due to the shortening of the moment arm about the plastic hinge points in the tube. Therefore, it appears that the slots are not particularly useful when used in conjunction with a plate indenter. In view of this, the compression of a SCIPDS with a cylindrical indenter was analysed. This system exhibited an improved response than its previous counterpart. This was due to the fact that the cylindrical indenter provided a longer moment arm and thereby the resulting force to maintain the deformation was less in magnitude.

It can be seen that the integration of slots into energy absorbers can be a very useful way of obtaining a desired deformation characteristic. However, the outcome of such devices containing slots depends very much on its interaction with the various forms of loading indenters used. Slots can be varied geometrically and placed at different locations around each tube to produce varying responses and hence, this provides for another topic of interesting research that can contribute to the literature of energy absorbing devices. A satisfactory correlation was found between both the numerical and experimental methods indicating the success in the applicability of the finite element method to simulate such devices.

8.1.3 Damped Systems. (IPDS)

The third and final concept for the response optimisation of nested system was based on the IPDS family of energy absorbers. This particular form of energy absorber employs a simple mechanism based on the concept of cylindrical rods inserted between the gaps of the nested tubes. This technique provided an excellent interaction between the three tubes and the indenter to produce the rectangular shaped response. The interaction was such that the three tubes deformed synchronously upon loading and in addition to this, the radius of curvature of the cylindrical rods optimised the response such that the central and inner tube was neither geometrically hardening nor softening. The CIPDS illustrated the most

desirable response followed by the OIPDS. The latter system exhibited a slight softening response in the early stages of deflection; this was due to the fact that the interaction between the plate

and the outer tube was acting as a point indenter. This arrangement will increase the moment arm about the plastic hinges of the outer tube and hence the resulting force to maintain the deformation will be reduced. However, despite this behaviour, the overall rectangular shaped response was maintained. Also, the energy efficiencies of both the CIPDS and the OIPDS were the highest in comparison to the CIPSS and the OIPSS. This was due to the fact that a rigid perfectly force-deflection reaction will produce a 100% energy efficiency and therefore, it can be seen that the response exhibited by the CIPDS and the OIPDS is an approximation of this idealised response.

A dynamic analysis using both experimental and numerical techniques was performed on the CIPSS, CIPDS, OIPSS and the OIPDS respectively. It was discovered that strain rate of the material mild steel for the given applied velocity of the striker was not significant in increasing the magnitude of force for such systems. Moreover, inertial effects did not reduce or enhance the force magnitude of the various energy absorbers analysed. Therefore, the design engineer being aware of these facts can be assured that the energy absorption capacities of the systems analysed may be accurately predicted using quasi-static experimental techniques. In terms of the finite element method used to simulate these devices, it was found the strain rate parameters used in the material model within LS-DYNA largely over predicted the magnitude of force in the four devices analysed. The values of the strain rate parameters were taken from samples that experienced 5% strain. However, the devices analysed in this work experience significantly larger strain and hence, the current parameters used will not accurately predict the dynamic response of such systems. It should be noted however, that a strain rate insensitive material model could be used to accurately predict the dynamic response of such systems since both the experimental quasi-static and dynamic devices exhibited a similar magnitude of response. The design engineer should be aware that such an approach can only be taken within the parameters specified in this work, such as the impact velocity, mass of the striker, material used and the geometric dimensions of the tubes. Jing and Barton [43] also discovered that little differences in the mode of deformation between the quasi-statically and dynamically compressed tube systems.

8.2 Specific Energy Maximization of Nested Systems.

The specific energy maximisation of nested systems was the second objective of the work as mentioned in chapter one and was based on the concept of using external constraints to subject the devices to a greater volume of deformation.

8.2.1 External Constraints.

The specific energy maximisation of nested systems was based on the CIPSS device which was subjected to three various forms of load application such as the plate, cylindrical and a point load indenter. The external constraints consisted of rigid walls inclined at fifteen degrees and vertical rigid walls. The compression of the CIPSS subjected to each individual form of constraint and a combination thereof, was conducted independently in order to examine the effect of such constraints on the output response. This approach was taken for each of the various indenters. It should be noted that the concept of using the different indenters is based on the fact that in real applications, the geometry profile of the rigid object impinging on the energy absorber may neither be a flat rigid surface nor a point shaped indenter. Indeed it may an intermediate condition between the two limiting cases. Performance characteristics as described in chapter three was used to analyse the various devices subjected to the various loading conditions. It was discovered that application of the external constraints to the CIPSS which was compressed under a plate indenter did not produce desirable results. This was due to the 'locking' effect in which the indenter was unable to compress any further and as a result, a large reactive force was generated indicating the rigidness of the system. The application of the combined constraints to the CIPSS subjected to compression using the cylindrical indenter was analysed. It was found that both the energy efficiencies and the weight effectiveness for this system exhibited favourable results. Finally, the CIPSS subjected to a point load indenter offered the best outcome with both the energy efficiencies and the weight effectiveness exhibiting the highest results. Both the quasi-static and dynamic analysis of a CIPDS subjected to combined constraints by means of both the cylindrical and point load indenter was also analysed using numerical techniques. For the point load indenter, it was discovered that the CIPDS absorbed 4% more energy than its CIPSS counterpart. For the CIPDS compressed under a cylindrical, it was found that it absorbed 11% less energy. This was due to the fact that the outer tube of the CIPSS was wrapped around the cylindrical indenter resulting in more energy being absorbed. Overall, it was found that the application of external constraints as a method to increase the energy absorbing capacity of such devices is a

feasible one, particularly for the CIPSS subjected to a point load indenter. Correlation of results between both the experimental and finite element technique also proved very satisfactory for these particular devices analysed.

8.3 Advantages of the CIPDS and the OIPDS over other Energy Absorbers.

Although the operating loads of laterally compressed tubes is less than tubes compressed axially or otherwise, the energy absorbing capacity can be increased by encouraging the tube to collapse in an alternative mode which involves plastic hinges. This can be achieved as outlined in chapter six.

Axial loaded tubes or tubes involving a splitting or inversion mode of deformation contain certain defects. For example, axially loaded tubes result in a force-deflection response which consists of a high peak collapse load followed by large fluctuations of force about a mean load. This fluctuation about the mean load can be as much as 50% of the collapse load [94]. This is an undesirable feature for the reason that the impact loads transmitted to the protected structure will not be at its minimum magnitude. It is good practice to design the energy absorber such that the peak load is relatively close to its mean operating load.

Hence, it can be seen from the analysis of the CIPDS and the OIPDS in this work that the peak load is at the same magnitude for the complete displacement stroke. This indicates that the resulting deceleration force will kept to a minimum. In addition to this, it should also be noted that the mode of deformation is one of bending and therefore the resulting response will smooth without any incidence of oscillations.

Further to this, in relation to axially compressed systems, successful loading can only occur if the angle of load application is less than 15% to the longitudinal axis of the tube itself. In terms of transport applications, such behaviour is undesirable since the line of action of the kinetic force may be outside of this range of 15% [62]. It is possible to laterally load the CIPDS and the OIPDS over an angle greater than 15% since the tubes will still begin to deform synchronously for most of the deformation stroke before symmetry is lost.

It was also discovered that square shaped tubes compressed axially were found to be unstable due to the fact that they often failed in an Euler type global buckling mode. As a result, the energy absorbing capacity of such systems is reduced considerably.

Laterally loaded tubes are easier devices to build in comparison to tubes which are axially split or inverted (External or Internally). This is due to the fact that special dies and mandrels must be manufactured to a high level of accuracy to ensure successful operation

and desired output responses. A typical example of a die used for axial inversion of tubes is shown in Figure 2-11

Successful inversion of tubes is only possible when the material is of certain ductility and its strain hardening is not significant. In addition to this, the global dimensions of the die radius and the die radius must be with a compatible range in conjunction with suitable material properties in order to achieve the desired energy absorbing behaviour. Therefore it can be seen that axial inversion of ductile material is a complex process.

For bending dominated systems, a wide of ductile material can employed in order to convert the kinetic energy into plastic work which can be achieved through relatively little design parameters involved as seen in this work.

9 Conclusions and Recommendations.

9.1 Conclusions.

9.1.1 Out of Plane Standard Systems.

- The modified version of the CIPSS namely the COPSS can exhibit a *monotonically increasing* force-deflection response due to the orientation of the tubes relative to one another.
- The energy absorbing capacity of this COPSS remains the same in comparison to the CIPSS despite its different mode of deformation.
- Application of Pythagoras's theorem can be used to eliminate the gaps between the tubes within the COPSS, in doing so, the fluctuation in force can be minimised.

9.1.2 Slotted Tube Systems.

- The modified version of the CIPSS namely the SCOPSS can also exhibit a *monotonically increasing* force-deflection response.
- Compression of a SCIPDS with a plate indenter did not produce positive results for the reason that the slots do not interact with the indenter in a desired manner.
- The SCIPDS compressed with a cylindrical indenter can exhibit a rectangular force-deflection response which is the most desirable feature in the design of energy absorbers.
- Integration of slots into a tube or a system of tubes can produce some interesting results depending on its position on the tube and also on its interaction with the type of load indenter used.

9.1.3 Damped Systems.

- Damped systems provided the best design in contrast to the previous two designs mentioned for achieving a rectangular shaped response.
- The design involved a simple mechanism in which cylindrical rods or spacers were inserted between the tubes of the nested systems in order to eliminate the gaps.
- In doing so, the tubes deformed synchronously upon loading whilst the radius of curvature of the spacers assisted in the prevention of both a geometrically hardening and softening response, particularly for the CIPDS
- The OIPDS exhibited slight strain softening response when the collapse load was reached; however, the overall response of this system still produced very desirable results.

- In terms of performance characteristics, the CIPDS and OIPDS produced greater energy efficiencies in contrast to the CIPSS and OIPSS.
- A dynamic analysis of the CIPDS and the OIPDS using both the numerical and experimental techniques was performed. It was observed from the numerical method that an over prediction in the magnitude of force occurred for both the OIPSS and the OIPDS.
- It was found experimentally that the magnitude of response from the dynamic cases was similar to their quasi-static counterparts indicating the insignificance of strain rate and inertial effects for the given applied velocity of the striker.
- From this point above, the design engineer can be confident that quasi-static numerical techniques may be sufficient for describing the behaviour of such systems but only under the condition that same parameters such as impact velocity material type and tube dimensions are applied.

9.1.4 External Constraints.

- The CIPSS subjected to combined constraints under the action of a plate indenter did not produce positive results due to the stiffness of this device.
- The CIPSS compressed under a cylindrical indenter offered improved results in terms of energy efficiency and weight effectiveness.
- Compression of the CIPSS under a point load indenter produced the highest results in terms of its energy efficiency and whilst the CIPSS compressed with a cylindrical indenter exhibited the highest weight effectiveness.
- Overall, it was found that the application of rigid walls as a form of external constraints is a feasible method for increasing the specific energy absorbing capacity of metallic energy absorbers.

9.2 Recommendations for Further Work.

- Analysis of the optimised COPSS as a result of using Pythagoras's theorem and compare the output response to that of the standard COPSS analysed in this work.
- Examine the effect of applying the concept of external constraints on the optimised COPSS with the aim of increasing its energy absorbing capacity.
- A greater in-depth study on the design of slotted tube systems with the aim of achieving a rectangular shaped response. Such an approach can involve slots of different dimensions placed at different locations around the tube. Examine how the

position and size of the slots affect the collapse mechanism when loading is applied. It is possible to have each tube collapsing in a desired manner which may contribute to achieving a desired output response.

- An analysis can be performed on increasing the specific energy absorbing capacity of the oblong tubes by exposing the systems to the external constraints. This may be applied in particular to both the OIPSS and the OIPDS.
- The concept of braced tubes which increases the collapse load and therefore increasing the specific energy capacity may be applied to the nested systems, particularly the CIPDS and OIPDS. However, it would be envisaged that only two instead of three tubes should be analysed for the reason that the system becomes too complex. An illustration of this concept is depicted in Figure 10-2 in Appendix One.
- All of the above recommendations can be analysed using numerical techniques and positive results may be validated using quasi-static experimental techniques.
- A mathematical analysis of the CIPDS using the EST method (Equivalent Structure Technique) with the purpose of obtaining an expression with predicts the force-deflection response or the collapse load of each tube. For starting purposes, only a two tube nested system should be examined using this technique.

9.3 Thesis Contribution.

- A new family of kinetic energy absorbers in the form of nested metallic systems have been designed which can dissipate kinetic energy via a lateral mode of deformation. In particular the CIPDS and the OIPDS provided a unique way of exhibiting a rectangular shaped response using a bending mode of deformation due to a simple mechanism incorporated into the design.
- This new family of nested system can enhance their energy absorbing capacities by exposing them to external constraints whilst compressed under the action of various indenters.
- Finally, these nested systems provide a distinct advantage over energy absorbers for the reason that the bending mode of deformation is less complex in comparison to axially loaded or inverted tubes in terms of load application, design criteria and preparation as outlined in section 8.3.

- Finally it can be concluded that a positive outcome was achieved for both objectives, namely the response optimisation and specific energy maximisation of nested systems, and can thereby contribute to the literature in the field of energy absorbers.

10 Appendices.

10.1 Appendix One.

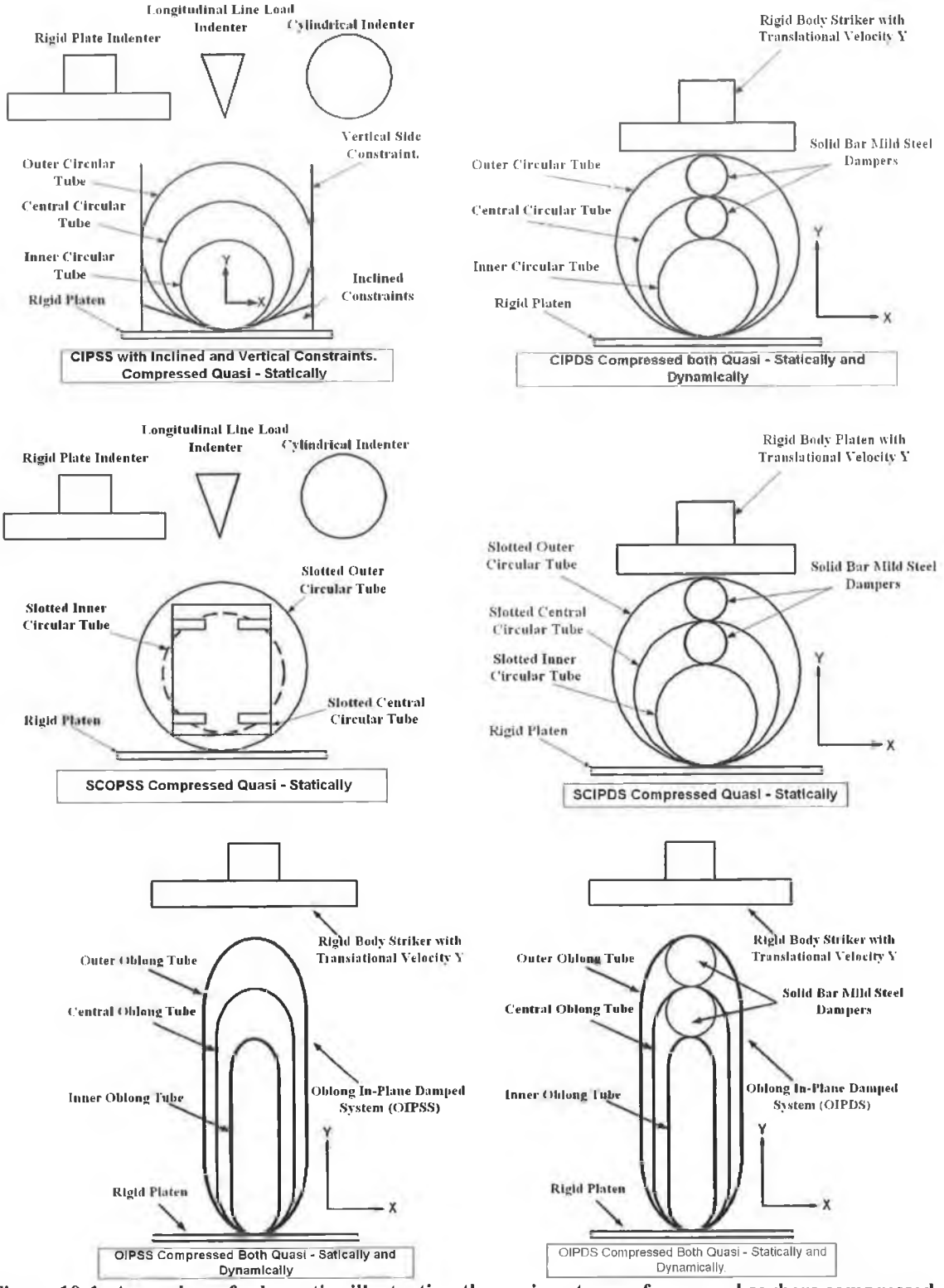

Figure 10-1: A number of schematics illustrating the various types of energy absorbers compressed either quasi – statically/dynamically or both.

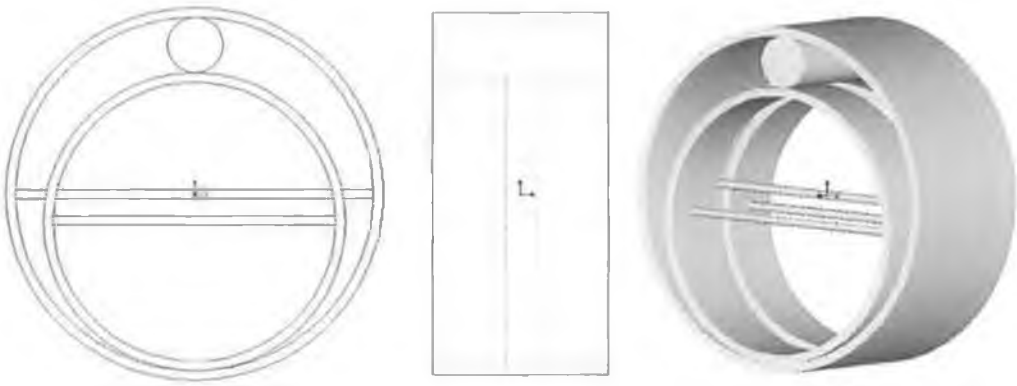

Figure 10-2: A CIPDS (2 tubes) with wire bracing as a means of increasing the collapse load.

10.2 Appendix Two.

Table 3. An Overview Table Illustrating the Various Types of Energy Absorbers Analysed.

Energy Absorber Category.	*Objective 1 or 2	External Constraints.	Dynamic Striker Velocity [m/s]	Quasi – Static Crosshead Speed.[m/s]
Plate Indenter.				
CIPSS	2	IC	N/A	166E-6
CIPSS	2	SC	N/A	166E-6
CIPSS	2	IC+SC	N/A	166E-6
COPSS	1	NC	N/A	16.6E-6
CIPSS	1	SLTS	N/A	50E-6
COPSS	1	SLTS	N/A	50E-6
SCOPSS	1	SLTS	N/A	83.33E-6
SCIPDS	1	SLTS	N/A	83.33E-6
SCIPSS	1	SLTS	N/A	83.33E-6
CIPSS	N/A	NC	5	50E-6
OIPSS	1	NC	5	83.33E-6
OIPDS	1	NC	5	83.33E-6
CIPDS	1	NC	5	83.33E-6
Point Indenter				
CIPSS	N/A	NC	N/A	100E-6
CIPSS	2	IC	N/A	166E-6
CIPSS	2	SC	N/A	50E-6
CIPSS	2	IC+SC	N/A	50E-6
COPSS	1	NC	N/A	16.6E-6
Cylindrical Indenter				
CIPSS	N/A	NC	N/A	16.6E-6
CIPSS	2	SC	N/A	16.6E-6
CIPSS	2	IC	N/A	16.6E-6
CIPSS	2	IC+SC	N/A	16.6E-6
COPSS	1	NC	N/A	16.6E-6

Table 4. Results obtained from experiments for the 11 samples tested.

	T_{final} (s)	$V_{initial}$ (mm/s)	V_{final} (mm/s)	Stroke (mm)	Energy (J)
CIPSS Length (10mm)					
SP1	0.0176	4.78	3.12	74	252
SP2	0.0174	4.61	3.03	70	233
SP3	0.0176	4.60	2.99	71	236
SP4	0.0176	4.61	3.03	71	233
SP5	0.0172	4.60	3.02	70	232
CIPDS Length(15mm)					
SP6	0.0196	3.72	0.75	45	246
SP7	0.0192	3.78	0.82	45	252
SP8	0.0194	4.49	1.48	59	332
SP9	0.0196	4.74	1.48	64	373
SP10	0.0196	4.60	1.55	62	346
SP11	0.0196	4.58	1.50	61	346

Table 5. Results obtained from experiments for the 10 samples tested.

	T_{final} (s)	$V_{initial}$ (mm/s)	V_{final} (mm/s)	Stroke (mm)	Energy (J)
OIPSS Length (10mm)					
SP1	0.0186	4.75	3.45	81	208
SP2	0.0188	4.76	3.50	82	210
SP3	0.0192	4.76	3.50	84	209
OIPDS Length(15mm)					
SP4	0.0196	4.76	1.62	63	369
SP5	0.0194	4.76	1.63	62	368
SP6	0.0192	4.74	1.90	64	349
SP7	0.0194	4.78	1.77	64	363
SP8	0.0194	4.78	1.82	64	360
SP9	0.0196	4.76	2.00	66	345
SP10	0.0194	4.75	1.84	64	355

Table 6. The Chemical Composition of Mild Steel Grade ST 37 – 2.

Grade of steel	Carbon %	Silicon %	Manganese %	Sulphur %	Phosphorous %	Aluminium %
ST 37-2	0.05 – 0.14	<0.30	0.4 – 0.65	<0.025	<0.025	0.02 – 0.07

10.3 Appendix Three.

Peer Reviewed Journals:

- Morris, E., Olabi, A., Hashmi, S., "Analysis of Nested Tube Type Energy Absorbers with Different Indenters and Exterior Constraints." Accepted for publication in the Journal of Thin-Walled Structures.

- Morris, E., Olabi, A., Hashmi, S., "The Quasi-Static Analysis of Circular and Oblong Type Energy Absorbers in a Nested Arrangement." 2006, Submitted for review to the International Journal of Mechanical Science.

- Morris, E., Olabi, A., Hashmi, Gilchrist, M.D., S., "Optimised Design of Nested Circular Tube Energy Absorbers under Lateral Impact Loading." 2006, Submitted for review to the International Journal of Mechanical Science.

- Morris, E., Olabi, A., Hashmi, Gilchrist, M.D., "Optimised Design of Nested Oblong Tube Energy Absorbers under Lateral Impact Loading." 2006, Accepted for publication in the International Journal of Impact Engineering.

- Morris, E., Olabi, A., Hashmi, S., "The Lateral Crushing of Circular and Non-Circular Tube Systems under Quasi-Static Conditions." Submitted for review to the Journal of Materials processing Technology.

Conference Proceedings:

- Morris, E., Olabi, A., Hashmi, S., "FE Simulation and Experimentation of Nested Systems under Static and Impact Loading Conditions." In: Proceedings of the 12th International Conference on Experimental Mechanics. Bari, (Italy) 2004. p. 196-203.

- Morris, E., Olabi, A., Hashmi, S., "Post Collapse Response of Nested Tube Systems with Side Constraints." In: Vickery, J., editor. Proceedings of the 22nd International Manufacturing Conference. Tallaght, Dublin (Ireland) 2005. p. 693-700.

- Morris, E., Olabi, A., Hashmi, S., "Experimental and Numerical Analysis of the Static Lateral Compression of Tube Type Energy Absorbers with Different Indenters." The Engineers Journal, 2005. 59(8) p. 505 - 510.

- Morris, E., Olabi, A., Hashmi, S., "Plastic Response of Nested Systems under Static and Dynamic Loading Conditions using FE and Experimental Techniques." In: Dulieu-Barton J., Quinn, S., editors. Proceedings of the 4th International Conference on Advances in Experimental Mechanics. Trans Tech Publications, 2005, Vol 3-4: p 377-382.

- Morris, E., Olabi, A., Hashmi, S., "The lateral crushing of circular and non-circular tube systems under quasi-static conditions." Accepted for the AMPT conference in August Las Vegas 2006.

- Morris, E., Olabi, A., Hashmi, S.," Experimental and Numerical Analysis of Slotted Tube Systems under quasi-static loading." Accepted for the International Manufacturing Committee 23 in Belfast September 2006.

11 References.

[1] W Johnson, A.G Mamalis. Crashworthiness of Vehicles, Mechanical Engineering Publications Limited, London, 1978.

[2] J Morton, Editor. Structural Impact and Crashworthiness, Volume 2, Conference Papers, Elsevier Applied Science Publishers, 1984.

[3] N Jones, T Wierzbicki. Structural Crashworthiness and Failure, Elsevier Science Publishers, New York, 1993.

[4] G Lu, T Yu. Energy Absorption of Structures and Materials, Woodhead Publishing Limited, Cambridge, 2003.

[5] J Zukas. Impact Dynamics, Wiley, Chichester, 1982.

[6] A Ezra, R Fay. An Assessment of Energy Absorbing Devices for Prospective use in Aircraft Situations. In: Dynamic behaviour of Structures. Editors: Hermann G, N Perrone, Pergammon Press, Oxford, 1972.

[7] W. Johnson. The elements of Crashworthiness: Scope and Actuality, Proc. Inst. Mech. Engrs., J. of Automobile Eng, Part D, 204, (1990), 255-273.

[8] United States Vehicle Accidents Statistics. [Online, Accessed from January 2005]. <www.nrd.nhtsa.dot.gov/departments/nrd-30/ncsa>

[9] Australian Transport Safety Bureau. [Online, Accessed January 2005]. <www.atsb.gov.au/pdf/anrev2000.pdf.>

[10] Vehicle Accidents Statistics, Metropolitan Police Service. [Online, Accessed January 2005]. <www.driving.co.uk/3a2.html>

[11] Irish Vehicle Accidents Statistics. [Online, Accessed January 2005]. < www.garda.ie/angarda/statistics98/nroadstats>

[12] C Calladine, R English. Strain rate and inertia effects in the collapse of two types of energy absorbing structure. International Journal of Mechanical Science. 1984; 26 (11-12):689-701.

[13] T Zhang, T Yu. A note on a velocity sensitive energy-absorbing structure. International Journal of Impact Engineering. 1989; 8 (1): 43-51.

[14] L Tam, C Callidine. Inertia and strain-rate effects in a simple plate-structure under impact loading. International Journal of Impact Engineering. 1991; 11 (3): 349-377.

[15] X Su, T Yu, S Reid. Inertia-sensitive impact energy-absorbing structures. Part 1: Effects of inertia and elasticity. International Journal of Impact Engineering. 1995; 16 (4): 651-672.

[16] X Su, T Yu, S Reid. Inertia-sensitive impact energy-absorbing structures. Part 2: Effect of strain rate. International Journal of Impact Engineering. 1995; 16 (4): 673-689.

[17] S Reid. Plastic deformation mechanisms in axially compressed metal tubes used as impact absorbers. International Journal of Mechanical Science. 1993; 35 (12): 1035-1052.

[18] S Reid, T Reddy. Static and dynamic crushing of tapered sheet metal tubes of rectangular cross-section. International Journal of Mechanical Science. 1986; 28 (9): 623-637.

[19] S Guillow, G Lu, R Grzebieta. Quasi-static axial compression of thin-walled circular aluminium tubes. International Journal of Mechanical Science. 2001; 43 (9): 2103-2123.

[20] B Wang, G Lu. Mushrooming of circular tubes under dynamic axial loading. Journal of Thin-Walled Structures. 2002; 40 (2): 167-182.

[21] S Hsu, N Jones. Quasi-static and dynamic axial crushing of thin-walled circular stainless steel, mild steel and aluminium alloy tubes. Internal Journal of Crashworthiness. 2004; 9 (2).

[22] M Zeinoddini, G Parke, J Harding. Axially pre-loaded tubes subjected to lateral impacts: an experimental study. International Journal of Impact Engineering. 2002; 27 (6): 669-690.

[23] M Langseth, O Hopperstad, T Berstad. Crashworthiness of aluminium extrusions: validation of numerical simulation, effect of mass ratio and impact velocity. International Journal of Impact Engineering. 1999; 22 (9-10): 829-854.

[24] A Rossi, Z Fawaz, K Behdinan. Numerical simulation of the axial collapse of thin-walled polygonal section tubes. Journal of Thin-Walled Structures. 2005; 43 (10): 1646-1661.

[25] G Nagel, D Thambiratnam. A numerical Study on the impact response and energy absorption of tapered thin-walled tubes. International Journal of Mechanical Science. 2004; 46 (2): 201-216.

[26] G Nagel, D Thambiratnam. Computer simulation and energy absorption of tapered thin-walled rectangular tubes. Journal of Thin-Walled Structures. 2004; 43 (8): 1225-1242.

[27] G Nagel, D Thambiratnam. Dynamic Simulation and energy absorption of tapered tubes under impact loading. Internal Journal of Crashworthiness. 2004; 9 (4).

[28] G Nagel, D Thambiratnam. Energy absorption and performance of a vehicle impact protection system. In: Structures under Shock and Impact (International Conference) Montreal 2002.

[29] N Gupta, S Gupta. Effect of annealing, size and cut-outs on axial collapse behaviour of circular tubes. International Journal of Mechanical Science. 1993; 35 (7): 597-613.

[30] A Colokoglu, T Reddy. Strain rate and inertial effects in free external inversion of tubes. International Journal of Crashworthiness. 1996; 1 (1).

[31] D Webb, J Webster, K Kormi. Finite element simulation of energy absorption devices under axial static compressive and impact loading. Internal Journal of Crashworthiness. 2001; 6(3).

[32] A Kinkead. Analysis for inversion load and energy absorption of a circular tube. Journal Of Strain Analysis. 1983; 18 (3).

[33] S Reid, J Harrigan. Transient effects in the quasi-static and dynamic internal inversion and nosing of metal tubes. International Journal of Mechanical Science. 1998; 40 (2-3): 263-280.

[34] J. Harrigan, S. Reid, C. Peng, Inertia effects in impact energy absorbing materials and structures. International Journal of Impact Engineering. 1999; 22 (9-10): 955-979.

[35] P Miscow, H Al-Qureshi. Mechanics of static and dynamic inversion processes. International Journal of Mechanical Science. 1997; 39 (2): 147-161.

[36] T Reddy, S Reid. Axial splitting of circular metal tubes. International Journal of Mechanical Science. 1986; 28 (2): 111-131.

[37] G Lu, L Ong, B Wang, H NG. An experimental study on tearing energy in splitting square metal tubes. International Journal of Mechanical Science. 1994; 36 (12): 1087-1097.

[38] P Jiang, W Wang, G Zhang. Size effects in the axial tearing of circular tubes during quasi-static and impact loadings. International Journal of Impact Engineering. 2005. Article in press.

[39] W Stronge, T Yu, W Johnson. Long stroke energy dissipation in splitting tubes. Int. International Journal of Mechanical Science. 1983; 25 (9): 637-647.

[40] X Huang, G Lu, T Yu. Energy absorption in splitting square metal tubes. Journal of Thin-Walled Structures. 2002; 40 (2): 153-165.

[41] Huang X, Lu G, Yu T. On axial splitting and curling of circular metal tubes. International Journal of Mechanical Science. 2002; 44 (11): 2369-2391.

[42] R Sowerby, W Johnson, S Samanta. The Diametric compression of circular rings by "point" loads. International Journal of Mechanical Science. 1968; 10: 369-383.

[43] Y Jing, D Barton. The response of square cross-section tubes under lateral impact loading. Internal Journal of Crashworthiness. 1998; 3 (4).

[44] S Thomas, S Reid, W Johnson. Large deformations of thin-walled circular tubes under transverse loading – 1. International Journal of Mechanical Science. 1976; 18: 325-333.

[45] S Thomas, S Reid, W Johnson. Large deformations of thin-walled circular tubes under transverse loading – 11. International Journal of Mechanical Science. 1976; 18: 387-397.

[46] S Thomas, S Reid, W Johnson. Large deformations of thin-walled circular tubes under transverse loading – 111. International Journal of Mechanical Science. 1976; 18: 501-509.

[47] Y Zhao, A Holmes, J Fang. The load carrying capacity of circular rings with arc shaped supports. International Journal of Pressure Vessel and Piping. 1996; 67: 7-10.

[48] Y Zhao, J Fang. Experimental investigation into the dynamic behaviour of circular rings with arc shaped supports. International Journal of Pressure Vessel and Piping. 1995; 62: 83-85.

[49] S Reid, W Bell. Influence of strain hardening on the deformation of thin rings subjected to opposed concentrated loads. International Journal of Solids and Structures 1983. 18: 643-658.

[50] G Lu. A study of the crushing of tubes by two indenters. International Journal of Mechanical Science. 1993; 35 (3-4): 267-278.

[51] K Liu, K Zhao, Z Gao, Yu T. Dynamic behaviour of ring systems subjected to pulse loading. International Journal of Impact Engineering. 2005; 31 (10): 1209-1222.

[52] V Shim, W Stronge. Lateral Crushing of thin-walled tubes between cylindrical indenters. International Journal of Mechanical Science. 1986; 28(10): 683-707.

[53] C Kardaras, G Lu. Finite element analysis of thin walled tubes under point loads subjected to large plastic deformation. In: Key Engineering Materials Vols 177-180 pp. 733-738. Trans Tech Publications Switzerland 2000.

[54] T Wierzbicki, M Suh. Indentation of tubes under combined loading. International Journal of Mechanical Science. Sci. 1988; 30 (3-4): 229-248.

[55] S Ghosh, W Johnson, S Reid, T Yu. On rings and short tubes subjected to centrally opposed concentrated loads. International Journal of Mechanical Science. 1981; 23: 183-194.

[56] J DeRuntz. P Hodge. Crushing of a tube between rigid plates. Transactions of ASME, Journal of Applied Mechanics 1963; 30: 391–395.

[57] R Redwood. Discussion of ref. 9. Transactions of ASME, Journal of Applied Mechanics 1964; 31: 357-358.

[58] S Reid, T Reddy. Effect of strain hardening on the lateral compression of tubes between rigid plates. International Journal of Solids and Structures. 1978; 14: 213-225.

[59] T Reddy, S Reid. Phenomena associated with the lateral crushing of metal tubes between rigid plates. International Journal of Solids and Structures.1980; 16: 545-562.

[60] N Gupta, G Sekhon, P Gupta. Study of lateral compression of round metallic tubes. Journal of Thin-Walled Structures 2005; 43(6): 895-922.

[61] M Avalle, L Goglio. Static lateral compression of aluminium tubes: strain gauge measurements and discussion of theoretical models. Journal of Strain Analysis 1997; 32 (5) 335-343.

[62] T Reddy, S Reid. Lateral compression of tubes and tube-systems with side constraints. International Journal of Mechanical Science. 1979; 21(3): 187-199.

[63] S Reid, T Reddy. Large deformation behaviour of thick rings under lateral compression. In: Proceedings Symposium on Large Deformations, Delhi, 1979.

[64] T Reddy, S Reid. On obtaining material properties from the ring compression test. Nuclear Engineering and Design 1979; 52: 257-263.

[65] N. Shrive, K. Andrews, G. England, The Impact Energy Dissipation of Cylindrical Systems. Structural Impact and Crashworthiness. J. Morton, editor. Elsevier Applied Science Publishers. London, England, 1984. Vol 2: p. 544-554.

[66] W. Johnson, S. R. Reid, T. Y. Reddy. The Compression of Crossed Layers of Thin Tubes. International Journal of Mechanical Science. 1977, 19(7):423-428.

[67] S Reid, T Reddy, C Austin. Dynamic deformation of tube and ring systems. In: Proceedings of the 5th symposium on engineering application of mechanics, 1980, 301-305.

[68] S Reid, T Reddy. Effects of strain rate on the dynamic lateral compression of tubes. In: Inst. Physics Conference. SERIAL. No. 47: Chapter 3. 1979, 288-298.

[69] S. R., Reid, T. Y. Reddy. Experimental Investigation of Inertia Effects in One-Dimensional Metal Ring Systems Subjected to End Impact -- I. Fixed-Ended Systems. International Journal of Impact Engineering. 1983, 1(1):85-106.

[70] T. Y. Reddy, S. R. Reid, R. Barr. Experimental Investigation of Inertia Effects in One-Dimensional Metal Ring Systems Subjected to End Impact--II. Free-Ended Systems. International Journal of Impact Engineering. 1991, 11(4):463-480.

[71] S. R. Reid, S. L. K. Drew, I.J.F. Carney. Energy Absorbing Capacities of Braced Metal Tubes. International Journal of Mechanical Science. 1983, 25(9-10):649-667.

[72] D Leu. Finite element simulation of the lateral compression of aluminium tube between rigid plates. International Journal of Mechanical Science.1999; 41: 621-638.

[73] N Gupta, P Ray. Collapse of thin-walled empty and filled square tubes under lateral loading between rigid plates. International Journal of Crashworthiness 1998; 3 (3).

[74] A Sherbourne, F Lu. Strain hardening in the moving hinge method. International Journal of Solids and Structures 1993; 30 (24): 3475-3489.

[75] L. Wu, J. F. Carney. Initial Collapse of Braced Elliptical Tubes Under Lateral Compression. International Journal of Mechanical Science. 1997, 39(9):1023-1036.

[76] L. Wu, J. F. Carney. Experimental Analyses of Collapse Behaviours of Braced Elliptical Tubes under Lateral Compression. International Journal of Mechanical Science. 1998, 40(8):761-777.

[77] M.J. Turner, R. W. Clough, H.C. Martin, L.J. Topp. Stiffness and Deflection Analysis of Complex Structures. Journal Of Aeronautical Science. Volume 23, 805-832.

[78] J.H. Argyris, S. Kelsey. Energy Theorems and Structural Analysis in Aircraft Engineering. (1955) Volumes 26 and 27.

[79] R.W. Clough. The Finite Element In Plane Stress Analysis. Proceedings of the 2nd A.S.C.E. Conference on Electronic Computation, Pittsburgh.

[80] K.J. Bathe. Finite Element Procedures. Prentice Hall. 1996.

[81] R.D. Cook. Concepts and Applications of Finite Element Analysis. Wiley. 1981

[82] M. A. Crisfield. Non-linear Finite Element Analysis of Solids and Structures. Wiley. 1991-1997.

[83] L.J. Segerlind. Applied finite element analysis. Wiley. 1984.

[84] http://en.wikipedia.org/wiki/Finite_element_method_in_structural_mechanics

[85] ANSYS 8.1 Online HTML Help Documentation.

[86] http://www.dynasupport.com/Support/tutorial/users.guide/time.integration/

[87] http://ansys.net/ansys/tips_sheldon/STI07_Lagrange_Multipliers.pdf

[88] J. Hallquist. LS Dyna-3D Theoretical Manual.: Livermore Software Technology Corporation. 1993.

[89] P. Thornton. Energy absorption by structural collapse. Chapter 4 Structural Crashworthiness. Editors: N. Jones and T. Wierzbicki,. Butterworths, London. 1993

[90] LS-Dyna Theoretical Manual, Livermore Software Technology Corporation: Livermore, California; May 1998.

[91] W. Johnson, Impact Strength of Materials, Edward Arnold, London 1972.

[92] V. P. Shim, W. J. Stronge. Lateral Crushing of Thin-Walled Tubes between Cylindrical Indenters," International Journal of Mechanical Science. 1986, 28(10):683-707.

[93] H.H. Ruan, Z.Y. Gao, T.X Yu. Crushing of thin-walled spheres and sphere arrays. International Journal of Mechanical Science. 2005. Article in Press.

[94] W. Abramowicz s, N. Jones. Dynamic Progressive Buckling of Circular and Square Tubes. International Journal of Impact Engineering. 1986, 4(4):243-270.